Quantum Effects for Spintronic Devices Optimization

Hugo Manuel Gonçalves da Silva

Dissertation submitted to the Faculty of Science
of the University of Porto in partial fulfillment
of the requirements for the degree of Doctor in Physics
2009

Title: Quantum Effects for Spintronic Devices Optimization

Author: Hugo Manuel Gonçalves da Silva

Dissertation submitted to the Faculty of Science of the University of Porto in partial fulfillment of the requirements for the degree of Doctor in Physics 2009

Advisory Committee:

Professor Yuriy G. Pogorelov, Advisor, and Professor João P. Araújo, Co-Advisor

from University of Porto

Professor Henrique L. Gomes, Co-Advisor from University of Algarve

The simplicity of these lines hide the tremendous complexity of writing them,

the insignificant results shown here do not reflect an unconditional dedication...

What we are as humans is much more important than what we can get or conquer,

our dreams are by far much more important than our triumphs or defeats in life.

This work is dedicated to my beloved Family and specially to Ana.

Acknowledgments

First of all, I will like to deeply acknowledge the crucial help and support of my Mother, Father, Sister and two special friends Victor and Angela Santos. Only, with their advises it was possible to face the various difficulties that appeared during the realization of this work. Once again, thank you very much.

I am very grateful to my supervisors Prof. Yuriy Pogorelov and Prof. João Pedro Araújo from the University of Porto and to Prof. Henrique Leonel Gomes from University of Algarve. For introducing me to the interesting topics studied during this thesis and for their unconditional help. With them I learned plenty of things as a physicist, but a lot more as a human being. Thank you once again.

I will, also, want to acknowledge Prof. João Bessa Sousa and Prof. João Lopes dos Santos, for their fascinating Solid State Physics lectures, and to Prof. Carlos Herdeiro for his incredible Quantum Mechanical lectures, they strongly motivated me to investigate various aspects of this thesis.

A particular recognition is made to Prof. José Mariano, from the Physics Department of the University of Algarve that gave me a fundamental support in the experimental realization of this work, introducing me to LabView and skillfully repairing the electromagnet supplied by Prof. J. J. Moura from the New University of Lisbon, to whom I give my thanks.

The fundamental help of Miguel Dias Costa, from the Physics Center of Porto (CFP), in performing part of the numerical calculations of this work (the most difficult ones, in fact) is here truly recognized and deeply acknowledge.

It is important to express my gratitude to Sylvie Alves and Ana Nunes for their help in the French revision of the Résumé. A special thanks is given here to Ana Nunes for the friendly support that she gave me during the writing process of this work, and for being an inspiration to finish it. Again, thank you very much Ana.

Acknowledgments are also given to my friends in the University of Algarve, especially, Bruno Romeira, but also to Pedro Pinto, Patrick Sousa, Prof. José Longras Figueiredo, Prof. Rui Guerra, Prof. Valentin Besserguenev, Paulo Silva, Mário Freitas, Sofia Cavaco and Odete Cordeiro, and to Catarina Casteleiro form the Prof. Reinhard Schwarz group at IST. In addition, the friendship and significant help of the rest of IFIMUP group is acknowledged too, mainly, João Ventura, André Pereira, Diana Leitão, and André Espinha, who gave me an indispensable help through this work, but also José Miguel Teixeira, Lino Pereira, João Amaral, Gleb Kakazei, Gonçalo Oliveira and all the other.

Thanks are given to Prof. Paulo Freitas, director of INESC-MN, and other members of his group, Susana Freitas, Jiangwei Cao and Helena Alves.

I am in debt with *Fundação para a Ciência e Tecnologia* for their funding of my doctoral years (SFRH/BD/24190/2005) and of research projects and conference attendances.

I will like to further thank the *Wikipedia Foundation* and *Skype Technologies S.A.* without them this work would have been, for certain, much more difficult.

Lastly, I am most grateful to God and to His marvelous creation!!!

Abstract

This work is mainly dedicated to the study of spin dependent transport in magnetic nanostructures. The principal objective is the optimization of the magnetoresistive performance of such structures, in order to built high density Magnetic Random Access Memories (MRAM). Nevertheless, new resistive properties are also found, that could be useful for another type of non-volatile memory device, in this case, Resistive Random Access Memories (ReRAM). The thesis is basically divided into two parts, the first one considers the theoretical analysis of multilayered magnetic junctions and the second one is dedicated to the experimental study of magnetic granular multilayers.

Theory: In this part, spin dependent coherent transport (in the current perpendicular to plane geometry) through single, double and triple spacer magnetic junctions were studied in the single-band tight binding approximation. From the exact calculation of wave states in the entire system it was possible to calculate both the transmission and reflection coefficients. These coefficients were then used in the Landauer-Büttiker formalism to calculate the conductance which is dependent on the specific magnetic configuration of the ferromagnetic electrodes. As a generalization, complex structures were investigated with the use of a matrix method developed to describe arbitrary multilayered systems. The main finding of these treatments was an impressive enhancement of the magnetoresistance performance, higher than $\sim 3000\%$ (at zero temperature), when the conduction regime crossed from tunnel to metallic, in the so called *shallow band regime*. In addition, two extensions were made in the simplest case of a single spacer magnetic junction: the effect of voltage and temperature in the magnetoresistance, and calculation of the transmission and reflection coefficients for an arbitrary angle between the magnetizations. The first consideration showed that the magnetoresistance enhancement still occurs at room-temperature, but it strongly decreases with the applied voltage. The second one will enable the calculation of both charge and spin-transfer dependencies on the relative angle between magnetizations. In addition, tunnel transport processes were considered in a square lattice of metallic nanogranules embedded into insulating host. Based on a simple model with three possible charging states ($\pm$, or 0) of a granule and three kinetic processes (creation or recombination of a $\pm$ pair, and charge translation) between neighbor granules, mean-field kinetic theory was developed. The interplay between charging energy and temperature, and between the applied electric field and the Coulomb fields by non-compensated charge density was carefully studied. The resulting charge and current distributions were found to differ essentially in free area (FA) or in contact areas (CA) of a granular layer with respect to macroscopic metallic contacts. Steady state dc transport in CA is accompanied with charge accumulation and non-ohmic behavior of conduction. Approximate analytic solutions were obtained for characteristic regimes (low or high charge density) of such conduction.

Experiment: This part was mainly focused on the study of diluted magnetic granular multilayered nanostructures. The films were composed of ten granular $Co_{80}Fe_{20}$ layers (with nominal thickness of 0.7 and 0.9 nm) embedded into an insulating Al_2O_3 matrix. The magnetization measurements revealed a slight deviation from the superparamagnetic state due to dipolar interactions among neighbor grains. The blocking temperatures are of the order of ~ 40 K, decreasing with the applied magnetic field. The anisotropy constant

values found, $\sim 1.4 \times 10^6$ erg cm^{-3}, are higher than the typical bulk ones, due to surface effects. Transport measurements were performed in the current in plane geometry using two gold contacts evaporated on top of the samples. The magneto-transport data revealed that room temperature magnetoresistance has a sizeable value of 6% at fields of $H \approx 10$ kOe. Moreover, from the extrapolation of the Inoue-Maekawa law fit it is expected that magnetoresistance could reach $\sim 8\%$ for saturation fields of $H_s \sim 50$ kOe. Further, resistive switching properties were also found in these samples (using the same current geometry). It was shown that the resistive switching is followed by a discrete capacitive switching, leading to the development of a new model for these phenomena, different from the common filamentary theory.

Resumo

Este trabalho está dedicado, principalmente, ao estudo do transporte electrónico dependente do "spin" em nano-estruturas magnéticas. O principal objectivo é a optimização da performance magnetoresistiva destas estruturas para a construção de Memórias Magnéticas de Acesso Aleatório (MRAM) de elevada densidade de armazenamento de dados. No entanto, foram também descobertas novas propriedades resistivas que poderão ser úteis para outro tipo de memórias não voláteis, neste caso, Memórias Resistivas de Acesso Aleatório (ReRAM). A tese divide-se, basicamente, em duas partes, a primeira parte considera a análise teórica de junções multicamada magnéticas e na segunda faz-se um estudo experimental de multicamadas granulares magnéticas.

Parte teórica: Nesta parte, foi estudado o transporte electrónico coerente e dependente do "spin" (na configuração de corrente perpendicular aos planos atómicos) em junções magnéticas com "espaçador" único, duplo e triplo utilizando a aproximação de electrões fortemente ligados restrita a processos com apenas uma banda electrónica. Do cálculo exacto das funções de onda em toda a estrutura foi possível calcular os coeficientes de transmissão e de reflexão. Estes coeficientes foram então utilizados, no contexto do formalismo de Landauer-Büttiker, no calculo da condutância que, naturalmente, depende da configuração magnética específica do eléctrodos ferromagnéticos. A generalização para estruturas complexas foi feita com recurso a um método matricial desenvolvido para descrever sistemas multicamada abirtrátios. O principal resultado destes tratamentos foi um impressionante aumento da magneto-resistência, maior que $\sim 3000\%$ (a temperatura zero), quando o regime de condução passa de túnel para metálico, designado *regime de banda pouco profundo*. Além disso, foram feitas duas extensões no caso mais simples de um único "espaçador": o efeito de voltagem e da temperatura na magneto-resistência e o cálculo dos coeficientes de transmissão e de reflexão para ângulos arbitrários entre as magnetizações. A primeira consideração mostrou que o aumento da magneto-resistência persiste mesmo à temperatura ambiente, mas decresce fortemente com a aplicação da voltagem. A segunda possibilitará o cálculo da dependência com ângulo relativo das magnetizações da transferência de carga e de "spin". Além disso, foram considerados os processos de transporte de túnel numa estrutura quadrada de nanogranulos metálicos incorporados numa matriz isoladora. Utilizando um modelo simples com três possíveis estados de carga ($\pm$, ou 0) de um grânulo e três processos cinéticos (criação ou recombinação de $\pm$ par, e transporte de carga) entre grânulos vizinhos, foi desenvolvida teoria de campo médio cinética. A interacção entre a carga de energia e a temperatura, e entre o campo eléctrico aplicado e os campos de Coulomb (resultantes de densidades de carga não compensadas) foi cuidadosamente estudada. A carga resultante e as distribuições de corrente foram encontradas e diferem essencialmente na área livre da área de contacto de uma camada granular com os contactos macroscópicos metálicos. Transporte no estado estacionário é acompanhado de acumulação de carga e de efeitos não-ohmicos de condução na área de contacto. Soluções analíticas aproximadas foram obtidas para dois regimes característicos de condução (alta ou baixa densidade de carga).

Parte experimental: Esta parte foi fundamentalmente focada no estudo de nanoestruturas multicamada magnéticas granulares no limite diluído. Os filmes eram compostos por dez camadas granulares de $Co_{20}Fe_{80}$ (com espessuras médias de 0.7 e 0.9 nm)

embebidos numa matriz isoladora de Al_2O_3. As medidas de magnetização revelaram um pequeno desvio do estado superparamagnético devido às interacções dipolares entre grãos vizinhos. As temperaturas de bloqueio são da ordem de ~ 40 K, diminuindo com o campo aplicado. Os valores encontrados para as constantes de anisotropia, $\sim 1.4 \times 10^6$ erg cm^{-3}, são maiores que os típicos de amostras macroscópicas, devido aos efeitos de superfície. As medidas de transporte foram feitas, neste caso, na geometria de corrente no plano utilizando dois contactos de ouro evaporados em cima das amostras. As medidas de magnetotransporte revelaram que a magneto-resistência à temperatura ambiente tem um valor significativo de 6% para campos $H \sim 10$ kOe. Sendo que extrapolando os dados experimentais utilizando a conhecida lei de Inoue-Maekawa é de esperar que a magneto-resistência possa chegar a $\sim 8\%$ para campos de saturação de $H_s \sim 50$ kOe. Finalmente, propriedades de "comutação resistiva" foram também encontradas nestas amostras (utilizando a mesma geometria de corrente). Foi demonstrado que a "comutação resistiva" é seguida de uma "comutação discreta da capacidade", o que levou ao desenvolvimento de um novo modelo para este fenómeno que é diferente da comum teoria filamentar.

Résumé

Ce travail est principalement dédié à l'étude du transport dépendant du spin en nanostructures magnétiques. Le principal objectif est l'optimisation de la performance magneto-résistive de ces structures, en vue de construire des mémoires magnétiques de haute densité de stockage de données Random Access Memories (MRAM). Néanmoins, de nouvelles propriétés de résistance qui pourraient être utiles pour un autre type de mémoire non-volatile, ont été découvertes, il s'agit des Resistive Random Access Memories (ReRAM).

La thèse est essentiellement divisée en deux parties, la première traite de l'analyse théorique des jonctions avec multicouches magnétiques et la seconde est consacrée à l'étude expérimentale des multicouches magnétiques granulaires.

Théorie: Dans cette partie, le transport cohérent du spin à travers des jonctions magnétiques avec une, deux et trois couches non-magnétiques a été étudiée (dans la géométrie de courant perpendiculaire au plan), dans la approximation de seule bande des électrons fortement contraignante. Depuis le calcul exact des états quantiques dans l'ensemble du système, il a été possible de calculer à la fois les coefficients de transmission et de réflexion. Ces coefficients sont ensuite utilisés dans le formalisme de Landauer-Büttiker pour le calcul de la conductance, qui dépend de la configuration magnétique des éléments ferromagnétiques. Comme une généralisation, des structures complexes ont été étudiées avec l'utilisation d'une méthode matricielle pour décrire les systèmes multicouches arbitraire. Le principal résultat de ces traitements a été un impressionnant renforcement de la magnétorésistance, supérieur à 3000% (à la température de zéro), lors de la traversée du régime de conduction tunnel pour métallique, dans le régime de bande peu profond. De plus, deux extensions ont été faites dans le cas d'une jonction magnétique simple: l'effet de voltage et de température dans la magnétorésistance, et le calcul des coefficients de transmission et de réflexion à l'angle arbitraire entre les magnétisations. Le premier examen a montré que l'amélioration de magnétorésistance persiste à température ambiante, mais il diminue fortement avec le voltage appliqué. Le second permettra le calcul des dépendances du transport de charge et spin avec l'angle relatif des magnétisations. En outre, les processus de transport tunnel ont été pris en compte dans un réseau carré de nanogranules métalliques intégrés dans une isolante d'accueil. Basé sur un modèle simple à trois états possibles de charge (±, ou 0) d'une granule et trois processus cinétiques (création ou la recombinaison d'un ± paire, et le transport de charge) entre granules voisines, de théorie cinétique de champ moyen a été développé. L'interaction entre la l'énergie de charge et la température, et entre le champ électrique appliqué et les champs de Coulomb (par la densité de charge non compensée) a été soigneusement étudiée. La charge et les distributions du courant ont premis de constater des différences, essentiellement dans la zone libre ou dans les zones de contact d'une couche granulaire par rapport aux contacts métalliques macroscopiques. L'état de transport d'équilibre dans la zone de contact est accompagnée d'une accumulation de charge et de comportements non-ohmiques de conduction. Des solutions analytiques approximatives ont été obtenues pour les régimes de caractéristiques (faible ou forte densité de charge) de conduction.

Expérience: Cette partie a été principalement axée sur l'étude des nanostructures, avec multicouches magnétiques granulaires dans la limite dilué. Les films ont été composés

de dix couches granulaires $Co_{20}Fe_{80}$ (avec épaisseur nominale de $0,7$ et $0,9$ nm) embarquées dans une matrice isolante de Al_2O_3. Les mesures de magnétisation ont révélé un léger écart par rapport à l'état de superparamagnétique en raison des interactions dipolaires entre les grains voisins. Les températures de blocage sont de l'ordre de 40 K, avec la diminution sur le champ magnétique appliqué. Les valeurs trouvées des constantes d'anisotropie, $\sim 1.4 \times 10^6$ erg cm^{-3}, sont plus élevées que la caractéristique pure des échantillons macroscopiques, en raison d'effets de surface. Des mesures de transport ont été effectuées dans la géométrie de courant dans le plane au moyen de deux contacts évaporés sur des films. Les données de magnéto-transport ont révélé, à la température ambiante, une importante valeur de magnétorésistance de 6% à des champs de $H \sim 10$ kOe. En outre, à partir de l'extrapolation du modèle de Inoue-Maekawa, on constate que la magnétorésistance pourrait atteindre $\sim 8\%$ pour les champs de saturation de $H_s \sim 50$ kOe. Enfin, des propriétés de commutation résistives ont également été découvertes dans ces échantillons (en utilisant la même géométrie de courant). Il a été montré que la commutation de résistance est suivie par une commutation capacitive discrète, ce qui conduit à l'élaboration d'un nouveau modèle de ces phénomènes, différent de la théorie filamenteuse.

Contents

List of Abbreviations **xvi**

List of Tables **xvii**

List of Figures **xviii**

1 Introduction **1**

1.1 Present Perspectives 1

1.2 Magnetoresistance 3

1.3 Overview 4

1.3.1 Magnetic Junctions 4

1.3.2 Spin-Transfer Torque 5

1.3.3 Magnetic Granular Films 5

1.3.4 Resistive Switching 6

1.4 Outline of the Thesis 7

2 Theoretical Methods and Experimental techniques **8**

2.1 Theoretical Methods 8

2.1.1 Electronic Properties of Solids 8

2.1.2 Tight-Binding Approximation 10

2.1.3 Electron Spin 14

2.1.4 Landauer-Büttiker Formalism 18

2.2 Experimental Techniques 23

2.2.1 Samples Preparation and Description 23

2.2.2 Electrical Characterization 25

2.2.3 Magnetic Characterization 28

3 Coherent Transport in Single Spacer Magnetic Junctions 30

3.1 Basic Chain Model 31

3.2 Transmission Through Discrete Chain Structure 33

3.3 3-Dimensional Multilayered Structure 38

3.3.1 Magnetoresistance and Numerical Results 41

3.4 Interfacial Effects 44

3.4.1 Magnetoresistance and Numerical Results 46

3.5 Temperature and Voltage Effects 46

3.5.1 Field Dependent Transmission 48

3.5.2 Magnetoresistance and Numerical Results 53

3.6 Electronic Distribution Functions 57

3.6.1 Model 57

3.6.2 Equilibrium 59

3.6.3 Transport 62

3.7 Charge and spin-torque transfer 63

3.7.1 Introduction 63

3.7.2 Model 65

3.7.3 Equations of motion 66

3.7.4 Transport properties 69

3.7.5 Numerical Results 72

3.8 Conclusions 75

4 Coherent Transport in Perfect Multilayered Magnetic Junctions 78

4.1 Introduction 78

4.2 Double-Spacer Magnetic Junctions 78

4.2.1 Model 80

4.2.2 Results and Discussion 83

4.3 Triple-Spacer Magnetic Junctions 85

4.3.1 Model 86

4.3.2 Results and Discussion 88

4.4 Matrix Description of Multilayered Junctions 90

4.4.1 Method 91

4.4.2 Analytical Results 97

4.4.3 Numerical Results and Discussion 98

4.5 Conclusions 101

5 Diluted metal-insulator granular layers: Theory and Experiment 103

5.1 Introduction 103

5.2 Theoretical description of transport processes 103

5.2.1 Charging states and kinetic processes 104
5.2.2 Mean-field densities in equilibrium 108
5.2.3 Steady state conduction in FA 110
5.2.4 Steady state conduction in CA 112
5.3 Experimental magnetic and transport properties 118
5.3.1 Magnetic Properties 119
5.3.2 Charge transport properties 122
5.3.3 Magnetotransport properties 126
5.4 Resistive switching effects 132
5.4.1 Resistive switching phenomena 132
5.4.2 Forming process 133
5.4.3 Memory resistive switching 135
5.4.4 Threshold resistive switching 135
5.4.5 New switching mechanism 136
5.5 Conclusions 139

6 Conclusions and Future Work **142**

6.1 Theory 142
6.1.1 Conclusions 142
6.1.2 Future Work 143
6.2 Experimental 144
6.2.1 Conclusions 144
6.2.2 Future Work 145

Appendix A 147

Appendix B 151

Appendix C 155

List of Communications 157

Bibliography 160

List of Abbreviations

1D	One-dimensional
2D	Two-dimensional
3D	Three-dimensional
AP	Antiparallel state
CIP	Current-in-plane
CPP	Current-perpendicular-to-the-plane
D	Drain
$\mathcal{D}$	Diffusion coeficient
DMTJ	Double tunnel junction
DMIM	Discontinuous metal/insulator multilayer
FC	Field-cooled
F or **FM**	Ferromagnetic
FM	Ferromagnetism
G	Gate
g	Conductivity
GMR	Giant magnetoresistance
I	Electrical current or Insulator
I-V	Current-voltage characteristics
I-T	Current versus temperature
LB	Landauer-Büttiker
MF	Mean field
MR	Magnetoresistance
N or **NM**	Non-magnetic
OFF	Low electrical conduction state
ON	High electrical conduction state
P	Parallel state
PM	Paramagnetic or Paramagnetism
QWS	quantum well states
RS	Resistive switching
RT	Room temperature
S	Source
SBR	Shallow band regime
SE	Schrödinger equation
SFM	Superferromagnetic
SPM	Superparamagnetic or Superparamagnetism
SSG	Super-spin glass
STT	spin-transfer torque
t	Hopping integral amplitude or Nominal thickness
TB	Tight-binding
TMR	Tunnel magnetoresistance
ZFC	Zero-field-cooled

List of Tables

2.1 *Single-band tight-binding parameters for Fe and Co (using the Fermi level reference, $\varepsilon_F = 0$).* 14

5.1 *Fitting parameters for the low-field magnetization curves in function of temperature.* 120

5.2 *Characteristic transport parameters for two nominal thickness values extracted from Fig. 5.11.* 126

List of Figures

1.1 ***(a)*** *Schematic illustration of the spin-dependent density of states (DOS) in a magnetic junction (red for majority spins and blue for minority ones) with parallel (upper panel) and anti-parallel (lower panel) magnetizations;* ***(b)*** *Schematic illustrations of incoherent electron tunneling through an amorphous barrier (upper panel) and coherent tunneling through a crystalline one (lower panel).* 2

2.1 *A typical crystalline periodic potential plotted along a line of ions (the rest of the crystal is not presented).* 9

2.2 *Contour-plot of the dispersion law for a 2D square lattice with* $\varepsilon_0 = 0$ *and* $t = 1/2$. 13

2.3 ***(a)*** *Band dispersion of bcc Fe in the [0 0 1] direction,* $\Gamma - H$*;* ***(b)*** *Band dispersion of bcc Co in the same direction. (Reprinted from [Yuasa and Djayaprawira, 2007]). Thick red and blue lines respectively represent majority-spin and minority-spin band dispersions,* $\Gamma - H$*, used in this work for a sc lattice.* 14

2.4 ***(a)*** *Schematic picture of basic elements of the Stern and Gerlach experiment.* ***(b)*** *Spin values for 1/2-fermions.* 15

2.5 *Schematic representation of both longitudinal* q *and transversal* $\mathbf{k}_{\|}$ *components of the total momentum* $\mathbf{k}$. 19

2.6 ***(a)*** *A conductor having a transmission probability of* T *is connected to two large contacts through two leads. Zero temperature is assumed such that the energy distributions of the incident electrons in the leads are step functions. Note that* q *is the longitudinal momentum.****(b)*** *A conductor is connected to two large contacts through two leads with energy distributions at non-zero temperatures.* 19

2.7 ***(a)****Restricted integration range* $K(\varepsilon)$ *as a function of* $\cos k_x a$, $\cos k_y a$ *and new integration variables* $u = \cos k_x a + \cos k_y a$ *and* $v = \cos k_x a - \cos k_y a$*.* ***(b)*** *The 2D density of states,* $\rho(u)$*, in the complete energy range,* $-2 \leq u \leq 2$. 22

2.8 *Schematic representation of the studied samples.* 25

2.9 ***(a)*** *Photograph of the experimental setup for measurements of electrical transport properties;* ***(b)*** *Detail of the electromagnet and close cycle refrigerator.* 26

2.10 *Schematic representation of the electromagnet setup used in the magnetoresistance measurements.* 28

3.1 *Finite atomic chain with tight-binding hopping amplitude t.* 31

3.2 ***(a)*** *Discrete energy spectrum for a chain with $n = 4$ and $t = 1/2$;* ***(b)*** *Eigenvectors $\psi(x)$ local amplitudes for the same chain.* 33

3.3 *Composite system of a finite n-chain (gate element, G) inserted between two semi-infinite chain leads (source, S, and drain, D). The energy diagram shows the on-site energy levels (dashed) for i-th element ($i = s, g, d$) and the Fermi level (dot-dashed) whose crossings with the continuous S- and D- dispersion curves define the wave numbers for incoming (q_s), reflected ($-q_s$) and transmitted (q_d) parts of the Fermi state. Notice that the Fermi level generally does not match any of the discrete levels (solid) in the central (G) element.* 35

3.4 *Transmission coefficient $|T|^2$ as a function of the on-site energy ε_g in the gate element of the composite chain system, for the choice of its parameters $\varepsilon_s = -0.4$ eV, $\varepsilon_d = -0.8$ eV (relative to the Fermi energy), $t_s = t_d = 0.5$ eV, $t_g = t_{sg} = t_{gd} = 0.25$ eV and $n = 5$. The shadowed areas indicate the (Stoner shifted) continuous bands, S (light grey) and D (dark grey).* 37

3.5 *Real multilayered structure where the current flows through two ferromagnetic electrodes, S and D, separated by a non-magnetic spacer G, and its model by the composite 3D system where a finite n-plane spacer is inserted between two semi-infinite leads.* 38

3.6 *Magnetoresistance of a Fe/NM/Fe junction (the parameters are given in the Chap. 2):* ***(a)*** *as a function of the on-site energy ε_g of the gate element for the same junction and various numbers of atomic planes in the gate element, $n_g = 3$, $n_g = 4$ and $n_g = 5$. Compare the resonance peaks in the* shallow band *regime with those in the 1D case of Fig. 3.3;* ***(b)*** *in function of the number n_g of spacer layers at fixed values of ε_g. Magnetoresistance of a Co/NM/Co junction (the parameters are given in the Chap. 2):* ***(c)*** *as a function of the on-site energy ε_g of the gate element for the same junction and various numbers of atomic planes in the gate element, $n_g = 3$, $n_g = 4$ and $n_g = 5$;* ***(d)*** *in function of the number n_g of spacer layers at fixed values of ε_g;* 42

3.7 *Discrete electronic spectrum for $n = 4$ and $t = -0.6$ eV in the shallow band condition, $\varepsilon_g = -1$ eV.* 44

3.8 *Schematic representation of the interface charge-energy, δ, created by a charge accumulation in the S/G and G/D interfaces, as a simplified description of the self-consistent behavior.* 45

3.9 *Effect of the interface charge energy on the MR for the same Fe/NM/Fe junction **(a)** as a function of ε_g, with $m_g = 4$ and δ varying from 0 to 0.4 eV; **(b)** in function of m_g with $\varepsilon_g = 1$ eV and δ varying from 0 to 0.4 eV. Effect of the interface charge energy on the MR for the same Co/NM/Co junction: **(c)** as a function of the ε_g, with $m_g = 4$ and δ varying from 0 to 0.4 eV; **(d)** in function of m_g with $\varepsilon_g = -0.5$ eV and δ varying from 0 to 0.4 eV.* 47

3.10 *Schematic representation of an S-G-D junction, where each element is composed of 2D atomic planes with respective hopping parameters, and the voltage spatial distribution (by a staircase potential with equal steps E within the* g *element).* . . . 48

3.11 ***(a)** Discrete energy spectrum for a chain with $n = 4$ and $t = 1/2$ as a function of $y = E/(2t)$; **(b)** Eigenvector $\psi(x, y)$ local amplitudes for the same chain.* 51

3.12 *Schematics of spin-dependent transport channels in P and AP regimes of the junction (wide arrows indicate polarizations of the FM leads). For each channel with a certain absolute spin index Σ, the relative indices σ, σ' are equal in P but different in AP.* 53

3.13 *MR dependencies on the gate bias parameter ε_g for different numbers n of atomic planes in the gate at different temperatures.* 55

3.14 ***(a)** Electric field dependencies of MR for different numbers n of atomic planes in the gate at room temperature; **(b)** Temperature dependencies of MR for the choices of gate bias ε_g adjusted to reaching SBR conditions at low and high temperatures.* . . 56

3.15 *Transmission and reflection processes at given energy ε and the q-projected distributions of majority and minority spins on both sides of the barrier in the AP magnetic state. Light and dark shading indicates absolute spin orientations (up and down, respectively).* 58

3.16 *Schematic picture of a magnetic junction: left ferromagnetic lead (source, S), non-magnetic spacer (gate, G) and right ferromagnetic lead (drain, D). It is important to emphasize the discrete structure of the system, as that by n-atomic planes in the gate.* 64

3.17 *Charge current, I_c, as a function of: (a) the on-site energy ε_g of the spacer; (b) the angle θ; (c) the bias voltage V.* 74

3.18 *The same dependencies as those presented for I_c, but for $\tau_\parallel$.* 75

3.19 *Variation of $\tau_\perp$ with the same variables as for other transport currents.* 76

4.1 *The energy diagram shows the on-site energy levels (dash-dot) for B- and G-spacers, the Fermi level (dashed) whose crossings with the continuous S- and D- dispersion curves (light grey for minority spins and grey for majority spins) define the spin-dependent wave numbers for incoming ($q_{s,\pm}$), reflected ($-q_{s,\pm}$) and transmitted ($q_{d,\pm}$) parts of the Fermi state. Notice that the Fermi level generally does not match any of the discrete levels (solid) in the central B and G elements.* . . 80

4.2 *Sketch of the double-spacer junction with epitaxially defined atomic planes in its elements. The solid arrows show polarization of FM leads, the dashed arrow indicates tunnel current.* 80

4.3 *[(a),(c)] The TMR dependencies on* ε_N *(at different widths* m_I *and* m_N*) show resonance enhancement, reaching* $\sim 3000\%$*; (b) TMR vs* m_I *for various important* ε_N *values, different conduction regimes are explored; (d) TMR vs* m_N *for the same* ε_N *values;* 84

4.4 *Sketch of two types of double magnetic junctions: (a) FNINF and (b) FNFNF. Solid arrows are for polarizations of magnetic elements and dashed arrows for propagation of current.* 86

4.5 *[(a),(c)] The TMR dependencies on* ε_N *(at different widths* m_I, m_N*) show resonance enhancement, exceeding* $\sim 6000\%$*; (b) TMR vs* m_I *for specific resonant* ε_N *values (at* $m_N = 4$*); (d) TMR vs* m_N *for the same* ε_N *values.* 88

4.6 *[(a),(c)] The TMR dependencies on* ε_N *(at different widths* m_I, m_N*) show resonance enhancement, almost reaching* $\sim 3000\%$*; (b) TMR vs* m_N *for various important* ε_N *values, different conduction regimes are explored; (d) TMR vs* m_F *for the same* ε_N *values.* 89

4.7 *Multiple-component system* $0, ..., n+1$*, the stripped view shows the atomically coherent internal structure of the layers and of the interfaces between them.* 92

4.8 *Magnetoresistance of a FNIFINF junction (with* $\varepsilon_I = 4.0$ *eV) as a function of different parameters: (a) on-site energy,* ε_N*, for* $m_N = 4, 5, 6$ *(shows a series of sharp peaks reaching* $\sim 4000\%$*); (b) TMR vs* m_I *for* $\varepsilon_N = -1, -0.5, 0.5, 1, 2$ *eV; (c) TMR vs* m_F *for the same* ε_N *values; (d) TMR vs* m_N *for the same* ε_N *values.* 99

4.9 *MMagnetoresistance of a FINFNIF junction with the same definition of sets of parameters and panels as in Fig. 4.8 differs mainly from that case by the presence of single broad peak reaching* $\sim 3000\%$ *in function of* ε_N*.* 100

4.10 *Magnetoresistance of a FINFINF junction with the same definition of sets of parameters and panels as in Figs. 4.8 and 4.9.* 101

4.11 *Magnetoresistance of a FIFNFIF junction with the same definition of sets of parameters and panels as in Figs. 4.8, 4.9, and 4.10 shows two prominent peaks reaching* $\sim 15000\%$ *in function of* ε_N*.* 102

5.1 *Square lattice of metallic granules in the insulating matrix.* 104

5.2 *Kinetic processes in a granular layer.* 106

5.3 *CIP conduction geometry.* 107

5.4 *Equilibrium density ρ_0 of charge carriers in function of temperature (solid line). The curve 1 (dashed line) corresponds to the low temperature asymptotics $\rho_0 \approx 2\exp -E_c/2k_BT$, and the curve 2 (dash-dotted line) to the high temperature asymptotics $\rho_0 \approx \rho_\infty - E_c/9k_BT$, converging to the limit $\rho_\infty = 2/3$ (dotted line).* 109

5.5 *The charge density σ in function of the carrier density ρ for different temperatures, corresponding to different thermal equilibrium values ρ_e.* 110

5.6 *Kinetic process between* **n***th granule and the metallic electrode in CA.* 113

5.7 *Formation of local electrical field by charged granules and their images at the surface of the metallic electrode (point a) and between the granules (point b).* . . . 114

5.8 *Relations between* **n***th longitudinal (j_x) and normal (j_z) currents in CA.* 116

5.9 ***(a)*** *Magnetization of Al_2O_3(3.0 nm)/[$Co_{80}Fe_{20}$(t)/Al_2O_3(4.0 nm) $]_{10}$ films with $t = 0.7$ and 0.9 nm under $H = 10$ Oe in function of temperature. Insets show the T_b decay with the applied magnetic field.* ***(b)*** *Magnetization vs field cycles at different temperatures.* 121

5.10 ***(a)*** *I-V characteristics for thickness $t = 0.9$ nm at different temperatures; Inset: logarithmic representation of the low-voltage ohmic conductivity, g(T), divided by $g(T = 100K)$ as a function of the inverse temperature.* ***(b)*** *Current vs temperature (with $V = 5$ V) for the same thickness.* 123

5.11 *Conductivity as a function of $T^{-1/2}$ for thicknesses $t = 0.7$, 0.9nm (fitted with the Sheng* et al. *law [Sheng* et al.*, 1973]).* 125

5.12 ***(a)*** *Field dependence of room-temperature MR at different thicknesses $t = 0.7, 0.9$, where the Inoue-Maekawa (IM) law for 3D granular films [Inoue and Maekawa, 1996] is used for fitting MR vs H;* ***(b)*** *IM fits at different temperatures for $t = 0.7$ nm (similar fits result for $t = 0.9$ nm).* 127

5.13 *Comparison between the mean magnetic moments of the granules (in unities of μ_B) calculated from the fits to the magnetoresistance, MR (•), and from the magnetization curves, $M(H)$ (■).* 129

5.14 *Critical behavior at the SPM-SFM transition vs nominal thickness t of a granular layer:* ***(a)*** *maximum MR ratio ($MR_{\max}$);* ***(b)*** *MR field sensitivity (dMR/dH) at room temperature;* ***(c)*** *field H_i of maximum field sensitivity. Solid symbols stand for the previous data [Kakazei* et al.*, 2003 and Sousa* et al.*, 2001] and open symbols are for present measurements. Vertical lines delimit the ranges of SPM, SFM, and FM phases at this temperature.* 130

5.15 *Maximum MR ($H \approx 9$ kOe) temperature dependence for both the thicknesses: $t = 0.7$ nm and $t = 0.9$ nm.* 131

5.16 *Sudden change from a noisy MR behavior to a low noise behavior at $T \sim 220$ K for $t = 0.9$ nm.* 132

5.17 ***(a)*** *Current-voltage (I-V) plots showing a sudden and irreversible change (forming process). In the positive-bias return-voltage scan the current becomes noisy and switches between a low and a high conductive state at around* 10 *V.* ***(b)*** *I-V characteristics of a device obtained after forming.(Notice the logarithmic vertical scale of these plots).* 134

5.18 *Low-bias region of the final bistable current-voltage characteristics observed after many ON/OFF cycles.* 136

5.19 ***(a)*** *Step change in capacitance accompanying the resistive switching (f =1 kHz).* ***(b)*** *Capacitance jumps between two discrete states occurring at a constant voltage.* 137

5.20 *Phenomenological model to explain the formation of a network of conducting paths across the sample.* 139

6.1 *An example of using the diagrammatic technics for calculation of orthogonal eigenstates. The set of diagrams defining the numerator of the orthogonalization coefficient* O_{41} *in Eq. (A4).* 149

6.2 *Charge density and current distribution in CA region (regime I).* 153

6.3 *Charge density in regime II. A fast decay is change to a slower exponential law, after density dropping below the characteristic value* ρ_0. 154

Chapter 1

Introduction

1.1 Present Perspectives

Nowadays, we live in an information based society where knowledge has an extreme importance. In order to store the increasing amount of data, higher and higher storage densities are required. In some way, this fact is in a strict relation with modern development. Thus, ultra-high density storage technologies are a demanding research priority, receiving for that reason much attention from the scientific community. In this area, as well as in many others, the advent of nanotechnologies triggered plenty of new ideas and unexplored opportunities for theorists and experimentalists with both academic and industrial proposes. At the nanoscale, spintronics (spin-dependent electronics) has played a fundamental role, mainly in the fabrication of the vastly used hard-drive magnetic discs. In fact, the 2007 Physics Nobel Prize was attributed to Albert Fert and Peter Grünberg for their contribution to this field. But definitely, this is not *the end of the road* for spintronics applications, and despite of the worldwide economical crisis, spintronics is still a growing field. For example, the designs of new spin-transfer torque random access memories (STT-RAM) [Krivorotov *et al.*, 2005] and magnetic-domain wall motion based devices (racetrack memories) [Hayashi *et al.*, 2008] are current research interests of leading companies such as IBM.

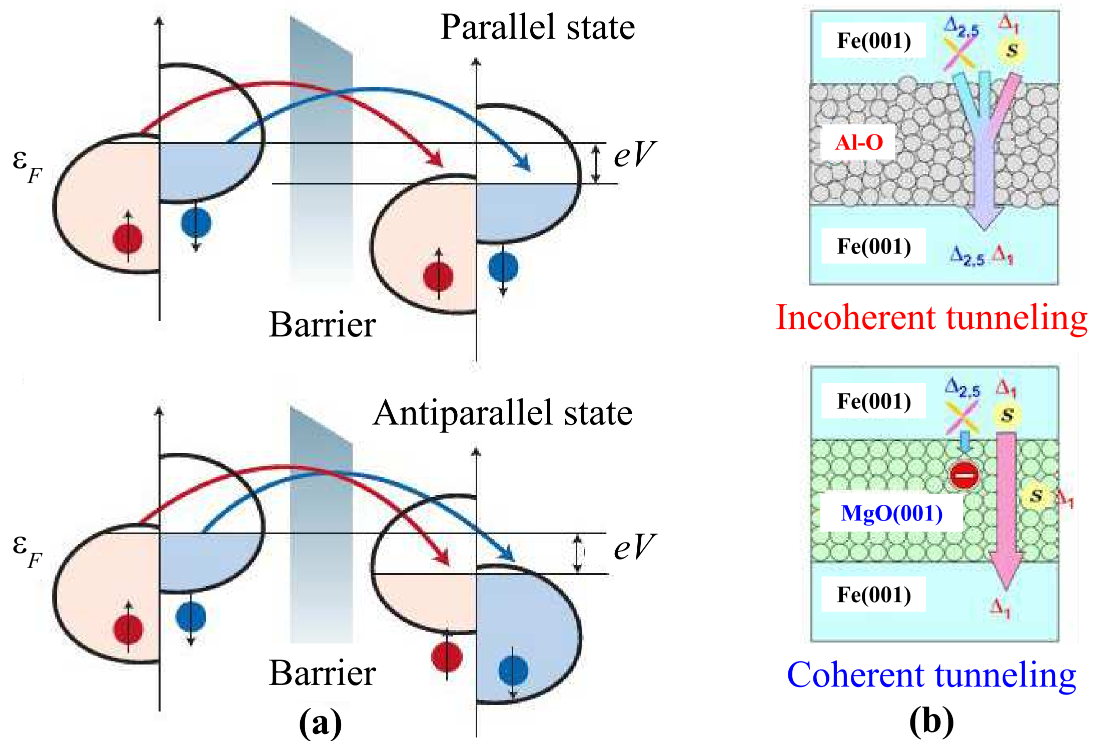

Figure 1.1: ***(a)*** *Schematic illustration of the spin-dependent density of states (DOS) in a magnetic junction (red for majority spins and blue for minority ones) with parallel (upper panel) and anti-parallel (lower panel) magnetizations;* ***(b)*** *Schematic illustrations of incoherent electron tunneling through an amorphous barrier (upper panel) and coherent tunneling through a crystalline one (lower panel).*

1.2 Magnetoresistance

The basic concept behind all these devices is the *magnetoresistance* (MR), the change of the electrical resistance (R) of a material when an external magnetic field (H) is applied, usually measured by the ratio:

$$MR(H) = \frac{R(H) - R(0)}{R(0)} \times 100\%, \tag{1.1}$$

here $R(H)$ is the resistance of the material subject to a magnetic field, H. This effect will obviously constitute the fundamental propriety studied in this thesis.

There is a variety of mechanisms responsible for such resistance variation. One example is the *normal magnetoresistance*, which is due to the effect of the Lorentz force on the electron's trajectory (normally negligible in spintronic devices). Also, the *anisotropic magnetoresistance* (AMR) caused by spin-orbit coupling in transition ferromagnetic materials (and their alloys) where the electrical resistance is a function of the angle between the magnetization and the direction of the current flow. Another example, is the *colossal magnetoresistance* (CMR) observed in doped manganate perovskites. In this kind of materials, the resistance changes by orders of magnitude as a result of a high magnetic field driven metal-insulator transition (near the Curie temperature). Furthermore, the most technologically relevant mechanisms are the *giant magnetoresistance* (GMR) and the *tunnel magnetoresistance* (TMR). They are related to a resistance variation of the MR devices promoted by a change of the relative angle between successive magnetizations in magnetic multilayers, or by a variation of the angle between neighboring grains magnetizations in magnetic granular films. An illustration of the underlying spin-resolved density of states (DOS) causing MR in magnetic junctions is given in Fig. 1.1a. Normally, the resistance increases when the magnetizations are anti-aligned (anti-parallel, AP) and decreases when they are aligned (parallel, P), for that reason, the maximum GMR and TMR ratios are both given by:

$$MR = \frac{R_{AP} - R_P}{R_P} \times 100\%, \tag{1.2}$$

where R_P (R_{AP}) is the electrical resistance in the parallel (antiparallel) configuration. For sufficiently high values of this ratio, a significant resistance difference between the P and

AP states can be used to store binary values: 0 and 1.

1.3 Overview

1.3.1 Magnetic Junctions

The first experiments in magnetic junctions were done by Tedrow and Meservey [Tedrow and Meservey, 1971] in Al/Al_2O_3/Ni junctions where spin-dependent tunneling emerged. This work was followed by Julliere [Julliere, 1975], who observed an expressive TMR ratio of $\sim 14\%$ at 4.2 K in a Fe/Ge-O/Co magnetic tunnel junction (MTJ). In this work, the famous Julliere formula was established: $\Delta R/R = 2PP'/(1+PP')$, where P, P' are the spin polarizations of the conduction electrons of the two ferromagnetic metals. Nevertheless, this effect was not observable at room-temperature (RT). For that reason it received little attention until the works of Albert Fert [Baibich *et al.*, 1988] and Peter Günberg groups [Binasch *et al.*, 1989] on Fe/Cr superlattices and Fe/Cr/Fe simple junctions, respectively. These studies lead to the discovery of *giant magnetoresistance* effect. At that time, different theories were brought up to describe spin-dependent transport in these multilayers, the early ones were based on spin-dependent scattering effects (causing different relaxation times for different spin-channels) in the diffusive regime, [Bauer, 1992] and [Valet and Fert, 1993]. Only later it was shown that the spin-dependent scattering is not crucial for GMR. Instead, the ballistic spin-dependent reflection and localization controlled by interface potentials was proposed as the GMR mechanism. This model described successfully experimental data available at that moment, [Schep *et al.*, 1995] and [Mathon *et al.*, 1995].

Another breakthrough was achieved in the Meservey's group by Moodera *et al.* with the discovery of large RT tunnel-magnetoresistance (TMR) in simple CoFe/Al_2O_3/Co junctions [Moodera *et al.*, 1995]. Inevitably, this finding attracted a great research effort, but even in the most optimized junctions TMR only reached a maximum of $\sim 70\%$, which is below the values required for magnetic random access memories (MRAM).

Nonetheless, two important theoretical works opened new perspectives, [Butler *et al.*, 2001] and [Mathon and Umerski, 2001], describing coherent electronic magneto-conductance in perfect epitaxial Fe/MgO/Fe tunnel junctions. In such structures, MR ratio reached values above $\sim 1000\%$ caused by the high spin polarized Fe Δ_1 states, Fig.

1.1b. Three years later a suggestive MR of $\sim 200\%$ was measured at RT in these type of junctions by groups of Yuasa [Yuasa *et al.*, 2004] and Parkin [Parkin *et al.*, 2004]. Since then, TMR values are continuously growing and for the moment, it reaches $\sim 604\%$ at RT and $\sim 1140\%$ at 5K [Ikeda *et al.*, 2008].

1.3.2 Spin-Transfer Torque

On the other hand, only recently spin-transfer torque (STT) is receiving much attention from the spintronics community once it offers the possibility of current-controlled magnetization reversal and therewith a resistance switch. However, early works on current induced spin-transfer effects started already in the middle of 70ies by Berger. These preliminary attempts resulted in the subsequent observation of domain wall motion in thin ferromagnetic films under large currents (~ 45 A) [Freitas and Berger, 1985]. Unfortunately, the high currents required for such motion did not attract much interest to the spin-transfer phenomena. In 1996, two crucial contributions to this field were presented by Slonczewski [Slonczewski, 1996] and Berger itself [Berger, 1996] predicting independently, that sufficiently high spin-polarized currents, flowing perpendicular to the plane in GMR multilayers, could generate a STT strong enough to switch the magnetization in one of the ferromagnetic leads. The experimental verification of spin-torque-driven excitations appeared three years later [Tsoi *et al.*, 1998], and was followed by the observation of magnetization reversal [Myers *et al.*, 1999]. Diverse works dealing with STT in GMR multilayers came afterwards. Although, development of high MR tunnel junctions (MgO based) shifted the researchers attention to STT phenomena in these devices. In fact, coherent tunneling can give rise to interesting effects such as anomalous bias dependence of the torque, as predicted by Theodonis and co-workers [Theodonis *et al.*, 2006], and experimentally confirmed two years latter [Kubota *et al.*, 2008].

1.3.3 Magnetic Granular Films

In parallel with the development of magnetic multilayered structures, as exposed above, magnetic granular films also involved an expressive research effort. This is due to the fact that these films have unique magnetic and transport properties, mainly controlled by the variation of concentration (x) or nominal thickness (t) of the magnetic materials.

The first works were done on *cermet* films, composed of isotropically dispersed

magnetic grains in a host matrix (metallic or insulating). In particular, the studies by Gittleman *et al.* [Gittleman *et al.*, 1972] on Ni/SiO_2 films revealed some interesting magnetic features. These were followed by the papers of Sheng and co-workers [Sheng *et al.*, 1973], which clarified several transport aspects and established, besides the widely used conductivity thermal law: $\sigma \propto \exp(-T^{-1/2})$. Two decades later Morawe and Zabel [Morawe and Zabel, 1995] succeeded in preparing discontinuous metal/insulator multilayer (DMIM) systems which presented similar magnetic properties but rather improved MR performance. Yet, one year later, Inoue and Maekawa [Inoue and Maekawa, 1996] proposed a simple law to describe MR performance in *cermet* films. This important law is also valid for DMIM, but only at high temperatures.

There are various potential applications of this class of materials: high coercivity films for information storage, high permeability, high resistivity films for shielding and bit writing at high frequencies, and moderate MR elements for read heads and magnetic sensors. Further on, different granular ferromagnetic elements, such as Ni, Co, Fe, $Co_{80}Fe_{20}$, and Py, embedded into different insulating hosts, SiO_2, TiO_2, ZrO_2, Al_2O_3, and HfO_2, have been combined and their properties are being extensively explored up to the present.

1.3.4 Resistive Switching

The resistive switching (RS) phenomena are characterized by large changes in the samples resistance, of the order of $\sim 10^3\%$ resulting from application of an electrical field. A proper voltage pulse can bring the device either into a high-resistance state (OFF) or into a low-resistance state (ON).

First experiments considering RS were performed by Hickmott in the beginnings of 1960s [Hickmott, 1962], studying capacitor-like metal-insulator-metal (MIM) structures, $Al/Al_2O_3/Al$. RS was thereafter reported in various MIM structures composed essentially of binary metal oxides, such as SiO [Simmons and Verderber, 1967] and NiO [Gibbons and Beadle, 1964]. Already in the 1990s, complex transition metal oxides, like perovskite-type manganites and titanates, became the main object of interest for RS studies. This happened thanks to the report of Asamitsu *et al.* [Asamitsu *et al.*, 1997], on $Pr_{0.7}Ca_{0.3}MnO_3$ (PCMO). This percussor results were followed by numerous studies exploring, principally, the driving mechanism of RS. Nevertheless, this mechanism is still elusive, preventing a large scale application of the effect. Thus, elucidation of the driving mechanism of RS is

currently a very important issue in the development of resistive random access memories (ReRAM).

1.4 Outline of the Thesis

The present thesis discusses two types of materials: magnetic multilayers and discontinuous metal/insulator multilayers.

In the next chapter, Chap. **2**, the theoretical methods and experimental techniques evolved in the realization of this work are explained. In Chap. **3**, different aspects of tight-binding quantum-coherent transport in simple magnetic junctions are explored and further MR consequences are discussed. These are followed by a general treatment of magnetoconductance for arbitrary multilayered systems presented in Chap. **4**. Then, in Chap. **5**, discontinuous metal/insulator multilayer systems (in the low-concentration limit) are considered, where transport and magnetic properties are analyzed. Still in this chapter, electrical resistive switching phenomena discovered in these films are investigated. Finally, in the last chapter, conclusions and future perspectives are presented.

Chapter 2

Theoretical Methods and Experimental techniques

The present chapter describes the basic theoretical methods and experimental techniques used during the realization of this thesis. The next section, Sec. 5.2, concerns the theoretical part and the following, Sec. 5.3, deals with the experimental one.

2.1 Theoretical Methods

This section is divided as follows: in Subsec. 2.1.1 the basic aspects of electronic properties in solids are presented; in the next subsection, Subsec. 2.1.2, the fundamentals of the common tight-binding approximation (TB) are formulated; Subsec. 2.1.3 depicts the basis of electronic spin degree of freedom and presents its implications for the quantum description of electrons; finally, in order to explore electronic transport, in Subsec. 2.1.4, the important Landauer-Büttiker formalism is revised and several formulas, as well as some technical aspects of their numerical evaluation, are also described.

2.1.1 Electronic Properties of Solids

Describing electrons in a solid is a very complex many-body problem, in which the atomic Hamiltonian, that considers the interactions between electrons and the lattice massive atomic nuclei, is perturbed by the presence of electron-electron interactions. Following the ideas of Landau, an independent electron approximation can be used regarding the effect of a potential $U(\mathbf{r})$ in the one-electron quasi-particle Hamiltonian that includes all

these perturbations. Even neglecting the details of $U(\mathbf{r})$, the periodicity of the crystal imposes that $U(\mathbf{r}+\mathbf{R}) = U(\mathbf{r})$ for all Bravais lattice vectors $\mathbf{R}$, and from this fact many important conclusions on the electronic properties of solids can be drawn. Typically, the effective potential (Fig. 2.1) approaches the individual atomic potential near the lattice ions and flats off in the mid-ion region. This potential profile led to the formulation of Bloch wave functions, a crucial aspect in the understanding of electronic properties of solids.

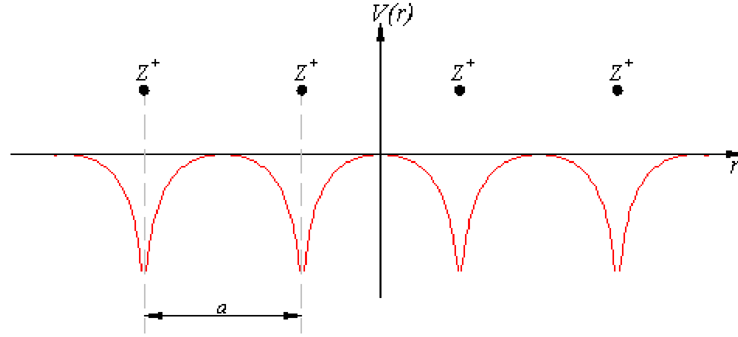

Figure 2.1: *A typical crystalline periodic potential plotted along a line of ions (the rest of the crystal is not presented).*

Bloch Wave Functions The three-dimensional (3D) single electron Schröndiger equation (SE) is then,

$$\mathcal{H}\psi = \left(-\frac{\hbar^2}{2m}\nabla^2 + U(\mathbf{r})\right)\psi = \varepsilon\psi, \tag{2.1}$$

which is solvable in terms of periodic *Bloch wave functions* commonly referred to as *Bloch electrons*. This periodic wave functions obey a very important theorem:

Bloch's Theorem *The eigenstates ψ of an one-electron Hamiltonian, Eq. 2.1, where $U(\mathbf{r}+\mathbf{R}) = U(\mathbf{r})$ for all $\mathbf{R}$ from a Bravais lattice, can be chosen as products of a plane wave with a function having a specific Bravais lattice periodicity as follows:*

$$\psi_{n,\mathbf{k}}(\mathbf{r}) = \mathrm{e}^{i\mathbf{k}\cdot\mathbf{r}} u_{n,\mathbf{k}}(\mathbf{r}), \tag{2.2}$$

where "n" is the band index and $u_{n,\mathbf{k}}(\mathbf{r}+\mathbf{R}) = u_{n,\mathbf{k}}(\mathbf{r})$ for all $\mathbf{R}$ from a Bravais lattice. This implies that: $\psi_{n,\mathbf{k}}(\mathbf{r}+\mathbf{R}) = \mathrm{e}^{i\mathbf{k}\cdot\mathbf{R}}\psi_{n,\mathbf{k}}(\mathbf{r})$. Proofs of this fundamental theorem can be found in [Ashcroft and Mermin, 1976] and [Kittel, 1963] among many others.

General Properties Obviously, this theorem has various consequences for the electronic structure:

1. The Bloch wave vector $\mathbf{k}$ is not proportional to the electronic momentum $\mathbf{p}/\hbar$.
2. The Bloch wave vector can always be confined to the first Brillouin zone, since $\exp(i\mathbf{K}\cdot\mathbf{R}) = 1$.
3. The band index n arises from different SE solutions for a given Bloch wave vector $\mathbf{k}$.
4. For a given n, the eigenstates and eigenvalues are periodic functions of $\mathbf{k}$ on the reciprocal lattice: $\psi_{n,\mathbf{k}+\mathbf{K}}(\mathbf{r}) = \psi_{n,\mathbf{k}}(\mathbf{r})$, $\varepsilon_{n,\mathbf{k}+\mathbf{K}} = \varepsilon_{n,\mathbf{k}}$.
5. The mean velocity in an electron state labeled by $(n,\mathbf{k})$ is given by: $\mathbf{v}_{n,\mathbf{k}} = \hbar^{-1}\nabla\varepsilon_{n,\mathbf{k}}$.

2.1.2 Tight-Binding Approximation

The tight-binding approximation (TB) is a very useful model to describe electronic properties in solids, since the atomic confinement does not exclude a weak overlap between wave functions of neighboring atoms, which generally causes a failure in the free-electron framework. The TB method was specially used to describe the energy bands of partially filled d-shells of transition metal atoms [Ashcroft and Mermin, 1976]. As an instructive exercise, the TB Hamiltonian can be derived from the SE describing electrons with effective mass m^*. So, considering a one-dimensional (1D) chain with the Hamiltonian:

$$\mathcal{H} = -\frac{\hbar^2}{2m^*}\frac{d^2}{dx^2} + U(x), \tag{2.3}$$

a matrix formulation of this operator can be obtained from the quantity $\mathcal{H}\psi(x)$, where $\psi(x)$ is any function of x. Now, it is possible to choose a discrete lattice with points at $x = la$ ($l \in \mathbb{Z}$) and write:

$$[\mathcal{H}\psi(x)]_{x=la} = \left[-\frac{\hbar^2}{2m^*}\frac{d^2\psi(x)}{dx^2}\right]_{x=la} + U_l\psi_l, \tag{2.4}$$

here $\psi_l \approx \psi(x = la)$ and $U_l \approx U(x = la)$. Further on, it is necessary to consider the method of finite differences to deal with the derivative operators. Assuming a small, the

first derivative is approximated by:

$$\left(\frac{d\psi}{dx}\right)_{x=\left(l+\frac{1}{2}\right)a} \approx \frac{\psi_{l+1}-\psi_l}{a}, \tag{2.5}$$

and the second derivative by:

$$\begin{aligned}\left(\frac{d^2\psi}{dx^2}\right)_{x=\left(l+\frac{1}{2}\right)a} &\approx \frac{1}{a}\left[\left(\frac{d\psi}{dx}\right)_{x=\left(l+\frac{1}{2}\right)a} - \left(\frac{d\psi}{dx}\right)_{x=\left(l-\frac{1}{2}\right)a}\right] \\ &\approx \frac{1}{a^2}\Big(\psi_{l+1} - 2\psi_l + \psi_{l-1}\Big). \end{aligned} \tag{2.6}$$

With this approximation, the SE becomes:

$$\left[\mathcal{H}\psi(x)\right]_{x=la} = \left(U_l + 2t\right)\psi_l - t\psi_{l+1} - t\psi_{l-1}, \tag{2.7}$$

with $t = \hbar^2/(2m^*a^2)$. Thus the matrix representation of the 1D Hamiltonian operator for electronic states on a linear chain is simply given by:

$$\mathcal{H} = \begin{pmatrix} \cdots & -t & 0 & 0 & 0 \\ -t & U_{-1}+2t & -t & 0 & 0 \\ 0 & -t & U_0+2t & -t & 0 \\ 0 & 0 & -t & U_1+2t & 0 \\ 0 & 0 & 0 & -t & \cdots \end{pmatrix}. \tag{2.8}$$

Using the second quantization notation, this matrix representation can be written in a compact form:

$$\hat{H} = \sum_l \left[\varepsilon_l \hat{a}_l^\dagger \hat{a}_l - t\left(\hat{a}_l^\dagger \hat{a}_{l+1} + \hat{a}_{l+1}^\dagger \hat{a}_l\right)\right], \tag{2.9}$$

where $\varepsilon_l = (U_l + 2t)$ is the on-site energy, and $\hat{a}_l^\dagger$ ($\hat{a}_l$) is the Fermi creation (annihilation) operator on l-th site. The parameter t, which defines the hopping amplitude, is also known as the *hopping integral*, and it can be written, in a more general way, as

$$t_{ij}(\mathbf{R}) = \int d\mathbf{r}\psi_i^*(\mathbf{r})\Delta U(\mathbf{r})\psi_j(\mathbf{r}-\mathbf{R}),$$

depending on the Bravais lattice vector $\mathbf{R}$. This integral involves the atomic wave functions in the ith, $\psi_i(\mathbf{r})$, and jth, $\psi_j(\mathbf{r}-\mathbf{R})$, atomic levels of two atoms separated by a Bravais

vector $\mathbf{R}$, and the perturbation term to the atomic (isolated) Hamiltonian, $\Delta U(\mathbf{r})$. This perturbation contains all the corrections required to produce the full periodic potential of a crystalline solid. The strength of the perturbation $\Delta U(\mathbf{r})$ obviously determines the hopping amplitude, in a way that stronger perturbations give rise to bigger overlap integrals. Nonetheless, $\Delta U(\mathbf{r})$ is typically weak, resulting in small hopping parameters. For instance, the d-bands of transition metals have values of $t_{ij}(\mathbf{R})$ running from 0.2 eV to 1 eV, justifying the usage of this approximation when dealing with ferromagnetic metals.

Considering overlap only between wave functions on the same atomic levels of nearest neighbors (subject to a specific lattice symmetry) reduces the general hopping integral $t_{ij}(\mathbf{R})$ to t. As a matter of fact, this simplified form will be used throughout this work.

If, instead of an atomic chain, an atomic plane is studied, the Hamiltonian is expressed as:

$$\hat{H} = \sum_{\mathbf{n}} \left[\varepsilon_{\mathbf{n}} \hat{a}^{\dagger}_{\mathbf{n}} \hat{a}_{\mathbf{n}} - t \sum_{\delta} \left(\hat{a}^{\dagger}_{\mathbf{n}+\delta} \hat{a}_{\mathbf{n}} + \text{h.c.} \right) \right], \tag{2.10}$$

with the 2D lattice sites, $\mathbf{n} = (l_x, l_y)a$, and the nearest neighbor vectors, δ. Further generalization for a three-dimensional (3D) lattice is straightforward.

In practical calculations, planar-wave states (with a given planar momentum $\mathbf{k}$) are frequently used to diagonalize the Hamiltonian by performing the Fourier transform: $\hat{a}_{\mathbf{k}} = N^{-1/2} \sum_{\mathbf{n}} \hat{a}_{\mathbf{n}} \exp(i\mathbf{k} \cdot \mathbf{n})$, with N being the number of lattice sites. With this transformation, the Hamiltonian is simply given as $\hat{H} = \sum_{\mathbf{k}} \varepsilon_{\mathbf{k}} \hat{a}^{\dagger}_{\mathbf{k}} \hat{a}_{\mathbf{k}}$, with the dispersion law, $\varepsilon_{\mathbf{k}} = \varepsilon_0 - t \sum_{\delta} \exp(i\mathbf{k} \cdot \delta)$ (assuming that $\varepsilon_{\mathbf{n}} = \varepsilon_0$). As an illustrative example, a 2D square lattice with $\delta = (\pm a, 0)$, $(0, \pm a)$ is considered. In this case, the energy dispersion law simplifies to:

$$\varepsilon_{\mathbf{k}} = \varepsilon_0 - 2t(\cos k_x a + \cos k_y a), \tag{2.11}$$

and its contour-plot is represented in Fig.2.2.

Single-Band Tight-Binding Parameters

For simplicity, the complex band structure of all the elements considered in this thesis will be simplified to a simple-cubic (sc) single-band tight-binding dispersion[1]. In particular, the complex band structure of the ferromagnetic metals employed, iron (Fe) [Callaway

[1] A simple analytical model for two-band calculations is being developed, but it is out of the scope of the present text.

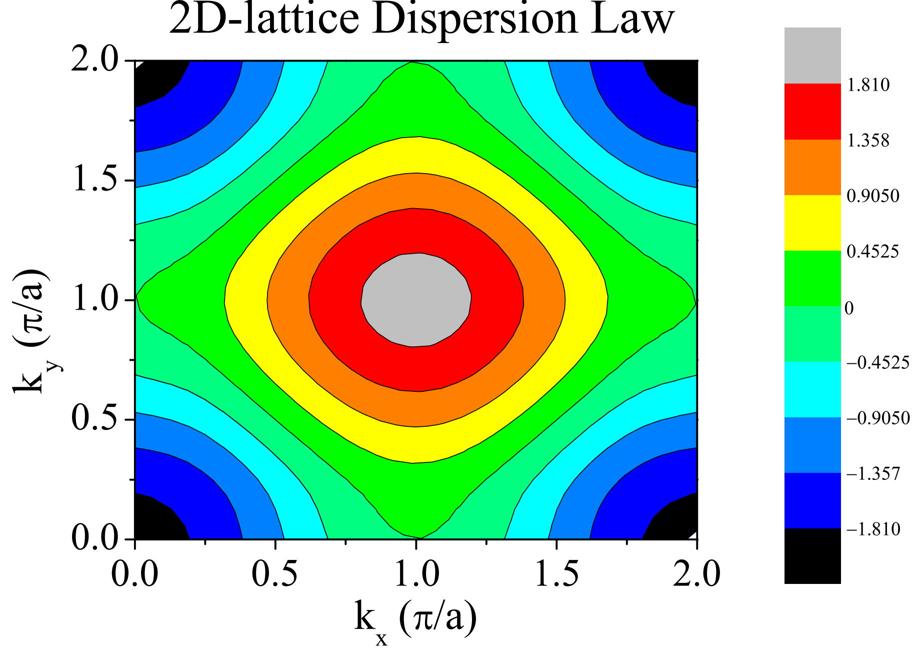

Figure 2.2: *Contour-plot of the dispersion law for a 2D square lattice with* $\varepsilon_0 = 0$ *and* $t = 1/2$.

and Wang, 1977] and cobalt (Co) [Bagayoko *et al.*, 1983], is simplified to a spin-dependent 3D dispersion law of the type:

$$\varepsilon_{\mathbf{k},\sigma} = \varepsilon_\sigma - 2t(\cos k_x a + \cos k_y a + \cos k_z a), \tag{2.12}$$

here $\varepsilon_{\uparrow(\downarrow)}$ is the on-site energy of the majority (minority) band and t is the hopping integral amplitude, considered to be equal for both spin components. These laws roughly model the real $d-$bands ($\Delta_{2'}$, Δ_5) that have an important contribution to the total electronic density of states (DOS) in these materials.

So, to adjust the *sc* parameters to the real dispersions of Fig. 2.3, the $\Gamma-$H direction, $k_x = k_y = 0$ and $k_z \in \{0, \pi/a\}$, is used and the resulting parameters are summarized in Tab. 2.1. It is important to mention that besides the simplification of equal hopping amplitudes, the Stoner splitting $\Delta_s = (\varepsilon_\downarrow - \varepsilon_\uparrow)/2$ is fixed for the entire band, even though this assumption is not correct for the generality of the ferromagnetic materials, and definitely not true for Fe [Callaway and Wang, 1977].

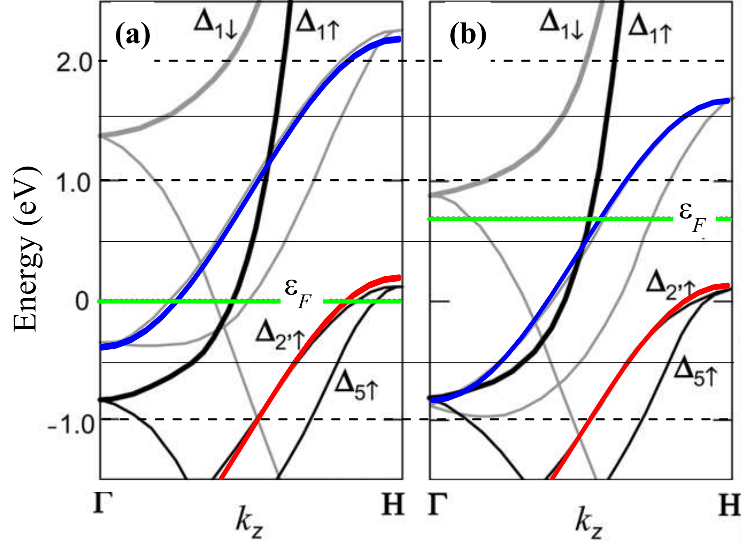

Figure 2.3: ***(a)*** *Band dispersion of bcc Fe in the [0 0 1] direction,* $\Gamma - H$*;* ***(b)*** *Band dispersion of bcc Co in the same direction. (Reprinted from [Yuasa and Djayaprawira, 2007]). Thick red and blue lines respectively represent majority-spin and minority-spin band dispersions,* $\Gamma - H$*, used in this work for a sc lattice.*

Element	$\varepsilon_{\uparrow}$(eV)	$\varepsilon_{\downarrow}$(eV)	t(eV)
Fe	1.42	3.34	0.62
Co	0.57	2.10	0.62

Table 2.1: *Single-band tight-binding parameters for Fe and Co (using the Fermi level reference,* $\varepsilon_F = 0$*).*

2.1.3 Electron Spin

For spintronics (spin electronics) the electron *spin* represents the basic degree of freedom exploited in spin-dependent transport. In fact, this intriguing property is a fundamental result of relativistic treatment of quantum mechanics introduced by the famous Dirac equation. This formulation implies a profound modification in the quantum description of the electron properties. Historically, electron spin was discovered experimentally before the introduction of Dirac equation. Indeed, one of the most relevant experiments, among others, was performed in 1922 by Otto Stern and Walther Gerlach at the University of Frankfurt. They studied the deflection of a beam constituted by neutral and paramagnetic silver atoms subjected to a strongly non-uniform magnetic field, Fig. 2.4a. Contrarily to what was classically expected, only *two main impact points* were found, and for that reason only two magnetic moments could be measured, Fig. 2.4b. Motivated

by the results of different experiments, Wolfgang Pauli five years later developed a theory which allowed *spin* to be incorporated into non-relativistic quantum mechanics by adding four new postulates to its initial formulation. Since this thesis is restricted to the level of this phenomenological theory, some of its aspects are now presented. More details can be found in any text book, for example, in the standard quantum mechanical book [Cohen-Tannoudji *et al.*, 1976].

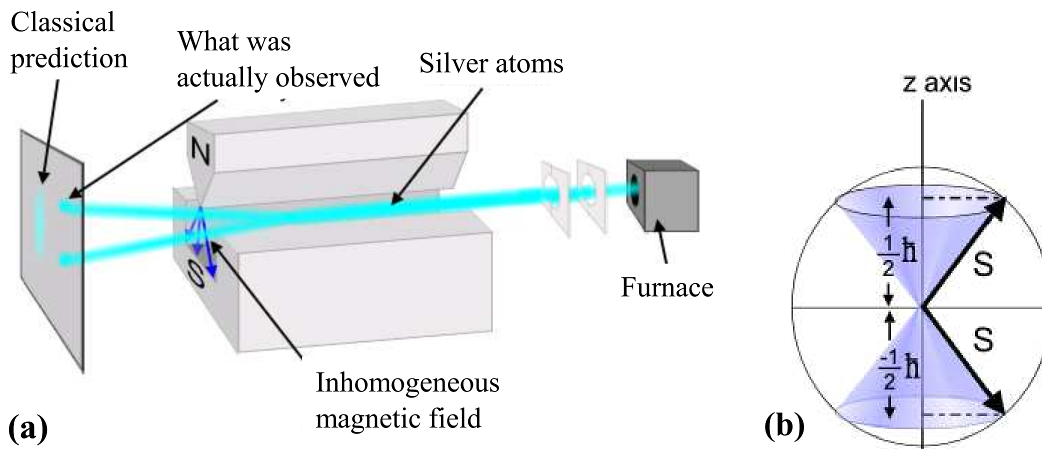

Figure 2.4: ***(a)*** *Schematic picture of basic elements of the Stern and Gerlach experiment.* ***(b)*** *Spin values for* 1/2*-fermions.*

Postulates of the Pauli Theory

In addition to *orbital variables*, Pauli added the *spin variables* that satisfy the following postulates:

First Postulate: The spin operator $\mathbf{s}$ corresponds to an angular momentum, that means that its three components are the observables which satisfy the commutation relations: $[s_x, s_y] = i\hbar s_z$, and the other two formulas which are deduced by cyclic permutation of the indices x, y, z.

Second Postulate: The spin operators act in a specific space, the *spin state space* $\mathcal{S}_\sigma$. It is spanned by the set of eigenstates $|s, m\rangle$ common to $\mathbf{s}^2$ and s_z: $\mathbf{s}^2|s, m\rangle = s(s+1)\hbar^2|s, m\rangle$ and $s_z|s, m\rangle = m\hbar|s, m\rangle$ and has finite dimension $(2s + 1)$.

Third Postulate: The state space $\mathcal{S}$ of any considered particle is the tensor product of $\mathcal{S}_\mathbf{r}$ (orbital space) and $\mathcal{S}_\sigma$: $\mathcal{S} = \mathcal{S}_\mathbf{r} \otimes \mathcal{S}_\sigma$. Consequently, *all the spin observables commute*

with all orbital observables.

Fourth Postulate: The electron is a spin 1/2 particle ($s = 1/2$) and its intrinsic magnetic moment is given by: $\mathbf{m}_s = 2(\mu_B/\hbar)\mathbf{s}$, where μ_B is the Bohr magnetron. For an electron, the space $\mathcal{S}_\sigma$ is therefore 2D.

Properties of spin 1/2

The spin state space $\mathcal{S}_\sigma$ is 2D and an orthonormal system, $\{|+\rangle, |-\rangle\}$, of eigenkets, common to $\mathbf{s}^2$ and s_z, is taken as a basis. These satisfy the equations:

$$\begin{cases} \mathbf{s}^2|\pm\rangle &= \frac{3}{4}\hbar^2|\pm\rangle, \\ s_z|\pm\rangle &= \pm\frac{1}{2}\hbar|\pm\rangle, \end{cases} \qquad \begin{cases} \langle+|-\rangle &= 0, \\ \langle+|+\rangle &= \langle-|-\rangle = 1. \end{cases}$$

The most general spin state is described by an arbitrary vector in $\mathcal{S}_\sigma$:

$$|\chi\rangle = c_+|+\rangle + c_-|-\rangle,$$

and any operator in this space can be represented by a 2×2 matrix, in the $\{|+\rangle, \ ,|-\rangle\}$ basis. In particular, the matrices for s_x, s_y, s_z spin components are written in a simple form, $\mathbf{s} = (\hbar/2)\sigma$, where σ represents the set of the three *Pauli matrices*:

$$\sigma_x = \begin{pmatrix} 0 & 1 \\ 1 & 0 \end{pmatrix}, \qquad \sigma_y = \begin{pmatrix} 0 & -i \\ i & 0 \end{pmatrix}, \qquad \sigma_z = \begin{pmatrix} 1 & 0 \\ 0 & -1 \end{pmatrix}. \tag{2.13}$$

These matrices have specific important properties:

$$\sigma_x^2 = \sigma_y^2 = \sigma_z^2 = 1,$$
$$\mathrm{Tr}\,\sigma_x = \mathrm{Tr}\,\sigma_y = \mathrm{Tr}\,\sigma_z = 0,$$
$$\mathrm{Det}\,\sigma_x = \mathrm{Det}\,\sigma_y = \mathrm{Det}\,\sigma_z = -1.$$

Furthermore, any 2×2 matrix can be written as a linear combination (with complex coefficients) of the three Pauli matrices and the identity. These four matrices form the Lee algebra for the $SU(2)$ unitary group.

Spinor States

Any state $|\psi\rangle$ from the $\mathcal{S}$ space can be expanded in the $\{|\mathbf{r},\sigma\rangle\}$ basis as:

$$|\psi\rangle = \sum_{\sigma} \int d\mathbf{r} |\mathbf{r},\sigma\rangle\langle\mathbf{r},\sigma|\psi\rangle.$$

The vector $|\psi\rangle$ can therefore be represented by the set of its components in the $\{|\mathbf{r},\sigma\rangle\}$ basis, $\langle\mathbf{r},\sigma|\psi\rangle = \psi_\sigma(\mathbf{r})$, which depend on three spacial coordinates x, y, z and on the spin index $\sigma = \pm$. Therefore, in order to characterize completely the state of an electron, it is necessary to specify two functions of the space variables: $\langle\mathbf{r},+|\psi\rangle = \psi_+(\mathbf{r})$ and $\langle\mathbf{r},-|\psi\rangle = \psi_-(\mathbf{r})$. These two functions are often represented in the form of *a two-component spinor*, which is written as:

$$[\psi](\mathbf{r}) = \begin{pmatrix} \psi_+(\mathbf{r}) \\ \psi_-(\mathbf{r}) \end{pmatrix} \tag{2.14}$$

with the respective adjoint: $[\psi]^\dagger(\mathbf{r}) = \big(\psi_+^*(\mathbf{r}),\, \psi_-^*(\mathbf{r})\big)$. In this notation, the scalar product of two state vectors $|\psi\rangle$ and $|\phi\rangle$, is equal to:

$$\langle\psi|\phi\rangle = \int d\mathbf{r}[\psi]^\dagger(\mathbf{r})[\phi](\mathbf{r}) = \int d\mathbf{r} \left[\psi_+^*(\mathbf{r})\phi_+(\mathbf{r}) + \psi_-^*(\mathbf{r})\phi_-(\mathbf{r})\right], \tag{2.15}$$

and obviously the normalization of a vector $|\psi\rangle$ is expressed by:

$$\langle\psi|\psi\rangle = \int d\mathbf{r} \left[|\psi_+(\mathbf{r})|^2 + |\psi_-(\mathbf{r})|^2\right] = 1.$$

Rotation of Spin States

It is known that the rotation operator $R_{\mathbf{u}}(\alpha)$, in the state space, associated with the geometrical rotation $\mathcal{R}_{\mathbf{u}}(\alpha)$ by an angle α about the unit vector $\mathbf{u}$, is expressed as $R_{\mathbf{u}}(\alpha) = \exp[-(i/\hbar)\alpha\mathbf{J}.\mathbf{u}]$, with $\mathbf{J}$ the total angular momentum. In the spin state space, $\mathcal{S}_\sigma$, it reads $R_{\mathbf{u}}^{(s)}(\theta) = \exp[-(i/\hbar)\theta\mathbf{s}.\mathbf{u}] = \exp[-i(\theta/2)\sigma.\mathbf{u}]$. For practical calculations it is rather convenient to use its Taylor expansion, which can be simplified with the help of the Pauli matrices properties mentioned above. In this way, the rotation operator becomes:

$$R_{\mathbf{u}}^{(s)}(\theta) = \cos\frac{\theta}{2} - i\sigma.\mathbf{u}\sin\frac{\theta}{2}.$$

Using this formula, is easy to express the rotation matrix in the $\{|+\rangle, |-\rangle\}$ basis as:

$$R_{\mathbf{u}}^{(1/2)}(\theta) = \begin{pmatrix} \cos\frac{\theta}{2} - iu_z \sin\frac{\theta}{2} & (-iu_x - u_y)\sin\frac{\theta}{2} \\ (-iu_x + u_y)\sin\frac{\theta}{2} & \cos\frac{\theta}{2} + iu_z \sin\frac{\theta}{2} \end{pmatrix}, \tag{2.16}$$

where u_x, u_y, u_z, are the Cartesian components of the vector $\mathbf{u}$.

2.1.4 Landauer-Büttiker Formalism

The Landauer-Büttiker (LB) formalism [Landauer, 1957] and [Büttiker, 1988] describing current passing through a finite mesoscopic region of non-interacting electrons has been largely used in various problems: universal conductance fluctuations, Aharonov-Bohm conductance oscillations, integer quantum Hall effect, and also commonly used in the spintronics studies [Bauer, 1992 and Schep *et al.*, 1995].

In this low-dimensional systems the typical Drude formula for conductivity (the mean value over a large macroscopic number of modes) ceases to be valid. Thus, the main interest of LB formalism is the possibility to express the current in terms of the system microscopic properties: electron probability to be transmitted through it and distribution functions in the connected reservoirs. Another appealing reason to use this formalism is the fact that for coherent[2] transport, the exclusion principle has no effect on the transmission and it is possible to accurately describe the current flow in degenerate conductors in terms of single-particle transmission coefficient [S. Datta, 1995].

At zero temperature ($\varepsilon = \varepsilon_F$) and low voltages, the LB conductance formula is simply written as a summation of the transmission probability, $|T(\varepsilon_F, \mathbf{k}_\parallel)|^2$, over the available region $K = K(\varepsilon_F)$ of transversal modes $\mathbf{k}_\parallel$ in the leads at the Fermi level (see Fig. 2.5), multiplied by half quantum of conductance $2e^2/h \sim 1/(12.9\text{k}\Omega)$:

$$G(\varepsilon_F) = \frac{e^2}{h} \sum_{\mathbf{k}_\parallel \in K} |T(\varepsilon_F, \mathbf{k}_\parallel)|^2. \tag{2.17}$$

This results from the linear current $I = I_1^+ - I_1^- = I_2^+ = G(\varepsilon_F)(\mu_1 - \mu_2)/e$, with μ_1 (μ_2) the chemical potential at the first (second) reservoir, Fig. 2.6a. Note that the pre-factor 2 due to spin degeneracy (appearing in the literature) is naturally not included since spin-dependent conduction rises up such degeneracy.

[2] Where the mean free path, l, is bigger than a certain characteristic dimension of the system, L.

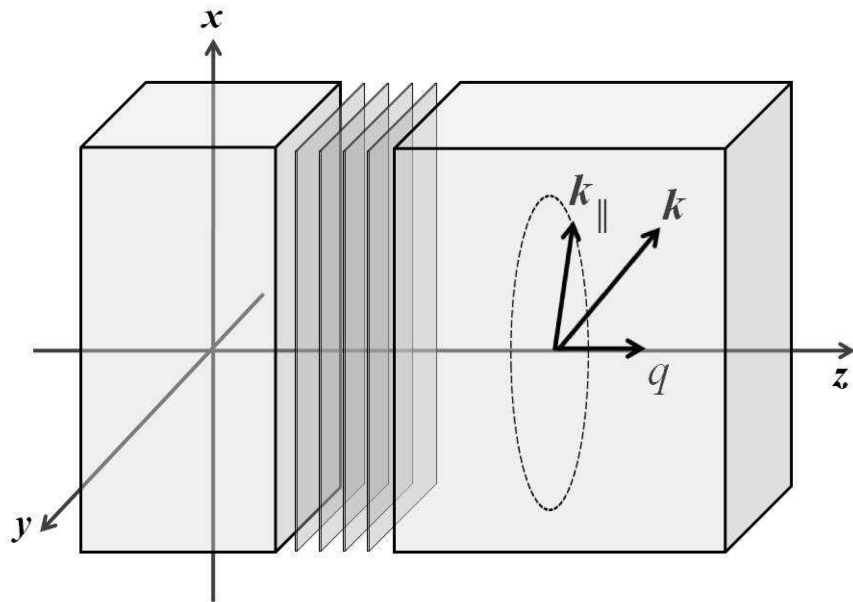

Figure 2.5: *Schematic representation of both longitudinal q and transversal $\mathbf{k}_{\|}$ components of the total momentum $\mathbf{k}$.*

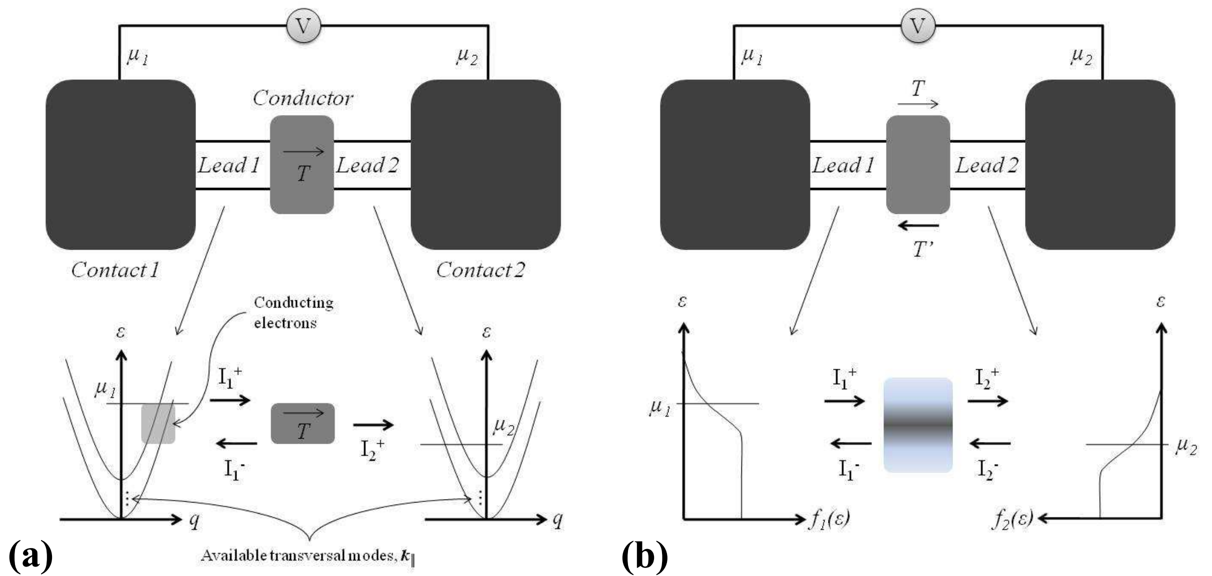

Figure 2.6: ***(a)*** *A conductor having a transmission probability of T is connected to two large contacts through two leads. Zero temperature is assumed such that the energy distributions of the incident electrons in the leads are step functions. Note that q is the longitudinal momentum.* ***(b)*** *A conductor is connected to two large contacts through two leads with energy distributions at non-zero temperatures.*

In general, temperature is not zero and transport does not occur only from contact 1 to 2, but also from 2 to 1. So, considering one mode with a given energy, the in- (i_1^+) and out- (i_1^-) flux of electrons from lead 1 are given by:

$$i_1^+ = \frac{e}{h} f_1(\varepsilon), \qquad i_1^- = |R|^2 i_1^+ + |T'|^2 i_2^-,$$

where $f_1(E)$ is the Fermi distribution (FD) function in the lead 1, the unprimed coefficients stand for process from lead 1 to 2 and the primed ones for those from 2 to 1, Fig. 2.6b. Similarly the fluxes from lead 2 are:

$$i_2^- = \frac{e}{h} f_2(\varepsilon), \qquad i_2^+ = |T|^2 i_1^+ + |R'|^2 i_2^-,$$

here $f_2(E)$ is the FD in the lead 2. The net current $i(E)$ flowing at any point in the device is given by:

$$i(E) = i_1^+ - i_1^- = i_2^+ - i_2^- = \frac{e}{h} \left[|T|^2 f_1(\varepsilon) + \left(|R'|^2 - 1 \right) f_2(\varepsilon) \right].$$

Including various modes and energies, the generalized current is:

$$I = \frac{e}{h} \int d\varepsilon \left[f_1(\varepsilon) \sum_{\mathbf{k}_\parallel \in K(\varepsilon)} |T(\varepsilon, \mathbf{k}_\parallel)|^2 - f_2(\varepsilon) \sum_{\mathbf{k}_\parallel \in K(\varepsilon)} \left(1 - |R'(\varepsilon, \mathbf{k}_\parallel)|^2 \right) \right]. \tag{2.18}$$

Obviously, the summation range $K(\varepsilon)$ depends on the energy, ε. In literature it is normally assumed that $|T'|^2 = 1 - |R'|^2$ and that $|T|^2 = |T'|^2$, and the previous formula becomes:

$$I = \frac{e}{h} \int d\varepsilon \sum_{\mathbf{k}_\parallel \in K(\varepsilon)} |T(\varepsilon, \mathbf{k}_\parallel)|^2 \left[f_1(\varepsilon) - f_2(\varepsilon) \right]. \tag{2.19}$$

Nevertheless, both assumptions are only valid for low voltages (near equilibrium) and for identical leads. Generally, the leads can be different so $|T|^2 + |R|^2 \neq 1$ and the applied voltage could change significantly the two transmission functions and make them unequal, $|T(\varepsilon, \mathbf{k}_\parallel)|^2 \neq |T'(\varepsilon, \mathbf{k}_\parallel)|^2$. Keeping in mind these considerations, it is possible to find from Eq. (2.19) a very useful formula in the linear response limit, $\mu_1 - \mu_2 \approx 0$. For small

deviations from equilibrium state, the current is proportional to the applied bias. Then,

$$\delta I = \frac{e}{h}\int d\varepsilon \left[\left(\sum_{\mathbf{k}_\parallel \in K(\varepsilon)} |T(\varepsilon,\mathbf{k}_\parallel)|^2 \right)_{\mathrm{eq}} \delta\left[f_1(\varepsilon) - f_2(\varepsilon)\right] + \delta \left(\sum_{\mathbf{k}_\parallel \in K(\varepsilon)} |T(\varepsilon,\mathbf{k}_\parallel)|^2 \right) \left[f_1(\varepsilon) - f_2(\varepsilon)\right]_{\mathrm{eq}} \right],$$

with *eq* for *equilibrium.* The second term is clearly zero and the first can be expanded in Taylor series:

$$\delta\left[f_1(\varepsilon) - f_2(\varepsilon)\right] \approx (\mu_1 - \mu_2)\left(\frac{\partial f}{\partial \mu}\right)_{\mathrm{eq}} = \left(-\frac{\partial f_0}{\partial \varepsilon}\right)(\mu_1 - \mu_2),$$

here $f_0(\varepsilon) = \{\exp[(\varepsilon - \varepsilon_F)/(k_B T)] + 1\}^{-1}$ is the FD function at equilibrium and k_B is the Boltzmann constant. Finally, a simple formula is found for the thermal dependency of the conductance:

$$G = \frac{\delta I}{(\mu_1 - \mu_2)/e} = -\frac{e^2}{h}\int d\varepsilon \left(\frac{\partial f_0}{\partial \varepsilon}\right) \sum_{\mathbf{k}_\parallel \in K(\varepsilon)} |T(\varepsilon,\mathbf{k}_\parallel)|^2, \tag{2.20}$$

which simplifies to:

$$G = \frac{e^2}{h}\frac{1}{4k_B T}\int d\varepsilon \cosh^{-2}\left(\frac{\varepsilon - \varepsilon_F}{2k_B T}\right) \sum_{\mathbf{k}_\parallel \in K(\varepsilon)} |T(\varepsilon,\mathbf{k}_\parallel)|^2.$$

Taking the limit of zero temperature in these equations the Eq. (2.17) is recovered.

Summation Procedure

In practical calculations the $\mathbf{k}_\parallel$-summation in Eqs. (2.18) and (2.20) is naturally replaced by an integration over k_x, k_y in the range $K(\varepsilon)$ within the irreducible 2D Brillouin zone, defined by $(k_x, k_y) \geq 0$ and $k_y \leq k_x$, providing the final result is multiplied by 8. The $K(\varepsilon)$ range is defined by the condition that the conducting longitudinal momentum in the leads is real. This establishes a transversal energy integration region: $a(\varepsilon) \leq \cos k_x + \cos k_y \leq b(\varepsilon)$ (the lattice parameter is set unity in what follows). These limits depend on the specific characteristics of the transport and the details about them are given in following chapters. The integration can be further simplified, regarding that the $\mathbf{k}_\parallel$-dependence of

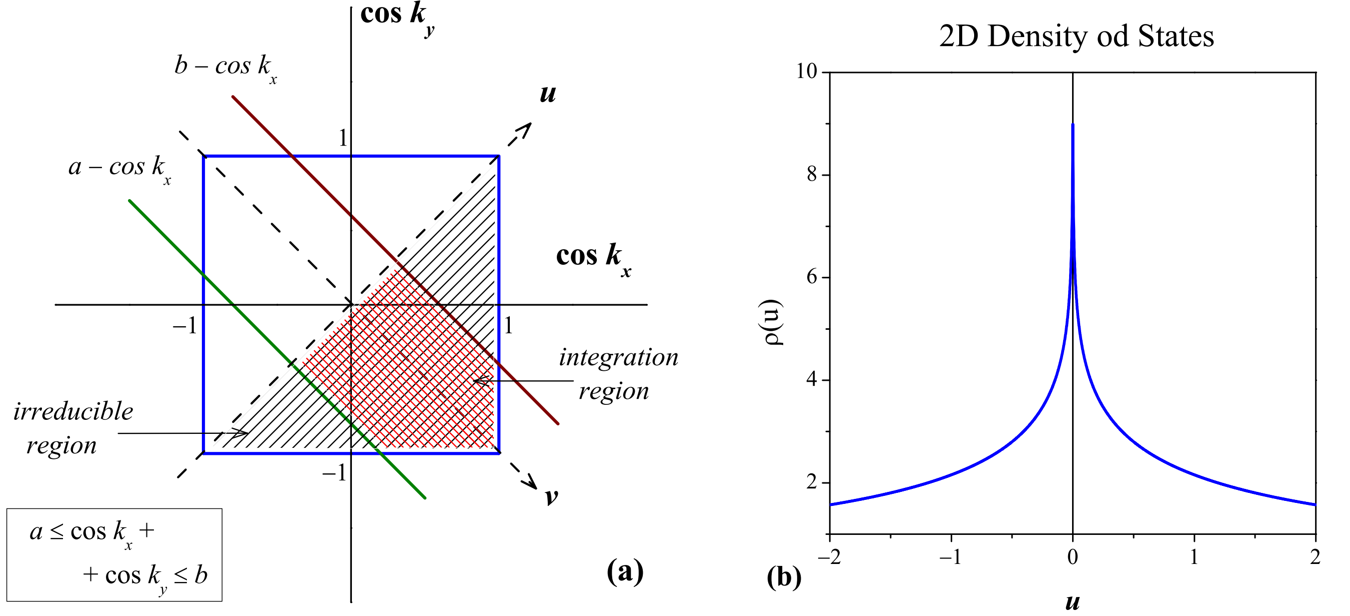

Figure 2.7: ***(a)****Restricted integration range* $K(\varepsilon)$ *as a function of* $\cos k_x a$, $\cos k_y a$ *and new integration variables* $u = \cos k_x a + \cos k_y a$ *and* $v = \cos k_x a - \cos k_y a$. ***(b)*** *The 2D density of states,* $\rho(u)$*, in the complete energy range,* $-2 \leq u \leq 2$.

the transmission coefficient $|T|^2$ is realized only through the transversal energy variable $u = \cos k_x + \cos k_y$ (conserved). With a proper change in variables, described in Fig. 2.7a, it is possible to reduce the numerical integration over two variables (k_x, k_y) to that in single variable u. This is done by integrating analytically the Jacobian determinant $J(u, v) = |\partial(u, v)/\partial(k_x, k_y)|$ over the variable $v = \cos k_x - \cos k_y$, in order to obtain the 2D density of states $\rho(u) = 8 \int_0^{2-|u|} J(u, v)dv$, [Gładysiewicz *et al.*, 2002]. Then, the Jacobian is given by:

$$J(u,v) = \begin{vmatrix} \partial_u k_x & \partial_v k_x \\ \partial_u k_y & \partial_v k_y \end{vmatrix} = \frac{1}{\begin{vmatrix} \partial_{k_x} u & \partial_{k_y} u \\ \partial_{k_x} v & \partial_{k_y} v \end{vmatrix}} = -\frac{1}{\sqrt{4-(|u|+v)^2}\sqrt{4-(|u|-v)^2}},$$

and the integration over v simply yields:

$$\rho(u) = N^{-1} \sum_{\mathbf{k}_\parallel} \delta(u - u_{\mathbf{k}_\parallel}) = \frac{4}{2+|u|} \mathrm{K}\left[\frac{(2-|u|)^2}{(2+|u|)^2}\right], \tag{2.21}$$

with the 1st kind full elliptic integral K(k) [Abramowitz and Stegun, 1964]. The density of states (DOS) is represented in Fig. 2.7b. With these considerations, the previous current and conductance formulas, Eqs. (2.18) and (2.20), are written as:

$$I = \frac{e}{h}\frac{1}{4\pi^2}\int d\varepsilon \int_{a(\varepsilon)}^{b(\varepsilon)} du\rho(u) \left[|T(\varepsilon,u)|^2 f_1(\varepsilon) - |T'(\varepsilon,u)|^2 f_2(\varepsilon)\right], \tag{2.22}$$

and

$$G = -\frac{e^2}{h}\frac{1}{4\pi^2}\int d\varepsilon \int_{a(\varepsilon)}^{b(\varepsilon)} du\rho(u) \left[\left(\frac{\partial f_0}{\partial \varepsilon}\right)|T(\varepsilon,u)|^2\right]. \tag{2.23}$$

Obviously, the u-integration limits depend on the system energy, ε, as well as the $K(\varepsilon)$ range.

2.2 Experimental Techniques

This section is divided in the following way: first, the samples studied are described, and second, experimental techniques used for their characterization are presented. The samples were prepared during the J. Santos Ph.D thesis work by himself and Dr. G. Kakazei, in the INESC-MN laboratories lead by Prof. P. Freitas at Lisbon. Indeed, extensive details on the sample preparation and structural characterization can be found in J. Santos thesis [J. Santos, 2005]. For that reason, many details are skipped here and only a brief description is made in Subsec. 2.2.1. In turn, a more detailed exposition of the electrical measurement set-up at the University of Algarve is made in Subsec. 2.2.2. In fact, preparation of the electrical measurement set-up took a substantial part of the present work. Finally, a short comment on the magnetic characterization set-up at University of Porto is made in Subsec. 2.2.3.

2.2.1 Samples Preparation and Description

Ion Beam Deposition

Ion beam deposition (IBD) technique presents a good control of the deposition conditions such as, the beam energy, incidence angle, deposition rates, and low pressure during the deposition. For that reason it is extensively used in the preparation of high quality nanostructures and devices.

INESC-MN is equipped with a fully automated Nordiko 3000 IBD machine, that

has a 6 targets holder (water cooled), coplanar with two RF ion sources (deposition and assist guns). A turbomolecular and a cryogenic pump assure the working base pressure of 7×10^{-8} Torr at which a Xe plasma is created through a discharge in the deposition gun, maintaining then a low pressure in the chamber (10^{-4} Torr) during deposition. The ions are accelerated by a three grid system, producing a lined up ion beam and preventing the contamination of the sample during deposition. It is important to mention that the deposition rates can be as low as $\sim (1-5) \times 10^{-2}$ nm/s, enabling a precise control of the film thickness. Normally, the angle between the beam and the target is set at 80°. The substrate holder rotates at $\sim$ 15 rpm and a permanent magnet array ($\sim$ 40 Oe) is mounted around the substrate holder to induce an anisotropy axis in the films.

A much more complete description of the system can be found in the Dr. S. Cardoso Ph.D thesis [S. Cardoso, 2003].

Samples

All the films were deposited on glass substrates using Xe ion beam sputtering acting alternatively on two separate targets. Alumina was sputtered from an Al_2O_3 target and the cobalt iron alloy from a $Co_{80}Fe_{20}$ target. The nominal thickness, t, of the $Co_{80}Fe_{20}$ layers was varied and that of the Al_2O_3 layers was fixed at 4.0 nm. The films with 10 Al_2O_3(4.0 nm)/ $Co_{80}Fe_{20}$(t) bilayers and a final Al_2O_3(3.0 nm) capping layer were deposited. Their complete structure presents as: Glass/[Al_2O_3(4.0 nm)/$Co_{80}Fe_{20}$(t$= 0.7, 0.9$ nm)]$_{10}$/Al_2O_3 (3.0 nm).

These samples (from the third deposition session by J. Santos) were labeled as N2. As was reported in his thesis, after the deposition of the first four samples, with $t = 0.7$, 0.9, 1.1, 1.3 nm, a problem occurred in the cooling system of the deposition gun and the deposition conditions were thereafter strongly modified. Even so, it did not affect the present study since only two diluted samples are addressed, with $t = 0.7, 0.9$ nm, prepared before the damage. These samples belong to a new class of granular materials, usually designated as discontinuous metal-insulator multi-layers (DMIM). Structural investigations performed before on these samples [G. Kakazei *et al.*, 2001 and Lesnik *et al.*, 2002] revealed formation of well defined spherical magnetic grains.

As already mentioned a deeper description of sample preparation and structural characterization can be found in J. Santos' Ph.D thesis [J. Santos, 2005].

2.2.2 Electrical Characterization

The electrical measurements were done in the current-in-plane (CIP) geometry, using two gold contacts, $\sim$ 3 mm long separated by $\sim$ 100 μm, evaporated on top of the films. The contacts evaporation (at CEOT in the University of Algarve) was done in high vacuum (imposed by a turbomolecular pump) through specially prepared shadow masks. Each sample was fixed on a shadow mask and mounted above a bridge were a piece of gold was evaporated by Joule heating produced by high-currents of $\sim$ 100 A. The high vacuum was maintained during 30 minutes after the evaporation, then the sample was left in low vacuum for more 30 minutes and finally the sample with evaporated contacts was removed from the chamber. A schematic representation of the samples is shown in Fig. 2.8.

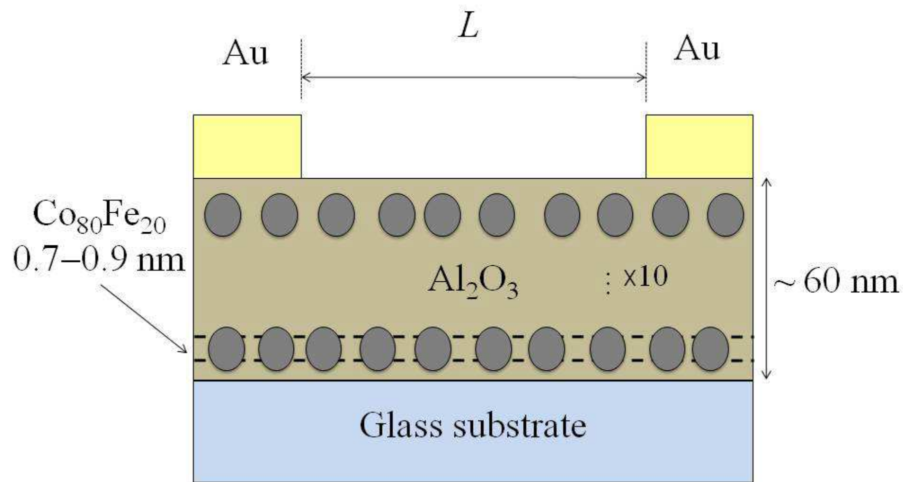

Figure 2.8: *Schematic representation of the studied samples.*

Two thin gold wires were glued with silver paint on the contacts and the samples were subsequently mounted on a sample holder of the ARS DE-202A close cycle He cryostat available at CEOT. The thin gold wires were glued (with silver paint) to the existing copper cryostat wires (carefully coiled around in different parts of the cryostat to prevent undesired heat propagation from the exterior) which finally connect to the instruments. Most of the measurements were performed in high vacuum in the temperature range of 30 K to 310 K. The temperature was controlled by a 331S Lakeshore temperature controller with use of a silicon diode sensor, model DT-470, to measure and control temperature.

Pictures of the experimental setup used for electrical transport measurements are presented in Fig. 2.9, more details will be given below.

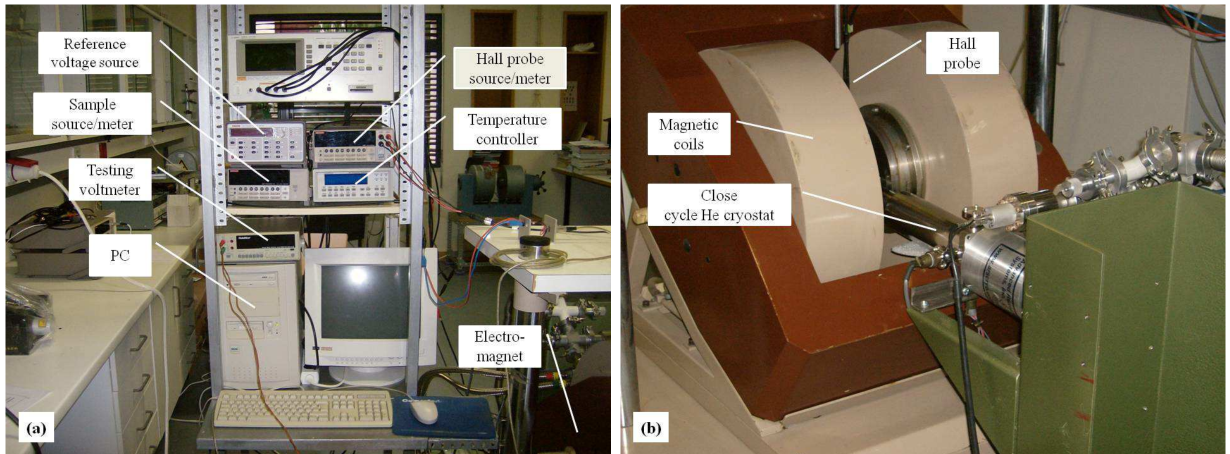

Figure 2.9: ***(a)*** *Photograph of the experimental setup for measurements of electrical transport properties;* ***(b)*** *Detail of the electromagnet and close cycle refrigerator.*

Instruments Control and Data Acquisition

Most measurements were done in a semi-automatic mode, the instruments control and data acquisition used LabView programs specially developed for this work. The programs allowed three types of measurements: current-voltage characteristics (I-V), current versus temperature (I-T), and finally magnetoresistance (MR).

Besides, almost all the measurements were done using GPIB communication through a National Instruments PCI-GPIB board, the programs were all written with a VISA protocol that enables an easy adaptation to RS-232 communication.

Current-Voltage Characteristics

Current-voltage characteristics were measured at fixed temperatures (stabilized by the temperature controller with a precision typically in the order of $\sim$ 10 mK) ranging from 30 K to 310 K. Due to the high resistance of the samples, a low-current/high-resistance picoammeter/voltage source Keithley 6487 was used. This instrument can measure resistances up to $\sim$ 1 TΩ. The voltage ramps were controlled by a LabView program with several parameters: voltage step typically $\Delta V \sim 0.1$ V, trigger time $\Delta t \sim$ 100 ms, maximum, V_{max}, and minimum voltages, V_{min}, and initial voltage, V_I, normally set to zero. The voltage cycles were as follows: starting from V_I up to V_{max}, then down

to V_{min} and finally to V_I again. The current passing through the films was in the range of $\sim 1 - 100$ nA with a typical resolution of ~ 10 pA.

The resistive switching measurements were done in a different setup employing a Keithley 487 (a previous version of the modern Keithley 6487), programmed by Prof. Peter Stallinga at CEOT using RS-232 communication. By default, in these measurements, voltage loops (starting from zero) decreased first to negative values.

Current versus Temperature

The current versus temperature data (I-T) were obtained by continuously changing the temperature at a typical rate of $\sim$ 1 K/min from 30 K to 310 K. The temperature ramps were controlled using an automatic proportional-integral-derivative (PID) algorithm installed in the 331S Lakeshore temperature controller. A PID control algorithm calculates control output based on the temperature setpoint and from feedback of the control sensor. Both current measurement and DC voltage biasing, typically $V = 20$ V, were made with use of the same Keithley 6487.

Magnetoresistance

The electromagnet used in the course of this work was extracted from a EPR Bruker ESR-200 TT spectrometer and was controlled by the respective Bruker B-MN90/30 C power supply. This magnet can go up to $\sim$ 1 T with use of two iron plates that reduce significantly the air gap between the magnetic poles. It is important to mention here that this electromagnet was kindly offered by Prof. J. J. Moura from the New University of Lisbon to Prof. J. F. L. Mariano of the Physics Department of the University of Algarve. After installing the magnet in the Solid State Physics and Magnetism Laboratory in the Physics Department of the University of Algarve, Prof. J. F. L. Mariano, that gave a fundamental support to the experimental realization of this work, skillfully repaired the electromagnet and provided all the procedure needed for its proper manipulation.

A schematic representation of the electromagnet setup is presented in Fig. 2.10. The current injected into the magnetic coils was controlled by a reference voltage source. The instrument used for that purpose was a Keithley 595 Quasistatic CV Meter, with locally (not by a remote PC control) programmable voltage ramps. In their course, both the magnetic field and the current passing through the sample (at a fixed voltage, $V = 20$ V)

were measured and data acquisition was performed by a LabView program. The magnetic field was measured by a calibrated Hall probe with a source-meter Keithley 2000 in the 4-wire configuration, yielding a constant current of 100 mA to the probe and measuring the Hall voltage. The current on the sample was measured by the Keithely 6487.

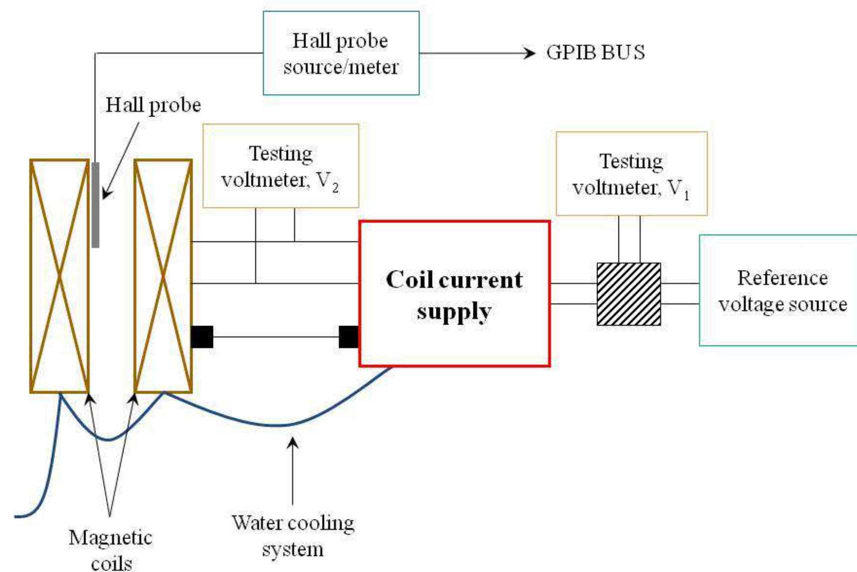

Figure 2.10: *Schematic representation of the electromagnet setup used in the magnetoresistance measurements.*

Capacitive Measurements

Capacitance versus voltage (C-V) was measured with a Fluke PM 6306 RCL meter with 0.1% basic accuracy. This device uses an external DC bias input signal modulated by an AC test signal. The test signal level can vary from 50 mV to 2 V, and the measuring frequency can go from 50 Hz to 1 MHz. The instrument control and data acquisition are made through a RS-232 interface with use of a program developed by Prof. Peter Stallinga at CEOT.

2.2.3 Magnetic Characterization

For the magnetic characterization of the samples, a SQUID (Superconducting Quantum Interference Device) magnetometer by Quantum Design, installed at IFIMUP, was used. This device has a sensitivity of 10^{-7} emu, and is equipped with a 5.5 T superconducting coil, and works typically in a temperature range, from 1.7 K to 400 K. More

details about the instrument can be found in other theses of the group, [M. Salgueiro, 1999] and [J. Santos, 2005].

Two types of magnetic measurements were done: magnetization curves as a function of the applied field, $M(H)$, (at fixed temperatures) and field-cooled (FC) and zero-field-cooled (ZFC) magnetization versus temperature measurements, $M(T)$. The latter measurements were done with a heating rate of 2.70 K/min, performing two consecutive scans (with total duration of $\sim$ 34 s) in temperature steps of 2 K. The samples were mounted inside plastic straws tied to a thin white cotton wire, which in turn was glued to the extremes of the straw with kapton tape. It is important to mention that before starting a new measurement the magnetometer was calibrated using a paramagnetic standard sample.

Chapter 3

Coherent Transport in Single Spacer Magnetic Junctions

This chapter is mainly devoted to the development of a simple tight-binding dynamics in single-band approximation, using the straightforward equations of motion for on-site quantum-mechanical amplitudes, to get a handy description of quantum magnetotransport in the ballistic regime for a trilayer system of spin-polarized electrodes with a thin and atomically coherent non-magnetic spacer. The motivation for the present approach is an easy generalization to different conduction regimes (including finite electric field effect) and more promising device geometries (double barriers or double junctions, as will be considered in the next chapter). The first sections are mainly limited to the basics of the method and to its most characteristic results. Thus, in Sec. 3.1 the explicit quantum wave functions are obtained for the 1-dimensional (1D) isolated atomic chain. In the following Sec. 3.2, the finite 1D chain is inserted between two 1D semi-infinite leads and the transmission and reflection coefficients for a collective electronic state are analytically calculated. Further, in Sec. 3.3, this result is generalized to the 3-dimensional (3D) case and the Landauer-Büttiker (LB) conductance formula [Landauer, 1957 and Büttiker, 1988] is adopted to yield a clear picture of basic quantum effects taking place in this coherent system. In Sec. 3.4, the important effects of electronic correlation are included, using the approximation of phenomenological interface potentials, which foresees a more consistent treatment in the spirit of density functional theory (DFT). In addition, in Sec. 3.5, the temperature and voltage effects on the magnetoresistance are explored.

The main objective is to understand in which way the zero temperature and voltage magnetotransport properties are altered by these effects. On the other hand, Sec. 3.6 deals with the perturbation of electronic distribution functions in the vicinity of the barrier, either in equilibrium and out-of-equilibrium (that can be important for the performance of spintronic devices). This effect is usually considered in the diffusive regime, but here it is treated in the ballistic regime. Then, in Sec. 3.7, the generalization of the previous considerations to coherent transport at arbitrary angle θ between the magnetizations of the magnetic electrodes is outlined. This treatment should enable the calculation of spin-torque transfer and further developments that will be done in future works. At last, in Sec. 3.8, a summary and principal results are presented and commented.

3.1 Basic Chain Model

The simplest model for transport over exact electronic states considers a linear chain of n identical atoms with single available electronic state $|l\rangle$ on each l-th atomic site and describes the single-electron dynamics in the tight-binding (TB) approximation with (real) hopping amplitude t between nearest neighbor sites (taking the distance between them as unit length), as shown in Fig. 3.1.

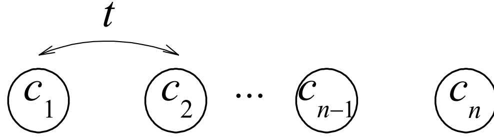

Figure 3.1: *Finite atomic chain with tight-binding hopping amplitude t.*

In this coupled chain, any collective electronic state can be expressed as $|\psi\rangle = \sum_{l=1}^{n} c_l|l\rangle$, with complex amplitudes c_l and atomic states $|l\rangle = \hat{a}_l^\dagger|0\rangle$, generated by the second quantization operators acting on the vacuum state $|0\rangle$. Choosing the 1D Hamiltonian discussed in the previous Chapter, with $\varepsilon_l = 0$:

$$\hat{H}^{(n)} = t\sum_{l=1}^{n-1}(\hat{a}_l^\dagger\hat{a}_{l+1} + \hat{a}_{l+1}^\dagger\hat{a}_l), \tag{3.1}$$

it is possible to obtain the electronic spectrum ε_m ($m = 1, \ldots, n$) as the set of roots of the

secular equation $D_n(\varepsilon) = \det(\varepsilon - \hat{H}^{(n)}) = 0$, with the corresponding Hamiltonian matrix $H^{(n)}_{l,l'} = \langle l|\hat{H}^{(n)}|l'\rangle = t\,(\delta_{l,l+1}\theta_{l-1} + \delta_{l,l-1}\theta_{n-l})$ (where $\delta_{l,l'}$ is the Kronecker delta and $\theta_l = 1$ if $l > 0$, otherwise zero). For the instance of $n = 4$, the determinant is written as:

$$\begin{vmatrix} \varepsilon & -t & 0 & 0 \\ -t & \varepsilon & -t & 0 \\ 0 & -t & \varepsilon & -t \\ 0 & 0 & -t & \varepsilon \end{vmatrix} = 0.$$

For any $n \geq 2$, these determinants satisfy the recurrent relation:

$$D_n(\varepsilon) = \varepsilon D_{n-1}(\varepsilon) - t^2 D_{n-2}(\varepsilon), \quad n \geq 2, \tag{3.2}$$

with the initial conditions $D_0(\varepsilon) = 1$, $D_1(\varepsilon) = \varepsilon$, that define them exactly as: $D_n(\varepsilon) = t^n u_n(\varepsilon/2t)$, where $u_n(x)$ are the 2nd kind Chebyshev polynomials [Abramowitz and Stegun, 1964]. It is convenient to rewrite Eq. (3.2) in terms of these dimensionless polynomials $u_n(x)$ as functions of the dimensionless variable $x = \varepsilon/2t$, as:

$$2xu_n(x) = u_{n+1}(x) + u_{n-1}(x), \tag{3.3}$$

with $u_0(x) = 1$, $u_1(x) = 2x$. Then a useful trigonometric parametrization $u_l(\cos\theta) = \sin[(l+1)\theta]/\sin\theta$ permits to present the general solution of Eq. (3.3) as:

$$u_l(x) = \frac{\sin[(l+1)q_x]}{\sin q_x}, \tag{3.4}$$

where $q_x = \arccos x$. Then the discrete energy spectrum given by zeros of $u_n(x)$ is explicitly written as:

$$\varepsilon_m = 2t\cos\frac{\pi m}{n+1}, \quad m = 1, \ldots, n. \tag{3.5}$$

Now let $\psi(x) = (c_1(x), \ldots, c_n(x))$ be the eigenvector of the Hamiltonian matrix, related to the eigenenergy $\varepsilon = 2tx$ (in what follows, the explicit energy arguments of the local amplitudes are often dropped, like c_l). Its components satisfy the TB equations of motion:

$$2xc_l = c_{l+1} + c_{l-1}, \quad \text{for} \quad 2 \leq l \leq n-1, \tag{3.6}$$

completed by $2xc_1 = c_2$ and $2xc_n = c_{n-1}$. Since Eq. (3.6) for c_l/c_1 is just equivalent to Eq. (3.3) for u_{l-1}, the eigenvector components can be written as:

$$c_l = \frac{\sin(lq_x)}{\sin q_x} c_1. \tag{3.7}$$

This solution also satisfies the above mentioned equations of motion for c_1 and c_n and provides the *closed* boundary conditions: $c_0 = c_{n+1} = 0$. As usual, the value of c_1 is fixed by the normalization condition, $\sum_l |c_l(x)|^2 = 1$, giving finally the l-th component of the eigenvector (related to the eigenenergy $\varepsilon_m = 2tx_m$) as:

$$c_l(x_m) = \sqrt{\frac{2}{n+1}} \sin\left(\frac{m\pi}{n+1} l\right). \tag{3.8}$$

The energy spectrum and the eigenvectors for a chain with $n = 4$ and $t = 1/2$ are presented in Fig. 3.2.

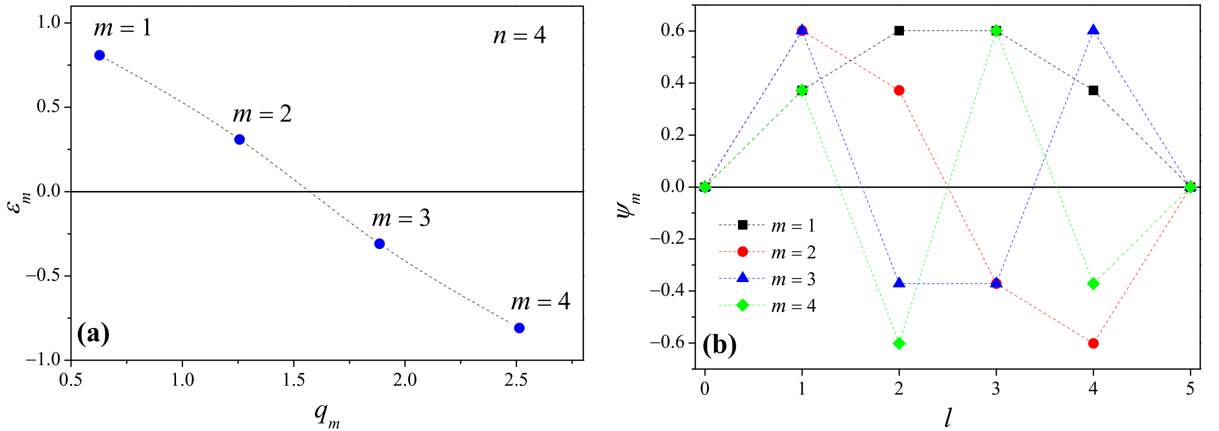

Figure 3.2: ***(a)*** *Discrete energy spectrum for a chain with $n = 4$ and $t = 1/2$;* ***(b)*** *Eigenvectors $\psi(x)$ local amplitudes for the same chain.*

Next, this finite chain is inserted into a *circuit* between two semi-infinite chain leads.

3.2 Transmission Through Discrete Chain Structure

For a composite system of finite n-chain (in what follows called the gate, G) between two semi-infinite chain leads, S (source) and D (drain), Fig. 3.3, the TB Hamiltonian, Eq.

(3.1), is extended to: $\hat{H} = \hat{h}^s + \hat{h}^{sg} + \hat{h}^g + \hat{h}^{gd} + \hat{h}^d$ where:

$$\begin{aligned} \hat{h}^i &= \sum_{l=l_i}^{l_{i+1}-1} \left[\varepsilon_i \hat{a}_{i,l}^\dagger \hat{a}_{i,l} + t_i \left(\hat{a}_{i,l}^\dagger \hat{a}_{i,l+1} + \text{h.c.} \right) \right], \\ \hat{h}^{sg} &= t_{sg} \left(\hat{a}_{s,0}^\dagger \hat{a}_{g,1} + \text{h.c.} \right), \\ \hat{h}^{gd} &= t_{gd} \left(\hat{a}_{d,1}^\dagger \hat{a}_{g,n+1} + \text{h.c.} \right), \end{aligned} \tag{3.9}$$

including the respective on-site energies ε_i and hopping parameters t_i for $i = s, g, d$. The summation limits l_i label the first atomic planes (in the left to right counting) in each ith element, defined as $l_s = -\infty$, $l_g = 1$, $l_d = n+1$. In this macroscopic system, the energy spectrum includes continuous S- and D-bands $\varepsilon_{i,q} = \varepsilon_i + 2t_i \cos q$, $i = s, d$ and possibly discrete G-levels outside these bands. The collective eigenvector for a given energy ε can be found from the equations of motion that generalize Eq. (3.6). The local amplitudes of the wave function are denoted by s_l, g_l or d_l and to simplify the mathematical calculations, the dimensionless dynamical variables are defined $x_i = (\varepsilon - \varepsilon_i)/2t_i$ $(i = s, g, d)$. Further, the wave amplitude in S is defined as a sum of an incident wave of intensity 1 (with wave number $q_s = \arccos x_s$) and a reflected wave of amplitude R (with wave number $-q_s$). In a similar way, the wave amplitude in D is set to T (with wave number $q_d = \arccos x_d$). That can be expressed through following equations:

$$\begin{cases} s_l = \mathrm{e}^{iq_s l} + R\mathrm{e}^{-iq_s l}, & l \le 0 \\ d_l = T\mathrm{e}^{iq_d l}, & l \ge n+1. \end{cases} \tag{3.10}$$

These refer to one of the two fundamental solutions for a given energy[1], ε. These forms automatically satisfy the equations of motion, Eq. (3.6), within S and D:

$$2x_s s_l = s_{l-1} + s_{l+1}, \quad 2x_d d_l = d_{l-1} + d_{l+1}, \tag{3.11}$$

[1] Another solution corresponds to an incident and a reflected wave in D and a transmitted one in S. This solution will be included in other sections of this chapter.

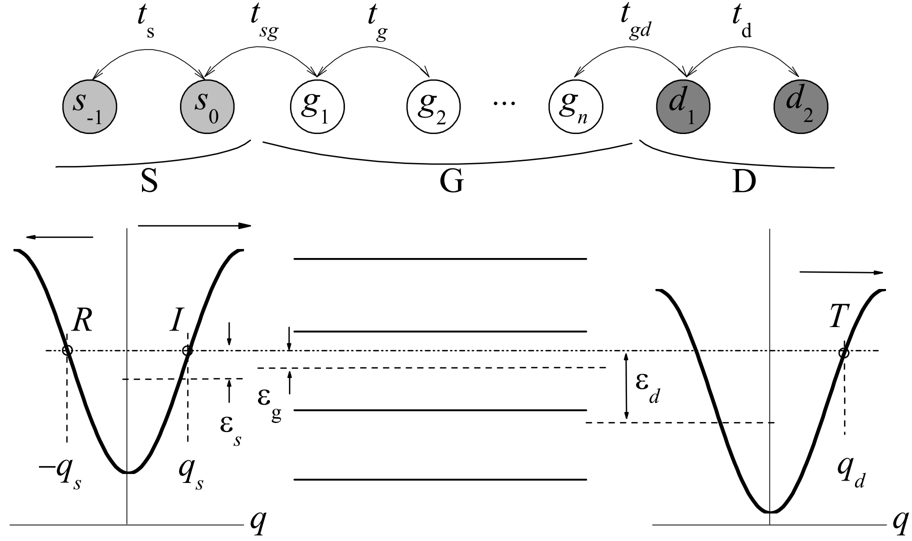

Figure 3.3: *Composite system of a finite n-chain (gate element, G) inserted between two semi-infinite chain leads (source, S, and drain, D). The energy diagram shows the on-site energy levels (dashed) for i-th element ($i = s, g, d$) and the Fermi level (dot-dashed) whose crossings with the continuous S- and D- dispersion curves define the wave numbers for incoming (q_s), reflected ($-q_s$) and transmitted (q_d) parts of the Fermi state. Notice that the Fermi level generally does not match any of the discrete levels (solid) in the central (G) element.*

while the pairs of equations on the (S/G) and (G/D) interfaces:

$$\begin{aligned} 2\cos q_s s_0 &= s_{-1} + \frac{t_{sg}}{t_s} g_1, \\ u_1 g_1 &= g_2 + \frac{t_{sg}}{t_g} s_0, \end{aligned} \tag{3.12}$$

and

$$\begin{aligned} 2\cos q_d d_1 &= d_2 + \frac{t_{gd}}{t_d} g_n, \\ u_1 g_n &= g_{n-1} + \frac{t_{gd}}{t_g} d_1, \end{aligned} \tag{3.13}$$

are the discrete analogs of usual boundary conditions for continuous wave function and its derivative [Slonczewski, 1989]. They permit to express the terminal pairs of G-amplitudes

through the asymptotic parameters R, T, q_s and q_d:

$$\begin{aligned} g_1 &= \frac{t_s}{t_{sg}}(1+R), \quad g_2 = \frac{t_s}{t_{sg}}\left[u_1 - \gamma_s^* + (u_1-\gamma_s)R\right], \\ g_n &= \frac{t_d}{t_{gd}}T, \qquad\qquad g_{n-1} = \frac{t_d}{t_{gd}}(u_1-\gamma_d)T, \end{aligned} \tag{3.14}$$

with the interface parameters $\gamma_s = \mathrm{e}^{iq_s}{t_{sg}}^2(t_g t_s)^{-1}$ and $\gamma_d = \mathrm{e}^{iq_d}{t_{gd}}^2(t_g t_d)^{-1}$. The polynomials $u_l \equiv u_l(x_g)$ are formally the same as given by Eq. (3.4) with the energy argument $x_g = (\varepsilon - \varepsilon_g)/(2t_g)$. But the energies ε of main interest for the transport processes are those close to the Fermi energy ε_{F} which is generally *not* an eigenvalue, Eq. (3.5), for the isolated G-element. Therefore the transient momentum $q_g = \arccos x_g$ (not necessarily real) breaks down the *closed* boundary conditions, Eq. (3.8), for G and thus enables continuity of quantum states along the composite system. Next, using Eq. (3.6) for this element in the form:

$$u_1 g_l = g_{l+1} + g_{l-1}, \tag{3.15}$$

it is possible to interrelate the terminal G-amplitudes:

$$\begin{aligned} g_{n-1} &= u_{n-2}g_1 - \frac{t_{sg}}{t_g}u_{n-3}s_0, \\ g_n &= u_{n-1}g_1 - \frac{t_{sg}}{t_g}u_{n-2}s_0. \end{aligned} \tag{3.16}$$

Then, Eqs. (3.15) and (3.17) yield two independent relations between the coefficients R and T. Those are readily solved to give:

$$\begin{aligned} R(x_s, x_g, x_d) &= -\frac{\overline{D}_n}{D_n}, \\ T(x_s, x_g, x_d) &= -2i\frac{t_{sg}t_{gd}}{t_g t_d}\frac{\sin q_s}{D_n}, \end{aligned} \tag{3.17}$$

where the resonance properties result from the denominator:

$$D_n(x_s, x_g, x_d) = u_n - (\gamma_s + \gamma_g)u_{n-1} + \gamma_s\gamma_d u_{n-2}, \tag{3.18}$$

with the relevant variables $x_i = (\varepsilon - \varepsilon_i)/(2t_i)$ as arguments of complex factors γ_i and real polynomials $u_l \equiv u_l(x)$, and $\overline{D}_n(x_s, x_g, x_d) \equiv D_n(x_s + \pi, x_g, x_d)$. Since, in the considered 1D case, all $x_i(\varepsilon) = (\varepsilon - \varepsilon_i)/(2t_i)$ are defined by the single energy variable ε, the coeffi-

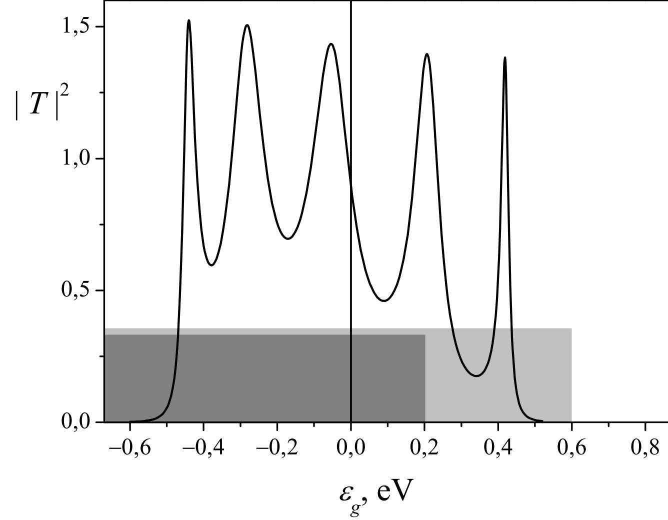

Figure 3.4: *Transmission coefficient $|T|^2$ as a function of the on-site energy ε_g in the gate element of the composite chain system, for the choice of its parameters $\varepsilon_s = -0.4$ eV, $\varepsilon_d = -0.8$ eV (relative to the Fermi energy), $t_s = t_d = 0.5$ eV, $t_g = t_{sg} = t_{gd} = 0.25$ eV and $n = 5$. The shadowed areas indicate the (Stoner shifted) continuous bands, S (light grey) and D (dark grey).*

cients R and T can be also defined as functions of energy: $R(\varepsilon) \equiv R\left(x_s(\varepsilon), x_g(\varepsilon), x_d(\varepsilon)\right)$ and $T(\varepsilon) \equiv T\left(x_s(\varepsilon), x_g(\varepsilon), x_d(\varepsilon)\right)$. It is important to notice that the result of Eqs. (3.17), (3.18) is just analogous to that obtained with the Green function techniques [Mathon *et al.*, 1995], the factors γ_s and γ_d playing the role of interface Green functions. A typical behavior of the transmission coefficient $|T(\varepsilon)|^2$ is presented in Fig. 3.4. It shows n transmission resonances generated by n discrete energy levels of the G-element (by n atoms in the chain) as they are passing over the Fermi level within the mutually displaced energy bands. The displacement can be due, for instance, to the Stoner splitting between majority and minority subbands of oppositely polarized S- and D-elements. Notice that the resonances become sharper as the levels approach the band edges, and the maximum transmission in the asymmetric S-D band configuration is not limited to unity (the flux conservation does not mean the density conservation if the in- and out-velocities are not equal). This coefficient enters the LB formula for the ballistic conductance through the 1D composite system (in zero temperature limit):

$$G = \frac{e^2}{h} |T\left(\varepsilon_{\mathrm{F}}\right)|^2, \tag{3.19}$$

with the Fermi energy ε_{F}. Now, allowing the S and D chains to support spin polarized

subbands $\varepsilon_{i,q,\sigma} = \varepsilon_{i,\sigma} + 2t_i \cos q$ (where $\varepsilon_{i,\sigma} = \varepsilon_i - \sigma\Delta_i$, $\sigma = \pm$, are the majority and minority spin indices and Δ_i are the Stoner splitting parameters for $i = s, d$), it is possible to introduce the energy and spin-dependent variables $x_{i,\sigma}(\varepsilon) = (\varepsilon - \varepsilon_{i,\sigma}) / (2t_i)$, $i = s, d$, for in- and out-channels and obtain from Eq. (3.19) the spin-dependent conductance values $G_{\sigma,\sigma'} = \left(e^2/h\right) |T\left(x_{s,\sigma}(\varepsilon_{\mathrm{F}}), x_{d,\sigma'}(\varepsilon_{\mathrm{F}}), x_g(\varepsilon_{\mathrm{F}})\right)|^2$. Finally, the (maximum) magnetoresistance is defined as usually through the difference between the conductance values $G_P = G_{+,+} + G_{-,-}$ for parallel and $G_{AP} = G_{+,-} + G_{-,+}$ for antiparallel (S/D) polarization: $MR = G_P/G_{AP} - 1$.

Although state-of-the-art technology already permits development of such genuinely 1D devices and the resonance behavior like that in Fig. 3.4 (different from the known quantized conductance steps vs voltage bias) can be directly sought in them, it is of major practical importance to generalize the above treatment for a more realistic multilayered structure and this will be done in the next section.

3.3 3-Dimensional Multilayered Structure

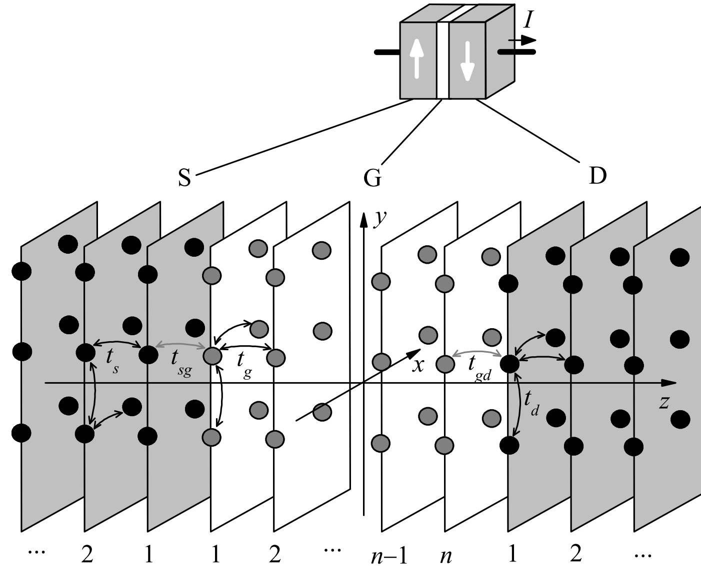

Figure 3.5: *Real multilayered structure where the current flows through two ferromagnetic electrodes, S and D, separated by a non-magnetic spacer G, and its model by the composite 3D system where a finite n-plane spacer is inserted between two semi-infinite leads.*

Passing from 1D composite chain to multilayered (and spin polarized) 3D lattice structure as shown in Fig. 3.5, the indexing of site operators is extended from $\hat{s}_l$, $\hat{d}_l$ and $\hat{g}_l$ to $\hat{s}_{l,\mathbf{m},\sigma}$, $\hat{d}_{l,\mathbf{m},\sigma}$ and $\hat{g}_{l,\mathbf{m},\sigma}$, where $\mathbf{m}$ runs over N sites in the lth plane and σ is $\pm$. The strategy in this case relies on the conservation of the transversal quasi-momentum $\mathbf{k}_\parallel$ in the transitions between the planes [Mathon *et al.*, 1995]. From the experimental point of view, this requires perfect interfaces that are only reachable with advanced deposition techniques [Ikeda *et al.*, 2008]. To describe the situation where $\mathbf{k}_\parallel$ is a good quantum number for independent 1D-like longitudinal transport channels, *planar wave operators* are used instead of the previous site operators. Thus, for the lth plane in the S element, the planar wave operators are defined as:

$$\hat{s}_{l,\mathbf{k}_\parallel,\sigma} = \frac{1}{\sqrt{N}} \sum_{\mathbf{m}} \mathrm{e}^{i\mathbf{k}_\parallel \cdot \mathbf{m}} \hat{s}_{l,\mathbf{m},\sigma}, \tag{3.20}$$

and similarly $\hat{d}_{l,\mathbf{k}_\parallel,\sigma}$ and $\hat{g}_{l,\mathbf{k}_\parallel,\sigma}$ are written for D and G elements. The related extension of the Hamiltonian is: $\hat{H} = \sum_{\mathbf{k}_\parallel,\sigma} \left(\hat{h}^s_{\mathbf{k}_\parallel,\sigma} + \hat{h}^{sg}_{\mathbf{k}_\parallel,\sigma} + \hat{h}^g_{\mathbf{k}_\parallel,\sigma} + \hat{h}^{gd}_{\mathbf{k}_\parallel,\sigma} \; + \hat{h}^d_{\mathbf{k}_\parallel,\sigma} \right)$, where the particular terms are analogous to those in Eq. (3.9) with the change of all the site operators by the planar wave ones and all the on-site energies ε_i by the transversal momentum subbands $\varepsilon_{i,\mathbf{k}_\parallel,\sigma} = \varepsilon_{i,\sigma} + 2t_i \left(\cos k_x + \cos k_y \right), \; i = s, d$ and $\varepsilon_{g,\mathbf{k}_\parallel,\sigma} = \varepsilon_g + 2t_g \left(\cos k_x + \cos k_y \right)$. The equations of longitudinal motion in terms of the *planar wave* amplitudes $s_{l,\mathbf{k}_\parallel,\sigma}$, $d_{l,\mathbf{k}_\parallel,\sigma}$ and $g_{l,\mathbf{k}_\parallel,\sigma}$ (for given energy ε of the collective state) are obtained in analogy with the 1D case. Thus, in the leads S and D (beyond the interfaces), they are analogs to Eq. (3.11):

$$\begin{aligned} 2x_{s,\mathbf{k}_\parallel,\sigma} s_{l,\mathbf{k}_\parallel,\sigma} &= s_{l-1,\mathbf{k}_\parallel,\sigma} + s_{l+1,\mathbf{k}_\parallel,\sigma}, \\ 2x_{d,\mathbf{k}_\parallel} d_{l,\mathbf{k}_\parallel,\sigma} &= d_{l-1,\mathbf{k}_\parallel,\sigma} + d_{l+1,\mathbf{k}_\parallel,\sigma}, \end{aligned} \tag{3.21}$$

with $x_{i,\mathbf{k}_\parallel,\sigma} = (\varepsilon - \varepsilon_{i,\mathbf{k}_\parallel,\sigma}) / \left(2t_i \right)$, $i = s, d$, while in the spacer G (at $1 < l < n$), they are [in analogy with Eqs. (3.7) and (3.15)]:

$$2x_{g,\mathbf{k}_\parallel} g_{l,\mathbf{k}_\parallel,\sigma} = g_{l-1,\mathbf{k}_\parallel,\sigma} + g_{l+1,\mathbf{k}_\parallel,\sigma}, \tag{3.22}$$

with $x_{g,\mathbf{k}_\parallel} = (\varepsilon - \varepsilon_{g,\mathbf{k}_\parallel})/(2t_g)$. Also the equations for interface amplitudes:

$$\begin{aligned}
2x_{s,\mathbf{k}_\parallel,\sigma} s_{\mathbf{k}_\parallel,1,\sigma} &= s_{\mathbf{k}_\parallel,2,\sigma} + \frac{t_{sg}}{t_s} g_{\mathbf{k}_\parallel,1,\sigma}, \\
2x_{g,\mathbf{k}_\parallel} g_{\mathbf{k}_\parallel,1,\sigma} &= g_{\mathbf{k}_\parallel,2,\sigma} + \frac{t_{sg}}{t_g} s_{\mathbf{k}_\parallel,1,\sigma}, \\
2x_{g,\mathbf{k}_\parallel} g_{\mathbf{k}_\parallel,n,\sigma} &= g_{\mathbf{k}_\parallel,n-1,\sigma} + \frac{t_{gd}}{t_g} d_{\mathbf{k}_\parallel,1,\sigma}, \\
2x_{d,\mathbf{k}_\parallel,\sigma} d_{\mathbf{k}_\parallel,1,\sigma} &= d_{\mathbf{k}_\parallel,2,\sigma} + \frac{t_{gd}}{t_d} g_{\mathbf{k}_\parallel,1,\sigma},
\end{aligned} \tag{3.23}$$

are analogous to Eqs. (3.12), (3.13) and (3.14). The next derivation, in full similarity with the 1D case, leads to the full dispersion laws in the leads $\varepsilon_{i,\mathbf{k}_\parallel,q,\sigma} = \varepsilon_{i,\mathbf{k}_\parallel,\sigma} + 2t_i \cos q$ (for $i = s,\, d$) and to the final conductance formula for particular in-out spin channels:

$$G_{\sigma\sigma'} = \frac{e^2}{h} \sum_{\mathbf{k}_\parallel \in K} |T_{\sigma\sigma'}(\varepsilon_\mathrm{F}, \mathbf{k}_\parallel)|^2. \tag{3.24}$$

Here the transmission coefficient depends on the relevant variables $\sigma, \sigma', \varepsilon$ and $\mathbf{k}_\parallel$ accordingly to: $T_{\sigma\sigma'}(\varepsilon, \mathbf{k}_\parallel) \equiv T(q_{s,\mathbf{k}_\parallel,\sigma}, q_{g,\mathbf{k}_\parallel}, q_{d,\mathbf{k}_\parallel,\sigma'})$ with $q_{i,\mathbf{k}_\parallel,\sigma} = \arccos x_{i,\mathbf{k}_\parallel,\sigma}$ for $i = s, d$ and $q_{g,\mathbf{k}_\parallel} = \arccos x_{g,\mathbf{k}_\parallel}$. The sum in $\mathbf{k}_\parallel$ is restricted to the *permitted summation* range K, such that simultaneous equalities $\varepsilon_{s,\mathbf{k}_\parallel,q_s} = \varepsilon_{d,\mathbf{k}_\parallel,q_d} = \varepsilon_\mathrm{F}$ result in certain *real* in- and out-momenta q_s and q_d. In particular, using the summation procedure developed in the Chap. **2**, the Eq. (3.25) becomes:

$$G_{\sigma\sigma'} = \frac{e^2}{h} \frac{1}{(2\pi)^2} \int_{a_{\sigma,\sigma'}}^{b_{\sigma,\sigma'}} du \rho(u) |T_{\sigma,\sigma'}(\varepsilon_\mathrm{F}, u)|^2, \tag{3.25}$$

with $\rho(u) = N^{-1} \sum_{\mathbf{k}_\parallel} \delta(u - u_{\mathbf{k}_\parallel}) = 4/(2+|u|)\mathrm{K}\left[(2-|u|)^2/(2+|u|)^2\right]$ and the integration limits:

$$\begin{aligned}
b_{\sigma,\sigma'} &= \min\left\{2, \min\left[x_{s,\sigma}(\varepsilon_\mathrm{F}), x_{d,\sigma'}(\varepsilon_\mathrm{F})\right] + 1\right\}, \\
a_{\sigma,\sigma'} &= \max\left\{-2, \max\left[x_{s,\sigma}(\varepsilon_\mathrm{F}), x_{d,\sigma'}(\varepsilon_\mathrm{F})\right] - 1\right\},
\end{aligned} \tag{3.26}$$

fully defining the integration procedure in the limit of continuous $\mathbf{k}_\parallel$, as discussed in the previous chapter. It should be noted that the internal momentum q_g can be either real

or imaginary in this course, depending on specific $\mathbf{k}_{\parallel}$ in K. Therefore the attribution of purely *tunneling* or purely *metallic* conduction regime is here conventional to a certain extent, for instance a predominant tunnel-like conductance can pass to metallic-like with growing n_g. Then, seeking for optimum performance of the model MR device it is of interest to evaluate it as a function of the system parameters, mainly the number n of atomic layers in the gate and the on-site energy level ε_g of the gate (which can be possibly controlled through the gate bias). Also, variation of the latter parameter from positive to negative values permits to model in a unified way the passage from TMR to GMR regime (in the above indicated sense).

3.3.1 Magnetoresistance and Numerical Results

The following numerical work can be guided accordingly to some evident qualitative arguments. The variation of the integrand in Eq. (3.25) is mainly controlled by that of the polynomials $u_l\left(x_{g,\mathbf{k}_{\parallel}}\right)$ in the denominator of Eq. (3.18). As seen from the explicit Eq. (3.4), they are oscillating if $\left|x_{g,\mathbf{k}_{\parallel}}\right| < 1$ (when the sampling point $\varepsilon_{g,\mathbf{k}_{\parallel}}$ in the G-spectrum is close enough to the Fermi energy ε_{F}) and exponentially growing if $|x_g| > 1$ (when $\varepsilon_{g,\mathbf{k}_{\parallel}}$ is far enough from ε_{F}). Therefore, the conductance is generally expected to oscillate (either in ε_g and in n) as far as the level ε_g is close enough to ε_{F} (which can be compared to the GMR regime) and to exponentially decay at ε_g far enough from ε_{F} (a generalized TMR regime). The latter decay should asymptotically tend to $MR(n) \propto \exp\left(-nx_{\min}\right)$ with $x_{\min} = \min_{\mathbf{k}_{\parallel}\in K}\left|x_{g,\mathbf{k}_{\parallel}}\right|$ at $n \gg 1$.

In the latter case, the direct calculation of MR may result in G_P and G_{AP} both exponentially small but the last one being much smaller and yielding (arbitrarily) huge MR values. However, they should not be physically attainable, taking into account that the real multiband electronic structure of transition metals (built from atomic s-, p- and d- orbitals) always includes some additional conduction channels, for instance due to the s-bands, whose tunnel contribution decays slower than that of spin-polarized d-bands and is almost spin independent. Therefore it should dominate the transport in the indicated regime and make the real MR exponentially small. A simple phenomenological account of this mechanism in the considered single-band model can be done by introducing a certain

spin-independent term G_0 either into G_P and G_{AP} values:

$$G_P = G_{++} + G_{--} + G_0, \quad G_{AP} = G_{+-} + G_{-+} + G_0, \tag{3.27}$$

to present the MR formula as:

$$MR = \frac{G_{++} + G_{--} - G_{+-} - G_{-+}}{G_{+-} + G_{-+} + G_0}. \tag{3.28}$$

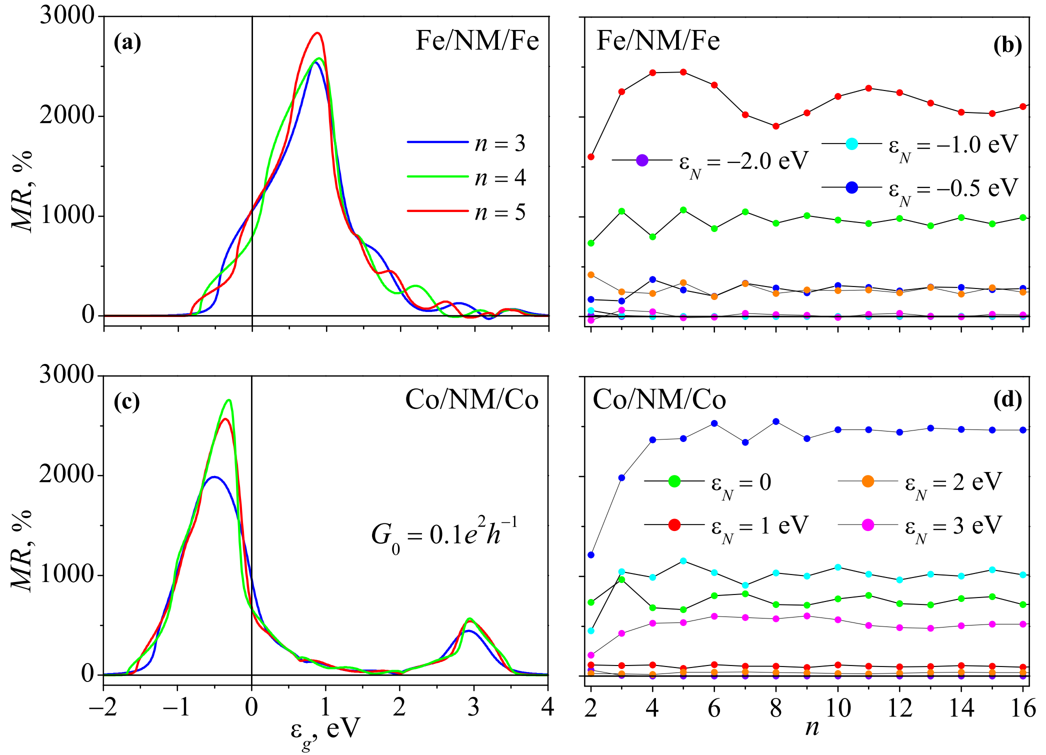

Figure 3.6: *Magnetoresistance of a Fe/NM/Fe junction (the parameters are given in the Chap. 2): **(a)** as a function of the on-site energy ε_g of the gate element for the same junction and various numbers of atomic planes in the gate element, $n_g = 3$, $n_g = 4$ and $n_g = 5$. Compare the resonance peaks in the* shallow band *regime with those in the 1D case of Fig. 3.3; **(b)** in function of the number n_g of spacer layers at fixed values of ε_g. Magnetoresistance of a Co/NM/Co junction (the parameters are given in the Chap. 2): **(c)** as a function of the on-site energy ε_g of the gate element for the same junction and various numbers of atomic planes in the gate element, $n_g = 3$, $n_g = 4$ and $n_g = 5$; **(d)** in function of the number n_g of spacer layers at fixed values of ε_g;*

It is just this formula that is used below for all practical MR calculations. In what follows the band structure parameters for Fe and Co highlighted in the previous

chapter[2] are employed, the spacer hopping amplitude is set equal to the one in FM leads, and a constant value $G_0 = 0.1e^2/h$ (about $\sim 10\%$ of the expected total conductance) is chosen. With such assumptions, it is found that the MR behavior vs n indeed changes qualitatively at different choices of ε_g for both FM elements, Figs. 3.6(b,d). The TMR-like behavior with fast exponential decay appears either at high enough gate level, $\varepsilon_g > 6|t_g|$ (which can be compared to a *positive* barrier in the continuum approximation), and at low enough $\varepsilon_g < -6|t_g|$ (a *negative* or *hole* barrier), but it develops GMR-like oscillations with greatly enhanced average MR amplitude at the intermediate ε_g values (which can be called the *shallow band regime*). The oscillating behavior reveals similar types of periods as those predicted by the Green function treatment [Mathon *et al.*, 1995], and it is in a qualitative agreement with that experimentally observed for MgO moderate (low barrier) tunnel junctions between Fe electrodes [Yuasa *et al.*, 2004], except for stronger first oscillation. However, it will be shown below that these strong oscillations are effectively attenuated when the specific interface effects between metal and insulator layers are taken into account. The most notable feature of the calculated MR is its amazingly high maximum value, of the order of $\sim$ 3000%, indicating a huge potentiality of the quantum coherent conduction regime. For the same choice of parameters, the calculated dependencies of MR vs ε_g (at fixed values of n = 3, 4, 5) are shown in Fig.3.6(a,c). In concordance with the above considered $MR(n)$ behavior, they practically vanish beyond the range of intermediate ε_g and display a finite number of resonance peaks within this range (reminiscent of n 1D resonances in Fig. 3.3), reaching the same highest order of magnitude in the *shallow band regime.* It is important to note the existence of a smaller peak for the Co junction at $\varepsilon_g \sim 3$ eV (near the tunnel regime), that it is not found in the Fe-based structures. Interestingly, it coincides with the experimental measurements, since Co/MgO/Co revealed higher MR values than Fe/MgO/Fe [Yuasa *et al.*, 2006]. Further, very high MR values in the present TB approach contrast with the known result for the model of almost free electrons through the continuous rectangular barrier [Slonczewski, 1989], where MR reaches zero at lower barrier heights. As yet, the $MR(\varepsilon_g)$ dependence was only studied experimentally for Al-O spacers [Tezuka and Miyazaki, 1998], possessing most probably polycrystalline or amorphous structure and high enough ε_g, so it could

[2]Notice that, for simplicity, in this chapter and the following, the hopping term of the Hamiltonian is taken as positive, so to be in accordance with the adjusted band structure of Chap. **2**, $t = -t_{\mathrm{Fe,Co}}$.

be of interest to try it also with epitaxial MgO spacers and possibly with those spacer materials that can realize the *shallow band condition*.

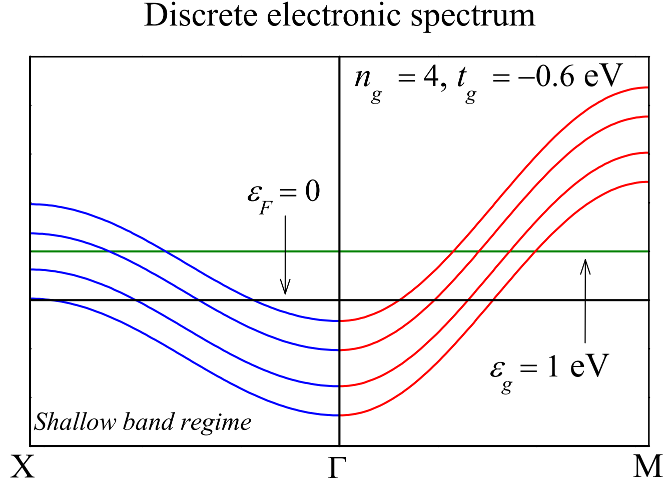

Figure 3.7: *Discrete electronic spectrum for* $n = 4$ *and* $t = -0.6$ *eV in the shallow band condition,* $\varepsilon_g = -1$ *eV.*

The model discrete electronic spectrum (composed of n-subbands, Sec. 3.2) in the *shallow band regime* for a spacer with $n = 4$ and $t = -0.6$ is shown in the Fig. 3.7. Notice the superposition of the highest subband with the Fermi level, ε_{F}, at the X point. This could be the important mechanism responsible for the resonant enhancement of the conductance that affects both parallel and anti-parallel configurations. Since this effect is much greater in the parallel configuration, high MR performance is reachable.

3.4 Interfacial Effects

In this section, the interfacial effects presented at the metal/insulator or metal/non-magnetic-spacer interfaces are discussed. This is motivated by the analogy with the well known case of Schottky barrier at metal/semiconductor interfaces, leading to such interesting physical effects as band bending [Sze, 1981]. It is known from X-ray and ultraviolet photoemission spectroscopy (XPS and UPS) that some charge transfer effects also appear at the metal-insulator interface, leading to the formation of an interfacial charge-dipole whose magnitude is defined by the localized states at interfaces. Since this dipole directly affects the efficiency of tunneling, it is also important to evaluate its effect

on the magnetoresistance.

The best treatment of this problem is to introduce *self-consistently* a charging energy (δ, commonly called the *built-up voltage*) due to charge accumulation in the framework of the density functional theory (DFT). Instead, a simple analytic model is developed below to take into account these interfacial effects qualitatively. Despite of its simplicity, the model can exemplify in which way the formation of charge dipoles affects the MR ratio.

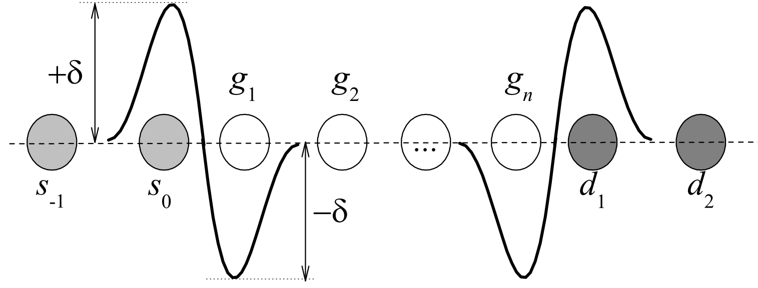

Figure 3.8: *Schematic representation of the interface charge-energy, δ, created by a charge accumulation in the S/G and G/D interfaces, as a simplified description of the self-consistent behavior.*

The present treatment starts from the same model of Sec. 3.3 but considering extra charge energies $\pm\delta$ on the sites pertaining to the two atomic planes of both interface sides (see Fig. 3.8). This is an approximation to a more realistic charge and potential distributions around the interfaces, obtained by numerical DFT calculations [Butler *et al.*, 2001]. The δ-perturbation results in new boundary conditions and, as a consequence, in a new transmission coefficient. In this approximation, there is no changes in the equations of motion within the particular elements (S, D and G), but new pairs of equations appear at the (S/G) and (G/D) interfaces, involving the charge energy δ:

$$\begin{aligned}
\left(2\cos q_s + \frac{\delta}{t_s}\right) s_0 &= s_{-1} + \frac{t_{sg}}{t_s} g_1, \\
\left(x_g - \frac{\delta}{t_g}\right) g_1 &= g_2 + \frac{t_{sg}}{t_g} s_1, \\
\left(2\cos q_b + \frac{\delta}{t_d}\right) d_1 &= d_2 + \frac{t_{gd}}{t_d} g_n, \\
\left(x_g - \frac{\delta}{t_g}\right) g_n &= g_{n-1} + \frac{t_{gd}}{t_g} d_1.
\end{aligned} \tag{3.29}$$

These boundary conditions allow to re-calculate two terminal G-amplitudes as a

function of the parameters R, T, q_s, q_d. Interconnecting these terminal amplitudes leads to the transmission formula, Eq. (3.17), but with the modified denominator $D_{n,\delta} = A_n - B_n + C_n$ where:

$$\begin{aligned} A_n &= \left(1+\frac{\delta}{t_d}e^{iq_d}\right)\left(1+\frac{\delta}{t_s}e^{iq_s}\right)\left[u_n - 2\frac{\delta}{t_g}u_{n-1} + \left(\frac{\delta}{t_g}\right)^2 u_{n-2}\right], \\ B_n &= \left[\gamma_s\left(1+\frac{\delta}{t_d}e^{iq_d}\right) + \gamma_d\left(1+\frac{\delta}{t_s}e^{iq_s}\right)\right]\left(u_{n-1} - \frac{\delta}{t_g}u_{n-2}\right), \\ C_n &= \gamma_s\gamma_d u_{n-2}. \end{aligned} \tag{3.30}$$

It is easy to see that $D_{n,\delta} \to D_n$ in the limit of $\delta \to 0$.

3.4.1 Magnetoresistance and Numerical Results

The MR defined from Eqs. (3.28), (3.30) in function of the number n_g of gate atomic planes and of the gate voltage ε_g (for three values of the interface potential δ) are presented in Figs. 3.9(a,b). The obtained softening of first oscillations makes these curves more similar to the experimental observations [Yuasa *et al.*, 2004].

The presence of an extra barrier (due to the charge energy) reduces the main MR peak in the *shallow band regime*, Fig. 3.9. Obviously, this barrier reduces the conductance in either P and AP configurations. However, this tendency is stronger in the P conductance and so the overall MR drops.

In spite of the this reduction, MR increases for higher ε_g. This effect is of particular interest in Fe/NM/Fe junctions where a new peak appears around $\varepsilon_g \sim 1.8$ eV (closer to the tunnel regime). For that reason it should be easier to attain high MR values with the technology available today. Apparently, this effect results from the wave function localization caused by coherent resonances in the interfacial potential wells.

3.5 Temperature and Voltage Effects

The *shallow band regime* (SBR) enhancement of the MR requires a long enough mean free path for charge carriers compared to the characteristic junction size. This is actually achieved by the modern methods of nanofabrication [Yuasa and Djayaprawira, 2007] and thus can be taken for granted. However, there can also appear other restrictive factors for sharp MR response in real operating conditions, the most important of them

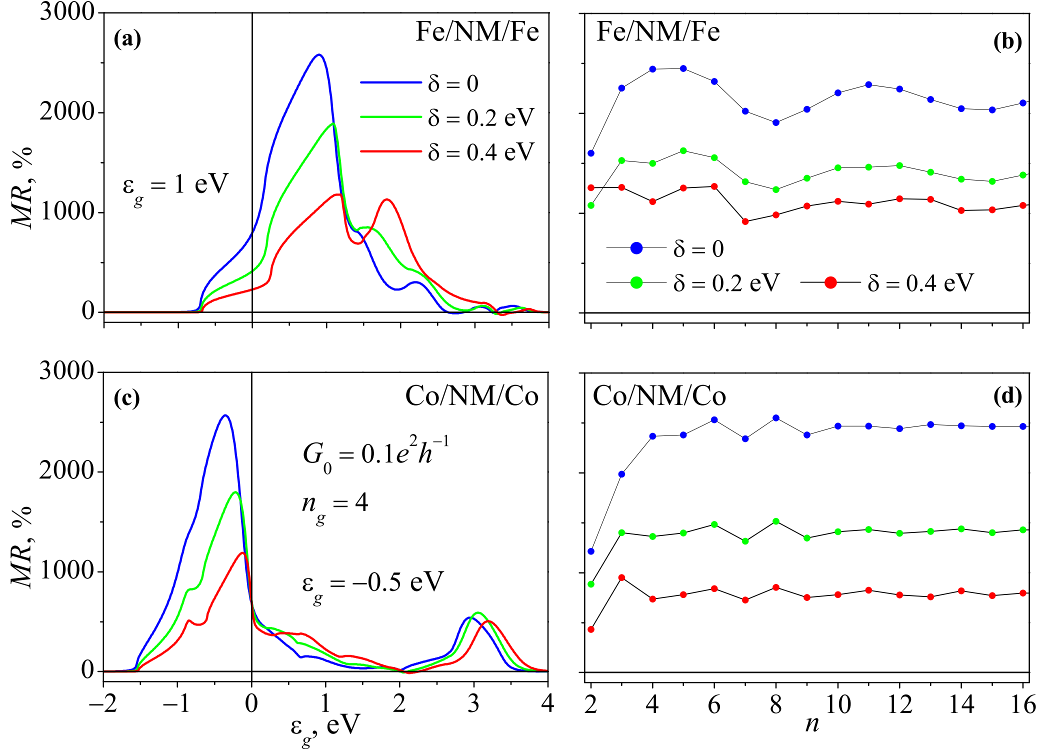

Figure 3.9: *Effect of the interface charge energy on the MR for the same Fe/NM/Fe junction **(a)** as a function of ε_g, with $m_g = 4$ and δ varying from 0 to 0.4 eV; **(b)** in function of m_g with $\varepsilon_g = 1$ eV and δ varying from 0 to 0.4 eV. Effect of the interface charge energy on the MR for the same Co/NM/Co junction: **(c)** as a function of the ε_g, with $m_g = 4$ and δ varying from 0 to 0.4 eV; **(d)** in function of m_g with $\varepsilon_g = -0.5$ eV and δ varying from 0 to 0.4 eV.*

resulting from the finite temperature effects on electronic distribution and from the effects on energy band structure by a finite electric field (especially strong in atomically thin junction structures). The effect of the applied bias on the transmission coefficient is often ignored in the theoretical works, for example, [Butler *et al.*, 2001 and Mathon and Umerski, 2001]. It is commonly argued that once the transmission coefficient is small, it would be a good approximation to consider it bias independent. Thus, the bias effect gets restricted to just the Fermi level shift, only reducing the MR value. However, as will be seen below coherent transport in perfect junctions can result in maximum transmission at certain *finite* voltage and its bias independence is no longer guaranteed. Also the temperature dependence of resonance conduction (even in the low field regime) is highly important for real efficiency of such devices. Apart from the common temperature effect in the spin-independent conduction channel, it can generally follow from two factors: (weak) thermal broadening of the Fermi distribution and (stronger) temperature dependence of the Stoner

subband splitting. The main purpose of this section is to study the mentioned voltage and thermal effects on MR.

3.5.1 Field Dependent Transmission

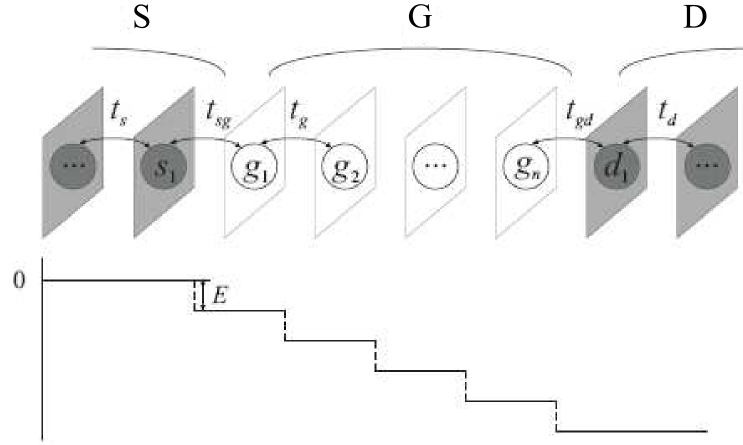

Figure 3.10: *Schematic representation of an S-G-D junction, where each element is composed of 2D atomic planes with respective hopping parameters, and the voltage spatial distribution (by a staircase potential with equal steps E within the* g *element).*

The calculation of the transmission coefficient for the present system in the TB approximation includes a staircase-like shifts of on-site energies by a finite electrical field along the gate element, neglecting it in the less resistive source and drain elements, as represented in Fig. 3.10. It should be noted that this approximation to a real situation, where the staircase potential distribution can generally interfere with some interface built-up voltages, is adopted mainly for simplicity reasons, believing that the corresponding effects on the relevant MR value can be rather additive.

Admitting the transport regime in such a junction beyond the common tunneling, the transmission coefficient can be sensibly dependent on the applied bias, resulting in a non-linear conduction. Even though, in order to avoid too strong non-linear effects and to assure the use of Landauer-Büttiker formalism, it is reasonable to restrict the voltage V on G to some safe value, for instance $|V_{max}| \leq 1$ V. Indeed, the maximum applied voltage in experimental systems amounts ~ 1 V on ~ 1 nm thick barriers, before the transport gets heavily affected by electromigration phenomena [Ventura *et al.*, 2008].

Accordingly to the TB approach for multilayered systems explained in the previous section, electron dynamics in the single-band approximation is described by the composite Hamiltonian: $\hat{H} = \sum_{\mathbf{n},\sigma}\left(\hat{h}^{s}_{\mathbf{n},\sigma} + \hat{h}^{sg}_{\mathbf{n},\sigma} + \hat{h}^{g}_{\mathbf{n},\sigma} + \hat{h}^{gd}_{\mathbf{n},\sigma} + \hat{h}^{d}_{\mathbf{n},\sigma}\right)$, where $\mathbf{n}$ and σ are the in-plane 2D lattice vector and spin (taking values $\uparrow$ or $\downarrow$ in the laboratory frame). The particular terms: $\hat{h}^{i}_{\mathbf{n},\sigma} = \hat{h}^{0}_{i,\mathbf{n},\sigma} + \hat{h}^{\parallel}_{i,\mathbf{n},\sigma} + \hat{h}^{\perp}_{i,\mathbf{n},\sigma}$, describe the on-site energy and the transversal and longitudinal nearest-neighbor hopping processes with spin σ within ith element, and the interface terms $\hat{h}^{i'i}_{\mathbf{n},\sigma}$ is responsible for the hopping between i and i' elements. In particular, the $\hat{h}^{0}_{i,\mathbf{n},\sigma}$ component of the Hamiltonian is modified to: $\hat{h}^{0}_{i,\mathbf{n},\sigma} = \sum_{l=l_i}^{l_{i+1}-1} \varepsilon_{i;l,\sigma}\hat{a}^{\dagger}_{l,\mathbf{n},\sigma}\hat{a}_{l,\mathbf{n},\sigma}$. The on-site energy $\varepsilon_{i;l,\sigma}$ is l-independent: $\varepsilon_{i;l,\sigma} \equiv \varepsilon_{i,\sigma} = \varepsilon_i + \sigma_i\Delta$ in the ferromagnetic leads ($i = S, D$), with the *paramagnetic* value ε_i, the *relative* spin $\sigma_i = \pm$ (for given absolute spin and polarization of i-th lead), and the Stoner splitting Δ. But it is l-dependent (and σ-independent) in the gate: $\varepsilon_{g;l,\sigma} \equiv \varepsilon_i - lE$, accordingly to the model in Fig. 3.10. The above referred interference effects on electric potentials by charge fluctuations are neglected as second order corrections in the considered moderate fields. Notice that the l-independent paramagnetic energies ε_i in D include the potential drop caused by the electrical field in G. Once again, the in-plane symmetry and transversal momentum $\mathbf{k}_{\parallel}$ conservation in a perfect junction suggest the 2D Fourier transform to planar wave operators, so that the paramagnetic energies ε_i are extended to the 2D dispersion laws $\varepsilon_{i,\mathbf{k}_{\parallel}} = \varepsilon_i + t_j\sum_{\delta}\exp(i\mathbf{k}_{\parallel}\cdot\delta)$ and define the spin-split subbands $\varepsilon_{i,\mathbf{k}_{\parallel},\sigma} = \varepsilon_{i,\mathbf{k}_{\parallel}} + \sigma_i\Delta$. Then the eigenstate of the Hamiltonian with given energy ε, transversal momentum $\mathbf{k}_{\parallel}$ and spin σ is written as a superposition over the elements: $|\psi_{\mathbf{k}_{\parallel}}\rangle = \sum_{i,\sigma}\sum_{l=l_i}^{l_{i+1}-1} i_{l,\mathbf{k}_{\parallel},\sigma}|l,\mathbf{k}_{\parallel},\sigma\rangle$, where the states $|l,\mathbf{k}_{\parallel},\sigma\rangle = a^{\dagger}_{l,\mathbf{k}_{\parallel},\sigma}|0\rangle$ enter with the amplitudes $i_{l,\mathbf{k}_{\parallel},\sigma}$ in ith element. In particular, to find the transmission from S to D lead, the S-amplitudes are defined as superpositions of incident and reflected waves and the D-ones as only transmitted waves:

$$\left\{\begin{array}{lcl} s_{l,\mathbf{k}_{\parallel},\sigma} & = & \mathrm{e}^{iq_{s,\mathbf{k}_{\parallel},\sigma}(l-1)} + R_s\mathrm{e}^{-iq_{s,\mathbf{k}_{\parallel},\sigma}(l-1)}, \\ d_{l,\mathbf{k}_{\parallel},\sigma} & = & T_{sd}\mathrm{e}^{iq_{d,\mathbf{k}_{\parallel},\sigma}(l-n)}, \end{array}\right. \tag{3.31}$$

where the lattice parameter is chosen as a unit of length and R_s, T_{sd} are the respective reflection and transmission amplitudes. Generally, each i-amplitude is expressed in function of a dimensionless energy parameter $x_{i,\mathbf{k}_{\parallel},\sigma} = (\varepsilon - \varepsilon_{i,\mathbf{k}_{\parallel},\sigma})/2t_i$ and longitudinal momentum: $q_{i,\mathbf{k}_{\parallel},\sigma} = \arccos x_{i,\mathbf{k}_{\parallel},\sigma}$ (real in the semi-infinite leads). Notice, that the energy argument

for D, $x_{d,\mathbf{k}_\parallel,\sigma} = (\varepsilon - \varepsilon_{d,\mathbf{k}_\parallel,\sigma})/2t_d + (n+1)yt_g/t_d$, depends on the electrical field through the parameter $y = E/2t_g$. In what follows, the abbreviated notations $x_{i,\sigma}$ and $q_{i,\sigma}$ are used for the energy and momentum parameters ($\mathbf{k}_\parallel$ is always well defined).

In similarity with the archetypal case of zero field and temperature, the transmission coefficient T_{sd} is found from matching the S and D amplitudes, Eq. (3.31), through the G amplitudes. The g_l amplitudes for $2 < l < n-1$ obey the equations of motion, following from the SE, $\left(\hat{h}^g_{\mathbf{k}_\parallel,\sigma} - \varepsilon\right)|\psi\rangle = 0$, in the form:

$$2x_{g,l}g_l = g_{l-1} + g_{l+1}, \tag{3.32}$$

with $x_{g,l} = x_g + ly$. Supposing first the G element isolated (no interface hoppings), the solution of Eq. (3.32) with initial conditions $g_0 = 0$ and $g_1 = 1$ is $g_l = p_l(x_g, y)$ where:

$$p_{l+1}(x,y) = (2y)^l \sum_{j=0}^{[l/2]} C_j^{l-j}(-4y^2)^{-j}\left(\frac{x}{y} + j + 1\right)_{l-2j}, \tag{3.33}$$

C_m^n is the binomial coefficient, $[w]$ is the integer part of w, and $(w)_n = w(w+1)\dots(w+n-1)$ is the Pochhammer symbol [Abramowitz and Stegun, 1964]. In conformity with the zero field limit, this solution tends to the 2nd kind Chebyshev polynomial in the limit of $y \to 0$: $p_l(x_g, y \to 0) \to u_l(x_g)$. It is important to note that eigenenergies of this isolated system are the roots of the secular equation $D_n(x,y) = 0$ given by $p_{n+1}(x,y) = 0$, similarly to the case of zero electrical field. Thus, for an 1D chain with $n = 4$, the secular equation reads:

$$\begin{vmatrix} x+y & -1 & 0 & 0 \\ -1 & x+2y & -1 & 0 \\ 0 & -1 & x+3y & -1 \\ 0 & 0 & -1 & x+4y \end{vmatrix} = 0,$$

which has four roots, $x_m = \varepsilon_m/(2t)$ $(m = 1, \dots, 4)$:

$$\begin{cases} x_1 &= \frac{1}{4}\left(-10y + \sqrt{2}\sqrt{3 + 10y^2 + \sqrt{5 + 48y^2 + 64y^4}}\right), \\ x_2 &= \frac{1}{4}\left(-10y + \sqrt{2}\sqrt{3 + 10y^2 - \sqrt{5 + 48y^2 + 64y^4}}\right), \\ x_3 &= \frac{1}{4}\left(-10y - \sqrt{2}\sqrt{3 + 10y^2 - \sqrt{5 + 48y^2 + 64y^4}}\right), \\ x_4 &= \frac{1}{4}\left(-10y - \sqrt{2}\sqrt{3 + 10y^2 + \sqrt{5 + 48y^2 + 64y^4}}\right), \end{cases}$$

with the mth eigenvector $\psi(x_m, y) = \Omega\,(p_1(x_m, y), \dots, p_n(x_m, y))$, where the normalizing factor is $\Omega = \left(\sum_l |p_l(x, y)|^2\right)^{-1/2}$ and *closed* boundary conditions: $p_0 = p_{n+1} = 0$ are implied. Choosing $|y| \leq 0.5$ with $t = 1/2$, the discrete energy spectrum as a function of $y = E/(2t)$ and eigenvector $\psi(x, y)$ (for $y = 0.5$) are presented in Fig. 3.11.

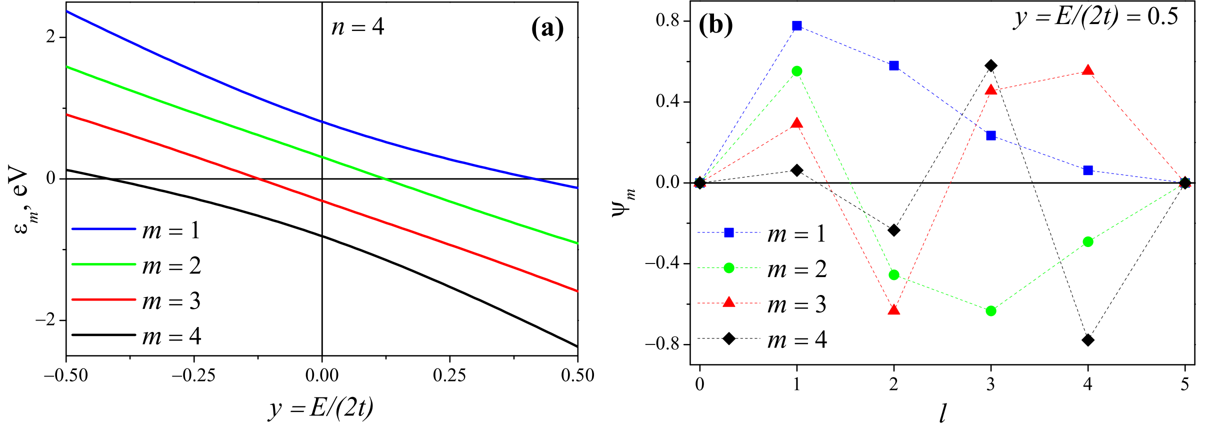

Figure 3.11: ***(a)*** *Discrete energy spectrum for a chain with $n = 4$ and $t = 1/2$ as a function of $y = E/(2t)$;* ***(b)*** *Eigenvector $\psi(x, y)$ local amplitudes for the same chain.*

On the other hand, in the free electron approximation, the bias effect on the continuous planar waves is expressed through a combination of the Airy functions $\mathrm{Ai}(Z)$ and $\mathrm{Bi}(Z)$:

$$\psi = a\mathrm{Ai}(Z) + b\mathrm{Bi}(Z),$$

where the argument Z depends on the longitudinal coordinate z,

$$Z(z) = \left[\sqrt{2m^*}/(\hbar e E)\right]^{2/3} (\phi - eEz - \varepsilon_\perp)\,,$$

with E denoting the electrical field applied to the junction, ϕ is barrier height, the distance

z in the barrier is referred to the interface with the source electrode, $\varepsilon_\perp = \varepsilon - (2m^*)^{-1}\hbar^2\mathbf{k}_\parallel^2$ is the electron energy associated with electron motion in the direction perpendicular to the layers, and m^* is the effective free electron mass, [Wilczyński *et al.*, 2008].

Now, to match Eqs. (3.31) and (3.32), two pairs of interface equations of motion are derived from the 2D Fourier transformed interface Hamiltonians $\hat{h}^{(i'i)}_{\mathbf{k}_\parallel,\sigma}$ (likewise to what was done in the previous sections):

$$\begin{aligned} 2x_s s_0 &= s_{-1} + \frac{t_{sg}}{t_s}\, g_1, \\ 2(x_g + y)g_1 &= g_2 + \frac{t_{sg}}{t_g}\, s_0, \end{aligned} \tag{3.34}$$

and

$$\begin{aligned} 2(x_g + n\, y)g_n &= g_{n-1} + \frac{t_{gd}}{t_g}\, d_{n+1}, \\ 2x_d d_{n+1} &= d_{n+2} + \frac{t_{gd}}{t_d}\, g_n. \end{aligned} \tag{3.35}$$

They permit to express the terminal pairs of G amplitudes: (g_1, g_2) through R_s, x_s, x_g, and (g_{n-1}, g_n) through T_{sd}, x_d, x_g. From matching of Eqs. (3.31) and (3.32) to Eqs. (3.33) and Eqs. (3.34) two equivalent forms of the wave amplitudes are found: $g_l = g_l^{sg}(R_s, x_s, x_g)$ from the (S/G) interface, and $g_l = g_l^{gd}(T_{sd}, x_d, x_g)$ from the (G/D) interface. Their comparison at two specific l values, $l = 1$ and $l = n$, results finally in the S-D transmission amplitude (at given ε, $\mathbf{k}_\parallel$ and relative in- and out-spin indices σ, σ') as:

$$T^{(sd)}_{\sigma,\sigma'} = -2i\frac{t_{sg}t_{gd}}{t_g\, t_d}\frac{\sin q_s}{D_{\sigma,\sigma'}}, \tag{3.36}$$

with the field dependent denominator given by:

$$D_{\sigma,\sigma'} = p_{n+1}(x_g, y) - \gamma_s^\sigma p_n(x_g + y, y) - \gamma_d^{\sigma'} p_n(x_g, y) + \gamma_s^\sigma \gamma_d^{\sigma'} p_{n-1}(x_g + y, y). \tag{3.37}$$

Here the interface factors are: $\gamma_s = e^{iq_s}t_{sg}^2(t_s t_g)^{-1}$ for (S/G) and $\gamma_d = e^{iq_d}t_{gd}^2(t_g t_d)^{-1}$ for (G/D) interfaces, and the momenta q_s, q_d depend on σ and σ'. The main formal distinction of the present solution, Eq. (3.36), from its zero field analogue is the change from Chebyshev polynomials to Pochhammer symbols with the explicit field argument y. Bearing in mind that the momentum q_d in γ_d also depends on y it is possible to restore

the continuous limit behavior of Airy functions mentioned above.

3.5.2 Magnetoresistance and Numerical Results

As is known [Camley and Barnaś, 1989] and [Valet and Fert, 1993], charge and spin accumulation occurs in the vicinity of junctions under current, perturbing the local equilibrium Fermi distribution. In the next Section, this effect is also traced in the ballistic regime and indeed a specific perturbation of the Fermi distribution is demonstrated, either in equilibrium ($E = 0$) or out-of-equilibrium ($E \neq 0$) regimes that could be of interest for transport phenomena. However, such effects are not included in the present calculations (expected to be small non-linear corrections).

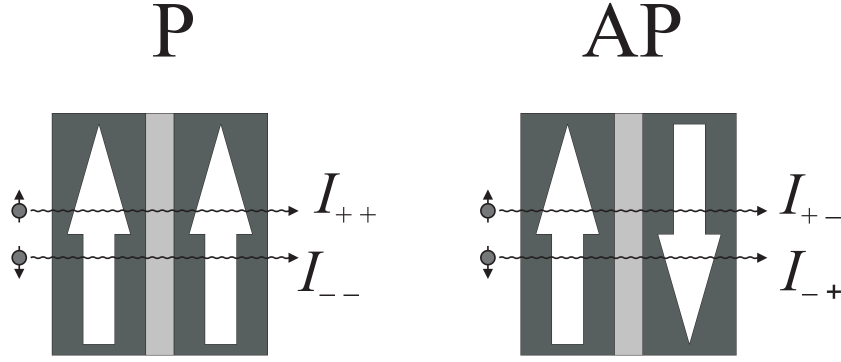

Figure 3.12: *Schematics of spin-dependent transport channels in P and AP regimes of the junction (wide arrows indicate polarizations of the FM leads). For each channel with a certain absolute spin index Σ, the relative indices σ, σ' are equal in P but different in AP.*

In the present context, the generalized LB formula is applied to calculate the current through the junction in a given spin channel σ, σ' (see Fig. 3.12):

$$I_{\sigma,\sigma'} = \frac{e}{h} \int d\varepsilon \sum_{\mathbf{k}_\parallel \in K(\varepsilon,V)} \left[\left| T^{(sd)}_{\sigma,\sigma'}(\varepsilon, \mathbf{k}_\parallel) \right|^2 f_s(\varepsilon) - \left| T^{(ds)}_{\sigma',\sigma}(\varepsilon, \mathbf{k}_\parallel) \right|^2 f_d(\varepsilon) \right], \tag{3.38}$$

where $f_i = \{\exp[\beta(\varepsilon - \mu_i)] + 1\}^{-1}$ is the equilibrium Fermi distribution in the leads ($i = S, D$) with inverse temperature β and electrochemical potentials subject to: $\mu_s - \mu_d = eV$. Further, $K(\varepsilon, V)$ is the *permitted* summation range for transversal momentum $\mathbf{k}_\parallel$ such that the related in-and out-momenta $q_s = q_{s,\mathbf{k}_\parallel,\sigma}$ and $q_d = q_{d,\mathbf{k}_\parallel,\sigma}$ (at given energy ε and voltage V) are real. For simplicity it is assumed that $\left| T^{(ds)}_{\sigma',\sigma}(\varepsilon, \mathbf{k}_\parallel) \right|^2 \approx 1 - \left| R^{(ds)}_{\sigma',\sigma}(\varepsilon, \mathbf{k}_\parallel) \right|^2$. Within the calculations performed in this section, deviations from this approximation constitute second order corrections. Nevertheless, important effects related to those deviations can

appear even at zero bias and for that reason they are analyzed in the next section. The *backward* transmission amplitude is then calculated as:

$$T^{(ds)}_{\sigma',\sigma} = -2i\frac{t_{sg}t_{gd}}{t_s t_g}\frac{\sin q_d}{D_{\sigma',\sigma}},$$

and defines the back current from D to S lead (only non-zero at finite temperatures).

The practical $\mathbf{k}_{\|}$-integration in Eq. (3.38) is realized by the formula:

$$I_{\sigma,\sigma'} = \frac{e}{h}\int d\varepsilon \int_{a(\varepsilon,V)}^{b(\varepsilon,V)} du\rho(u)\left[\left|T^{(sd)}_{\sigma,\sigma'}(\varepsilon,u)\right|^2 f_s(\varepsilon) - \left|T^{(ds)}_{\sigma',\sigma}(\varepsilon,u)\right|^2 f_d(\varepsilon)\right]. \qquad (3.39)$$

Here the (ε- and V-dependent) limits for u-integration:

$$\begin{aligned} b(\varepsilon,V) &= \min\left\{2, \min\left[x_{s,\sigma}(\varepsilon), x_{d,\sigma'}(\varepsilon - eV)\right] + 1\right\}, \\ a(\varepsilon,V) &= \max\left\{-2, \max\left[x_{s,\sigma}(\varepsilon), x_{d,\sigma'}(\varepsilon - eV)\right] - 1\right\}, \end{aligned}$$

with $x_{i,\sigma}(\varepsilon) = (\varepsilon - \varepsilon_{i,\sigma})/(2t_i)$, just correspond to the $K(\varepsilon,V)$ range. After obtaining from Eq. (3.39) the net currents for both parallel $I_P = I_{++} + I_{--}$ and antiparallel $I_{AP} = I_{+-} + I_{-+}$ configurations, the voltage-dependent MR ratio is defined as:

$$MR(V) = \frac{I_P - I_{AP}}{I_{AP} + I_0}, \qquad (3.40)$$

taking into account a certain spin-insensitive current $I_0 = G_0 V$ (through some spin-degenerate channels with supposedly Ohmic conductance G_0).

In practical calculations of Eqs. (3.39) and (3.40), the same model parameters for Fe electrodes are used and a Bloch-like temperature dependence of the Stoner splitting parameter is applied, $\Delta = \Delta_0\left(1 - \alpha T^{3/2}\right)$ with $\Delta_0 = 0.96$ eV and $\alpha = 10^{-4}$ K$^{-3/2}$ [Ashcroft and Mermin, 1976]. The α value is chosen to be slightly high in order to give a *pessimist* picture of the temperature dependence of MR. The above mentioned spin-independent conductance was taken as $G_0 = 0.1e^2/h$. The behavior of MR in the reference case of $T \to 0$, $V \to 0$ follows from the simple LB conductance formula:

$$G_{\sigma,\sigma'} = \frac{e^2}{h}\frac{1}{4\pi^2}\int_{a_\Sigma}^{b_\Sigma} du\rho(u)|T^{(sd)}_{\sigma,\sigma'}(\varepsilon_{\mathrm{F}},u)|^2, \qquad (3.41)$$

with $(a, b) = (a, b)(\varepsilon_F, 0)$, resulting in the low-temperature-low-voltage (LTLV) value: $MR = (G_{++} + G_{--} - G_{+-} - G_{-+}) / (G_{+-} + G_{-+} + G_0)$. The main effect of quantum coherence in this case is a series of strong peaks of MR as a function of the specific tuning parameter, the on-site energy ε_g in the gate element, as exposed in the former sections. The strongest of these peaks, related to the so called *shallow band regime*, indicates a theoretical maximum efficiency (at least in the present simple model) of the coherent transport mechanism for magnetic junction. Naturally, the analysis of possibly adverse voltage and temperature effects on MR is most important for the SBR conditions. From Eq. (3.41) for LTLV and Eqs. (3.39), (3.40) for $V \to 0$, it is possible to compare positions of SBR peaks (and also of weaker satellite peaks) at different temperatures for given numbers $n = 4$, 5, 6 of atomic planes in the G-element, as shown in Fig. 3.13.

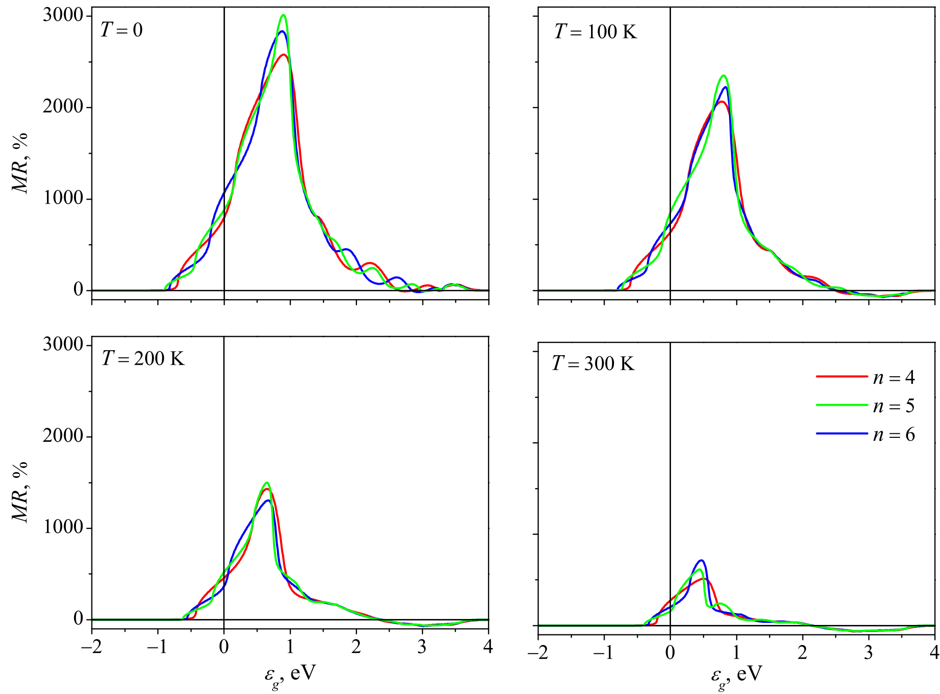

Figure 3.13: *MR dependencies on the gate bias parameter ε_g for different numbers n of atomic planes in the gate at different temperatures.*

The main tendencies in this behavior are the shift of SBR peaks to lower ε_g values and their decreasing height with temperature. However, the latter effect can be less pronounced if the value of G_0 also decreases with temperature (as could be naturally expected). The sensible difference of peak positions at low and high temperatures suggests that the choice of optimum ε_g value for the device functioning at room temperature should

be based on the temperature dependent formulas, Eqs. (3.39), (3.40), rather than on the zero-temperature limit of Eq. (3.41).

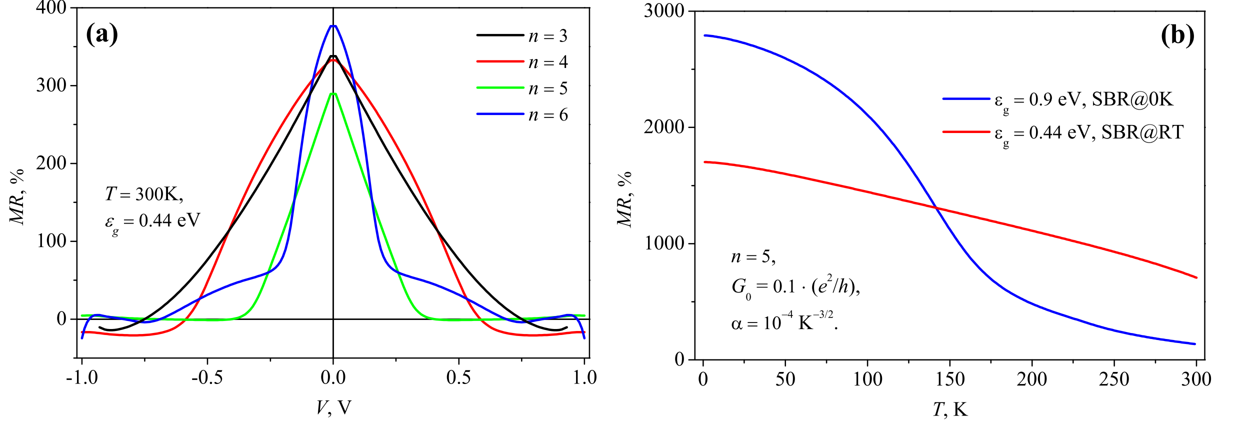

Figure 3.14: ***(a)*** *Electric field dependencies of MR for different numbers n of atomic planes in the gate at room temperature;* ***(b)*** *Temperature dependencies of MR for the choices of gate bias ε_g adjusted to reaching SBR conditions at low and high temperatures.*

Having done such a choice, the next issue of practical interest is the stability of MR performance against the applied voltage. The corresponding results with the use of Eqs. (3.39), (3.40) at RT and finite (positive and negative) voltages are shown in Fig. 3.14a. The symmetric character of obtained $MR(V)$ curves for all n values is apparently due to the adopted symmetry between S- and D-leads. A monotonous decrease of MR away from zero voltage is found, this behavior being in agreement with the experiments [Yuasa, 2004], often explained in terms of magnon excitations [Moodera, 1998]. Interestingly, in the present condition of SBR, this decrease is rather unusual and becomes more significant for thicker junctions.

Finally, for the above indicated choices of SBR-adjusted structures at low and high temperatures, their temperature stability away from the prescribed range can be also studied. To this end, two specific structures were compared: **i)** the low-temperature SBR-structure with $\varepsilon_g = 0.9$ eV and **ii)** the RT one with $\varepsilon_g = 0.44$ eV, both with the gate thickness of $n = 5$. The calculated $MR(T)$ curves in Fig. 3.14b are in both cases monotonically decreasing, but more rapidly for the first device whose higher performance at low temperatures turns to be less stable and is surpassed by the slower decreasing curve for the second device (already at about 150 K). The origin of this change of domination between the two structures is evidently due to the competition of the two tendencies indicated in Fig. 3.13, therefore the relative thermal stability of the second

device can be yet enhanced by the above mentioned thermal degradation effect on G_0. Similarly, a specific SBR-adjustment of the ε_g parameter can be found for any temperature domain of interest which may add technological flexibility to the class of quantum coherent spintronics devices.

3.6 Electronic Distribution Functions

The analytical treatment of electron transport processes in spintronic layered nanostructures is commonly restricted to classical or semi-classical framework [Camley and Barnaś, 1989] and [Valet and Fert, 1993]. In these treatments the equilibrium Fermi distribution is perturbed under an applied electric field E, and gets dependent on the quasi-momentum $\mathbf{k} = (\mathbf{k}_{\parallel}, q)$, spin $\sigma = \pm$, and position z in each ith layer: $f_{i,\sigma}(\mathbf{k}, z)$. Such perturbation is described accordingly to the Boltzmann equation for diffusive transport at given (spin-sensitive) mean free path l_σ. However, in highly perfect epitaxial junctions [Ikeda *et al.*, 2008], an essentially ballistic regime is expected at distances closer than l_σ from the junction. In this condition a new specific perturbation of electronic distribution can appear, either in equilibrium or out-of-equilibrium, which can be important for the spintronic performance. A similar effect is known for electrons near atomic point contacts [Agraït *et al.*, 2003].

3.6.1 Model

To model the junction, the preceding trilayer structure is once more considered, Fig. 3.15. The device conductance in the two-current model [Valet and Fert, 1993] for in- and out-spins σ, σ' (with the same absolute value, $\uparrow$ or $\downarrow$) is $\mathcal{G}_{\sigma\sigma'} = \left(G^{-1}_{\sigma\sigma'} + G^{-1}_{s,\sigma} + G^{-1}_{d,\sigma'}\right)^{-1}$, where the Landauer conductance, $G_{\sigma\sigma'} = dI_{\sigma\sigma'}/dV$, is written through the spin-dependent current (Chap. **2**):

$$I_{\sigma\sigma'} = \frac{e}{h}\int d\varepsilon \sum_{\mathbf{k}_{\parallel}\in K(\varepsilon,V)} \left[f_{s,\sigma}(\varepsilon)|T_{\sigma\sigma'}(\varepsilon,\mathbf{k}_{\parallel})|^2 - f_{d,\sigma'}(\varepsilon)\left(1 - |R'_{\sigma\sigma'}(\varepsilon,\mathbf{k}_{\parallel})|^2\right)\right]. \qquad (3.42)$$

The domain K is the restricted summation range, $|T_{\sigma\sigma'}|^2$ the transmission amplitude from S to D and $|R'_{\sigma\sigma'}|^2$ the reflection amplitude from D to S, being related to conservation of energy, $\varepsilon_{s,\sigma}(\mathbf{k}_s) = \varepsilon_{d,\sigma}(\mathbf{k}_d) = \varepsilon$, and transversal momentum, $\mathbf{k}_{s,\parallel} = \mathbf{k}_{d,\parallel} = \mathbf{k}_{\parallel}$. The inverse

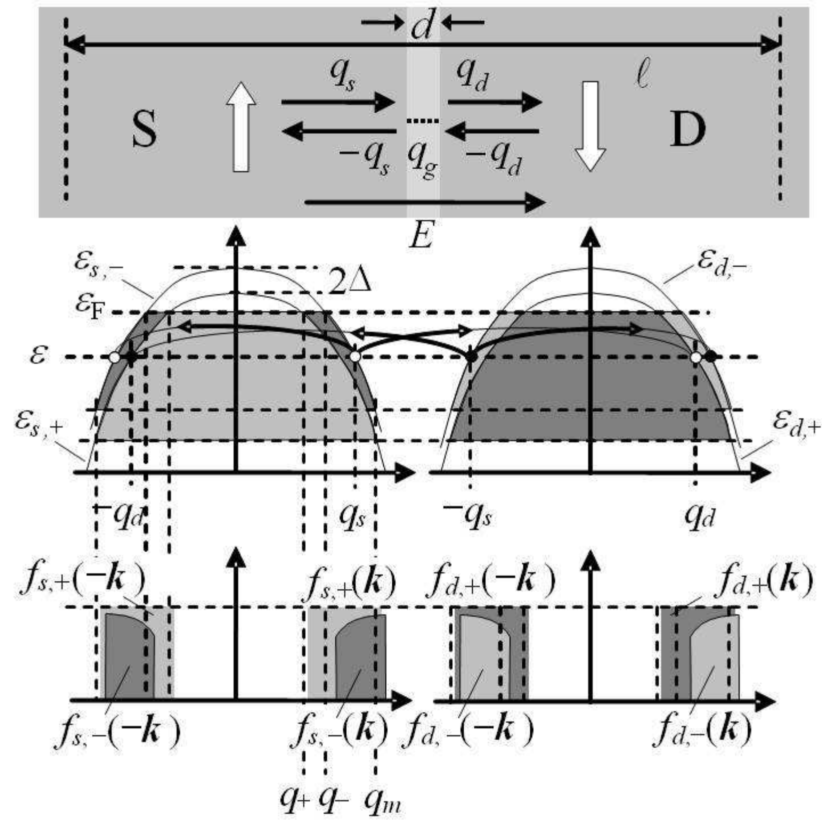

Figure 3.15: *Transmission and reflection processes at given energy ε and the q-projected distributions of majority and minority spins on both sides of the barrier in the AP magnetic state. Light and dark shading indicates absolute spin orientations (up and down, respectively).*

LB conductance typically prevails over the Drude contributions $G_{i,\sigma} = An_i l_\sigma/(L_i m_i v_i)$ by the leads (A is the junction area, L_i is the length of i-th lead, and n_i, m_i, v_i are respectively the electronic concentration, effective mass, and Fermi velocity).

The distribution $f_{i,\sigma'}(\mathbf{k}_i, z)$ in Eq. (3.42) essentially varies with the distance z from the barrier on the scale of $z \sim l_\sigma$, tending to the z-independent limit at $z \gg l_\sigma$: $f_{i,\sigma'}(\mathbf{k}_i, z) \rightarrow f^{\infty}_{i,\sigma'}(\mathbf{k}_i)$, defined by the uniform Boltzmann equation for respective l_σ. But in the opposite limit, $z \ll l_\sigma$, it tends to $f_{i,\sigma'}(\mathbf{k}_i, z) \rightarrow f_{i,\sigma'}(\mathbf{k}_i)$, defined by the transmission and reflection coefficients, $T_{\sigma\sigma'}$ and $R_{\sigma\sigma'}$ (with energy and $\mathbf{k}$ conservation):

$$
\begin{aligned}
|T_{\sigma\sigma'}(\mathbf{k}_s)|^2 f_{s,\sigma}(\mathbf{k}_s) + |R_{\sigma\sigma'}(-\mathbf{k}_d)|^2 f_{d,\sigma'}(-\mathbf{k}_d) &= f_{d,\sigma'}(\mathbf{k}_d)\,, \\
|T_{\sigma\sigma'}(-\mathbf{k}_d)|^2 f_{d,\sigma'}(-\mathbf{k}_d) + |R_{\sigma\sigma'}(\mathbf{k}_s)|^2 f_{s,\sigma}(\mathbf{k}_s) &= f_{s,\sigma}(-\mathbf{k}_s)\,; \qquad (3.43)
\end{aligned}
$$

$$
f_{i,\sigma}(\mathbf{k}_i) - f_{i,\sigma}(-\mathbf{k}_i) = f^{\infty}_{i,\sigma}(\mathbf{k}_i) - f^{\infty}_{i,\sigma}(-\mathbf{k}_i)\,. \qquad (3.44)
$$

Eqs. (3.43) are the kinetic relations on the barrier and Eq. (3.44) expresses the current conservation close to and far from the barrier in each ($\mathbf{k}$, σ)-channel. Together they fully define the distributions $f_{i,\sigma}$ on the barrier through the known asymptotics $f^{\infty}_{i,\sigma}$ and coefficients $T_{\sigma\sigma'}$, $R_{\sigma\sigma'}$. Their solution essentially depends on the relative magnetic configuration (parallel, P, or antiparallel, AP) of the junction. For the P case (symmetric barrier with $\mathbf{k}_s = \mathbf{k}_d$, $\sigma = \sigma'$, and $|T_{\sigma\sigma'}(\mathbf{k})|^2 = 1 - |R_{\sigma\sigma'}(\mathbf{k})|^2$), one has trivially $f_{i,\sigma}(\mathbf{k}) = f^{\infty}_{i,\sigma}(\mathbf{k})$. But for the AP case the ratio $|T_{\sigma\sigma'}(\mathbf{k}_s)|^2/(1 - |R_{\sigma\sigma'}(\mathbf{k}_d)|^2) = v_{s,\sigma}/v_{d,\sigma'}$, (where $v_{i,\sigma} = \hbar^{-1}\partial_q \varepsilon_{i,\sigma}(\mathbf{k})$ is i-th longitudinal velocity) differs from unity, leading to a non-trivial effect.

3.6.2 Equilibrium

This effect is already seen in the equilibrium state ($E = 0$), when Eq. (3.44) implies the symmetry $f_{i,\sigma}(\mathbf{k}) = f_{i,\sigma}(-\mathbf{k})$. Then, Eqs. (3.43) become:

$$
|T_{\sigma\sigma'}(\mathbf{k}_s)|^2 f_{s,\sigma}(\mathbf{k}_s) = \left(1 - |R_{\sigma\sigma'}(-\mathbf{k}_d)|^2\right) f_{d,\sigma'}(\mathbf{k}_d)\,.
$$

For the free-electron parabolic dispersion (negative): $\varepsilon_{i,\sigma}(\mathbf{k}) = \varepsilon_0 - \sigma\Delta_i - (2m^*)^{-1}\hbar^2(k_\parallel^2 + q^2)$, it reads

$$
q_s f_{s,\sigma}(\mathbf{k}_s) = q_d f_{d,\sigma'}(\mathbf{k}_d),
$$

and for $T = 0$ (when $\varepsilon = \varepsilon_F$), a simple analytic solution of Eqs. (3.43) providing minimum total energy, $\mathcal{E} = \sum_{i,\mathbf{k},\sigma} f_{i,\sigma}(\mathbf{k})\varepsilon_{i,\sigma}(\mathbf{k})$, is:

$$f_{i,+}(\mathbf{k}) = 1 \quad \text{and} \quad f_{i,-}(\mathbf{k}) = \sqrt{1-(q_\Delta/q)^2} < 1,$$

over the momentum range $\varepsilon_\sigma < \varepsilon_{i,\sigma}(\mathbf{k}) < \varepsilon_F$. Here the energy band limits are defined by the conditions:

$$\int_{\varepsilon_\sigma}^{\varepsilon_F} \rho_\sigma(\varepsilon) f(\varepsilon, 0) d\varepsilon = n_\sigma \tag{3.45}$$

for partial densities of states, $\rho_{i,\sigma}(\varepsilon) = N^{-1}\sum_{i,\mathbf{k}} \delta(\varepsilon - \varepsilon_{i,\sigma}(\mathbf{k}))$, they correspond to the limiting values q_m and q_σ of q: $\varepsilon_0 - \sigma\Delta - \hbar^2 q_m^2/(2m^*) = \varepsilon_\sigma$ and $\varepsilon_0 - \sigma\Delta - \hbar^2 q_\sigma^2/(2m^*) = \varepsilon_F$, so that $q_\Delta = \sqrt{4m^*\Delta}/\hbar < q_-$ (seen in the middle panel of Fig. 3.15). The obtained incomplete equilibrium occupation of minority subband[3] at $T = 0$ is the principal result of this section. Since in fact $f_{i,-}(\mathbf{k})$ only depends on the longitudinal part q, it is suitable to construct the effective 1D distribution $f_{i,-}(q)$ by integration of $f_{i,-}(\mathbf{k})$ in all the permitted $\mathbf{k}_\parallel$ values. This results explicitly in:

$$f_{i,-}(q) = \coth\theta_{\Delta,q} - \theta_{\Delta,q}/\sinh^2\theta_{\Delta,q} \tag{3.46}$$

where $\theta_{\Delta,q} = \operatorname{arcsinh}(\mathrm{q}/\mathrm{q}_\Delta)$, for $q_m > q > q_-$ as shown in the lower panel of Fig 3.15. The incomplete minority occupation (at the same dispersion laws $\varepsilon_{i,\sigma}(\mathbf{k})$ and energy band limits as in the bulk leads) would locally enhance the spin polarization:

$$p_i(z) = \frac{\sum_{\mathbf{k}}[f_{i,+}(\mathbf{k},z) - f_{i,-}(\mathbf{k},z)]}{\sum_{\mathbf{k}}[f_{i,+}(\mathbf{k},z) + f_{i,-}(\mathbf{k},z)]}, \tag{3.47}$$

comparatively with its asymptotic value $p_i^\infty = \lim_{z\to\infty} p_i(z)$, and evoke a charge accumulation,

$$\delta_i(z) = \sum_{\sigma,\mathbf{k}}[f_{i,\sigma}^\infty(\mathbf{k}) - f_{i,\sigma}(\mathbf{k},z))] > 0,$$

near the barrier. This should produce local enhancement of band splitting $\Delta(z) = Jp(z)$ (with an exchange parameter J) and lowering of the energy bands by $e\varphi_i(z)$. The extra

[3] The analogous consideration for the case of positive dispersion would lead to $f_{i,-}(\mathbf{k}) = 1$ and $f_{i,+}(\mathbf{k}) < 1$, and hence to locally reduced spin polarization.

potential $\varphi_i(z)$ can be found self-consistently from the Poisson equation:

$$\partial_z^2 \varphi_i(z) = 4\pi e \delta_i(z)$$

solved for the modified dispersion laws:

$$\varepsilon_{i,\sigma}(\mathbf{k}, z) = \varepsilon_0 - \sigma\Delta_i(z) - e\varphi_i(z) - \hbar^2 k^2/(2m^*).$$

This task is simplified by noting that $\varphi_i(z)$ decays over distances of the order of mean free path $\sim l_\sigma \gg n_e^{-1/3}$ (the natural length scale of the charge accumulation), so that the maximum charge accumulation turns to be small: $\delta_i(0) = \varphi_i(0)/(el_\sigma^2) \ll n_e$. This permits to approximately obtain the local electronic density from local densities of states $\rho_\sigma(\varepsilon, z) = \sum_{i,\mathbf{k}} \delta(\varepsilon - \varepsilon_{i,\sigma}(\mathbf{k}, z))$ integrated in energy up to $\varepsilon = \varepsilon_F$:

$$\begin{aligned} n_e(z) = \tfrac{1}{6\pi^2}\left(\tfrac{2m^*}{\hbar}\right)^2 \Big\{ & W^{3/2} + [W + 2\Delta(z)]^{3/2} - [\varepsilon_F - \varepsilon_0 - e\varphi(z) + \Delta(z)]^{3/2} - \\ & [\varepsilon_F - \varepsilon_0 - e\varphi(z) - \Delta(z)]^{3/2} - \tfrac{3}{2}\sqrt{\Delta(z)}\,[\varepsilon_F - \varepsilon_0 - e\varphi(z)] \Big\}, \end{aligned} \quad (3.48)$$

where W is the total bandwidth. Then the expansion of $n_e(z)$, Eq. (3.48) up to leading orders in supposedly small ratios $(e\varphi_i, \Delta_i)/(W, \varepsilon_0 - \varepsilon_F)$, referred to the asymptotic value $n_e = \lim_{z\to\infty} n_e(z)$, gives rise to a relation between the parameters φ_i and Δ_i. Another relation between them follows from a similar expansion of local band splitting:

$$\Delta(z) = J\frac{3\Delta(z)\left[\sqrt{\varepsilon_0 - \varepsilon_F} - \sqrt{W}\right] + \sqrt{2\Delta(z)}\,(W - \varepsilon_0 + \varepsilon_F)}{2\left[W^{3/2} + (\varepsilon_0 - \varepsilon_F)^{3/2}\right]}, \quad (3.49)$$

referred to the asymptotic (lower) value Δ_∞, and permits to estimate the maximum splitting as $\Delta_i(0) \sim J^2/(4W)$. Then, using it in Eq.(3.44), it is possible to estimate the maximum band lowering as

$$\varphi_i(0) \sim J\sqrt{(\varepsilon_0 - \varepsilon_F)^{-1} - W^{-1}}.$$

All these results show that quantum coherence between oppositely polarized electrodes can essentially perturb local electronic equilibrium near the barrier.

However, the obtained charge accumulation and the related voltage on the barrier

are fully compensated by the above mentioned $|T|^2/(1-|R|^2)$ asymmetry to result in no current, in agreement with Eq. (3.44). Also it should be underlined that this extra spin polarization (localized near the barrier) can not relate to the known RKKY-like mechanism (of volume origin).

3.6.3 Transport

At $E \neq 0$, the steady state ballistic transmission should be defined between the electrochemical potential levels: ε_F and $\varepsilon_F - deE$, (for the barrier width d), instead of the same Fermi level, on the sides of the barrier. This defines the same coupling between the in- and out- states in the steady-state transport regime as in the equilibrium regime. Then the conservation of equal spin currents in AP configuration requires a bigger non-equilibrium shift of $f_{i,-}(\mathbf{k})$ than of $f_{i,+}(\mathbf{k})$, as shown in the lower panel in Fig. 3.15, which would enhance the AP resistance and so the MR of the device. The relaxation of the accumulated charge and spin on scales $\sim l_-$ and $\sim l_{sf}$ (the spin-flip mean free path) from the barrier should also contribute to this enhancement.

3.7 Charge and spin-torque transfer

Recently, the works of Slonczewski [Slonczewski, 1996] and Berger [Berger, 1996] predicting current-driven excitations of magnetic multilayers gained an enormous relevance. This is due to the possibility of magnetic-field-free switching of relative orientations of the magnetizations. Since their works, a tremendous experimental effort was triggered (Refs. [Rippard *et al.*, 2004, Tulapurkar *et al.*, 2005, Petit *et al.*, 2007, Ozatay *et al.*, 2008], among many others). But, also various theoretical works have been done, considering current-perpendicular-to-plane giant magnetoresistance (CPP-GMR) junctions, [Barnaś *et al.*, 2005, Edwards *et al.*, 2005, and Manchon *et al.*, 2006], and tunnel magnetoresistance (TMR) junctions, [Theodonis *et al.*, 2007, Wang *et al.*, 2008, and Wilczyński *et al.*, 2008].

3.7.1 Introduction

This section considers coherent transport in fully epitaxial structures with arbitrary angle θ between magnetizations of magnetic electrodes, where charge and spin transfer can be enhanced by quantum resonances from discrete subbands in the electronic spectrum of the spacer. Starting from the single-band TB model presented in this chapter, the θ-dependent transmission and reflection coefficients for the coherent wave function are calculated. With these, the θ-dependencies of charge and spin transfer are evaluated through the expectation values of a generalized transport density operator.

Once again a perfect sandwiched structure consists of successive stacks of coherent atomic planes (Fig. 3.16), but in this case a semi-infinite left ferromagnetic block (S) with *fixed* magnetization $\mathbf{M_1}$, connected through a finite non-magnetic n-plane spacer (G) to a semi-infinite right ferromagnetic block (D) with *free* magnetization $\mathbf{M_2}$, admitting an arbitrary angle θ between $\mathbf{M_1}$ and $\mathbf{M_2}$. It is important to mention that for simplicity in this section a different referenial is used as clearly depicted in Fig. 3.16. Since the spacer G is much thinner than the mean-free path l (typically $\sim$ 50 nm), transport through the junction is essentially *ballistic* within a $\sim l$ range around G. Lets call it *ballistic range* (BR), included into the overall transport circuit in series with the *outer* parts ($\gtrsim l$ away from G) of S and D leads, called *diffusive ranges* (DR's). The dominant part of the overall junction resistance is supposed to come from the BR resistance defined by the Landauer formula for coherent quantum states, the eigen-states of the TB Hamiltonian

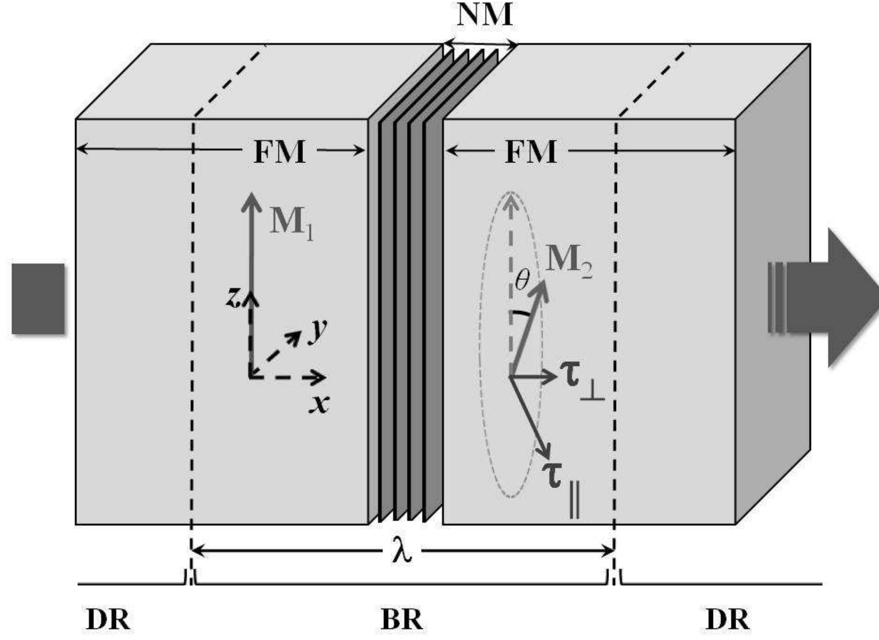

Figure 3.16: *Schematic picture of a magnetic junction: left ferromagnetic lead (source, S), non-magnetic spacer (gate, G) and right ferromagnetic lead (drain, D). It is important to emphasize the discrete structure of the system, as that by n-atomic planes in the gate.*

given below. Practically, they are constructed from the in-plane states $|j, \mathbf{k}_\|, \sigma\rangle$ for each jth plane labeled by the conserved in-plane momentum $\mathbf{k}_\|$ and spin ($\sigma = \pm$, relative to the local magnetization $\mathbf{M}$ in this plane).

However, an important issue for the ballistic transport is that generally these eigen-states are *not orthogonal*, since there can be transmissions and reflections of any incident wave of any spin polarization to outcoming waves of both polarizations. This rises a problem on definition of local electronic distribution on BR (either equilibrium and non-equilibrium) and its matching with such distribution on DR, found from common Boltzmann kinetic equation. It can also involve the temperature effects, even though the very concept of temperature is not well defined for isolated (non-thermalized) coherent states. Such a problem was considered in Sec. 3.6 for a simpler case of a junction in collinear (parallel or antiparallel) magnetic configurations. Although in the general case of non-collinear configurations, the matching conditions become rather tedious and a simpler solution can be found, using a certain system of orthogonal eigen-states for any $\varepsilon, \mathbf{k}_\|$ conduction channel. Specifically, the orthogonalized BR-states should mix the above mentioned left- and right-incident states with the weight coefficients dependent on

thermal steady-state occupation numbers in DR's (taking into account also their specific electrochemical potentials). Once these states are built, their occupation numbers are simply given by the common Fermi function $f(\varepsilon, T)$, while more complicate occupations (possibly fractional even at $T = 0$) would result from the above mentioned matching conditions (Sec. 3.6). In a sense, this situation is similar to that well known in the Landau theory of Fermi liquid, where occupation numbers for interacting electrons can be fractional but they pass to common Fermi numbers for exact (composite) quasi-particles [Landau and Lifshitz, 1985]. A more detailed description will be given below.

3.7.2 Model

Now the coherent (ballistic) Hamiltonian in the single-band TB approximation is written as

$$\hat{H} = \hat{H}_0 + \hat{H}', \tag{3.50}$$

here $\hat{H}_0$ is just similar to the Hamiltonian given in Sec. 3.3, but the spin-rotation matrix $\hat{U} = \exp(-i\hat{\sigma}_x\theta/2)$ with the Pauli matrix $\hat{\sigma}_x$ is introduced in the S/G interface term to adjust the local quantization axes between S and D blocs. Further, the $\hat{H}'$ part of the Hamiltonian contains the electric potential term, due to the external voltage source:

$$\hat{H}' = e\sum_{\mathbf{n},\sigma}\sum_{j}\phi_j \hat{a}^{\dagger}_{j,\mathbf{n},\sigma}\hat{a}_{j,\mathbf{n},\sigma}, \tag{3.51}$$

where the local potentials on each jth layer are distributed as follows:

$$\phi_j = \frac{V}{2}\begin{cases} 1, & j \leq 0, \\ 1 - 2j/(n+1), & 1 \geq j \geq n+1, \\ -1, & j \geq n+1 \end{cases} \tag{3.52}$$

(supposing that the potential drop only occurs within the barrier).

Ballistic eigen-states of the Hamiltonian, Eq. (3.50), with given energy ε and transversal momentum $\mathbf{k}_{\|}$, can be yet characterized by their incidence, left (l) or right (r), and incident spin, majority ($+$) or minority ($-$). For brevity, the conserved values of ε and $\mathbf{k}_{\|}$ can be dropped, while the incidence and spin can be labeled by a single index α

as:

$$(l,+) \quad \rightarrow \quad \alpha = 1, \quad (l,-) \rightarrow \alpha = 2, \tag{3.53}$$

$$(r,+) \quad \rightarrow \quad \alpha = 3, \quad (r,-) \rightarrow \alpha = 4. \tag{3.54}$$

Each eigen-state with given α can be expanded over the *planar wave* states $|j, \mathbf{k}_{\|}, \sigma\rangle = \hat{a}^{\dagger}_{j,\mathbf{k}_{\|},\sigma}|0\rangle$ on subsequent jth planes as:

$$|\alpha\rangle = \Omega_{\alpha} \sum_{j,\sigma} \psi_{j,\alpha,\sigma} |j, \mathbf{k}_{\|}, \sigma\rangle, \tag{3.55}$$

where $\Omega_{\alpha} = (\sum_{j,\sigma} |\psi_{j,\alpha,\sigma}|^2)^{-1/2}$ is the normalization constant and $\psi_{j,\alpha,\sigma}$ are the amplitudes for an electron with the incident spin σ_{α} (related to α) to have spin σ at jth plane. As will be seen below, the ψ-amplitudes are functions of some dimensionless energy parameters in each block. Within the leads, these parameters are:

$$x_{s,\sigma} = \frac{\varepsilon - \varepsilon_{s,\mathbf{k}_{\|},\sigma} - eV/2}{2t_s}, \quad x_{d,\sigma} = \frac{\varepsilon - \varepsilon_{d,\mathbf{k}_{\|},\sigma} + eV/2}{2t_d}, \tag{3.56}$$

and, for given transversal momentum $\mathbf{k}_{\|}$, the related longitudinal momenta $q_{i,\sigma} = \arccos x_{i,\sigma}/\left(2t_i\right)$ should be both real. The latter condition defines a certain range K_{ε} of admissible $\mathbf{k}_{\|}$ values for a given energy ε from the energy band of the Hamiltonian, Eq. (3.50). Within the gate block, the relevant parameters $x_{g,j} \equiv x_j = (\varepsilon - \varepsilon_{g,\mathbf{k}_{\|}} - e\phi_j)/\left(2t_g\right)$, yet depend on the layer number $1 \leq j \leq n$.

3.7.3 Equations of motion

The ψ-amplitudes are found from simple algebraic equations of motion, setting zero the coefficients beside each planar wave state $|j, \mathbf{k}_{\|}, \sigma\rangle$ in the SE $\left(\hat{H} - \varepsilon\right)|\alpha\rangle = 0$ as done previously. Grouping ψ-amplitudes into 2-spinors:

$$\hat{\psi}_{j,\alpha} = \begin{pmatrix} \psi_{j,\alpha,+} \\ \psi_{j,\alpha,-} \end{pmatrix}, \tag{3.57}$$

these are presented equations in a spinor form, e.g., for the semi-infinite magnetic leads:

$$\hat{X}_i \hat{\psi}_{j,\alpha} = \hat{\psi}_{j-1,\alpha} + \hat{\psi}_{j+1,\alpha}, \tag{3.58}$$

involving the 2×2 diagonal on-site-energy matrices $\hat{X}_i = 2x_{i,\sigma}\delta_{\sigma\sigma'}$ $(i = s, d)$. Taking into account that if the S- and D-magnetizations are non-collinear each incident spin can produce reflected and transmitted spins of both signs [Zheng *et al.*, 1999], the solutions to Eq. (3.58) within the leads can be written as:

$$\hat{\psi}_{j,\alpha} = \begin{cases} \hat{S}^{j-1}\hat{e}_\alpha + \hat{S}^{1-j}\hat{r}_\alpha, & j \leq 0, \\ \hat{D}^{j-n}\hat{t}_\alpha, & j \geq n+1, \end{cases} \tag{3.59}$$

for l-incident states $(\alpha = 1, 2)$, and as:

$$\hat{\psi}_{j,\alpha,\sigma} = \begin{cases} \hat{D}^{n-j}\hat{e}_\alpha + \hat{D}^{j-n}\hat{r}_\alpha, & j \geq n+1, \\ \hat{S}^{1-j}\hat{t}_\alpha, & j \leq 0, \end{cases} \tag{3.60}$$

for r-incident states $(\alpha = 3, 4)$. Here $\hat{S}$ and $\hat{D}$ are diagonal matrices with σ, σ'-components $\mathrm{e}^{iq_{s,\sigma}}\delta_{\sigma,\sigma'}$ and $\mathrm{e}^{iq_{d,\sigma}}\delta_{\sigma,\sigma'}$ respectively, the σ-components of the spinors $\hat{e}_\alpha$ are $\delta_{\sigma_a,\sigma}$, and those of the spinors $\hat{r}_\alpha$, and $\hat{t}_\alpha$ are respectively $R_{\alpha,\sigma}$ and $T_{\alpha,\sigma}$, the reflection and transmission coefficients (yet unknown) for α-incident states. Also the normalization constants in Eq. (3.55) are expressed through the norms $|r_\alpha|^2 = \sum_\sigma |R_{\alpha,\sigma}|^2$ and $|t_\alpha|^2 = \sum_\sigma |T_{\alpha,\sigma}|^2$ as:

$$\Omega_\alpha = \sqrt{\frac{2}{1 + |t_\alpha|^2 + |r_\alpha|^2}}.$$

Similarly, one has the spinor equations of motion within the finite non-magnetic G-element:

$$2x_j \hat{\psi}_{j,\alpha} = \hat{\psi}_{j+1,\alpha} + \hat{\psi}_{j-1,\alpha}, \quad 2 \leq j \leq n-1, \tag{3.61}$$

with the scalar x-factors which depend on the layer number: $x_j = x_g - e\phi_j/(2t_g)$ $(1 \leq j \leq n)$. The solution to Eq. (3.61) can be expressed through the spinor values $\hat{\psi}_{1,\alpha}$ and

$\hat{\psi}_{0,\alpha}$ at the S/G interface:

$$\hat{\psi}_{j,\alpha} = p_{j-1}\left(x_1, \ldots x_{j-1}\right)\hat{\psi}_{1,\alpha} - p_{j-2}\left(x_2, \ldots x_{j-1}\right)\hat{\psi}_{0,\alpha}. \tag{3.62}$$

Here the polynomials p_j of j arguments, are defined for particular j values as $p_{-1} = 0$, $p_0 = 1$, and

$$\begin{aligned}
&p_1(x) = 2x,\\
&p_2\left(x_1, x_2\right) = 4x_1x_2 - 1,\\
&p_3\left(x_1, x_2, x_3\right) = 8x_1x_2x_3 - 2x_1 - 2x_3,\\
&p_4\left(x_1, x_2, x_3, x_4\right) = 16x_1x_2x_3x_4 - 4x_1x_4 - 4x_3x_4 - 4x_1x_2 + 1,\\
&\ldots
\end{aligned}$$

Thus generally $p_j(x_1, \ldots x_j)$ is a sum of products of factors $2x_k$ where k runs over $1, \ldots, j$, except all possible voids of even length with total length of $2l \leq j$, each product taken with the sign $(-1)^l$. In the limit of weak fields, $V \to 0$ and $x_j \to x_g$, these polynomials tend to the 2 kind Chebyshev polynomials u_j [Abramowitz and Stegun, 1964] of a single argument x_g: $p_j \to u_j\left(x_g\right)$, in accordance with the former results. Similarly, if one solves Eqs. (3.61) starting from the end of G-block, their solutions are expressed as: $\hat{\psi}_j = p_{n-j}\left(x_{j+1} \ldots x_n\right)\hat{\psi}_n - p_{n-j-1}\left(x_{j+1}, \ldots x_{n-1}\right)\hat{\psi}_{n+1}$, through the G/D interface spinors.

Now, in order to fully solve the TB problem for the $|\alpha\rangle$ state, it is necessary yet to interrelate the interface spinors from the spinor equations of motion (boundary conditions) at the S/G interface:

$$\begin{aligned}
\hat{X}_s\hat{\psi}_{0,\alpha} &= \hat{\psi}_{-1,\alpha} + \frac{t_{sg}}{t_s}\hat{U}^{-1}\hat{\psi}_{1,\alpha},\\
2x_1\hat{\psi}_{1,\alpha} &= \hat{\psi}_{2,\alpha} + \frac{t_{sg}}{t_g}\hat{U}\hat{\psi}_{0,\alpha},
\end{aligned} \tag{3.63}$$

and also at the G/D interface:

$$\begin{aligned}
\hat{X}_d\hat{\psi}_{n+1,\alpha} &= \hat{\psi}_{n+2,\alpha} + \frac{t_{gd}}{t_d}\hat{\psi}_{n,\alpha},\\
2x_n\hat{\psi}_{n,\alpha} &= \hat{\psi}_{n-1,\alpha} + \frac{t_{gd}}{t_g}\hat{\psi}_{n+1,\alpha}.
\end{aligned} \tag{3.64}$$

Eventually, the ψ-spinors within the G-element can be expressed through either reflection or transmission coefficients. Thus, for l-incidence ($\alpha = 1, 2$), it can be expressed from Eqs. (3.63) as:

$$\hat{\psi}_{j,\alpha} = \hat{U}\left(\hat{\Gamma}^*_{s,j}\hat{e}_\alpha + \hat{\Gamma}_{s,j}\hat{r}_\alpha\right), \tag{3.65}$$

with the diagonal matrix:

$$\hat{\Gamma}_{s,j} = \frac{t_s}{t_{sg}} p_{j-1}\left(x_1, \ldots, x_{j-1}\right) - \frac{t_{sg}}{t_g} p_{j-2}\left(x_2, \ldots, x_{j-1}\right)\hat{S}.$$

Otherwise, these spinors are expressed from Eqs. (3.64) as:

$$\hat{\psi}_{j,\alpha} = \hat{\Gamma}_{d,j}\hat{t}_\alpha, \tag{3.66}$$

with

$$\hat{\Gamma}_{d,j} = \frac{t_d}{t_{gd}} p_{n-j}\left(x_{j+1}, \ldots, x_n\right) - \frac{t_{gd}}{t_g} p_{n-j-1}\left(x_{j+1}, \ldots, x_{n-1}\right)\hat{D}.$$

Then matching Eqs. (3.65) and (3.66) at two specific sites, for instance, $j = 1$ and $j = n$, yields the explicit transport coefficients (for l-incidence) as:

$$\begin{aligned} \hat{r}_\alpha &= -\left(1 - \hat{A}\right)^{-1}\left(1 - \hat{B}\right)\hat{e}_\alpha, \\ \hat{t}_\alpha &= -\frac{t_g}{t_{sg}}\hat{\Gamma}^{-1}_{d,1}\hat{U}(1 - \hat{A})^{-1}(\hat{A} - \hat{B})\hat{e}_\alpha, \end{aligned} \tag{3.67}$$

where the matrix

$$\hat{A} = \frac{t_{sg}t_{gd}}{t_s t_d}\hat{U}^{-1}\hat{\Gamma}_{d,1}\hat{U}\hat{\Gamma}_{s,n},$$

describes distribution of incident carriers into all the spin channels, and $\hat{B}$ only differs from $\hat{A}$ by the change of the last factor $\hat{\Gamma}_{s,n}$ by its complex conjugate $\hat{\Gamma}^*_{s,n}$.

Similarly, the transport coefficients for r-incident carriers ($\alpha = 3, 4$) are obtained in the forms identical to Eq. (3.67) but with permuted s and d indices and inverted angle $\theta \to -\theta$ (this results in simple transposition of the distribution matrix: $\hat{A} \to \hat{A}^{\mathrm{T}}$).

3.7.4 Transport properties

Now the transmission and reflection coefficients permit to calculate both charge and spin density currents, through the expectation values of the generalized density transport

operators. These operators are defined at jth plane as

$$\hat{I}_{j,\nu} = Q_\nu \, (2h)^{-1} \sum_{\varepsilon,\mathbf{k}_\parallel \in K} t_j \hat{\imath}_{j,\nu,\mathbf{k}_\parallel}$$

where ν labels charge ($\nu = c$, $Q_c = e$) or spin ($\nu = x, y$, $Q_{x,y} = h/2$) components, $K = K(\varepsilon, V)$ is the restricted summation region that ensures $q_{s,\mathbf{k}_\parallel,\sigma}$ and $q_{d,\mathbf{k}_\parallel,\sigma'}$ to be real, and t_j is the hopping amplitude at jth plane, with:

$$\hat{\imath}_{j,\nu,\mathbf{k}_\parallel} = -i\hat{\Psi}^\dagger_{j,\mathbf{k}_\parallel} \hat{\sigma}_\nu \left(\hat{\Psi}_{j+1,\mathbf{k}_\parallel} - \hat{\Psi}_{j-1,\mathbf{k}_\parallel} \right) + \text{h.c.}, \tag{3.68}$$

here the 2-spinor operators are:

$$\hat{\Psi}_{j,\mathbf{k}_\parallel} = \begin{pmatrix} \hat{a}_{j,\mathbf{k}_\parallel,+} \\ \hat{a}_{j,\mathbf{k}_\parallel,-} \end{pmatrix}.$$

The averaged values of the current operators, Eq. 3.68, are obtained as traces over a complete set of eigenstates of the full Hamiltonian, Eq. 3.50. However, the above defined spin-incidence eigenstates, Eq. 3.55, can not be directly used for this end since they are not mutually orthogonal at non-collinear magnetic configuration of the junction. Therefore, the observable values are obtained using a properly orthogonalized set of states, being certain linear combinations of the spin-incidence states.

As shown in Appendix A those orthogonal eigenstates $|\zeta\}$ can be built from the spin-incidence states $|\alpha\rangle$ in the form:

$$|\zeta\} = \sum_\alpha O_{\zeta\alpha} |\alpha\rangle, \tag{3.69}$$

where the transformation coefficients $O_{\zeta\alpha}$ form a triangular matrix:

$$\hat{O} = \begin{pmatrix} 1 & 0 & 0 & 0 \\ O_{21} & O_{22} & 0 & 0 \\ O_{31} & O_{32} & O_{33} & 0 \\ O_{41} & O_{42} & O_{43} & O_{44} \end{pmatrix}, \tag{3.70}$$

and their expressions through the scalar products $\langle\alpha|\alpha'\rangle$ are given in Appendix A. Finally,

the sought average values of currents are obtained as traces in the full orthogonal set of eigenstates $|\varepsilon, \mathbf{k}_{\|}, \zeta\}$ (here to remind their complete notation):

$$I_{j,\nu} = \sum_{\varepsilon,\mathbf{k}_{\|}\in K} \sum_{\zeta} \{\varepsilon, \mathbf{k}_{\|}, \zeta | \hat{I}_{j,\nu} | \varepsilon, \mathbf{k}_{\|}, \zeta\} f(\varepsilon), \tag{3.71}$$

including also the Fermi thermal weights $f(\varepsilon) = 1/\left(\mathrm{e}^{\beta\varepsilon} + 1\right)$. This is also expressed through the matrix elements of the current operators in the spin-incidence basis (again omitting for simplicity their $j, \varepsilon, \mathbf{k}_{\|}$ dependencies):

$$I_{j,\nu} = \frac{Q_\nu}{h} \sum_{\varepsilon,\mathbf{k}_{\|}\in K} \sum_{\alpha,\alpha'} \mathrm{Re}\left(A_{\alpha\alpha'} I^{\nu}_{\alpha\alpha'}\right) f(\varepsilon). \tag{3.72}$$

The coefficients $A_{\alpha\alpha'}$ are written as:

$$\begin{aligned}
A_{11} &= 1 + |O_{21}|^2 + |O_{31}|^2 + |O_{41}|^2, \\
A_{22} &= |O_{22}|^2 + |O_{32}|^2 + |O_{42}|^2, \\
A_{33} &= |O_{33}|^2 + |O_{43}|^2, \\
A_{44} &= |O_{44}|^2, \\
A_{12} &= A^*_{21} = O^*_{21} O_{22} + O^*_{31} O_{32} + O^*_{41} O_{42}, \\
A_{13} &= A^*_{31} = O^*_{31} O_{33} + O^*_{41} O_{43}, \\
A_{23} &= A^*_{32} = O^*_{32} O_{33} + O^*_{42} O_{43}, \\
A_{24} &= A^*_{42} = O^*_{42} O_{44}, \\
A_{34} &= A^*_{43} = O^*_{43} O_{44}, \\
A_{14} &= A^*_{41} = O^*_{41} O_{44}.
\end{aligned} \tag{3.73}$$

For definiteness, the plane $j = n + 1$, that is the next one to the G/D interface, will be considered to calculate both spin and charge-transport. Then, the $I^{\nu}_{\alpha\alpha'}$ values for the states incident from the left $(\alpha, \alpha') = (1, 2)$, are found as:

$$I^{\nu}_{\alpha\alpha'} = \frac{\Omega_\alpha \Omega_{\alpha'}}{2} \hat{t}^{\dagger}_{\alpha} \hat{D}^{-1} \hat{\sigma}_\nu \hat{v}_d \hat{D} \hat{t}_{\alpha'}, \tag{3.74}$$

while for the states incident from the right $(\alpha, \alpha') = (3, 4)$, they are:

$$I^{\nu}_{\alpha\alpha'} = \frac{\Omega_\alpha \Omega_{\alpha'}}{2} (\hat{e}^\dagger_\alpha \hat{D} + \hat{r}^\dagger_\alpha \hat{D}^{-1}) \hat{\sigma}_\nu \hat{v}_d (-\hat{D}^{-1} \hat{e}_{\alpha'} + \hat{D} \hat{r}_{\alpha'}). \tag{3.75}$$

Besides these, two crossed terms appear, one for $\alpha = (1, 2)$ and $\alpha' = (3, 4)$:

$$I^{\nu}_{\alpha\alpha'} = \frac{\Omega_\alpha \Omega_{\alpha'}}{2} \hat{t}^\dagger_\alpha \hat{D}^{-1} \hat{\sigma}_\nu \hat{v}_d (-\hat{D}^{-1} \hat{e}_{\alpha'} + \hat{D} \hat{r}_{\alpha'}), \tag{3.76}$$

and other for $\alpha = (3, 4)$ and $\alpha' = (1, 2)$:

$$I^{\nu}_{\alpha\alpha'} = \frac{\Omega_\alpha \Omega_{\alpha'}}{2} (\hat{e}^\dagger_\alpha \hat{D} + \hat{r}^\dagger_\alpha \hat{D}^{-1}) \hat{\sigma}_\nu \hat{v}_d \hat{D} \hat{t}_{\alpha'}. \tag{3.77}$$

In Eqs.(3.74−3.77), the velocity matrix $\hat{v}_d$ is used, given by:

$$\hat{v}_d = \begin{pmatrix} 2 \sin q_{d,+} & 0 \\ 0 & 2 \sin q_{d,-} \end{pmatrix} \tag{3.78}$$

These formulas together with the $O_{\zeta\alpha}$ values presented in Appendix A, Eqs. (A4), are basic for practical calculation of the physical characteristics of spin- and charge-transfer in ballistic magnetic junctions. Moreover, the parallel and perpendicular torque components at a given jth plane are defined as: $\tau_{j,\parallel} = I_{j,y} - I_{j+1,y}$, and $\tau_{j,\perp} = I_{j,x} - I_{j+1,x}$, respectively. Following Theodonis *et al.* [Theodonis *et al.*, 2006], the total torque acting on the right (free) magnetization is found by summation of the above terms:

$$\begin{aligned} \tau_\parallel &= \sum_{j=n+1}^{\infty} \tau_{j,\parallel} = I_{n+1,y}, \\ \tau_\perp &= \sum_{j=n+1}^{\infty} \tau_{j,\perp} = I_{n+1,x}. \end{aligned} \tag{3.79}$$

Their numerical values for certain choice of the system parameters are found from Eqs. (3.72−3.77) as presented below.

3.7.5 Numerical Results

It is important to mention that the present calculations are restricted to zero temperature. In addition, the similar model parameters for Fe electrodes are used ($\varepsilon_+ =$

1.3 eV, $\varepsilon_- = 3.25$ eV), and the hopping parameter is chosen to be $t = -0.65$ eV for all the planes. Further, the number of atomic planes in the gate is set to $n_g = 3$, the field independent part of the atomic level of this element is chosen to be $\varepsilon_g/(2t) = 4$, the angle between the leads magnetizations is assigned to $\theta = \pi/2$, and the voltage is fixed to $eV/(2t) = 0.5$ (exception is made when the currents are calculated as a function of one of this parameters, but the others are fixed to the ascribed values). In this case the integration is done in both total energy and transversal momentum following a similar procedure to that in the above sections. In fact, as was done in the previous sections, the $\mathbf{k}_{\|}$-summation is replaced by the integration facilitated by the fact that the transmission and reflection coefficients only depend on $\mathbf{k}_{\|}$ through the transversal energy u. Thus it is possible to use the 2D density of states $\rho(u)$, Eq. (3.25). The integration limits are restricted to $K(\varepsilon, V)$ imposing that, at a given energy ε and voltage V, the values of $q_{s,\sigma}$ and $q_{d,\sigma'}$ (depending on the specific transition considered) are real.

The results of such calculation are presented in Figs. 3.17−3.19, for different types of current (charge current I_c and spin currents $I_{n+1,x}$, and $I_{n+1,y}$) in functions of various parameters (voltage V on junction, gate bias ε_g, and magnetization angle θ). It is important to mention that these are *preliminary calculations* and more work is still needed to properly establish the present results.

As seen from Fig. 3.17a, the ε_g dependence $I_c(\varepsilon_g)$ generally displays a similar behavior to what was previously found for the Landauer conductance, a strong increase in the *shallow band regime* (SBR). As discussed above, this enhancement is due to resonant transport and it also appears in both spin-torque components (see below). Moreover, in Fig. 3.17b the dependence of charge current on the angle θ is presented, $I_c(\theta)$. This shows the typical $\propto \cos\theta$ behavior. In preceding calculations an important deviation from this behavior was found in the SBR, nevertheless, further study is still needed to confirm such a scenario. As seen from Fig. 3.17c, the $I_c(V)$ curve exhibits an ohmic behavior in the low voltage range ($V \lesssim 0.25$ V, followed by a non-ohmic effect at higher voltages. However the latter behavior seems less reliable, since the present model does not include important effects as charge and spin accumulation indicated in Sec. 3.6.

The dependencies of $\tau_{\|}$ on different variables are presented in Fig. 3.18. In Fig. 3.18a, an important feature is revealed besides the expected increase of this torque component in the SBR: $\tau_{\|}$ oscillates as a function of ε_g. In literature, changes of sign of this

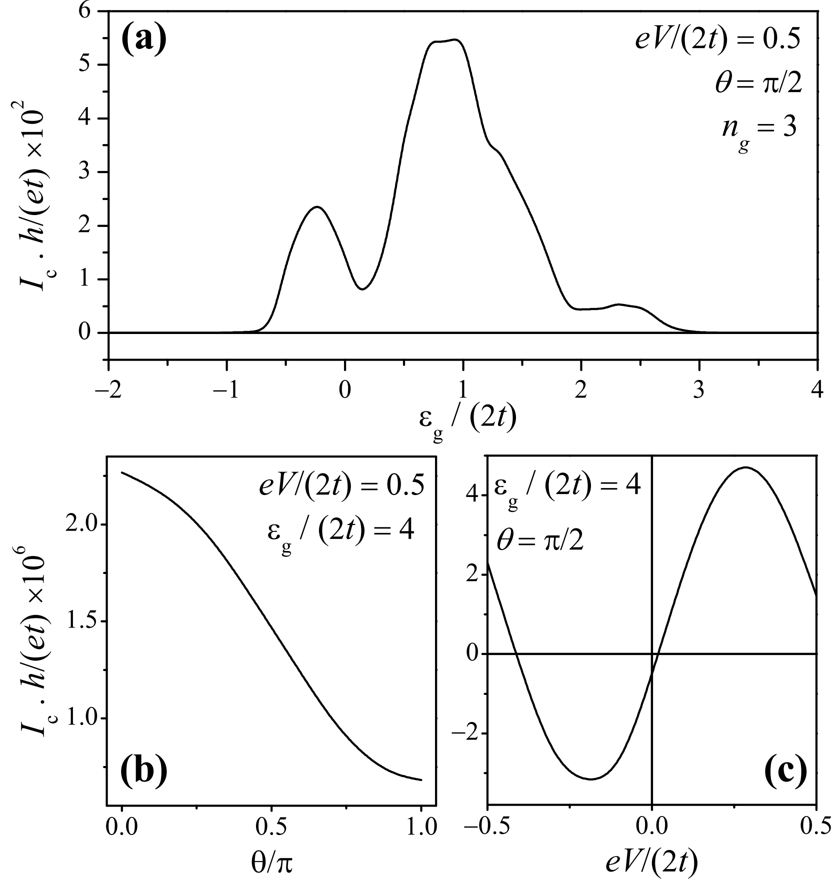

Figure 3.17: *Charge current, I_c, as a function of: (a) the on-site energy ε_g of the spacer; (b) the angle θ; (c) the bias voltage V.*

torque component have already been reported [Edwards *et al.*, 2005], nevertheless this is the first time that an oscillatory behavior is clearly identified. This effect could suggest an interesting way to manipulate the spin-transfer torque by controlling its sign by means of the gate bias, ε_g. Additionally, fixing $\varepsilon_g/(2t) = 4$, it is shown in Fig. 3.18b that $\tau_{\|}$ follows a typical $\propto \sin\theta$ law, characteristic of magnetic tunnel junctions. Furthermore, Fig. 3.18c shows $\tau_{\|}(V)$ a linear behavior in the low voltage range.

Finally, the results for $\tau_{\perp}$ are drawn in Fig. 3.19. As seen from Fig. 3.19a, this torque component does not show the same SBR oscillations vs ε_g as those found for $\tau_{\|}$, but it still passes through a relevant enhancement (similarly to I_c) without changing its sign. Like in the $\tau_{\|}$ case, a $\tau_{\perp} \propto \sin\theta$ law is found for $\varepsilon_g/(2t) = 4$, Fig. 3.19b. It is expected from some preliminary calculations that sizeable deviations from this sinusoidal law (for both torque components) can take place at ε_g approaching the SBR range, but a more

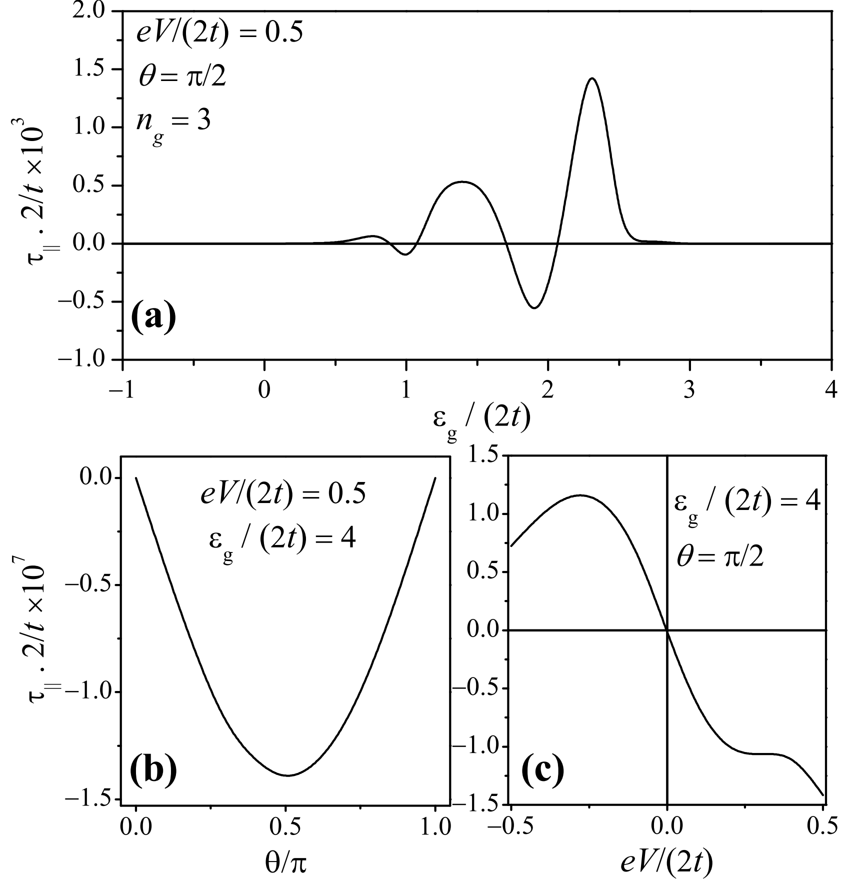

Figure 3.18: *The same dependencies as those presented for I_c, but for $\tau_{\|}$.*

detailed analysis is needed to confirm this. If so, these effects could also give a valuable insight on the design of new *ballistic* spintronics devices. At the end, in Fig. 3.19c, the voltage dependence of $\tau_{\perp}$ is presented, which is close to quadratic in the low voltage, in qualitative agreement with the recent results by Theodonis *et al* obtained within the Green function formalism [Theodonis *et al.*, 2006].

3.8 Conclusions

In this chapter a theoretical approach was developed to describe coherent spin-dependent quantum transport in nanolayered magnetic junctions, using a single-band tight-binding model with explicit equations of motion for the wave-function amplitudes. Analytic solutions for the transmission and reflection coefficients were generalized for a 3D magnetic junction structure. Simple zero temperature calculations have revealed the most

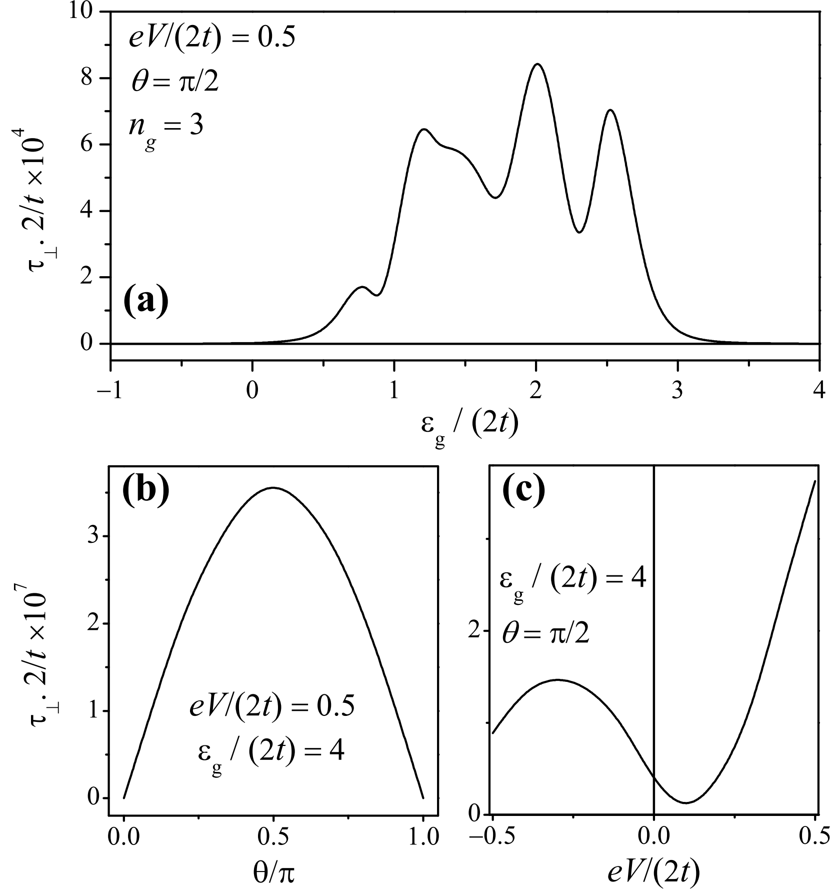

Figure 3.19: *Variation of $\tau_\perp$ with the same variables as for other transport currents.*

pronounced enhancement of the magnetoresistance in the *shallow band regime*, defined by low gate voltages. Another important feature for this gate voltage regime is the calculated oscillatory behavior of MR with the number of atomic planes in the spacer, which was already predicted by [Mathon *et al.*, 1995] and experimentally observed by [Yuasa *et al.*, 2004] at low enough gate voltage barrier $\varphi \sim 0.4$ eV in the Fe/MgO/Fe structure. Further, the important effect of charge build-up on the junction interface was also considered. Though in a simple phenomenological approach, its effect on the magnetoresistance could be roughly estimated showing an important decrease of the major shallow band peaks, but reinforcing a higher gate voltages range (with new MR peaks appearing).

The direct effect of an applied electrical voltage on the partially quantized energy band structure of the system and fractional occupation of coherent electronic states at finite temperatures was then studied. This permitted to obtain a more broad information on the system magnetoresistance behavior in function of all relevant parameters. In

particular, at the low voltage regime, the temperature effect on the magnetoresistance response is found to monotonically shift the position of quantum resonance peak and reduce its intensity. All the same, at fixed band parameters and temperature, the effect of applied finite voltage monotonously reduces magnetoresistance being rather sensitive to the thickness of the gate.

The treatment of the specifics of electronic distribution function at short distances from the magnetic tunnel junction showed that already in absence of external electrical fields, an essential local perturbation of the equilibrium Fermi distribution appears for the antiparallel magnetic configuration of electrodes. This leads to a reduction of the occupation of one of the spin subbands (minority for negative or majority for positive band dispersion). This effect can locally influence (respectively, enhance or reduce) the polarization of charge carriers and, subsequently, the magnetoresistance of the device.

At the end, the basic formalism for charge and spin-transfer current calculations with arbitrary angle between magnetizations was developed and preliminary results were presented. An interesting oscillatory behavior of the parallel torque component with (the field independent part of) the atomic level of the gate was found.

As a final remark, it is concluded that the best magnetoresistance values for a quantum magnetic junction could be reached using *shallow band* materials for spacer layers, the possible candidates sought among transition metals (Cr [Greullet *et al.*., 2007] in junctions of the type Fe/Cr/Fe or Zn in junctions of the type Co/Zn/Co), semiconductors (Ge, Si), or semimetals (Sb, As). Probably, the highest experimental value of TMR $\sim$ 608% [Ikeda *et al.*, 2008] in the $Co_{20}Fe_{60}B_{20}$/MgO/$Co_{20}Fe_{60}B_{20}$ junctions is due to going closer to this regime.

Chapter 4

Coherent Transport in Perfect Multilayered Magnetic Junctions

4.1 Introduction

This chapter is dedicated to complex multilayered magnetic junctions. These structures present several advantages as compared with simple junctions (considered in the previous Chapter), namely, a better stability upon voltage and temperature. In addition, it is also expected that a significant increase of the magnetoresistance (in perfect junctions) can appear due to quantum resonant effects. Thus the study of complex junctions could bring an interesting inset to potential new geometries attaining high magnetoresistive performances.

This Chapter is organized in the following way: Sec. 4.2 deals with spin-dependent transport in double-spacer magnetic junctions; Sec. 4.3 treats the spin-dependent transport in triple-spacer magnetic junctions; Sec. 4.4 describes a matrix method to model multilayered structures, with arbitrary number and width of layers; finally, technological perspectives are outlined and comments are made in Sec. 4.5.

4.2 Double-Spacer Magnetic Junctions

To the present, various spin-resonant devices of F/I/N/F type were studied with different choices of the ferromagnetic leads (F): Co, CoFe, NiFe, etc.; thin insulating barrier (I): Al_2O_3, MgO, etc.; and non-magnetic metal spacer (N): Cu, Ru, Au, etc.

First attempts to reach enhanced tunnel magnetoresistance (TMR) using spin-resonant devices were done by Sun and Freitas, on the basis of CoFe/Al_2O_3/Cu/CoFe junctions [Sun and Freitas, 1999]. However, their results revealed that TMR exponentially decayed with Cu thickness. Later on, Moodera *et al.* found evidence for quantum well states (QWS), in the Co/Au/Al_2O_3/NiFe structures [Moodera *et al.*, 1999] though at rather low TMR levels; also negative TMR was found above a certain critical Au thickness. Otherwise, LeClair *et al.*, observed TMR oscillations with Ru thickness in Co/Ru/Al_2O_3/Co structure [LeClair *et al.*, 2000], but doubted that QWS may survive under the effect of broad diffuse interface as stated elsewhere [LeClair *et al.*, 2001]. However, Yuasa *et al.* found large TMR oscillations in Co/Cu/Al-O/NiFe junctions [Yuasa *et al.*, 2002] explaining them in terms of minority-spin QWS formed in the Cu spacer. This finding corroborated the previous theoretical works, beginning from Vedyayev *et al.* suggestion on TMR resonant enhancement and oscillation upon variation of the non-magnetic metal (N) thickness, attributed to QWS within this element [Vedyaev *et al.*, 1997]. Enhanced TMR by QWS was predicted by Zhang and Levy [Zhang and Levy, 1998] in the scope of Slonczewski model [Slonczewski, 1989], indicating also a TMR decay with N width due to the coherence loss by the interface roughness. Further, Mathon and Umerski demonstrated that the coherence loss in presence of QWS does not necessarily destroy TMR [Mathon and Umerski, 1999]. Indeed, taking into account barrier roughness and electron scattering, Vedyayev reproduced successfully [Vedyaev *et al.*, 2000] the results of Sun and Freitas. Recently, the data presented by Yuasa *et al.* were well explained within the general Kubo formalism [Itoh *et al.*, 2003] and the ballistic analytic approach [Yang *et al.*, 2005].

Following the treatment of the preceding Chapter, in this Section a correct account of the energy spectra (composed of a finite number of subbands) in I and N elements is undertaken, Fig. 4.1. The discrete spectrum structure that follows from the finite number of atomic planes in the spacer elements (Chap. **3**) is different from the infinite QWS due to the common size-confinement mechanism in the continuous approach and leads to different transport effects.

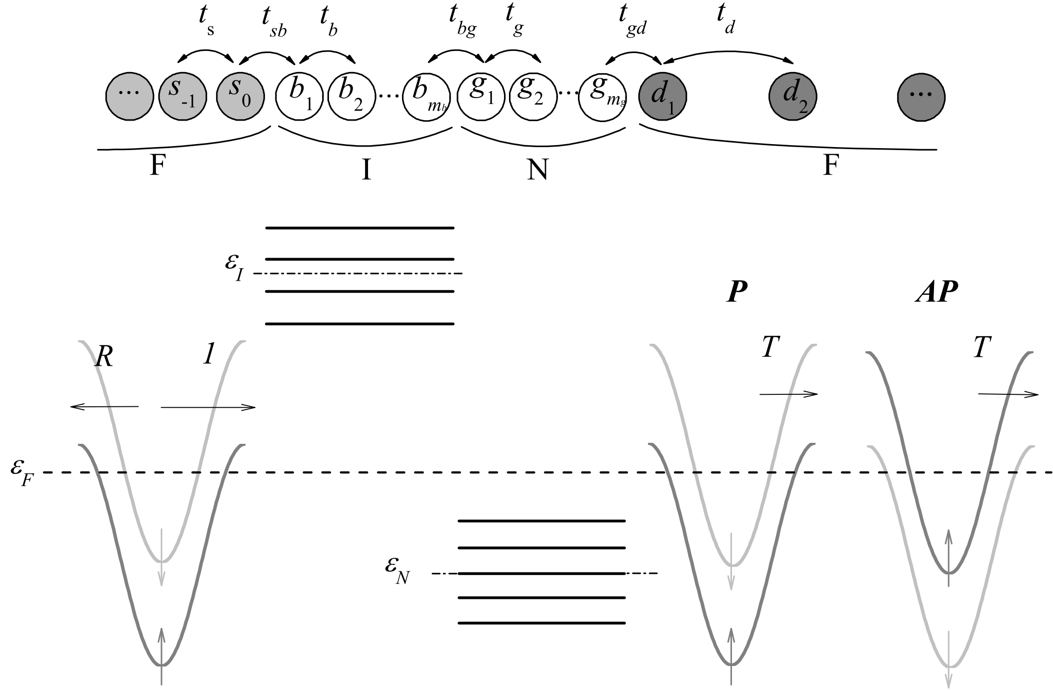

Figure 4.1: *The energy diagram shows the on-site energy levels (dash-dot) for B- and G-spacers, the Fermi level (dashed) whose crossings with the continuous S- and D- dispersion curves (light grey for minority spins and grey for majority spins) define the spin-dependent wave numbers for incoming ($q_{s,\pm}$), reflected ($-q_{s,\pm}$) and transmitted ($q_{d,\pm}$) parts of the Fermi state. Notice that the Fermi level generally does not match any of the discrete levels (solid) in the central B and G elements.*

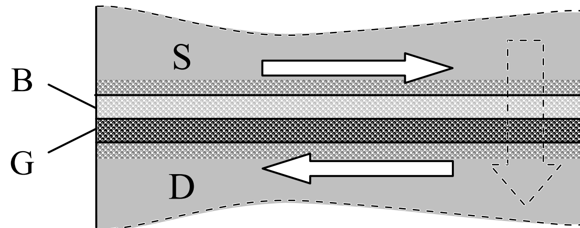

Figure 4.2: *Sketch of the double-spacer junction with epitaxially defined atomic planes in its elements. The solid arrows show polarization of FM leads, the dashed arrow indicates tunnel current.*

4.2.1 Model

Like in Chap. **3**, a single-band TB model is used here to describe the quantum collective states in the composite nanostructure shown in Fig. 4.2 where two semi-infinite F lead blocks (denominated source, S, and drain, D) are separated by two spacer blocks (insulating barrier B, and normal metal gate G), each i-th block being a coherent stack of m_i atomic planes (for $i = s, b, g, d$) with simple cubic lattice structure and unit lattice

constant. The fundamental point in the derivation is a proper account of the boundary conditions on (S/B), (B/G), and (G/D) interfaces. The respective Hamiltonian $\hat{H} = \sum_{i,i'}\sum_{\mathbf{k}_\parallel,\sigma}\hat{h}_{i,\mathbf{k}_\parallel,\sigma} + \hat{h}_{i,i',\mathbf{k}_\parallel,\sigma}$, includes the block terms $\hat{h}_{i,\mathbf{k}_\parallel,\sigma}$ (where i runs from S to D) and the interface terms $\hat{h}_{i,i',\mathbf{k}_\parallel,\sigma}$, given by:

$$\hat{h}_{i,\mathbf{k}_\parallel,\sigma} = \sum_{l=l_i}^{l_{i+1}-1}\varepsilon_{i,\mathbf{k}_\parallel,\sigma}\hat{a}^\dagger_{l,\mathbf{k}_\parallel,\sigma}\hat{a}_{l,\mathbf{k}_\parallel,\sigma} + t_i\sum_{l=l_i}^{l_{i+1}-2}\left(\hat{a}^\dagger_{l+1,\mathbf{k}_\parallel,\sigma}\hat{a}_{l,\mathbf{k}_\parallel,\sigma} + \text{h.c.}\right),$$
$$\hat{h}_{i,i+1,\mathbf{k}_\parallel,\sigma} = t_{i,i+1}\left(\hat{a}^\dagger_{l_i-1,\mathbf{k}_\parallel,\sigma}\hat{a}_{l_i,\mathbf{k}_\parallel,\sigma} + \text{h.c.}\right). \quad (4.1)$$

Here t_i and $t_{i,i+1}$ are the hopping amplitudes for ith block and $(i,i+1)$th interface and the planar wave operators $\hat{a}_{l,\mathbf{k}_\parallel,\sigma} = N^{-1/2}\sum_{\mathbf{n}}\hat{a}_{l,\mathbf{n},\sigma}\exp(i\mathbf{k}_\parallel\cdot\mathbf{n})$ are the 2D Fourier transforms of local operators $\hat{a}_{l,\mathbf{n},\sigma}$ for spin $\sigma = \pm$ on $\mathbf{n}$ site in lth atomic plane of ith block. The summation limits involve l_i, the first atomic plane of the ith element (setting $l_s = -\infty$, $l_b = 1$). The TB electronic spectrum in each ith block (all with the same square lattice and unity lattice parameter), $\varepsilon = \varepsilon_{i,\mathbf{k}_\parallel,\sigma} + 2t_i\cos q_i$ displays the in-plane dispersion $\varepsilon_{i,\mathbf{k}_\parallel,\sigma} = \varepsilon_i + 2t_i(\cos k_x + \cos k_y) - \sigma\Delta_i$, with the on-site atomic energy ε_i, the transversal wave vector $\mathbf{k}_\parallel = (k_x,\, k_y)$, the Stoner splitting Δ_i (zero for non-magnetic elements, and non-zero (equal) for all F blocks), and the longitudinal wave number q_i, real in the leads.

The collective wave function, for given energy ε, transversal momentum $\mathbf{k}_\parallel$, and spin σ, is written as: $|\psi_{\mathbf{k}_\parallel}\rangle = \sum_{i,\sigma}\sum_{l=l_i}^{l_{i+1}-1} c_{l,\mathbf{k}_\parallel,\sigma}|l,\mathbf{k}_\parallel,\sigma\rangle$, where the amplitudes $c_{l,\mathbf{k}_\parallel,\sigma}$ of planar wave states $|l,\mathbf{k}_\parallel,\sigma\rangle = \hat{a}^\dagger_{l,\mathbf{k}_\parallel,\sigma}|0\rangle$, obey the TB equations of motion (Chap. **3**):

$$2x_{i,\mathbf{k}_\parallel,\sigma}c_{l,\mathbf{k}_\parallel,\sigma} = c_{l+1,\mathbf{k}_\parallel,\sigma} + c_{l-1,\mathbf{k}_\parallel,\sigma}, \quad (4.2)$$

within the ith block, $l_i + 2 \le l \le l_{i+1} - 2$, with the dimensionless variable $x_{i,\mathbf{k}_\parallel,\sigma} = (\varepsilon - \varepsilon_{i,\mathbf{k}_\parallel,\sigma})/(2t_i)$. Their solutions in the finite elements (B, G) are readily expressed through the 2 kind Chebyshev polynomials $u_l(x)$ [Abramowitz and Stegun, 1964]: $c_{l,\mathbf{k}_\parallel,\sigma} = c_{l_i,\mathbf{k}_\parallel,\sigma}u_{l-l_i}(x_i)$ starting from the initial value $c_{l_i,\mathbf{k}_\parallel,\sigma}$, or $c_{l,\mathbf{k}_\parallel,\sigma} = c_{l_i+m_i,\mathbf{k}_\parallel,\sigma}u_{l_i+m_i-l}(x_i)$ down to the final value $c_{l_i+m_i,\mathbf{k}_\parallel,\sigma}$, for all $l_i + 1 \le l \le l_{i+1} - 1$. Here the initial (final) amplitude $c_{l_i,\mathbf{k}_\parallel,\sigma}$ ($c_{l_i+m_i,\mathbf{k}_\parallel,\sigma}$) is related to the final (initial) amplitude $c'_{l_i-1,\mathbf{k}_\parallel,\sigma'}$

($c'_{l_{i+1},\mathbf{k}_\parallel,\sigma'}$) in the $(i-1)$th $[(i+1)$th$]$ block, through the interface equations of motion:

$$\begin{aligned} 2x_{i,\mathbf{k}_\parallel,\sigma}c_{\mathbf{k}_\parallel,l_{i'}-1,\sigma} &= c_{\mathbf{k}_\parallel,l_{i'}-2,\sigma} + \frac{t_{i,i'}}{t_i}c'_{\mathbf{k}_\parallel,l_{i'},\sigma'}, \\ 2x_{i',\mathbf{k}_\parallel,\sigma}c'_{\mathbf{k}_\parallel,l_{i'},\sigma'} &= c'_{\mathbf{k}_\parallel,l_{i'}+1,\sigma'} + \frac{t_{i,i'}}{t'_i}c_{\mathbf{k}_\parallel,l_{i'}-1,\sigma}. \end{aligned} \tag{4.3}$$

The sequence of the block and interface equations gets completed by the asymptotic solutions for in- and out-amplitudes in the semi-infinite leads:

$$\begin{cases} s_{l,\mathbf{k}_\parallel,\sigma} = \mathrm{e}^{iq_{s,\mathbf{k}_\parallel,\sigma}(l-l_b-1)} + R\mathrm{e}^{-iq_{s,\mathbf{k}_\parallel,\sigma}(l-l_b-1)}, \\ d_{l,\mathbf{k}_\parallel,\sigma} = T\mathrm{e}^{iq_{d,\mathbf{k}_\parallel,\sigma}(l-l_d)}, \end{cases} \tag{4.4}$$

these include the S incident and reflected waves with the longitudinal momentum $q_{s,\mathbf{k}_\parallel,\sigma} = \arccos x_{s,\mathbf{k}_\parallel,\sigma}$ and the D transmitted wave with respective $q_{d,\mathbf{k}_\parallel,\sigma'}$ (where $\sigma' = \sigma$ in P, and $\sigma' = -\sigma$ in AP one). The spin-dependent reflection and transmission amplitudes R and T are the most important objects in the calculations and after some algebra, the ith-amplitudes can be eliminated resulting in analytical solutions for R and T as functions of the variables $x_{i,\mathbf{k}_\parallel,\sigma}$ for all $i = s,\ldots,d$. In this way, the transmission amplitude is presented as $T_{\sigma,\sigma'} = -2i(t_st_bt_g)(t_{sb}t_{bg}t_{bd})^{-1}\sin q_{s,k,\sigma}/D_{\mathbf{k}_\parallel,\sigma,\sigma'}$ with the denominator:

$$\begin{aligned} D_{\mathbf{k}_\parallel,\sigma,\sigma'} &= (u^b_{m_b} - \gamma_{s,\sigma}u^b_{m_b-1})(u^g_{m_g} - \gamma_{d,\sigma'}u^g_{m_g-1}) - \\ &\quad -\gamma_{gb}(u^b_{m_b-1} - \gamma_{s,\sigma}u^b_{m_b-2})(u^g_{m_g-1} - \gamma_{d,\sigma'}u^g_{m_g-2}). \end{aligned} \tag{4.5}$$

Here the fundamental interface parameters are: $\gamma_{s,\sigma} = t^2_{sb}(t_st_b)^{-1}\exp(iq_{s,\mathbf{k}_\parallel,\sigma})$, $\gamma_{d,\sigma'} = t^2_{gd}(t_gt_d)^{-1}\exp(iq_{d,\mathbf{k}_\parallel,\sigma'})$ and $\gamma_{gb} = t^2_{bg}(t_bt_g)^{-1}$; the polynomials $u^i_{m_i} \equiv u_{m_i}(x_{i,\mathbf{k}_\parallel,\sigma})$. These amplitudes, calculated at the Fermi energy $\varepsilon = \varepsilon_F$ (zero temperature and voltage), define the LB conductance [Landauer, 1957] and [Büttiker, 1988]:

$$G_{\sigma\sigma'} = \frac{e^2}{h}\sum_{\mathbf{k}_\parallel\in K,\sigma}|T_{\sigma\sigma'}(\varepsilon_\mathrm{F},\mathbf{k}_\parallel)|^2 \equiv \frac{e^2}{h}\int_{a_{\sigma,\sigma'}}^{b_{\sigma,\sigma'}} du\rho(u)|T_{\sigma,\sigma'}(\varepsilon_\mathrm{F},u)|^2. \tag{4.6}$$

with precisely the same limits as those used in Chap. **3**:

$$\begin{aligned} b_{\sigma,\sigma'} &= \min\left\{2, \min\left[x_{s,\sigma}(\varepsilon_\mathrm{F}), x_{d,\sigma'}(\varepsilon_\mathrm{F})\right] + 1\right\}, \\ a_{\sigma,\sigma'} &= \max\left\{-2, \max\left[x_{s,\sigma}(\varepsilon_\mathrm{F}), x_{d,\sigma'}(\varepsilon_\mathrm{F})\right] - 1\right\}. \end{aligned}$$

Obviously, this integration is sensitive to the magnetic configuration and the final MR is found as:

$$MR = \frac{G_P - G_{AP}}{G_{AP} + G_0}, \tag{4.7}$$

where the additional term G_0 models the spin-independent conduction channel, like *s*- and *p*-bands in transition metals, acting in parallel with the explicit contribution in Eq. (4.7) by the *d*-band. Though small (in e^2/h units), this value can essentially reduce the peak TMR values (at exponentially vanishing G_{AP}) and thus effectively accounts for the multiband effects in magneto-transport.

4.2.2 Results and Discussion

In numerical calculations, the band parameters exposed in Chap. **2** are applied to resemble the real case of Fe *d*-band leads separated by an epitaxial double-spacer, formed by a moderate barrier $\varepsilon_I = 4$ eV, and a non-magnetic element with variable on-site energy, ε_N.

Further on, for the structures having I elements the spin-independent conductance in Eq. (4.6) is modeled (here and thereafter) as:

$$G_0 = e^2 h^{-1}[10^{-7} + 10^{-2}\exp(-2m_I)],$$

where the two terms in the brackets model respectively the m_I-independent band contributions and m_I-dependent ones with typical localization length in the insulator barrier of the order of $l_I \sim 0.5$. Otherwise, for structures without I elements, $G_0 = 0.1e^2h^{-1}$ similarly to the simple junction case.

The results are shown in Figs. 4.3 as functions of the relevant parameters: ε_N, number m_N of atomic planes, and the barrier thickness, m_I.

The MR dependencies on ε_N, reveal an important enhancement in the *shallow band regime*, with a similar behavior of Chap. **3**. The found MR values reach $\sim 5000\%$ for $\varepsilon_N \sim 0.9$ eV, attributed to one of the m_N quantized subbands in the gate spectrum. This effect is even more pronounced in more complex structures. Notably, MR surpasses the $\sim 100\%$ TMR value of the common FIF junctions and is much greater than the $\sim 10\%$ value in the experimental FINF junctions [Yuasa *et al.*, 2002]. On the other hand, an easier system control at some fixed ε_N level can be sought by varying G width, m_N. The

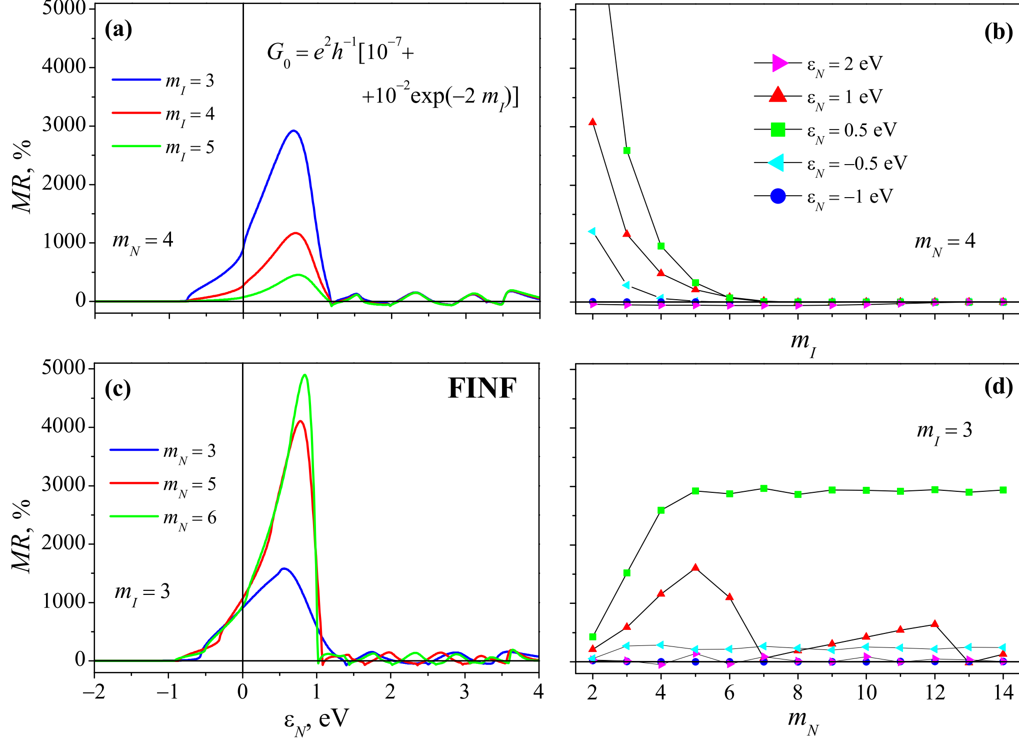

Figure 4.3: *[(a),(c)] The TMR dependencies on ε_N (at different widths m_I and m_N) show resonance enhancement, reaching* $\sim$ 3000%*; (b) TMR vs m_I for various important ε_N values, different conduction regimes are explored; (d) TMR vs m_N for the same ε_N values;*

results in Fig.4.3d reveal oscillatory TMR with m_N. Actually, similar oscillations are well known, both theoretically, [Itoh *et al.*, 2003 and Yang *et al.*, 2005], and experimentally [Yuasa *et al.*, 2002]. However, the main difference in the epitaxial junctions considered in this work is the high amplitude of oscillations.

In the present model, the TMR oscillations arise from oscillations of both parallel (G_P) and anti-parallel (G_{AP}) conductance upon ε_N and m_N variation. The oscillation periods do not depend much on the specific magnetic state since they result from the aforementioned discrete subband energy structure, instead of the usual QWS formation in rectangular continuous barriers [Vedyaev *et al.*, 1997 and Mathon and Umerski, 1999]. In fact, the TMR oscillations as a function of m_N are very important, and a similar behaviour was already reported [Jonkers, 2002], as a result of general quantum-mechanical mechanism in different junctions. Indeed, according to Jonkers [Jonkers, 2002], this TMR behaviour is due to the wave function oscillations inside the N layer. Obviously, changing N width causes oscillations of wave amplitudes at the interfaces with neighbour elements,

resulting in oscillations of the transmission amplitude. This mechanism affects both spin channels and is obviously more noticeable if the atomic energies in the nearby elements are higher than in the N element. This mechanism not only agrees well with the results for the given junction, but also with those to be considered below. In the present theory, the discrete subband nature of the electronic spectrum dependent on the m_N width can reinforce this mechanism.

At varying energy ε_N, the gate spectrum is rigidly shifted and some subbands can cross the Fermi level. This will enhance the conductance when the Fermi level gets aligned with a (maximum DOS of) subband, but suppress it when out of such alignment. After the entire spectrum (of a finite number of the subbands) is passed in this way, the oscillations will disappear. Otherwise, the TMR oscillations vs the gate width m_I, result from the variation of the subband structure. When a new atomic plane is added to G, a new subband is formed, varying the distribution of subbands at the same maximum 1D band width, $4|t|$, Chap. **3**. Thus, for some m_N values, the Fermi level is approached by a (maximum DOS of) subband closer than for others, causing oscillating conductance.

Finally, MR exponentially decreases with m_I thickness favoring ultra-thin junction $m_I \sim 2 - 4$, where the effects of pinholes are attenuated by the presence of a second N spacer.

4.3 Triple-Spacer Magnetic Junctions

Nowadays various fields of applications are devoting plenty of work to the study of resonant transport effects in triple-spacer junctions (principally, double tunnel junctions). For example, resonant tunnel diodes (RTD) with negative differential resistance (NDR) I-V characteristics are being used as simple amplifiers, but also applied to advanced chaotic optoelectronics communications [Romeira *et al.*, 2008].

In spintronics, resonant effects in single magnetic tunnel junctions (MTJ) with coherent spin-dependent transport boosted the tunnel-magnetoresistance (TMR) values to $\sim$ 608% [Ikeda *et al.*, 2008]. So, in order to further enhance resonance behaviors, hybrid triple-spacer magnetic junctions are considered to be good candidates. Additionally, double-magnetic tunnel junctions (DMTJ) of FIFIF type, one class of triple-spacer junctions, are also being considered for spin-torque transfer applications [Theodonis *et al.*,

2007] and reveal several potential resonance features. For these reasons these structures are a very important issue to be explored. The earliest work concerning DMTJ was performed by Zhang *et al.* establishing, at that time, the highest TMR value of $\sim 90\%$ [Zhang *et al.*, 1997]. Further, oscillations of tunnel conductance with the applied bias were predicted in these structures. This study was followed by Sheng *et al.*, who used the Landauer-Büttiker scattering approach to show that TMR can be enhanced in DMTJ, as compared to the single-barrier ones [Sheng *et al.*, 1999]. Later on, Jonkers explored a variety of hybrid structures with different elements, and a special focus was put on the NFNINFN (F≡Co) structure, because of its high TMR ratio [Jonkers, 2002]. In sequel, Mathon and Umerski predicted a TMR up to $\sim 1000\%$, studying a conceptually similar Fe/Au/MgO/Au/Fe triple-spacer junction in the Green's function formalism [Mathon and Umerski, 2005]. Even though the film preparation techniques have been significantly improved in the last decade, no such high TMR values were yet found experimentally. However, some resonant features were checked, as conductance bias oscillations [Nozaki *et al.*, 2006], but with small TMR ratios at room-temperature $\sim 136\%$ attributed to a thin Fe middle layer and formation of Fe-islands within it.

Therefore, this Section is dedicated to the study of FNINF and FNFNF structures exploring new coherent systems with special adjustment of either the geometric and electronic structure of the interlayers.

4.3.1 Model

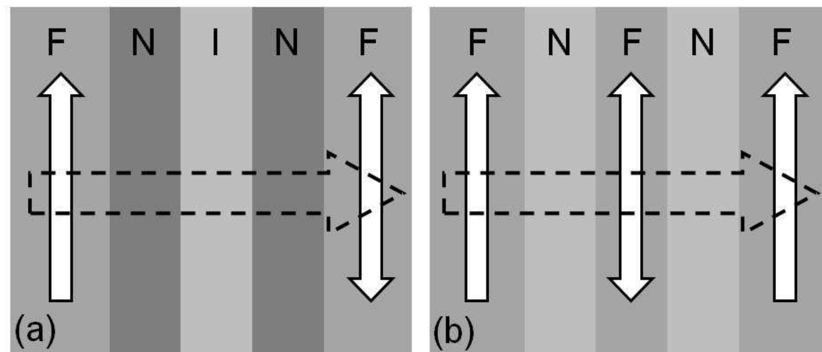

Figure 4.4: *Sketch of two types of double magnetic junctions: (a) FNINF and (b) FNFNF. Solid arrows are for polarizations of magnetic elements and dashed arrows for propagation of current.*

To this end, the previous single-band TB model is used to calculate the spin-

dependent transmission coefficient. The triple-spacer junction is composed, as in former junctions, by two semi-infinite leads, a source (S), and a drain (D), separated, in this case, by three finite elements: the first gate G_1; followed by the middle element (A), that can be an insulating barrier I (in the FNINF structure) or another ferromagnetic metal F (in a FNFNF junction); and the second gate G_2, each i-th element (below referred to as block) being a coherent stack of m_i atomic planes (Fig. 4.4). For simplicity, the calculations are restricted to symmetrical junctions ($G_1 = G_2$); though the generalization to non-symmetrical barriers is straightforward and will be presented in the next Section.

The crucial point is to describe properly the four interfaces: (S/G_1), (G_1/A), (A/G_2), and (G_2/D). The complete Hamiltonian is similar to the above one and all the interface and equations of motion are similar with the exception for an extra interface (A/G_2). The calculation of the transmission amplitude is feasible and results simply in: $T_{\sigma,\sigma'} = -2i(t_s t_g^2 t_a)(t_{sg} t_{ga}^2 t_{gd})^{-1} \sin q_{s,\mathbf{k}_\parallel,\sigma} / D_{\mathbf{k}_\parallel,\sigma,\sigma'}$ with the resonant denominator:

$$D_{\mathbf{k}_\parallel,\sigma,\sigma'} = u^a_{m_a}\left(u^g_{m_g}\delta^{m_g}_{\sigma,\sigma'} + \gamma_{s,\sigma}\gamma_{d,\sigma'}\right) - u^a_{m_a-1}\gamma_{ag}\left(2u^g_{m_g-1}\delta^{m_g}_{\sigma,\sigma'} + \gamma_{s,\sigma} + \gamma_{d,\sigma'}\right) + \\ + u^a_{m_a-2}\gamma^2_{ag}\left(2u^g_{m_g-2}\delta^{m_g}_{\sigma,\sigma'} + 1\right). \quad (4.8)$$

In this case, the interface parameters are: $\gamma_{s,\sigma} = t^2_{sg}(t_s t_g)^{-1}\exp(iq_{s,\mathbf{k}_\parallel,\sigma})$, $\gamma_{d,\sigma'} = t^2_{gd}(t_g t_d)^{-1} \exp(iq_{d,\mathbf{k}_\parallel,\sigma'})$ and $\gamma_{ag} = t^2_{ga}(t_g t_a)^{-1}$; once again, the polynomials $u^i_{m_i} \equiv u_{m_i}(x_{i,\mathbf{k}_\parallel,\sigma})$, and $\delta^{m_g}_{\sigma,\sigma'} = u^g_{m_g} - \left(\gamma_{s,\sigma} + \gamma_{d,\sigma'}\right) u^g_{m_g-1} + \gamma_{s,\sigma}\gamma_{d,\sigma'} u^g_{m_g-2}$. It is the denominator, Eq. (4.8), that allows for the possibility of resonances in the electronic transport with a great enhancement or suppression of MR ratio. The transmission amplitude, calculated at the Fermi energy $\varepsilon = \varepsilon_F$ (for zero temperature and voltage) defines the LB conductance with equal limits to the ones employed in the Sec. 4.2. In the present junctions, only two configurations are considered: P or AP, these are evident for FNINF, but for FNFNF is it necessary to define them. The experimental data for this type of junction, for example [Feng *et al.*, 2006], show that the maximum MR is achieved for AP configuration with the middle F layer magnetization antiparallel to both F leads, and the P configuration with all magnetizations parallel. Those will be used in what follows.

4.3.2 Results and Discussion

The numerical results for MR are presented in Figs. 4.5 and 4.6, for FNINF and FNFNF structures, respectively. In addition, the same spin-independent conductance is employed for the FNINF junction and $G_0 = 0.1e^2h^{-1}$ for FNFNF.

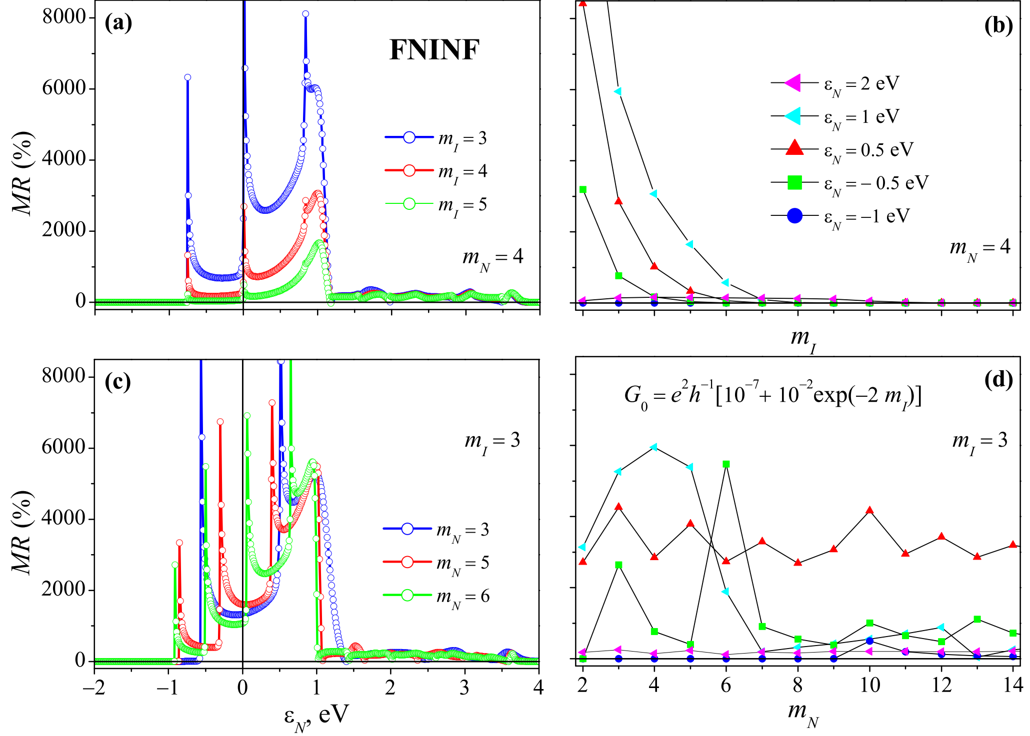

Figure 4.5: *[(a),(c)] The TMR dependencies on ε_N (at different widths m_I, m_N) show resonance enhancement, exceeding* $\sim 6000\%$*; (b) TMR vs m_I for specific resonant ε_N values (at $m_N = 4$); (d) TMR vs m_N for the same ε_N values.*

FNINF Junction MR is calculated as a function of the on-site atomic energy ε_N and number of atomic planes m_N in the N-spacers, and the atomic planes m_I in the I-barrier. This junction presents rather interesting resonant peaks in the MR dependence with ε_N reaching in some cases values $\sim 8000\%$. Fascinatingly, the number of *sizeable* MR peaks is related to the number of N-spacer atomic planes (m_N), as can be clearly seen in Figs. 4.5[(a),(c)]. The reason is the above mentioned discrete subband electronic spectrum in N, with the number of such subbands equal to m_N. As they cross the Fermi level huge G_P conductance peaks appear, caused by the fully symmetrical resonator structure formed in the junction. Otherwise, in the *AP* configuration, the broken symmetry in

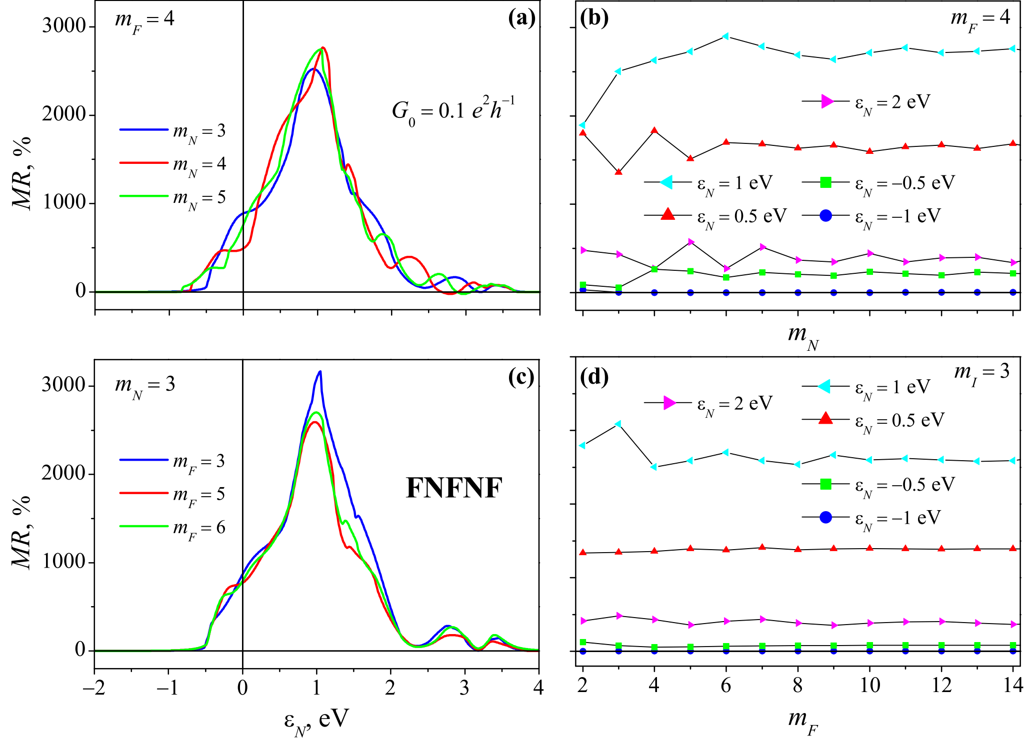

Figure 4.6: *[(a),(c)] The TMR dependencies on ε_N (at different widths m_I, m_N) show resonance enhancement, almost reaching* ~ 3000%*; (b) TMR vs m_N for various important ε_N values, different conduction regimes are explored; (d) TMR vs m_F for the same ε_N values.*

the leads prevents such sharp transmission resonances. These transport effects, obviously, lead to very pronounced MR peaks. Furthermore, the resonant conditions only appear for specific values of both m_N and ε_N, Fig. 4.5d, where MR shows a significant increase (when $m_N = 4$) for ε_N values specifically chosen to form the resonant MR peaks.

FNFNF Junction MR dependence is evaluated as a function of the on-site atomic energy ε_N and of the number m_N of atomic planes in the N-spacers, and m_F of the atomic planes in the middle F element. This junction does not present the preceding sharp peaks, even so, the MR as a function of the on-site atomic energy ε_N reaches $\sim 3000\%$ (for the indicated choices of G_0 term) at $\varepsilon_N \sim 0.9$ eV, and has a very similar behavior to the case of simple FNF junctions. Fascinatingly, MR shows (weak) oscillations in the m_F dependence, besides the above discussed oscillations with m_N.

In fact, the TMR oscillations in the m_F dependence are very important, and a similar behavior was already reported by Jonkers [Jonkers, 2002] as a result of a general quantum mechanism appearing in different junctions. Indeed, for Jonkers this behavior

of TMR is due to wave function oscillations inside the F layer. Obviously changing F width causes wave amplitude oscillations at the interfaces with the neighbor elements, this results in oscillations of the transmission amplitude. This mechanism affects both spin channels, and is obviously more noticeable if the atomic energy levels in the nearby elements are higher than those in the F element. Eventually, for sufficiently low atomic energies in those elements the oscillations disappear. This mechanism agrees well not only with the results for the given junction, but also with the ones that will be presented below. In the present theory, the discrete subband nature of the electronic spectrum dependent on m_F width can reinforce this mechanism.

4.4 Matrix Description of Multilayered Junctions

Multilayered junctions studied in the literature are often composed of periodic stacks of successive magnetic/non-magnetic bilayers, for example $[Co/Cu]_n$ and $[Fe/Cr]_n$ superlattices. The periodicity of these junctions strongly simplifies their theoretical description and makes it possible to account for additional factors, such as impurity scattering [Bauer, 1992], interface roughness [Asano *et al.*, 1993] and multiband electronic structures, [Shep *et al.*, 1995] and [Mathon, 1997]. More recently, non-periodic structures are being studied, for instance, Jonkers studied different types of 1D and 2D hybrid structures [Jonkers, 2002].

Even though actual theoretical analyses are well elaborated and, in principle, quite general, they do not explicitly apply for complex multilayered structures. Thus, the purpose of this section is to generalize the previous treatments using a simple theoretical formalism, developed in order to treat all possible numbers and types of layers in a multilayered system. The formalism also enables an easy manipulation of various parameters of the system, namely number of elements in a junction, layer thickness, atomic energy values, interface effects, etc., to reach magnetoresistive structures with MR responses well above $\sim 500\%$ as required for non-volatile logic-device applications.

Accordingly single-band TB matrix method is developed to calculate in a simple way the transmission and reflection coefficients for any multilayered system. Within the scope of ballistic LB conductance [Landauer, 1957] and [Büttiker, 1988], these readily define the spin-dependent transport and MR for real three-dimensional (3D) structures. In a way

this treatment is similar to previous works considering one-dimensional (1D) waveguide spin modulation where many parameters of the system were allowed to vary [Wang *et al.*, 2002]. But, the present 3D calculations, although more demanding than the simple 1D studies, have the advantage of considering multiple transversal modes and for that reason the results should be more realistic. In fact, common spintronic devices are normally 3D [Yuasa *et al.*, 2004], so it is relevant to understand whether the spin-dependent resonant modulation of the electronic transmission prevails for such dimensionality in order to find the best devices.

Below, explicit analytical formulae for single-, double and triple-spaced junctions are derived and compared with the ones derived before. Finally, numerical calculations for promising (non-periodic) complex magnetic junctions are presented. They admit variation of the junction parameters, such as the on-site energy of N-elements, in order to pass from metallic to insulating spacer regime, and also of the width of different elements to optimize MR. Taking advantage of modern epitaxial deposition techniques [Yuasa and Djayaprawira, 2007], these complex junctions could be important candidates to accommodate real memory devices.

It is important to mention that the restriction to singleband processes is a great simplification, compared with real multiband processes. However, trying to get a more general description of arbitrary junctions by including multiband effects, it might even obscure understanding of the system physics. For that reason, the simplicity of the present treatment is justified by its generality in describing any multilayered junction. For this reason, the results should be seen rather as an indication of potentially interesting spintronic structures than as accurate estimations of the MR values. Once a promising structure is found, a more cautious and advanced study could then be made with the use of common techniques, such as the density functional theory (DFT) or first principles calculations, in order to evaluate more rigorously the MR values. In fact, such advanced studies were not yet done for complex multilayered structures, due to its intrinsic complications.

4.4.1 Method

To start with, the multilayered system is modeled by a coupled stack of atomically perfect lattice elements, including two semi-infinite leads (the in-lead, labeled by $i = 0$, and out-lead, $i = n+1$) and n finite slabs, $i = 1, ..., n$, each consisting of m_i atomic planes,

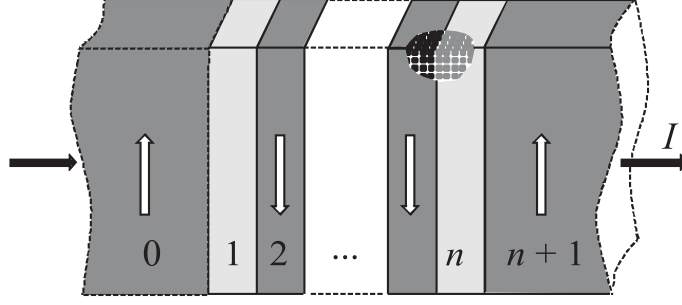

Figure 4.7: *Multiple-component system* $0, ..., n{+}1$*, the stripped view shows the atomically coherent internal structure of the layers and of the interfaces between them.*

Fig. 4.7. Likewise the former treatments, the corresponding TB Hamiltonian is:

$$\hat{H} = \sum_{\mathbf{n},\sigma} \left(\sum_{i=0}^{n+1} \hat{h}_{i,\mathbf{n},\sigma} + \sum_{i=1}^{n+1} \hat{h}_{i-1,i;\mathbf{n},\sigma} \right), \tag{4.9}$$

where ith element contributes with a sum of terms, $\hat{h}_{i,\mathbf{n},\sigma} = \hat{h}^{(0)}_{i,\mathbf{n},\sigma} + \hat{h}^{(\perp)}_{i,\mathbf{n},\sigma} + \hat{h}^{(\|)}_{i,\mathbf{n},\sigma}$, related to the on-site energy, the transversal and longitudinal nearest-neighbor hopping, and the interface between $i-1$ and i elements contributes with the interface hopping as follows:

$$\begin{aligned}
\hat{h}^{(0)}_{i,\mathbf{n},\sigma} &= \textstyle\sum_{l=l_i}^{l_{i+1}-1} \varepsilon_{i,\sigma} \hat{a}^{\dagger}_{l,\mathbf{n},\sigma} \hat{a}_{l,\mathbf{n},\sigma}, \\
\hat{h}^{(\|)}_{i,\mathbf{n},\sigma} &= t_i \textstyle\sum_{\delta} \left(\hat{a}^{\dagger}_{l,\mathbf{n},\sigma} \hat{a}_{l,\mathbf{n}+\delta,\sigma} + \text{h.c.} \right), \\
\hat{h}^{(\perp)}_{i,\mathbf{n},\sigma} &= t_i \textstyle\sum_{l=l_i}^{l_{i+1}-2} \left(\hat{a}^{\dagger}_{l,\mathbf{n},\sigma} a_{l+1,\mathbf{n},\sigma} + \text{h.c.} \right), \\
\hat{h}_{i-1,i;\mathbf{n},\sigma} &= t_{i-1,i} \left(\hat{a}^{\dagger}_{l_i-1,\mathbf{n},\sigma} \hat{a}_{l_i,\mathbf{n},\sigma} + \text{h.c.} \right).
\end{aligned}$$

Here $\hat{a}_{l,\mathbf{n},\sigma}$ is a Fermi operator for electron with spin σ on the 2D lattice site $\mathbf{n}$ in lth atomic plane, and δ are the in-plane nearest neighbor vectors. The parameter $\varepsilon_{i,\sigma} = \varepsilon_i + \sigma\Delta_i$ includes the (paramagnetic) on-site atomic energy ε_i and the Stoner splitting Δ_i (only non-zero if ith element is of F-type), and t_i and $t_{i-1,i}$ are the hopping amplitudes within ith element and at the $(i-1)/i$ interface respectively. The summation limits involve l_i, the index of first atomic plane of ith element (setting $l_0 = -\infty$, $l_1 = 1$, $l_{n+2} = \infty$). Then the in-plane symmetry of the problem suggests use of planar wave operators, and the related energies $\varepsilon_{i,\mathbf{k}_\|,\sigma} = \varepsilon_i + t_i \sum_\delta \exp(i\mathbf{k}_\| \cdot \delta)$. An important issue is to properly characterize the spin states of conduction electrons when passing through elements with different polarizations p_i (being ± 1 or 0). To this end, it is supposed that the absolute

(conserved) spin index $s =\uparrow,\downarrow$ (up, down) are referred to the leftmost F-element (with polarization 1), but seen as relative ones $\sigma = \pm$ (majority, minority) in other F-elements. Namely: $s =\uparrow$ relates in ith F-element to $\sigma_i = \mathrm{sign}(p_i)$, and $s =\downarrow$ to $\sigma_i = -\mathrm{sign}(p_i)$. Of course, spin indices are irrelevant in the non-polarized elements ($p_i = 0$).

The coherent electronic wave, eigenvector of the Hamiltonian, Eq. (4.9), with energy ε, conserved transversal momentum, and absolute spin s, is built from the planar wave states $|l, \mathbf{k}_\parallel, \sigma\rangle = a^\dagger_{l,\mathbf{k}_\parallel,\sigma}|0\rangle$:

$$|\Psi_{\mathbf{k}_\parallel,s}\rangle = \sum_{i=0}^{n+1}\sum_{l=l_i}^{l_{i+1}-1} c_{l,\mathbf{k}_\parallel,\sigma_i}|l, \mathbf{k}_\parallel, \sigma_i\rangle, \tag{4.10}$$

the values of σ_i being related to the particular magnetic configuration of the system. The c-amplitudes in the leads are suitably chosen as superpositions of incident, reflected and transmitted waves:

$$c_{l,\mathbf{k}_\parallel,s} = \begin{cases} \mathrm{e}^{iq_{0,\mathbf{k}_\parallel,s}l} + R\mathrm{e}^{-iq_{0,\mathbf{k}_\parallel,s}l} & \text{at} \quad -\infty < l \leq 0, \\ T\mathrm{e}^{iq_{n+1,\mathbf{k}_\parallel,\sigma}(l-l_{n+1})} & \text{at} \quad l_{n+1} \leq l < \infty, \end{cases}$$

where the lattice parameter is set to unit. The transmission and reflection amplitudes T and R generally depend on the transversal momentum $\mathbf{k}_\parallel$ at given energy (fixed to $\varepsilon = \varepsilon_\mathrm{F}$ at zero temperature), through the energy arguments $x_{i,\mathbf{k}_\parallel,\sigma_i} = (\varepsilon - \varepsilon_{i,\mathbf{k}_\parallel,\sigma_i})/(2t_i)$ for all i. The longitudinal momentum, $q_{i,\mathbf{k}_\parallel,\sigma_i} = \arccos x_{i,\mathbf{k}_\parallel,\sigma_i}$ must be real in both leads, $i = 0, n+1$ (but not in the intermediate slabs, $i = 1, \ldots, n$), and this defines a range K of $\mathbf{k}_\parallel$ values in the 2D Brillouin zone that implies the aforemention integration limits in the (zero temperature) LB conductance:

$$G = \frac{e^2}{h}\int_{a_{\sigma,\sigma'}}^{b_{\sigma,\sigma'}} du\rho(u)|T(\mathbf{k}_\parallel)|^2, \tag{4.11}$$

with $b_{\sigma,\sigma'} = \min\left\{2, \min\left[x_{0,\sigma}, x_{n+1,\sigma'}\right] + 1\right\}$ and $a_{\sigma,\sigma'} = \max\left\{-2, \max\left[x_{0,\sigma}, x_{n+1,\sigma'}\right] - 1\right\}$. The dependence of $|T(\mathbf{k}_\parallel)|^2$ on the input data $\mathbf{k}_\parallel$ and s in fact requires the knowledge of all intermediate amplitudes. Commonly, this problem is solved in the continuum approximation, as a set of differential boundary conditions on all interfaces [Slonczewski, 1989], giving rise to an infinite number of quantum-well states by the size confinement in each slab. In the present method, the electronic spectrum is rather different, consisting of

m_i subbands due to m_i atomic planes in the ith slab (Chap. **3**). Evidently, this should result in new transport properties.

In what follows, abbreviated notations: x_i and q_i for the energy parameters, and c_l and $|l\rangle$ for the planar wave amplitudes and states respectively (assuming $\mathbf{k}_\parallel$ and σ_i always well defined) are applied.

The important step of the method is the passage from planar wave amplitudes to planar wave spinors: $\Psi_l = (c_l,\, c_{l+1})^{\mathrm{T}}$, defined separately for each ith element in the range of $l_i \leq l \leq l_{i+1} - 2$. These spinor forms for the in- and out-leads are

$$\Psi_l = \begin{cases} \mathrm{e}^{iq_0(l-1)}\varphi_{q_0} + R\mathrm{e}^{-iq_0(l-1)}\varphi_{-q_0}, & l \leq 0 \\ T\mathrm{e}^{iq_{n+1}(l-l_{n+1})+1}\varphi_{q_{n+1}}, & l_{n+1} \leq l, \end{cases} \tag{4.12}$$

involving the *phase* spinor: $\varphi_q = \left(1,\, \mathrm{e}^{iq}\right)^{\mathrm{T}}$. Using the TB dynamics, simple algebraic relations between the planar wave spinors are readily obtained from the Hamiltonian, Eq. (4.9). First, the equations of motion for planar wave amplitudes c_l within ith slab follow from the coefficients at $|l\rangle$ in the SE (restricted to this slab), $\left(\hat{h}_{i,\mathbf{k}_\parallel,\sigma} - \varepsilon\right)|\Psi\rangle = 0$:

$$2x_i c_l = c_{l-1} + c_{l+1} \quad \text{for} \quad l_i + 2 \leq l \leq l_{i+1} - 2,$$

and are equivalent to the recursion relation for 2nd kind Chebyshev polynomials $u_l(x)$ [Abramowitz and Stegun, 1964]. This enables us to express these amplitudes as $c_l = f_i u_{l+1-l_i}(x_i)$, with the factor f_i to be defined from the interface conditions. In terms of spinors, the above equations of motion are presented as:

$$\Psi_l = \hat{U}_i \Psi_{l-1}, \qquad l_i + 2 \leq l \leq l_{i+1} - 2, \tag{4.13}$$

with the 2×2 transfer matrix $\hat{U}_i = (1 - \sigma_z)\, x_i + i\sigma_y$, including the Pauli matrices σ_i. Notice that $\varphi(\pm q_i)$ are eigenspinors of $\hat{U}_i$ with the eigenvalues $\exp(\pm iq_i)$, which automatically assures Eq. (4.13) for the in- and out-spinors, Eq. (4.12). Also, Eq. (4.13) can be presented in terms of $u_{l,i} \equiv u_l(x_i)$ (with $u_{-1,i} = 0$, $u_{0,i} = 1$, $u_{1,i} = 2x_i$, etc), then the recursion for the Chebyshev polynomials results in the product formula

$$\hat{U}_i{}^m = u_{m,i}\left(1-\sigma_z\right)/2 - u_{m-2,i}\left(1+\sigma_z\right)/2 + i\sigma_y u_{m-1,i} = \begin{pmatrix} -u_{m-2,i} & u_{m-1,i} \\ -u_{m-1,i} & u_{m,i} \end{pmatrix},$$

for any integer $m \geq 1$, that simplifies the relation between the two terminal spinors within ith slab: $\Psi_{l_{i+1}-2} = \hat{U}_i^{m_i-2}\Psi_{l_i}$. Next, the linkage between the $(i-1)/i$ interface amplitudes, c_{l_i-1} and c_{l_i}, is given by the interface equations of motion derived again from the interface SE, $\left(\hat{h}_{i-1,\mathbf{k}_\parallel,\sigma} + \hat{h}_{i-1,i;\mathbf{k}_\parallel,\sigma} + \hat{h}_{i,\mathbf{k}_\parallel,\sigma} - \varepsilon\right)|\Psi\rangle = 0$, restricted to $l_i - 2 \leq l \leq l_i + 1$. This results in:

$$\begin{aligned} 2x_{i-1}c_{l_i-1} &= c_{l_i-2} + \frac{t_{i-1,i}}{t_{i-1}}\, c_{l_i}, \\ 2x_i c_{l_i} &= \frac{t_{i-1,i}}{t_i}\, c_{l_i-1} + c_{l_i+1}. \end{aligned} \tag{4.14}$$

In the spinor notation, Eq. (4.14) can be presented as: $\Psi_{l_i} = \hat{I}_i\Psi_{l_i-2}$, relating the interface spinors through the important interface matrix:

$$\hat{I}_i = \frac{t_{i-1}}{t_{i-1,i}} \begin{pmatrix} -1 & 2x_{i-1} \\ -2x_i & 4x_i x_{i-1} - \eta_i \end{pmatrix}, \tag{4.15}$$

with $\eta_i = t_{i-1,i}^2\left(t_{i-1}t_i\right)^{-1}$. Now, combining Eqs. (4.13) and (4.14), the in- and out-spinors are related by:

$$\Psi_{l_{n+1}} = \hat{A}_n \Psi_{-1}, \tag{4.16}$$

with the total transfer matrix $\hat{A}_n = \hat{I}_{n+1}\prod_{i=n}^{1}\hat{U}_i^{m_i-2}\hat{I}_i$ (notice the reversed order of the matrix product). Inserting here Eq. (4.12), a matrix equation is obtained for the in- and out-amplitudes:

$$T\varphi_{q_{n+1}} = \hat{A}_n\left(\mathrm{e}^{-iq_0}\varphi_{q_0} + R\mathrm{e}^{iq_0}\varphi_{-q_0}\right), \tag{4.17}$$

explicitly given by:

$$T\begin{pmatrix} 1 \\ \mathrm{e}^{iq_{n+1}} \end{pmatrix} = \begin{pmatrix} A_n^{11} & A_n^{12} \\ A_n^{21} & A_n^{22} \end{pmatrix}\left[\begin{pmatrix} \mathrm{e}^{-iq_0} \\ 1 \end{pmatrix} + R\begin{pmatrix} \mathrm{e}^{iq_0} \\ 1 \end{pmatrix}\right],$$

and resulting in the transmission amplitude:

$$T = \frac{2i \sin q_0 \det(\hat{A}_n)}{e^{iq_{n+1}} (A_n^{11} e^{iq_0} + A_n^{12}) - (A_n^{21} e^{iq_0} + A_n^{22})}.$$

Using the general relation:

$$\det(\hat{C}_1 \hat{C}_2 \cdots \hat{C}_n) = \det(\hat{C}_1) \cdots \det(\hat{C}_n),$$

and the results:

$$\det(\hat{I}_i) = t_{i-1,i}/t_i \quad \text{and} \quad \det(\hat{U}_i^{m_i-2}) = -u_{m_i-4} u_{m_i-2} + u_{m_i-3} u_{m_i-3} = 1,$$

the transmission coefficient is readily given by: $T = -2i \sin q_0 / D_n$ with the denominator,

$$D_n = \frac{t_{n+1}}{t_0} \overline{\varphi}_{q_{n+1}}^{\dagger} \hat{A}_n \varphi_{-q_0}, \tag{4.18}$$

here $\overline{\varphi}_q^{\dagger} = \left(-e^{iq}, 1\right)$ is the co-spinor orthogonal to φ_q. Hence the transport problem for any composite system is reduced to calculation of the scalar product $\varphi_{q_{n+1}}^{\dagger} \hat{A}_n \varphi'_{q_0}$. Generally, it is a complex-valued function of the problem parameters ε_i, m_i, σ_i and can give rise to diverse resonance effects in LB formula, Eq. (4.13), with respect to all these parameters. The conductance through the multilayers, $G_{s,\{p\}}$, depends on particular magnetic state $\{p\} = (p_0, \ldots, p_{n+1})$ of the system, and magnetoconductance is written as the ratio between the maximum conductance with all F polarizations parallel, P, and the minimum conductance, usually (but not necessarily) resulting from antiparallel alignment of successive F polarizations, AP:

$$MR = \frac{\sum_s G_{s,\{P\}} + G_0}{\sum_s G_{s,\{AP\}} + G_0} - 1. \tag{4.19}$$

Here G_0 is a certain phenomenological spin-independent (multiband) contribution to conductance, present at each magnetic configuration, as discussed before. The definition of magnetic configurations can be exemplified for the FNIFINF junction (studied below): it has $\{p\} = (1, 0, 0, 1, 0, 0, 1)$ as a P configuration and $\{p\} = (1, 0, 0, -1, 0, 0, 1)$ as an AP configuration.

4.4.2 Analytical Results

To illustrate the general result of Eq. (4.18), lets begin from a generalized MTJ with n non-magnetic slabs between two F-leads. Concretizing it for $n = 1, 2, 3$, one can obtain useful analytic formulae for spin-dependent transmission in the single-, double-, and triple-spacer junctions. Basically, they only differ in the denominator D_n, accordingly to the growing complexity of the matrix $\hat{A}_n$.

Single spacer: In this case, the denominator, Eq. (4.18), is reduced to a binomial:

$$D_1 = d_1 \left(B^1_{m_1} - \gamma_2 B^1_{m_1-1} \right), \tag{4.20}$$

where the pre-factor $d_1 = t_1 t_2 (t_{01} t_{12})^{-1}$, $B^j_m = u_m - \gamma_j u_{m-1}$, and the interface factors are $\gamma_1 = \eta_1 \exp(iq_0)$, $\gamma_2 = \eta_2 \exp(iq_2)$ with η_j explained before.

Double spacer: The respective denominator contains a more complex binomial:

$$D_2 = d_2 \left(B^3_{m_2} B^1_{m_1} - \eta_2 B^3_{m_2-1} B^1_{m_1-1} \right), \tag{4.21}$$

with $d_2 = t_1 t_2 t_3 (t_{01} t_{12} t_{23})^{-1}$ and $\gamma_3 = \eta_3 \exp(iq_3)$.

Triple spacer: Yet more complicated structure of the denominator is:

$$D_3 = d_3 \left(B^{1,2}_{m_1,m_2} B^4_{m_3} - \eta_3 B^{1,2}_{m_1-1,m_2-1} B^4_{m_3-1} \right), \tag{4.22}$$

with $d_3 = t_1 t_2 t_3 t_4 (t_{01} t_{12} t_{23} t_{34})^{-1}$, $B^{j,j'}_{m,m'} = u_{m'} B^j_m - \eta_{j'} u_{m'-1} B^j_{m-1}$, and $\gamma_4 = \eta_4 \exp(iq_4)$.

These formulae are similar to the ones found for single-, double-, and triple-spacer junctions with use of simple boundary conditions. The accordance between the results of the two approaches validates the numerical studies on more evolved multilayers performed in the next Subsection.

4.4.3 Numerical Results and Discussion

In this Subsection, the following complex junctions are considered: FNIFINF, FINFNIF, FINFINF, and FIFNFIF. In numerical calculations, the parameters of the F elements are equal to the ones in the preceding Sections, and the atomic energy level of the I-slabs is set as $\varepsilon_I = 4.0$ eV (mimicking MgO barriers of ~ 1 eV), while the value ε_N is used for the N-slabs. The same hopping parameter is employed for all the elements and interfaces, as discussed before. The numbers of atomic planes of different elements are allowed to vary (for various ε_N values) in order to correlate the multilayer geometry with the physics involved in the spin-dependent transport and, in particular, to investigate what element width best improves TMR.

FNIFINF: The calculated TMR reveals sharp resonant peaks as a function of ε_N (Fig. 4.8a), reaching $\sim 4000\%$ (much larger than the maximum value realized, to date, in simple junctions [Ikeda *et al.*, 2008]). Moreover, the number of peaks is related to the number of N-spacer atomic planes, as can be clearly seen in Fig. 4.8a for $m_N = 4, 5, 6$ (thicker junctions have more peaks). Also, Fig. 4.8b shows that TMR decays exponentially with the number of I atomic planes (as expected). Further, oscillations as a function of m_N and m_F are found (Fig. 4.8[(c),(d)]), as expected for perfect magnetic junctions.

FINFNIF: Though this junction does not present the previous sharp resonant peaks, it still displays a significant enhancement of TMR in the crossover from metallic to insulator atomic energies of the N- elements (*shallow band regime*, SBR) reaching $\sim 3000\%$ (for the indicated choices of G_0 term), Fig. 4.9a. This effect is similar to the case of simple FNF junctions studied before. Further on, TMR decays with m_I, Fig. 4.9b, and in some cases oscillates with m_F and m_N, Fig. 4.9[(c),(d)]. Even so, the oscillations are generally weaker as compared with the preceding system. In particular the oscillations with m_F almost disappear for $|\varepsilon_N| > 1$ eV.

FINFINF: This structure is studied to explore the possible effects of its asymmetry on TMR. Nevertheless, the TMR behavior resembles much the last junction with the SBR peak slightly deviated towards higher ε_N, all the same, attaining $\sim 3000\%$, Fig. 4.10a. Also, the TMR dependence with m_I, Fig. 4.10b, m_F, Fig. 4.10c, and m_N, Fig. 4.10d, are

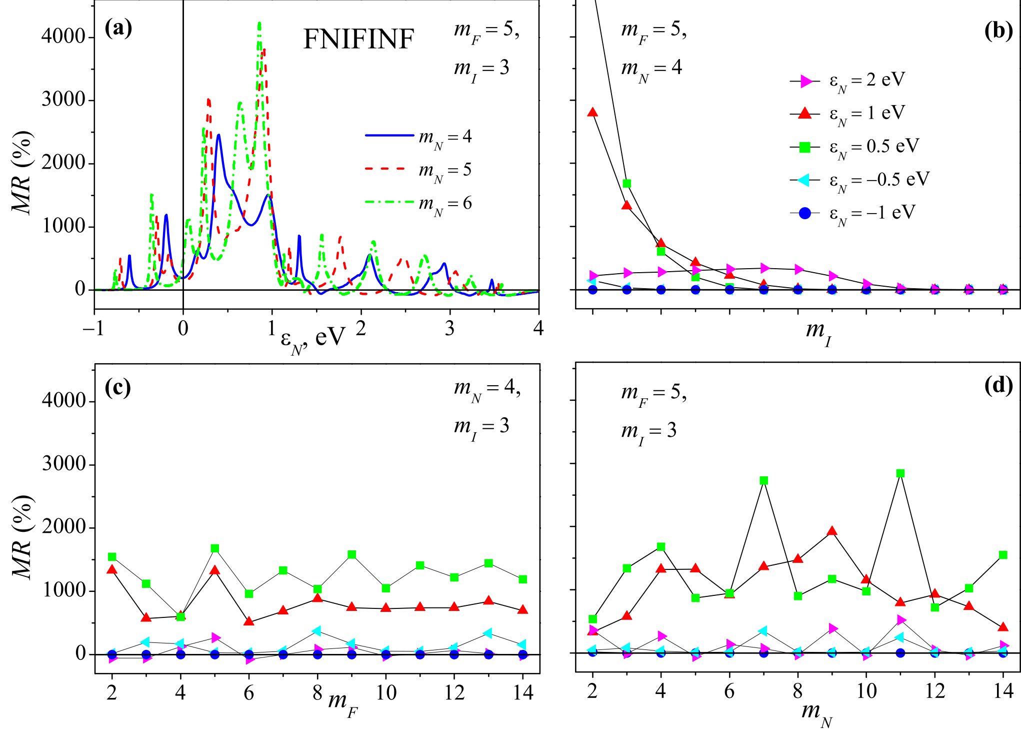

Figure 4.8: *Magnetoresistance of a FNIFINF junction (with $\varepsilon_I = 4.0$ eV) as a function of different parameters: (a) on-site energy, ε_N, for $m_N = 4, 5, 6$ (shows a series of sharp peaks reaching $\sim 4000\%$); (b) TMR vs m_I for $\varepsilon_N = -1, -0.5, 0.5, 1, 2$ eV; (c) TMR vs m_F for the same ε_N values; (d) TMR vs m_N for the same ε_N values.*

similar to the preceding one. This indicates that asymmetry of the system geometry does not significantly affect the TMR behavior.

FIFNFIF: The TMR performance of this system is rather distinct from others, realizing nearly 15000% at two different peaks for $\varepsilon_N \sim 0.6, 4.2$ eV, Fig. 4.11a. Such TMR values are more than four times higher than the above maximum values. In addition, TMR as a function of m_I, Fig. 4.11b, does not follow the typical decaying behavior found in the previous junctions. Furthermore, its dependence with m_F presents strong oscillations, Fig. 4.11c, which can go (for some ε_N) from $\sim 18000\%$ to nearly zero. Interestingly TMR versus m_N does not show typical oscillations found in other devices.

Summary for composite junctions: The above examples show that a great variety of results can be obtained in multilayered magnetic junctions composed from the same elements (even at same number of them) when changing the sequence of *letters* in a formula

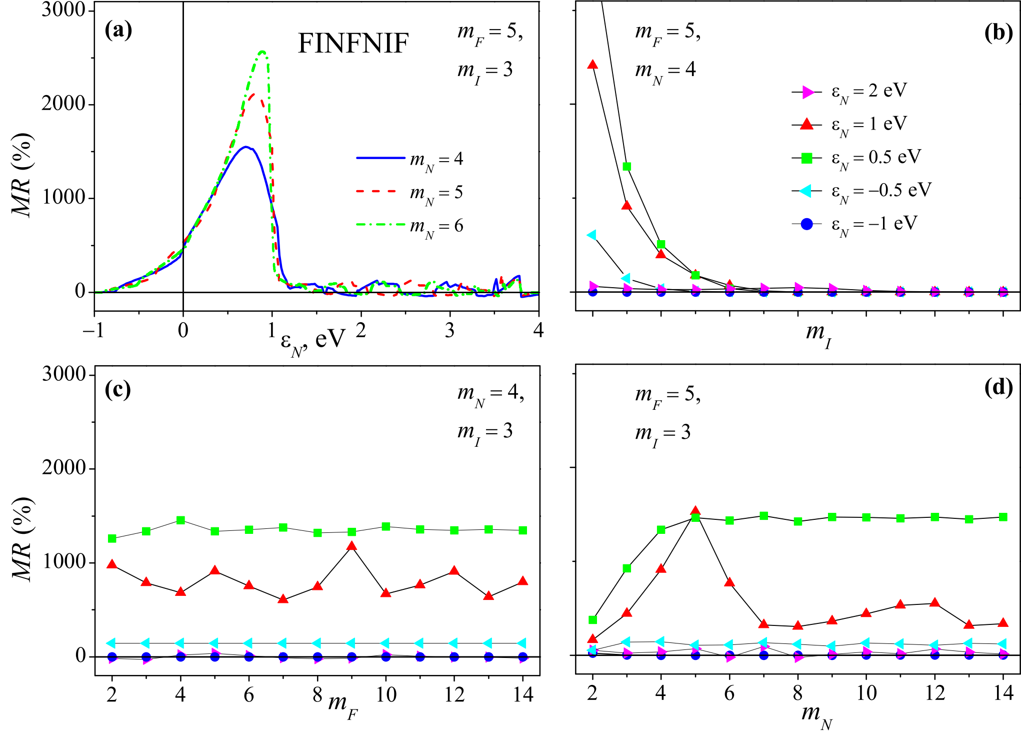

Figure 4.9: *MMagnetoresistance of a FINFNIF junction with the same definition of sets of parameters and panels as in Fig. 4.8 differs mainly from that case by the presence of single broad peak reaching* $\sim 3000\%$ *in function of* ε_N*.*

word (as FINFNIF to FIFNFIF). The possibility of analysing the changes from monotonic to oscillatory behavior, changing the number of oscillations and their amplitudes, etc., the analytical description shows its validity for recognition and design of optimum functional regimes of advanced magnetoresistive devices. It is worth mentioning that important variations similar to those reported here were found in the above-cited 1D studies [Wang *et al.*, 2002].

At least, it is important to note that a consistent treatment of TMR dependence on the thickness of particular ferromagnetic layers would benefit from using a more evolved Hubbard model or even a full spin-density functional theory, where the discrete local states could induce relevant quantum magnetic effects as, for instance, dependence of the Stoner splitting on the thickness of F-layers, obviously not considered in the present model.

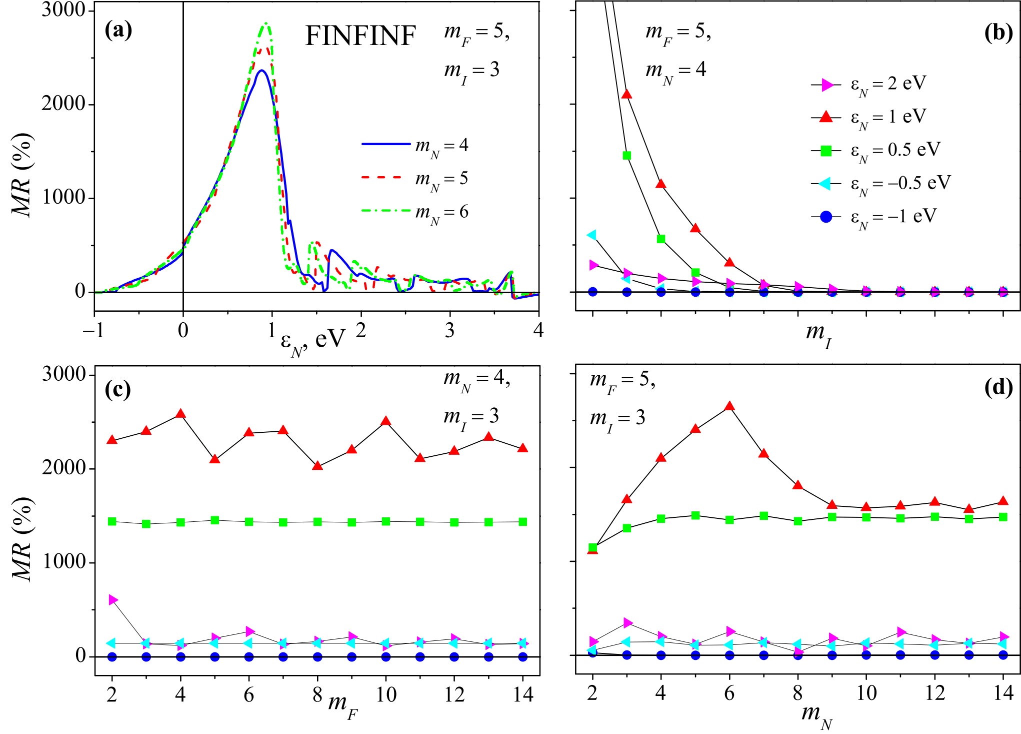

Figure 4.10: *Magnetoresistance of a FINFINF junction with the same definition of sets of parameters and panels as in Figs. 4.8 and 4.9.*

4.5 Conclusions

In this Chapter various types of junctions where analyzed: FINF, FNFNF, FN-INF, and more complex ones FNIFINF, FINFNIF, FINFINF, and FIFNFIF. All showed high TMR efficiencies related to a proper adjustment of the on-site energy in N-spacers, suggesting, as in Chap. **3**, a search of new materials to realize the *shallow band regime*, as semiconductors and semimetals (provided a reasonable lattice matching for epitaxial growth exists).

In order to describe the spin-dependent transport in general multilayered structures a matrix method was developed and tested in the above mentioned complex junctions, FNIFINF, FINFNIF, FINFINF, and FIFNFIF. In particular, the calculation for the latter junction revealed a very high TMR performance that could be sought in future works. Probably a very interesting experimental realization of this junction would be a Fe/MgO/Fe/Cr/Fe/MgO/Fe structure, regarding that a perfect lattice matching and epitaxial growth is fundamental for this coherent effects. It is likely that the developed method may be a useful tool in the design of more efficient spintronics devices.

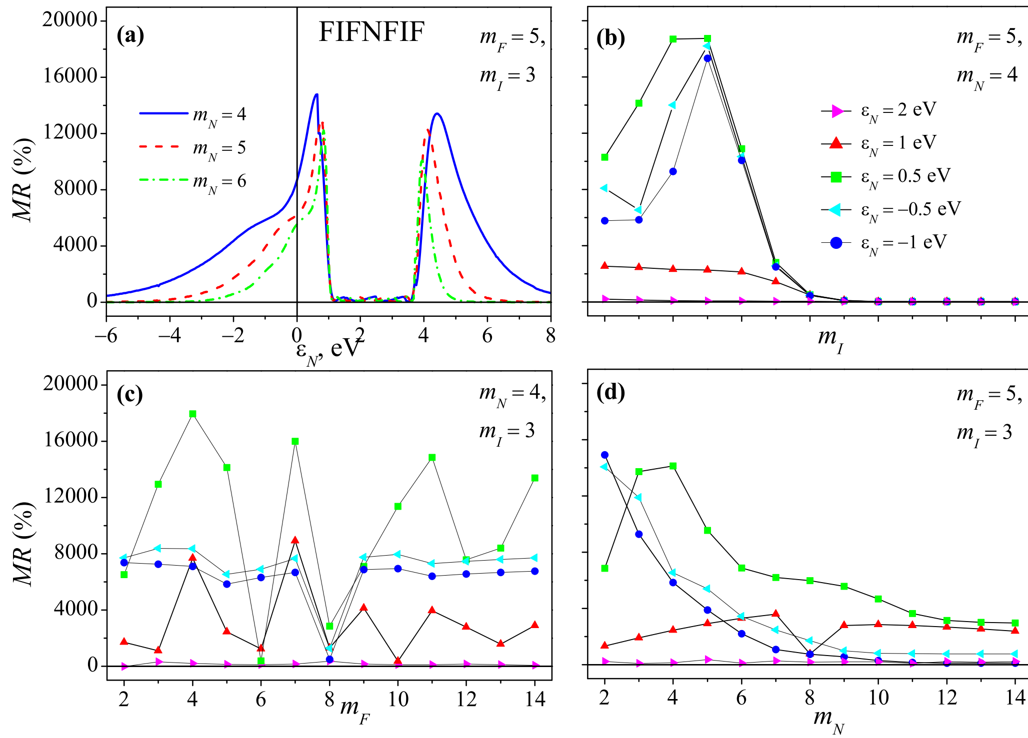

Figure 4.11: *Magnetoresistance of a FIFNFIF junction with the same definition of sets of parameters and panels as in Figs. 4.8, 4.9, and 4.10 shows two prominent peaks reaching* $\sim 15000\%$ *in function of* ε_N.

Chapter 5

Diluted metal-insulator granular layers: Theory and Experiment

5.1 Introduction

The organization of this Chapter is as follows. In Sec. 5.2 theoretical analysis of electronic transport in nanostructured granular films is undertaken. Further, Sec. 5.3 studies the magnetic and transport properties of the diluted metal/insulator $Co_{80}Fe_{20}/Al_2O_3$ granular multilayers. The next Section, Sec. 5.4, considers new resistive switching properties found in these materials with low nominal thickness of magnetic granular layer. Finally, in Sec. 5.5 some conclusions focusing on the found results are presented.

5.2 Theoretical description of transport processes

Transport phenomena in nanostructured granular films is still a great challenge and presently various works are addressing such problem, [Tran *et al.*, 2008 and Dorn *et al.*, 2004], just to mention two. For an extended review of this topic the interested reader is referred to Ref. [Beloborodov *et al.*, 2007].

The main reason is that granular systems reveal certain characteristics which cannot be obtained neither in the classical transport regimes (in metallic, electrolyte, or gas discharge conduction) nor in the hopping regime (in doped semiconductors or in common tunnel junctions). Their specifics is mainly determined by the drastic difference between the characteristic time of an individual tunneling event ($\sim \hbar/\varepsilon_F \sim 10^{-15}$ s) and the interval

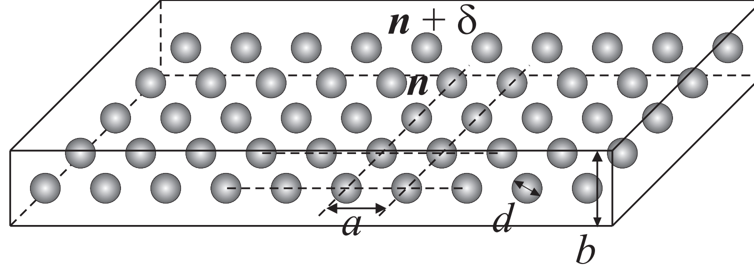

Figure 5.1: *Square lattice of metallic granules in the insulating matrix.*

between such events on the same granule $\sim e/(jd^2) \sim 10^{-3}$ s, at typical current density $j \sim 10^{-3}$ A/cm^2 and granule diameter $d \sim 5.0$ nm. Other important moments are the sizeable Coulomb charging energy $E_c \sim e^2/(\varepsilon_{\rm eff} d)$ (typically ~ 10 meV) and the fact that the tunneling rates across the layer may be even several orders of magnitude slower than along it. The interplay of all these factors leads to unusual macroscopic effects, thus, a peculiar slow relaxation of electric charge was recently discovered in experiments on tunnel conduction through granular layers and granular films [Schaadt *et al.*, 1999 and Kakazei *et al.*, 2000].

For theoretical description of such processes a model is developed where a single layer of identical spherical particles is located in sites of a simple square lattice, with three possible charging states ($\pm$, or 0) of a granule and three kinetic processes (creation or recombination of a $\pm$ pair, and charge translation) between neighbor granules. Even such simple model reveals a variety of possible dynamical and thermodynamical regimes, to be presented below.

5.2.1 Charging states and kinetic processes

A system of identical spherical metallic nanogranules with diameter d, located in sites of simple square lattice of period a within a layer of thickness $b \sim a$ of insulating host with a dielectric constant ε (Fig. 5.1) is considered. In the charge transfer processes, each granule can bear different numbers σ of electrons in excess (or deficit) to the constant number of positive ions and the resulting excess charge σe defines a Coulomb charging energy $\sim \sigma^2 E_c$. At not too high temperatures, $k_{\rm B}T \lesssim E_c$, the consideration can be limited only to the ground neutral state $\sigma = 0$ and single charged states $\sigma = \pm 1$. Actually, for low metal contents (well separated, small grains), E_c reaches $\sim 10-50$ meV, so this approach can be reasonable even above room temperature. For a three-dimensional (3D) granular

array with constant ratio between the mean spacing s and granule diameter d, E_c was given in the classic paper by Sheng and Abeles [Sheng and Abeles, 1972] in the form $E_c = e^2 f(s/d)/(\varepsilon d)$, where the dimensionless function $f(z) = 1/(1+1/2z)$. Otherwise, the mutual dielectric response of 3D insulating host ($\varepsilon_h = \varepsilon$) with volume fraction $f < 1$ of metallic particles ($\varepsilon_m \to \infty$) can be characterized by an effective value $\varepsilon_{\text{eff}} = \varepsilon/(1-f)$.

For the planar lattice of granules, such effective constant can be estimated, summing the own energy $e^2/\varepsilon d$ of a charged granule at a given site and the energy of its interaction with electric dipolar moments $\approx (e/\varepsilon_{\text{eff}})(d/2n)^3\mathbf{n}$, induced in granules on sites $\mathbf{n} = a(n_1, n_2)$:

$$E_c = \frac{e^2}{d}\left[\frac{1}{\varepsilon} - \frac{\alpha}{\varepsilon_{\text{eff}}}\left(\frac{d}{a}\right)^4\right] = \frac{e^2}{\varepsilon_{\text{eff}} d}. \tag{5.1}$$

Here the constant $\alpha = \frac{1}{8}\sum_{n\neq 0} n^{-4} \approx 0.92$, and the resulting $\varepsilon_{\text{eff}} = \varepsilon\left[1+\alpha(d/a)^4\right]$. However, Eq. (5.1) may underestimate considerably the most important screening from nearest neighbor granules at $d \to a$, and in what follows the composite of insulating matrix and metallic granules is generally characterized by a certain $\varepsilon_{\text{eff}} = e^2/dE_c \gg \varepsilon$.

Following the approach proposed in Ref. [Kakazei *et al.*, 2000], the microscopic states of the system are classified attributing the charging variable $\sigma_{\mathbf{n}}$ with values ± 1 or 0 to each site $\mathbf{n}$ and then considering three types of kinetic processes between two neighbor granules $\mathbf{n}$ and $\mathbf{n}+\Delta$ (Fig. 5.2):

1. *Electron hopping from neutral* $\mathbf{n}$ *to neutral* $\mathbf{n}+\Delta$, creating a pair of oppositely charged granules: $(\sigma_{\mathbf{n}} = 0, \sigma_{\mathbf{n}+\Delta} = 0) \to (\sigma_{\mathbf{n}} = +1, \sigma_{\mathbf{n}+\Delta} = -1)$; only this process was included in the Sheng and Abeles' theory;

2. *Hopping of an extra electron or hole from* $\mathbf{n}$ *to neutral* $\mathbf{n}+\Delta$, that is charge transfer: $(\sigma_{\mathbf{n}} = \pm 1, \sigma_{\mathbf{n}+\Delta} = 0) \to (\sigma_{\mathbf{n}} = 0, \sigma_{\mathbf{n}+\Delta} = \pm 1)$;

3. *Recombination of a electron-hole pair*, the inverse to the process 1.: $(\sigma_{\mathbf{n}} = +1, \sigma_{\mathbf{n}+\Delta} = -1) \to (\sigma_{\mathbf{n}} = 0, \sigma_{\mathbf{n}+\Delta} = 0)$.

Note that all the processes 1) to 3) are conserving the total system charge $Q = \sum_{\mathbf{n}} \sigma_{\mathbf{n}}$, hence the possibility for charge accumulation or relaxation only appears due to the current leads. A typical configuration for current-in-plane (CIP) tunneling conduction includes two macroscopic metallic electrodes on top of the granular layer, forming the contact areas (CA) where the current is being distributed from the electrodes into granules

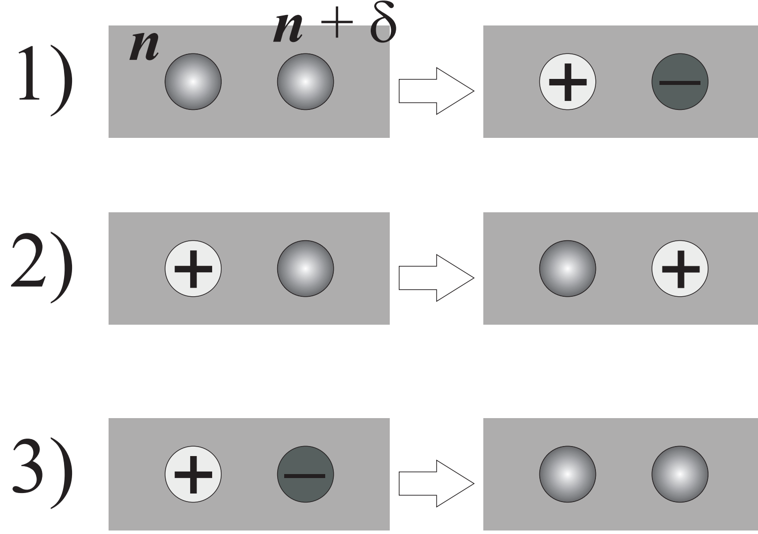

Figure 5.2: *Kinetic processes in a granular layer.*

through an insulating spacer of thickness b', and a free area (FA) where the current propagates between the contacts (Fig. 5.3). To begin with, the simpler case of FA is considered while the specific analysis for CA with an account for screening effects by metallic contacts will be given later in Sec. 5.2.4.

The respective transition rates $q_{\mathbf{n},\Delta}^{(i)}$ for ith process are determined by the instantaneous charging states of two relevant granules and by the local electric field $\mathbf{F_n}$ and temperature T, accordingly to the expressions:

$$\begin{aligned} q_{\mathbf{n},\Delta}^{(1)} &= \left(1-\sigma_{\mathbf{n}}^2\right)\left(1-\sigma_{\mathbf{n}+\Delta}^2\right)\varphi\left(e\mathbf{F_n}\cdot\Delta+E_c\right) \\ q_{\mathbf{n},\Delta}^{(2)} &= \sigma_{\mathbf{n}}^2\left(1-\sigma_{\mathbf{n}+\Delta}^2\right)\varphi\left(-e\sigma_{\mathbf{n}}\mathbf{F_n}\cdot\Delta\right) \\ q_{\mathbf{n},\Delta}^{(3)} &= \frac{1}{2}\sigma_{\mathbf{n}}\sigma_{\mathbf{n}+\Delta}\left(\sigma_{\mathbf{n}}\sigma_{\mathbf{n}+\Delta}-1\right)\varphi\left(e\sigma_{\mathbf{n}+\Delta}\mathbf{F_n}\cdot\Delta-E_c\right). \end{aligned} \tag{5.2}$$

Thus the charging energy, E_c, is positive for pair creation, zero for transport, and negative, $-E_c$, for recombination processes. The function $\varphi(E)=\omega N_{\mathrm{F}}E/[\exp(\beta E)-1]$ expresses the total probability, at given inverse temperature $\beta=(k_{\mathrm{B}}T)^{-1}$, for electron transition between granules with Fermi density of states N_{F} and Fermi levels differing by E. The hopping frequency $\omega=\omega_a\exp(-2\chi s)$ involves the *attempt frequency*, $\omega_a\sim E_{\mathrm{F}}/\hbar$, the inverse tunneling length χ (typically ~ 10 nm^{-1}), and the inter-granule spacing $s=a-d$. Local electric field $\mathbf{F_n}$ on $\mathbf{n}$th site consists of the external applied field $\mathbf{A}$ and the Coulomb

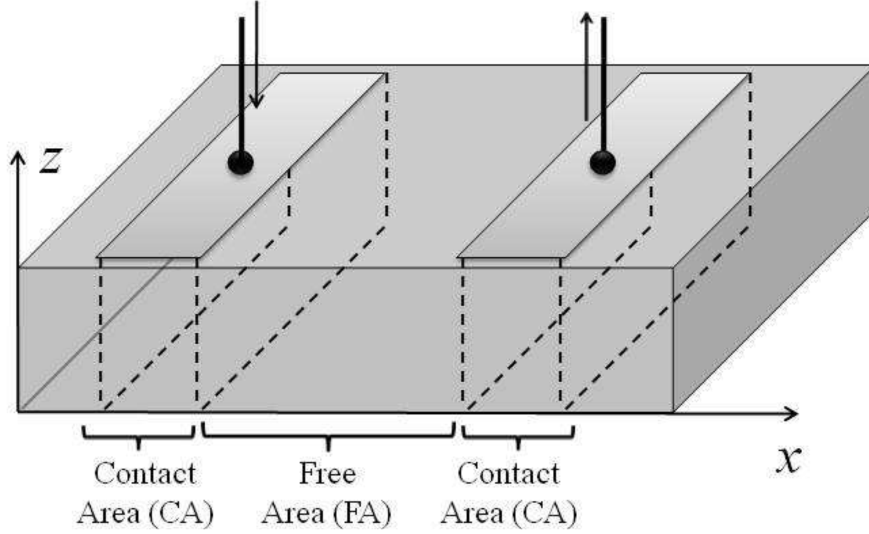

Figure 5.3: *CIP conduction geometry.*

field $\mathbf{C_n}$ due to all other charges in the system:

$$\mathbf{C_n} = \frac{e}{\varepsilon_{\text{eff}}} \sum_{\mathbf{n'} \neq \mathbf{n}} \sigma_{\mathbf{n'}} \frac{\mathbf{n'} - \mathbf{n}}{|\mathbf{n'} - \mathbf{n}|^3}. \tag{5.3}$$

A suitable approximation is achieved with passing from discrete-valued functions $\sigma_{\mathbf{n}}$ of discrete argument $\mathbf{n} = a(n_1, n_2)$ to their continuous-valued mean-field (MF) equivalents $\sigma_{\mathbf{r}} = \langle \sigma_{\mathbf{n}} \rangle_{\mathbf{r}}$ (mean charge density) and $\rho_{\mathbf{r}} = \langle \sigma_{\mathbf{n}}^2 \rangle_{\mathbf{r}}$ (mean charge carrier density). These densities are obtained by averaging over a wide enough area (that is, great compared to the lattice period but small compared to the size of the entire system or its parts) around *any* point $\mathbf{r}$ in the plane (for simplicity, the position index at averages $\langle \rangle_{\mathbf{r}}$ is dropped in what follows). This also implies passing to a smooth local field:

$$\mathbf{F_r} = \mathbf{A} + \frac{e}{\varepsilon_{\text{eff}} a^2} \int \sigma(\mathbf{r'}) \frac{\mathbf{r'} - \mathbf{r}}{|\mathbf{r'} - \mathbf{r}|^3} d\mathbf{r'}. \tag{5.4}$$

and to the averaged transition rates $q_{\mathbf{r},\Delta}^{(i)} = \left\langle q_{\mathbf{n},\Delta}^{(i)} \right\rangle$ and $p_{\mathbf{r},\Delta}^{(i)} = \left\langle \sigma_{\mathbf{n}} q_{\mathbf{n},\Delta}^{(i)} \right\rangle$. These rates fully define the temporal evolution of mean densities:

$$\dot{\sigma}_{\mathbf{r}} = \sum_{\Delta} \left[q_{\mathbf{r},\Delta}^{(1)} - q_{\mathbf{r}+\Delta,-\Delta}^{(1)} - p_{\mathbf{r},\Delta}^{(2)} + p_{\mathbf{r}+\Delta,-\Delta}^{(2)} - p_{\mathbf{r},\Delta}^{(3)} \right], \tag{5.5}$$

$$\dot{\rho}_{\mathbf{r}} = \sum_{\Delta} \left[q^{(1)}_{\mathbf{r},\Delta} + q^{(1)}_{\mathbf{r}+\Delta,-\Delta} - q^{(2)}_{\mathbf{r},\Delta} + q^{(2)}_{\mathbf{r}+\Delta,-\Delta} - q^{(3)}_{\mathbf{r},\Delta} \right]. \tag{5.6}$$

The set of Eqs. (5.2)-(5.6) provides a continuous description of the considered system, once a proper averaging procedure is established.

5.2.2 Mean-field densities in equilibrium

The above defined averages are performed in the simplest assumption of no correlations between different sites: $\langle f_{\mathbf{n}} g_{\mathbf{n}'} \rangle = \langle f_{\mathbf{n}} \rangle \langle g_{\mathbf{n}'} \rangle$, $\mathbf{n}' \neq \mathbf{n}$, and using the evident rules: $\langle \sigma^{2k+1}_{\mathbf{n}} \rangle = \sigma_{\mathbf{r}}$, $\langle \sigma^{2k}_{\mathbf{n}} \rangle = \rho_{\mathbf{r}}$. The resulting averaged rates are:

$$\begin{aligned}
q^{(1)}_{\mathbf{r},\Delta} &= \sigma^0_{\mathbf{r}} \sigma^0_{\mathbf{r}+\Delta} \varphi\left(e\mathbf{F}_{\mathbf{r}} \cdot \Delta + E_c\right), \\
q^{(2)}_{\mathbf{r},\Delta} &= \sigma^0_{\mathbf{r}+\Delta} \left[\sigma^+_{\mathbf{r}} \varphi\left(-e\mathbf{F}_{\mathbf{r}} \cdot \Delta\right) + \sigma^-_{\mathbf{r}} \varphi\left(e\mathbf{F}_{\mathbf{r}} \cdot \Delta\right)\right], \\
p^{(2)}_{\mathbf{r},\Delta} &= \sigma^0_{\mathbf{r}+\Delta} \left[\sigma^+_{\mathbf{r}} \varphi\left(-e\mathbf{F}_{\mathbf{r}} \cdot \Delta\right) - \sigma^-_{\mathbf{r}} \varphi\left(e\mathbf{F}_{\mathbf{r}} \cdot \Delta\right)\right], \\
q^{(3)}_{\mathbf{r},\Delta} &= \left[\sigma^+_{\mathbf{r}} \sigma^-_{\mathbf{r}+\Delta} \varphi\left(-e\mathbf{F}_{\mathbf{r}} \cdot \Delta - E_c\right) + \sigma^-_{\mathbf{r}} \sigma^+_{\mathbf{r}+\Delta} \varphi\left(e\mathbf{F}_{\mathbf{r}} \cdot \Delta - E_c\right)\right], \\
p^{(3)}_{\mathbf{r},\Delta} &= \left[\sigma^+_{\mathbf{r}} \sigma^-_{\mathbf{r}+\Delta} \varphi\left(-e\mathbf{F}_{\mathbf{r}} \cdot \Delta - E_c\right) - \sigma^-_{\mathbf{r}} \sigma^+_{\mathbf{r}+\Delta} \varphi\left(e\mathbf{F}_{\mathbf{r}} \cdot \Delta - E_c\right)\right],
\end{aligned} \tag{5.7}$$

where the mean occupation numbers for each charging state $\sigma^{\pm}_{\mathbf{r}} = (\rho_{\mathbf{r}} \pm \sigma_{\mathbf{r}})/2$ and $\sigma^0_{\mathbf{r}} = 1 - \rho_{\mathbf{r}}$ satisfy the normalization condition: $\sum_i \sigma^i_{\mathbf{r}} = 1$.

In a similar way to Eq. (5.5), the vector of average current density $\mathbf{j}_{\mathbf{n}}$ at $\mathbf{n}$th site is expressed as:

$$\mathbf{j}_{\mathbf{n}} = \frac{e}{a^2 b} \sum_{\Delta} \Delta \left[-q^{(1)}_{\mathbf{n},\Delta} + q^{(1)}_{\mathbf{n}+\Delta,-\Delta} + p^{(2)}_{\mathbf{n},\Delta} - p^{(2)}_{\mathbf{n}+\Delta,-\Delta} + p^{(3)}_{\mathbf{n},\Delta} \right], \tag{5.8}$$

and then its MF extension $\mathbf{j}_{\mathbf{r}}$ is obtained by simple replacing $\mathbf{n}$ by $\mathbf{r}$ in the arguments of $q^{(i)}$ and $p^{(i)}$. Expanding these continuous functions in powers of $|\Delta| = a$, it is concluded that Eq. (5.5) gets reduced to usual continuity equation:

$$\dot{\sigma}_{\mathbf{r}} = -\frac{a^2 b}{e} \nabla_2 \cdot \mathbf{j}_{\mathbf{r}}, \tag{5.9}$$

with the two dimensional (2D) nabla: $\nabla_2 = (\partial_x, \partial_y)$. First, the analysis of Eqs. (5.5)-(5.9) is done for the simplest situation of thermal equilibrium in absence of electric field, $\mathbf{F}_{\mathbf{r}} \equiv 0$. Then Eq. (5.5) turns into evident identity: $\sigma_{\mathbf{r}} \equiv 0$, that means zero charge density, and

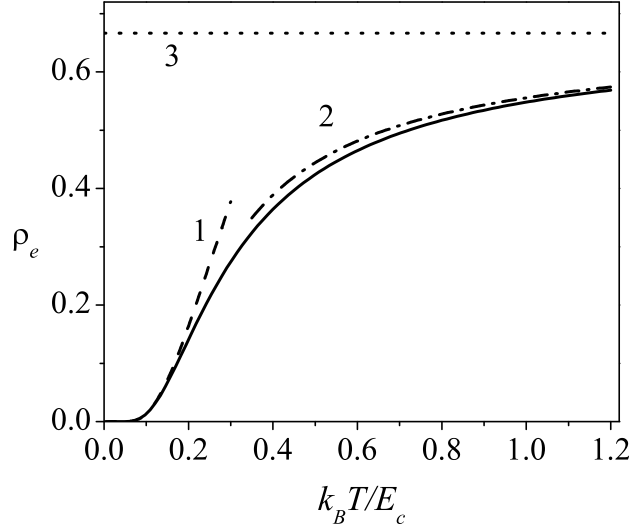

Figure 5.4: *Equilibrium density ρ_0 of charge carriers in function of temperature (solid line). The curve* 1 *(dashed line) corresponds to the low temperature asymptotics $\rho_0 \approx 2\exp -E_c/2k_BT$, and the curve 2 (dash-dotted line) to the high temperature asymptotics $\rho_0 \approx \rho_\infty - E_c/9k_BT$, converging to the limit $\rho_\infty = 2/3$ (dotted line).*

Eq. (5.8) yields in zero current density: $\mathbf{j_r} \equiv 0$, while Eq. (5.6) provides a finite and constant value of charge carrier density:

$$\rho_{\mathbf{r}} \equiv \rho_e = \frac{2}{2 + \exp(\beta E_c/2)}. \tag{5.10}$$

At low temperatures, $\beta E_c \gg 1$, this value is exponentially small: $\rho_e \approx 2\exp(-\beta E_c/2)$, and for high temperatures, $\beta E_c \ll 1$, it tends as $\rho_e \approx \rho_\infty - \beta E_c/9$ to the limit $\rho_\infty = 2/3$, corresponding to equipartition between all three fractions σ^i (Fig. 5.4).

In presence of electric fields $\mathbf{F_r} \neq 0$, the local equilibrium should be perturbed and the system should generate current and can generally accumulate charge. Then, from Eq. (5.6), the charge density $\sigma_{\mathbf{r}}$ is related to the carrier density $\rho_{\mathbf{r}}$ as:

$$\sigma_{\mathbf{r}}^2 = \frac{(\rho_{\mathbf{r}} - \rho_e)(\rho_{\mathbf{r}} + \rho_e - 2\rho_e\rho_{\mathbf{r}})}{(1-\rho_e)^2}, \tag{5.11}$$

describing the increase of charge density when going away from equilibrium. As seen from Fig. 5.5, for not too high temperatures $T \lesssim E_c/k_{\mathrm{B}}$ where the neglect of multiple charged states is justified, this dependence is reasonably close to the simplest low-temperature

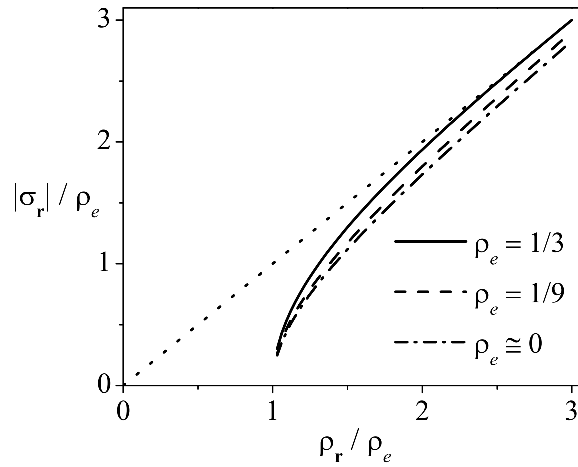

Figure 5.5: *The charge density σ in function of the carrier density ρ for different temperatures, corresponding to different thermal equilibrium values ρ_e.*

form:

$$\sigma \approx \sqrt{\rho^2 - \rho_e^2}, \tag{5.12}$$

that will be practically used in what follows.

Now it is possible to pass to the out-of-equilibrium situations, beginning from a simpler case of dc current flowing through the FA.

5.2.3 Steady state conduction in FA

In presence of (generally non-uniform) fields $\mathbf{F}_\mathbf{r}$ and densities $\sigma_\mathbf{r}$, $\rho_\mathbf{r}$, Eq. (5.8) is expanded up to 1st order terms in $|\Delta| = a$ and obtain the local current density is obtained as a sum of two contributions, field-driven and diffusive:

$$\mathbf{j}_\mathbf{r} = \mathbf{j}_\mathbf{r}^{\text{field}} + \mathbf{j}_\mathbf{r}^{\text{dif}} = g\left(\rho_\mathbf{r}\right)\mathbf{F}_\mathbf{r} - e\mathcal{D}\left(\rho_\mathbf{r}\right)\nabla_2\sigma_\mathbf{r}, \tag{5.13}$$

where the effective conductivity g and diffusion coefficient $\mathcal{D}$ are functions of the local charge carrier density, $\rho \equiv \rho_\mathbf{r}$:

$$
\begin{aligned}
g(\rho) &= \frac{e^2}{b}\left|2(1-\rho)^2\varphi'(E_c) + \rho(1-\rho)\varphi'(0) + \frac{1}{2}(\rho^2-\sigma^2)\varphi'(-E_c)\right|, \\
\mathcal{D}(\rho) &= \frac{\rho(1-\rho_e)^2\varphi(0) + (1-\rho)\rho_e^2\varphi(-E_c)/2}{\rho(1-2\rho_e)+\rho_e^2}.
\end{aligned} \tag{5.14}
$$

In view of Eqs. (5.11), (5.12), it can be considered that g and $\mathcal{D}$ are *even* functions of local charge density σ, and just this dependence will be mostly used below. Also g and $\mathcal{D}$ depend on temperature, through the functions φ and φ'. The system of Eqs. (5.11)-(5.14), together with Eq. (5.4), is closed and self-consistent, defining the distributions of $\sigma_{\mathbf{r}}$ and $\rho_{\mathbf{r}}$ at given $\mathbf{j}_{\mathbf{r}}$. For the FA case, with the local field $\mathbf{F}_{\mathbf{r}}$ defined by Eq. (5.4) with the only relevant $\mathbf{r}$ component being x, that along the current $\mathbf{j}_{\mathbf{r}} \equiv \mathbf{j} = \text{const}$ (Fig. 5.3), and under steady state condition ($\dot{\sigma} = 0$) Eq. (5.13) leads to a (non-linear) integral equation for σ_x:

$$
\sigma_x = \int_0^x \frac{g(\sigma_{x'})(A + C_{x'}) - j}{e\mathcal{D}(\sigma_{x'})} dx'. \tag{5.15}
$$

Here the Coulomb field from charged granules is defined at the position x by the Hilbert transform [Abramowitz and Stegun, 1964] of the FA charge density:

$$
C_x = \frac{e}{\varepsilon_{\text{eff}} a^2} \int_{-L/2}^{L/2} \frac{\sigma_{x'}}{x - x'} dx', \tag{5.16}
$$

for all x within FA, except its boundaries of the order of the thickness of the metallic contact where this field is strongly screened and therefore can be set zero. Also the dimensionless external field (necessary to adjust the given current j) is defined by:

$$
A = \frac{1}{L} \int_{-L/2}^{L/2} \left[\frac{j + e\mathcal{D}(\sigma_x)\partial_x\sigma_x}{g(\sigma_x)} - C_x\right] dx. \tag{5.17}
$$

The evident antisymmetry with respect to inversion $x \to -x$ suggests the initial condition $\sigma(0) = 0$. Practical solution of the system, Eqs. (5.15)-(5.17), can be found numerically,

in an iterative way, $\sigma_x = \lim_{k\to\infty} \sigma_x^{(k)}$, and using its dimensionless form:

$$\begin{aligned}
\sigma_\zeta &= \int_0^\zeta \frac{\tilde{g}\left(\sigma_{\zeta'}\right)\left(\tilde{A}+\tilde{C}_{\zeta'}\right)-\tilde{\jmath}}{\tilde{\mathcal{D}}\left(\sigma_{\zeta'}\right)} d\zeta', \\
\tilde{C}_\zeta &= \frac{Ld}{a^2}\int_0^1 \frac{\sigma_{\zeta'}\zeta'}{\zeta^2-(\zeta')^2} d\zeta', \\
\tilde{A} &= \int_0^1 \left[\frac{\tilde{\jmath}+\tilde{\mathcal{D}}\left(\sigma_\zeta\right)\partial_\zeta\sigma_\zeta}{\tilde{g}\left(\sigma_\zeta\right)} - \tilde{C}_\zeta\right] d\zeta.
\end{aligned}$$

with the adimensional variables defined as: $\zeta = x/x_0$, $\tilde{g}_\zeta = g_\zeta/g_0$, $\tilde{\mathcal{D}}_\zeta = \mathcal{D}_\zeta/\mathcal{D}_0$ and $\tilde{\jmath} = j/j_0$, where the *normalizing* parameters are: $x_0 = L/2$, $g_0 = e^2\omega N_F/b$, $\mathcal{D}_0 = \omega N_F E_c/b$ and $j_0 = 2e\mathcal{D}_0/L$. So, in the interactive procedure, the consecutive $\sigma_\zeta^{(k)}$ are related through the equations:

$$\begin{aligned}
\sigma_\zeta^{(k)} &= \int_0^\zeta \frac{\tilde{g}\left(\sigma_{\zeta'}^{(k-1)}\right)\left(\tilde{A}^{(k-1)}+\tilde{C}_{\zeta'}^{(k-1)}\right)-\tilde{\jmath}}{\tilde{\mathcal{D}}_{\zeta'}^{(k-1)}} d\zeta', \\
\tilde{C}_\zeta^{(k)} &= \frac{Ld}{a^2}\int_0^1 \frac{\sigma_{\zeta'}^{(k)}\zeta'}{\zeta^2-(\zeta')^2} d\zeta', \\
\tilde{A}^{(k)} &= \int_0^1 \left[\frac{\tilde{\jmath}+\tilde{\mathcal{D}}\left(\sigma_\zeta^{(k)}\right)\partial_\zeta\sigma_\zeta^{(k)}}{\tilde{g}\left(\sigma_\zeta^{(k)}\right)} - \tilde{C}_\zeta^{(k)}\right] d\zeta,
\end{aligned}$$

with the zero iteration corresponding to the (quasi) ohmic conditions: $\sigma_\zeta^{(0)} = \tilde{C}_\zeta^{(0)} \equiv 0$, $\tilde{A}^{(0)} = (1-10^{-b})\tilde{\jmath}/\tilde{g}$ (with $b \sim 5$), $\tilde{\mathcal{D}}_\zeta^{(0)} = \text{const}$, and $\tilde{g}_\zeta^{(0)} = \text{const}$.

The numerical analysis shows that it has no other solution but the trivial one: $\sigma_{\mathbf{r}} \equiv 0$. Hence there is no diffusive contribution to the current, and the steady state of FA in out-of-equilibrium conditions has an ohmic resistivity $r = 1/g\left(\rho_e\right)$. In fact, estimation (based in the experimental system discussed below) of this quantity suggests that the contribution of the FA to the overall resistance is approximately two orders of magnitude lower compared with typical values found below for CA. Thus, it is expected that transport is mainly controlled by CA.

5.2.4 Steady state conduction in CA

The kinetics in CA includes, besides the processes 1) to 3) of Sec.5.2.2 and 5.2.3, also four additional microscopic processes between **n**th granule and the electrode (Fig. 5.6)

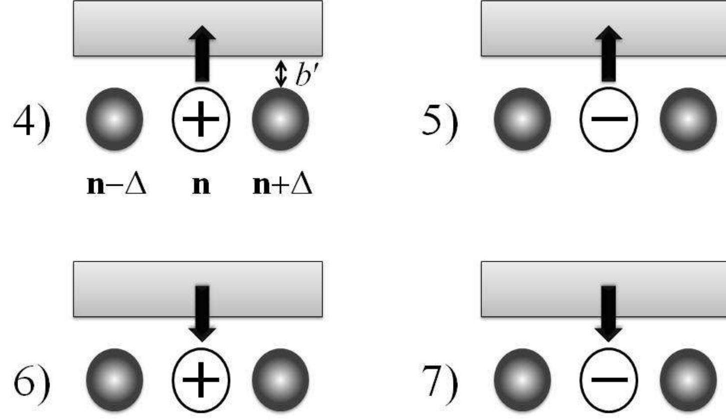

Figure 5.6: *Kinetic process between* **n***th granule and the metallic electrode in CA.*

which are just responsible for variations of total charge Q by ± 1. The respective rates $q^{(i)}$, $i = 4 \ldots 7$, are also dependent on the charging state $(\sigma_{\mathbf{r}}, \rho_{\mathbf{r}})$ of the relevant granule and, using the same techniques that before, their mean values are:

$$
\begin{aligned}
q_{\mathbf{r}}^{(4)} &= (\rho_{\mathbf{r}} + \sigma_{\mathbf{r}})\, \psi\left(-U - E_c'\right), \\
q_{\mathbf{r}}^{(5)} &= (\rho_{\mathbf{r}} - \sigma_{\mathbf{r}})\, \psi\left(U - E_c'\right), \\
q_{\mathbf{r}}^{(6)} &= (1 - \rho_{\mathbf{r}})\, \psi\left(U + E_c'\right), \\
q_{\mathbf{r}}^{(7)} &= (1 - \rho_{\mathbf{r}})\, \psi\left(-U + E_c'\right).
\end{aligned}
\tag{5.18}
$$

Here the function $\psi(E)$ formally differs from $\varphi(E)$ only by changing the pre-factor: $\omega \to \omega' = \omega_a \mathrm{e}^{-2\chi b'} \ll \omega$, but the arguments of these functions in Eq. (5.18) include other characteristic energies. Thus, $U = eb'F_{\mathrm{c}}$ is generated by the electric field F_{c} between granule and contact surface. This field is always normal to the surface (see Fig. 5.7) and its value is defined by the local charge density σ. At least, the charging energy E_c' for a granule under the contact can be somewhat reduced (e.g., by $\sim 1/2$) compared to E_c. Then the kinetic equations in the interface region present a generalization of Eqs. (5.5)-(5.6), as follows:

$$
\dot{\sigma}_{\mathbf{r}} = \sum_{\Delta} \left[q_{\mathbf{r},\Delta}^{(1)} - q_{\mathbf{r}+\Delta,-\Delta}^{(1)} - p_{\mathbf{r},\Delta}^{(2)} + p_{\mathbf{r}+\Delta,-\Delta}^{(2)} - p_{\mathbf{r},\Delta}^{(3)} - q_{\mathbf{r}}^{(4)} + q_{\mathbf{r}}^{(5)} + q_{\mathbf{r}}^{(6)} - q_{\mathbf{r}}^{(7)} \right], \tag{5.19}
$$

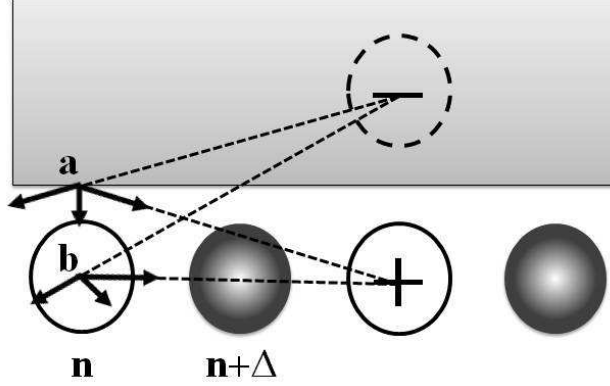

Figure 5.7: *Formation of local electrical field by charged granules and their images at the surface of the metallic electrode (point a) and between the granules (point b).*

$$\dot{\rho}_{\mathbf{r}} = \sum_{\Delta} \left[q^{(1)}_{\mathbf{r},\Delta} + q^{(1)}_{\mathbf{r}+\Delta,-\Delta} - q^{(2)}_{\mathbf{r},\Delta} + q^{(2)}_{\mathbf{r}+\Delta,-\Delta} - q^{(3)}_{\mathbf{r},\Delta} - q^{(4)}_{\mathbf{r}} - q^{(5)}_{\mathbf{r}} + q^{(6)}_{\mathbf{r}} + q^{(7)}_{\mathbf{r}} \right]. \quad (5.20)$$

The additional terms, by the *normal* processes 4) to 7), are responsible for appearance of a *normal* component of current density:

$$j^z_{\mathbf{r}} = \frac{e}{a^2} \left[q^{(4)}_{\mathbf{r}} - q^{(5)}_{\mathbf{r}} - q^{(6)}_{\mathbf{r}} + q^{(7)}_{\mathbf{r}} \right], \quad (5.21)$$

besides the planar component, still given by Eq. (5.8). But an even more important difference from FA case is the fact that the Coulomb field here is formed by a *double layer* of charges, those of granules themselves and of their images in the metallic electrode (Fig. 5.7). Summing the contributions from all the charged granules and their images (except for the image of **n**th granule itself, already included in the energy E'_c), the expression for the above mentioned field S at the contact surface is found as a *local* function of the charge density $\sigma_{\mathbf{r}}$:

$$S_{\mathbf{r}} = C_{\mathbf{r}}(z = b) = -\frac{4\pi e}{\varepsilon_{\text{eff}} a^2} \sigma_{\mathbf{r}},$$

replacing the integral relations, Eqs. (5.3)-(5.4), in FA. Then, the planar component of the field by charged granules $\mathbf{F}^{\text{pl}}_{\mathbf{r}} = \mathbf{C}_{\mathbf{r}}(z = 0)$ is determined by the above defined normal field $C_{\mathbf{r}}$ through the relation $\mathbf{F}^{\text{pl}}_{\mathbf{r}} = b' \nabla_2 C_{\mathbf{r}}$. The density of planar current is

$\mathbf{j}_{\mathbf{r}}^{\mathrm{pl}} = g\mathbf{F}_{\mathbf{r}}^{\mathrm{pl}} - e\mathcal{D}\nabla_2\sigma_{\mathbf{r}}$, accordingly to Eq. (5.11), that is both field-driven and diffusive contributions into $\mathbf{j}_{\mathbf{r}}^{\mathrm{pl}}$ are present here and both they are proportional to the gradient of $\sigma_{\mathbf{r}}$. In the low temperature limit, this proportionality is given by:

$$\mathbf{j}_{\mathbf{r}}^{\mathrm{pl}} \approx -\left[\frac{8\pi e^3\omega N_{\mathrm{F}} b'}{\varepsilon_{\mathrm{eff}} a^3} g\left(\sigma_{\mathbf{r}}\right) + \frac{e\omega N_{\mathrm{F}} k_{\mathrm{B}} T}{a}\right] \nabla_2\sigma_{\mathbf{r}}. \tag{5.22}$$

Note that presence of a non-linear function:

$$g\left(\sigma\right) = \sqrt{\rho_e^2 + \sigma^2} - 2\rho_e^2 - \sigma^2,$$

defines a *non-ohmic* conduction in CA. In fact, this function should be defined only for charge density below its maximum possible value $|\sigma_{max}| = \sqrt{1-\rho_e^2}$, turning zero for $|\sigma| > |\sigma_{max}|$ (note that the latter restriction just corresponds to our initial limitation to the single charged states, see Sec. 5.2.1). In the same limit of low temperatures, the normal current density is obtained from Eqs. (5.16),(5.18) as $\mathbf{j}_{\mathbf{r}}^{z} = g_z\mathbf{C}_{\mathbf{r}}$ where $g_z \approx \omega' N_{\mathrm{F}} E_c' \varepsilon_{\mathrm{eff}}/4\pi$. Finally, the kinetic equation in this case is obtained, in analogy with Eq. (5.8), as:

$$\dot{\sigma}_{\mathbf{r}} = -\frac{a^2 b}{e}\nabla_2 \cdot \mathbf{j}_{\mathbf{r}}^{\mathrm{pl}} + \frac{a^2}{e} j_{\mathbf{r}}^{z}. \tag{5.23}$$

This equation permits to describe the steady state conduction as well as various time dependent processes. The first important conclusion is that steady state conduction in interface turns only possible at non-zero charge density gradient, that is, *necessarily* involving charge accumulation, in contrast to the above considered situation in bulk.

The present analysis is restricted to the steady state regime which is simpler, a more involved case when an explicit temporal dependence of charge density included in Eq. (5.23) is left for future work.

Choosing the contacts geometry in the form of a rectangular stripe of planar dimensions $L \times L'$, along and across the current respectively. In neglect of relatively small effects of current non-uniformity along the lateral boundaries, the only relevant coordinate for the problem is longitudinal, x (Fig. 5.8). In the steady state regime, the temporal derivative $\dot{\sigma}$ in Eq. (5.23) is zero and the total current $I = \mathrm{const}$, defined by the action of external source. Then, using the above approximation for $g\left(\sigma\right)$, a non-linear 2nd order

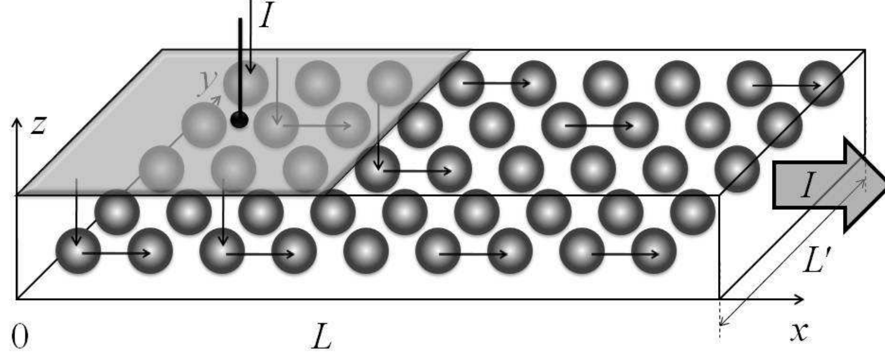

Figure 5.8: *Relations between* **n***th longitudinal (j_x) and normal (j_z) currents in CA.*

equation for charge density is found:

$$\frac{d}{dx}\left[g\left(\sigma_x\right)+\tau\right]\frac{d\sigma_x}{dx}-k^2\sigma_x=0. \tag{5.24}$$

The parameters in Eq. (5.24) are: $k^2=(\omega' E_c')/(ab\omega k_\mathrm{B}T_1)$ and $\tau=T/T_1$, where T is the actual temperature and $T_1=8\pi e^2 b'/a^2 k_\mathrm{B}\varepsilon_\mathrm{eff}$. To define completely its solution, the following boundary conditions are imposed:

$$\left.\frac{d\sigma_x}{dx}\right|_{x=0}=\frac{k^2 b'\sigma_{x=0}}{g\left(\sigma_{x=0}\right)+\tau}, \tag{5.25}$$

$$\left.\frac{d\sigma_x}{dx}\right|_{x=L}=\frac{aT_1}{Le\omega bN_\mathrm{F}k_\mathrm{B}}\frac{I}{g\left(\sigma_{x=L}\right)+\tau}. \tag{5.26}$$

The condition 5.25 corresponds to the fact that the longitudinal current j^x at the initial point of contact-granular sample interface (the leftmost in Fig. 5.8) is fully supplied by the normal current j^z entering from the contact to granular sample, and the condition 5.26 corresponds to current continuity at passing from CA (of length L along the current) to FA.

Now, a qualitatively discussion of the solution of Eq. (5.24) is done. Generally, to fulfill the conditions, Eqs. (5.25), (5.26), one needs a quite subtle balance to be maintained between the charge density and its derivatives at both ends of contacts interface. But the situation is radically simplified when the length L is much greater than the characteristic decay length for charge and current density: $kL \gg 1$. In this case, the relevant coordinate is $\xi=L-x$, so that the boundary condition 5.25 corresponds to $\xi=L\to\infty$, when both

its left and right hand side turn zeros:

$$\sigma_\xi|_{\xi\to\infty} = 0, \qquad \left.\frac{d\sigma_\xi}{d\xi}\right|_{\xi\to\infty} = 0. \tag{5.27}$$

The numeric solution shows that, for any initial [with respect to ξ, that is related to $x = L$, Eq. (5.26)] value of charge density $\sigma_{\xi=0} = \sigma_0$, there is a *unique* initial value of its derivative $d\sigma_\xi/d\xi|_{\xi=0} = \mathcal{D}(\sigma_0)$ which just assures the limits 5.27, while for $d\sigma_\xi/d\xi|_{\xi=0} > \mathcal{D}(\sigma_0)$ the asymptotic value diverges as $\sigma_{\xi\to\infty} \to \infty$, and for $d\sigma_\xi/d\xi|_{\xi=0} < \mathcal{D}(\sigma_0)$ it diverges as $\sigma_{\xi\to\infty} \to -\infty$. Then, using the boundary condition 5.26 and taking into account the relation $V = V_0\sigma_0$ with $V_0 = 4\pi eb'/(\varepsilon_{\rm eff}a^2)$, it is possible to conclude that the function $\mathcal{D}(\sigma_0)$ generates the I-V characteristics:

$$I = I_1 b'\mathcal{D}\left(\frac{V}{V_0}\right)\left[g\left(\frac{V}{V_0}\right) + \tau\right] \tag{5.28}$$

where $I_1 = e\omega N_{\rm F}k_{\rm B}T_1$.

A more detailed analysis of Eq. (5.24) is presented in Appendix B. In particular, for the weak current regime (Regime I) when $\sigma_0 \ll \sigma_1 = \sqrt{32\rho_e(\rho_e+\tau)} \ll 1$, so that $g(\sigma) \approx \rho_e + \sigma^2/2\rho_e$ along whole the contact interfaces, Eq. (5.24) admits an approximate analytic solution:

$$\sigma_\xi = \sigma_0 {\rm e}^{-\lambda\xi}\left[1 + 6\left(\frac{\sigma_0}{\sigma_1}\right)^2\left(1 - {\rm e}^{-2\lambda\xi}\right)\right], \tag{5.29}$$

with the exponential decay index $\lambda = k/\sqrt{\rho_e+\tau}$.

This results in the explicit I-V characteristics for Regime I:

$$I = G_0 V\left[1 + \left(\frac{V}{V_1}\right)^2\right], \tag{5.30}$$

for $V < V_1 = \sigma_1 V_0$, Eq. (5.30) describes the initial ohmic resistance (dependent on temperature τ):

$$G_0 = \frac{I_1 kb'}{V_0}\sqrt{\rho_e(\tau) + \tau}, \tag{5.31}$$

which turns non-ohmic for $V \sim V_1$. But at so high voltages another conduction regime already applies (called Regime II), where $\sigma_1 \ll \sigma_0 \ll 1$ and one has $g(\sigma) \approx \sigma$. Following

the same reasoning as for the Regime I, a non-linear I-V characteristics is found for Regime II:

$$I \approx \frac{I_1 k b'}{\sqrt{3V_0^3}} (V + V_0 \tau)^{3/2} \tag{5.32}$$

this law is weaker temperature dependent than Eq. (5.30), which is related to the fact that the conductance in Regime II is mainly due to dynamical accumulation of charge and not to thermic excitation of charge carriers. A $I \propto V^{3/2}$ is, in fact, found experimentally and will be discussed in the next section. Further, such dependence can be more pronounced if multiple charging states are engaged, as may be the case in real granular layers with a certain statistical distribution of granule sizes present.

At least, for even stronger currents, when already $\sigma_0 \sim 1$, the solutions of Eq. (5.24) can be obtained numerically, following the above discussed procedure of adjustment of the derivative $\mathcal{D}(\sigma_0)$ to a given σ_0. Such solutions have an asymptotic behavior of the type: $I \propto V^{5/4}$.

5.3 Experimental magnetic and transport properties

Various granular films have been experimentally tested with granules of different ferromagnetic metals (Ni, Co, Fe, CoFe, NiFe) and distinct insulating hosts (SiO_2, TiO_2, ZrO_2, Al_2O_3, MgO). Between them, especially interesting objects are the discontinuous magnetic layers and multilayers, since 2D geometry favors to more pronounced effects of dipolar coupling between magnetic granules. Experiments on such films show that their magneto-electric properties are mainly controlled by the concentration of magnetic material, or by the nominal thickness (t) of a 2D granular layer (that is its thickness if it were continuous). Presently, the correlation between the transport processes and the film topology (obviously dependent on the nominal thickness of granular layers) is the main objective in all these studies. Three principal transitions are observed with varying concentration (at fixed and high enough temperature). The first one is that from metallic to activated electrical conduction, controlled by the structural percolation of metallic granules in the insulating matrix [Kakazei *et al.*, 2001], immediately followed by a second one, that from ferromagnetic (FM) to superferromagnetic (SFM) state [Sousa *et al.*, 2004]. The third one is that from SFM to superparamagnetic (SPM) (accompanied by

the so called superspin glass (SSG) phase at low enough temperatures [Chen *et al.*, 2005]). The SFM state is attributed to preferable alignment of magnetic moments on randomly distributed separate granules due to the dipolar coupling between them, controlled by the so-called magnetic percolation [Kakazei *et al.*, 1999 and Kleemann *et al.*, 2001]. In fact, the SFM-SPM transition (above a certain glass transition temperature, T_g [Bedanta and Kleemann, 2009]) brings about the most pronounced MR effects, in particular, its sensitivity to low magnetic field. However, up to this moment, certain technical problems prevented more detailed study of granular layers of lower nominal thickness (due to their very high resistivity values) that could clarify magnetotransport mechanisms in these materials.

With this purpose, granular films with low concentration of ferromagnetic material, below the metal-insulator and SFM-SPM thresholds, are studied here. This regime, where the system contains granules of few nm size at bigger separation, is usually referred to as *diluted limit*. Although the magnetic properties of these systems have been exhaustively studied (see, e.g., [Chen *et al.*, 2005 and Sahoo *et al.*, 2003], for a review in supermagnetism the interested reader is referred to [Bedanta and Kleemann, 2009]), in the literature, there is lack of transport studies in this limit, as compared to that of higher concentration. Therefore, in order to complement the previous works, (magneto)transport and magnetic analyses are presented below. Particular interest is given to the relationship between magnetization and TMR (for different temperatures) and how they are affected upon variation of the nominal thickness of granular layer (or the intergranule distance).

Due to the high resistance of the samples the analysis is mainly restricted to high temperatures ($T \gtrsim 100$ K), above the glass temperature T_g, so that a SPM or modified SPM approximation is reasonable. Lacking any precise measurement of T_g, it is roughly estimated by blocking temperature T_b ($T_b \geqslant T_g$), determined from the splitting of conventionally obtained field-cooled (FC) and zero-field-cooled (ZFC) magnetization curves (see below).

5.3.1 Magnetic Properties

The low-field magnetization curves as a function of temperature, $M(T)$, are shown in Fig. 5.9a. They have typical aspect for disordered granular systems, with Curie-Weiss behavior at high temperatures and onset of irreversibility at a blocking temperature, T_b,

t (nm)	M_s (Gs)	d (nm)	s	K_{eff} (10^6 erg cm^{-3})
0.7	1947	4.1	0.17	1.56
0.9	2410	5.4	0.19	1.30

Table 5.1: *Fitting parameters for the low-field magnetization curves in function of temperature.*

below which the FC and ZFC curves split out. As seen from Fig.5.9a, its values $T_b \approx 25$ K and ≈ 50 K for $t = 0.7$ and 0.9 nm respectively, display the expected decrease with decreasing nominal thickness. Also T_b somewhat decreases with applied magnetic field (insets in Fig. 5.9a), in agreement with the previous studies for higher t values [Kakazei *et al.*, 2003]. This shift is probably related to a de Almeida-Thouless-type phase boundary of the low-T SSG state [Sahoo *et al.*, 2002]. In the same agreement, the extrapolation of ZFC data vs applied field to $H \to 0$ (not shown) indicates absence of SFM state even at low temperatures.

Then, fitting essentially the high temperature behavior within a SPM approximation, it is possible to estimate the mean diameter of granules (d), its standard deviation (s), and the effective anisotropy constant (K_{eff}). To do this, the model expression suggested by Respaud *et al.* [Respaud *et al.*, 1998] for SPM granules with log-normal size distribution is solved analytically (see Appendix B). The resulting formulas with the fitting parameters given in Table 5.1 provide a fair fit to the experimental data as shown in Fig. 5.9a. The inferred average granule diameters of 4.1 nm and 5.4 nm are in a fair agreement with the structural analysis in these samples [Kakazei *et al.*, 2001 and Lesnik *et al.*, 2002], and the values of mean dispersion s confirm a narrow (quasi-monodisperse) distribution. The obtained K_{eff} values also fairly agree with those reported in literature [Hattink *et al.*, 2006]. It should be mentioned here that a more comprehensive magnetic analyses on these systems should involve a detailed inspection of the SSG state as done in Refs. [Chen *et al.*, 2005 and Sahoo *et al.*, 2003], where the ageing, memory and rejuvenation effects [Bedanta and Kleemann, 2009] clarify the nature of this state. Nevertheless, as mentioned above, such a treatment is beyond the scope of the present work, focused instead in the higher temperatures with approximately SPM behavior.

Keeping in mind the previous considerations, the magnetization curves as a function of the applied field, $M(H)$, for different temperatures are presented in Fig. 5.9b. Their high-field saturation was assured after subtraction of a notable diamagnetic contribution

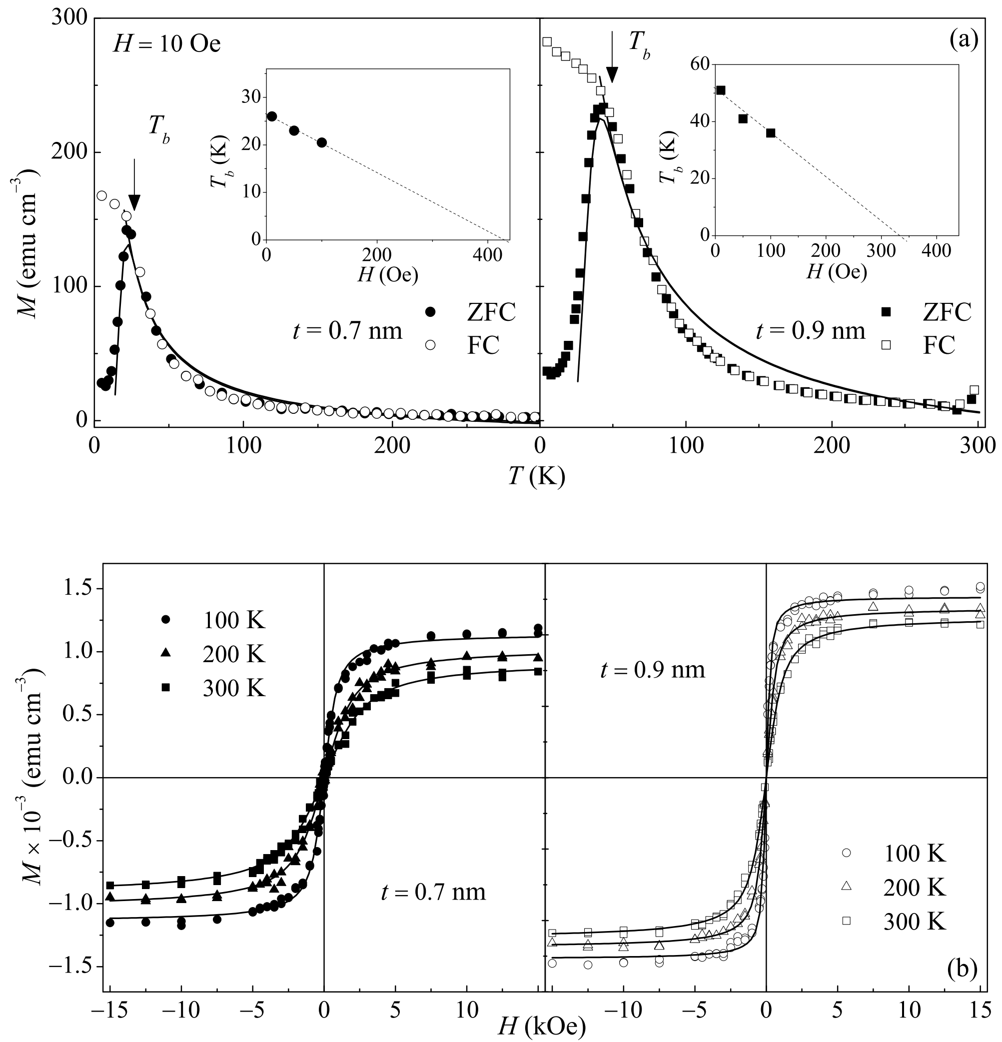

Figure 5.9: ***(a)*** *Magnetization of Al_2O_3(3.0 nm)/[$Co_{80}Fe_{20}$(t)/Al_2O_3(4.0 nm) $]_{10}$ films with $t = 0.7$ and 0.9 nm under $H = 10$ Oe in function of temperature. Insets show the T_b decay with the applied magnetic field.* ***(b)*** *Magnetization vs field cycles at different temperatures.*

from the glass substrate and amorphous Al_2O_3 matrix. The magnetization curves for granular systems are oftenly described in the approximation of two uncoupled subsystems of magnetic granules, large- and small-sized [Chen *et al.*, 2005]. A similar treatment by Zhu *et al.* in Fe-Al_2O_3 films [Zhu *et al.*, 1999] considered three uncoupled SPM subsystems (of small, medium and large granules). Subsequently, Hattink *et al.* [Hattink *et al.*, 2006] regarded a log-linear distribution of SPM granules. For the present case, reduction of the granule size distribution to a simple monodisperse justifies the use of the expression: $M(H) = N\mu L(\mu H/k_{\mathrm{B}}T)$, where N is the total number of granules in the sample, μ is the mean granule magnetic moment, $L(x) = \coth x - 1/x$ is the Langevin function, and k_{B} is the Boltzmann constant. In spite of its simplicity, this approach fits reasonably the experimental data (see Fig. 5.9b), in agreement with the expected SPM state of diluted systems and the narrow size distribution by the $M(T)$ fit.

5.3.2 Charge transport properties

Current-voltage (I-V) characteristics are generally non-ohmic, as shown in Fig. 5.10. They are only linear at low voltages, while a $I \propto V^{\gamma}$ power law dominates at electrical fields above ~ 500 V/cm. Non-linear I-V characteristics in diluted granular films have been reported previously by Chayka *et al.* [Chayka *et al.*, 2006]. They argued this to be a result of impurity mediated conductivity in the insulator Al_2O_3 matrix. Actually, non-linear I-V behavior is typical of charge injection into insulators and has been intensively studied since the Mott and Gurney works [Mott and Gurney, 1940] in the context of space-charge-limited currents (SCLC). That model predicts ohmic behavior at low-voltages followed by a $I \propto V^2$ law, for trap-free solids [Mott and Gurney, 1940 and Rose, 1955], or by $I \propto V^{1+l}$ with the trap/carrier ratio $l \geq 1$, for trap-limited insulators [Rose, 1955, Lampert, 1956, and Chandra *et al.*, 2007]. Due to its accuracy, SCLC has been largely used to measure charge mobilities and trap characteristic energies in a variety of materials [Tanase *et al.*, 2004]. However the SCLC models cannot satisfactorily describe our data since the inferred γ values are typically $\approx 3/2$, well below the minimum SCLC value of $\gamma = 2$ (for the trap-free case). As previously discussed this is apparently due to the specifics of tunnel conduction in the considered system, where the space charge effects are due to extra charges localized on nanometric metallic granules rather than on atomic traps. Besides, the 2D distribution of granules in a layer favors to faster convergence of Coulomb

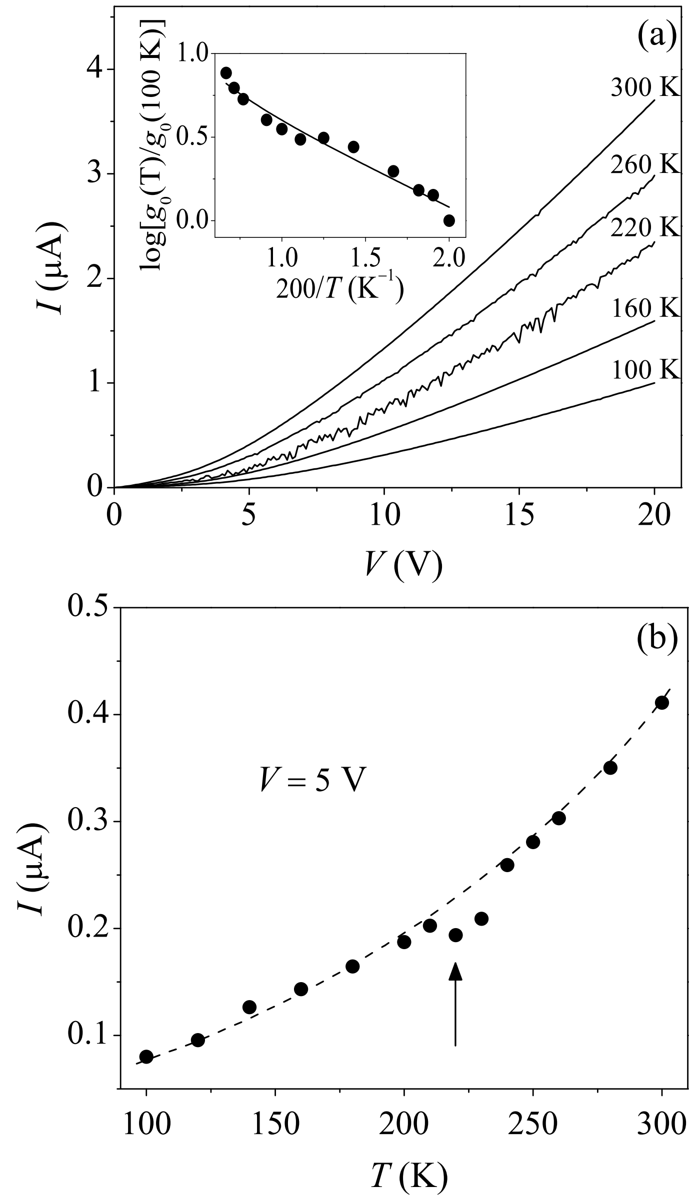

Figure 5.10: ***(a)*** *I-V characteristics for thickness $t = 0.9$ nm at different temperatures; Inset: logarithmic representation of the low-voltage ohmic conductivity, g(T), divided by $g(T = 100K)$ as a function of the inverse temperature.* ***(b)*** *Current vs temperature (with $V = 5$ V) for the same thickness.*

fields from local charge fluctuations in the average distribution of accumulated charge. The theory presented above (for references see [Kakazei *et al.*, 2000 and Sousa *et al.*, 2001]), provides the $I \propto V^{3/2}$ law at high enough voltages, while the low-voltage, ohmic conductivity g_0 is predicted to depend on temperature as:

$$g_0(T) \propto \left[\left(\frac{T}{T_1}+1\right)\frac{2}{2+\exp\left(T_c/T\right)}\right]^{1/2}, \tag{5.33}$$

where $T_c = e^2/(2\varepsilon_{\mathrm{eff}}\overline{d}k_{\mathrm{B}})$ relates to the charging energy for a granule of mean size $\overline{d}$ in the medium with effective dielectric constant $\varepsilon_{\mathrm{eff}}$ and $T_1 \propto T_c$. This formula displays a non-exponential temperature dependence for activated transport in the granular system due to the interplay between temperature dependent number of charge carriers and their mobility. As shown in the inset to Fig. 5.10a, our experimental data on $g(T)$ for the $t = 0.9$ nm sample are fairly fitted with the choice of $T_c = 200$ K, corresponding to the parameter values $\varepsilon = 100$ (high values of the dielectric constant were also deduced by J. Santos during his PhD. thesis work [J. A. M. Santos, 2004 and Kakazei *et al.*, 2000]) and $\overline{d} = 5$ nm, in a reasonable concordance with the above analysis of magnetization data. The most notable deviation of the experimental points from the fitted dependence of $\log[g_0(T)/g_0(100\mathrm{K})]$ vs T^{-1} is observed in the range of $T \sim 200 - 220$ K (see below).

The temperature dependence of current at a finite, but moderate voltage (5 V) for the $t = 0.9$ nm sample is shown in Fig. 5.10b. As expected, the current generally grows with increasing temperature, except for a narrow temperature range around ~ 220 K, where a clear dip is observed. Such an anomaly can be compared with anomalies reported around $200 \div 220$ K in a variety of materials and attributed to a phase transition of unknown origin [Jin *et al.*, 2002]. In fact, it was recently shown in organic thin film transistors [Gomes *et al.*, 2006] that a metastable state of confined water, known as *super-cooled water*, persisting near the film surface below the common freezing point down to $T \sim 200 - 220$ K can cause important carrier trapping. In spite of high vacuum kept during the measurements in our films, there could still remain water contamination and the related carrier trapping could reduce conductance. Carrier trapping by surface water explains qualitatively the observed behavior: there are no water-related traps at low temperatures but, as the temperature of phase transition for surface water is reached, emerging defects can suddenly trap carriers. If the current through the device is low

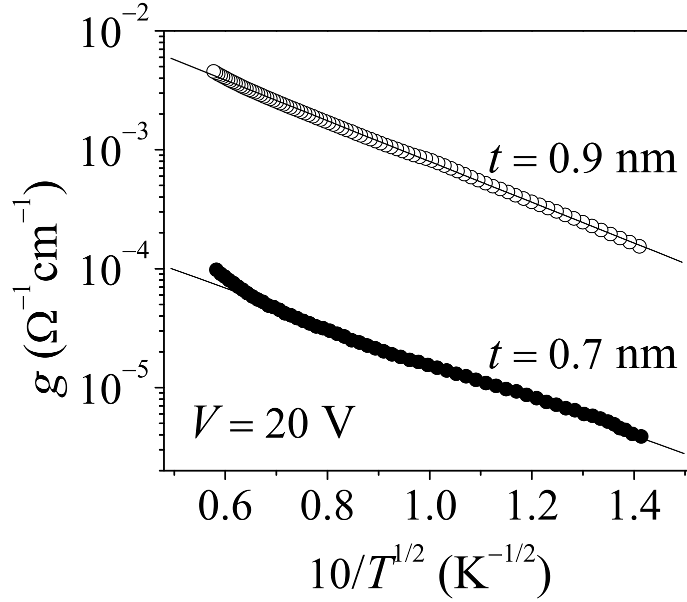

Figure 5.11: *Conductivity as a function of* $T^{-1/2}$ *for thicknesses* $t = 0.7, 0.9nm$ *(fitted with the Sheng* et al. *law [Sheng* et al.*, 1973]).*

enough, this causes a sizeable decrease in the overall current (through device + through surface) until all the traps are filled. Once all the traps are exhausted (filled), the overall current recovers the monotonous behavior by thermal activation. This carrier trapping model is in agreement with the observation that the lower applied voltage (lower current) the more pronounced is the dip in the temperature dependent curves: the greater part of current has to be spent to fill all the traps generated by the phase transition. Notably, such effect was not detected previously in granular layers of higher nominal thickness (and higher conductivity) and it could be also responsible for the outburst of noise in the I-V curves at $T \sim 220$ K shown in Fig. 5.10a. Similar effects in magnetoresistance will be discussed in the next Subsection.

To further clarify the charge transport mechanism, current vs temperature measurements were done at higher voltages ($V = 20$ V). For comparison with the literature data, it is suitable to consider again electrical conductivity, g, rather than current. In Fig. 5.11, the plots of g as a function of temperature are shown for the two samples. The straight lines are the fits to the Sheng *et al.* law [Sheng *et al.*, 1973]:

$$g(T) = g^{(0)} + g^{(1)} \exp\left[-\sqrt{C_0/\left(k_B T\right)}\right], \tag{5.34}$$

t (nm)	$g^{(0)}$ (Ω^{-1}cm^{-1})	$g^{(1)}$ (Ω^{-1}cm^{-1})	C_0 (meV)
0.7	2.1×10^{-5}	5.9×10^{-4}	27.4
0.9	1.3×10^{-3}	4.1×10^{-2}	33.5

Table 5.2: *Characteristic transport parameters for two nominal thickness values extracted from Fig. 5.11.*

where $g^{(0)}$ is the zero temperature conductivity, $g^{(1)}$ is the temperature independent prefactor, and C_0 is the tunnel activation energy. The fitting parameters are presented in Tab. 5.2 and they agree with the literature data [Hattink *et al.*, 2006 and Chayka *et al.*, 2006]. The C_0 values are almost the same for both thicknesses and indicate thermally assisted tunneling between neighbor granules, as expected for these disordered diluted systems.

5.3.3 Magnetotransport properties

In magnetic granular films, charge-carrier tunneling depends on the relative angle θ between magnetic moments of neighbor granules as $\propto \cos\theta/2$ [Gittleman *et al.*, 1972]. In the superparamagnetic (SPM) state at $B \sim 0$, the mean magnetic moments of granules are randomly oriented, producing a significant tunnel resistance. With applied magnetic field, the moments get aligned along the field direction, then decreasing tunnel resistance defines a negative magnetoresistance (MR).

Fig. 5.12a shows representative room-temperature MR curves for both thickness values. Notice steeper dependence of $MR(H)$ at low fields on growing thickness from $t = 0.7$ to 0.9 nm. Such decrease of the low field MR sensitivity with decreasing thickness prevails at all the measured temperatures. In this context, the low field $MR(H)$ sensitivity was reported before to reach its sharp maximum at critical thickness $t^* = 1.3$ nm (at room temperature) [Kakazei *et al.*, 2001 and Sousa *et al.*, 2001] and then to decrease upon decreasing thickness, mainly due to weakening of magnetic dipolar interactions $\sim 1/r^3$, with increasing inter-granule distance r. In the SPM state, one can try to fit the MR data with the known Inoue-Maekawa law for three-dimensional granular films [Inoue and Maekawa, 1996]:

$$MR = \frac{P^2 M^2}{1 + P^2 M^2},$$

with the ratio $P = (D_\uparrow - D_\downarrow)/(D_\uparrow + D_\downarrow)$ of densities of states $D_{\uparrow(\downarrow)}$ of majority (minority) Fermi electrons and the magnetization M (again expressed by the Langevin function).

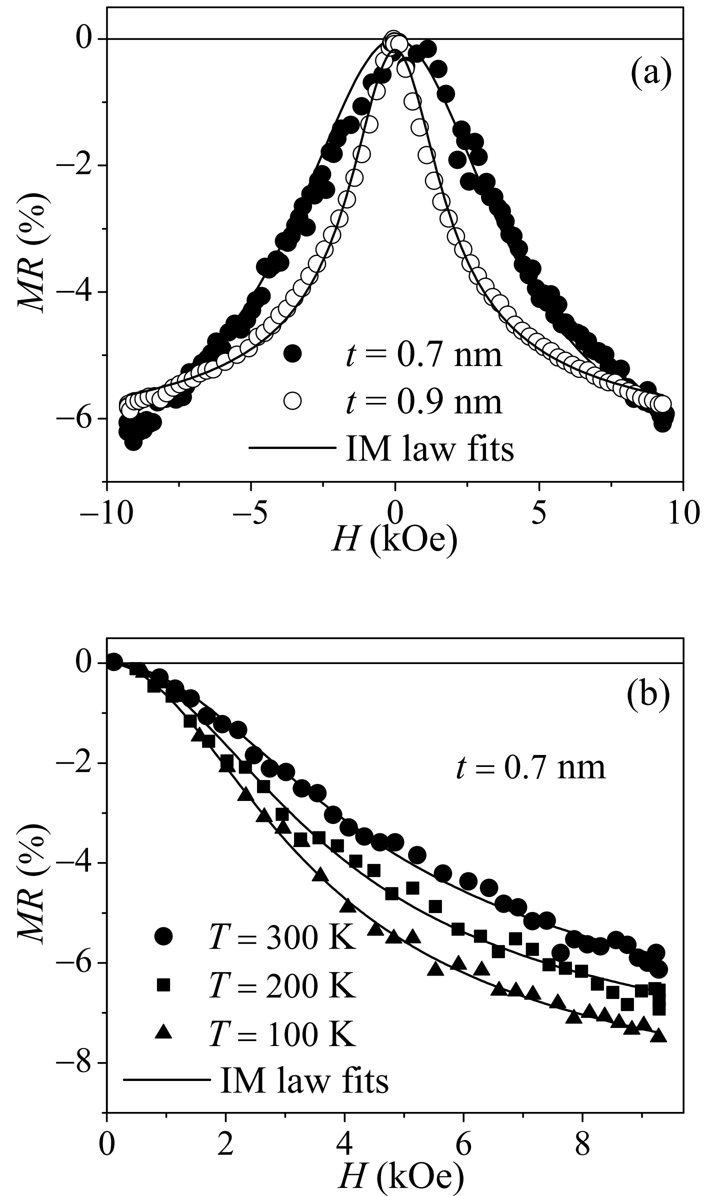

Figure 5.12: ***(a)*** *Field dependence of room-temperature MR at different thicknesses* $t = 0.7, 0.9$, *where the Inoue-Maekawa (IM) law for 3D granular films [Inoue and Maekawa, 1996] is used for fitting* MR *vs* H; ***(b)*** *IM fits at different temperatures for* $t = 0.7$ *nm (similar fits result for* $t = 0.9$ *nm).*

Even though the Inoue-Maekawa law can reasonably fit the magnetoresistance data, the found fitting parameters are different from those estimated from the magnetization curves, $M(H)$. The respective μ/μ_B values (μ_B the Bohr magneton) inferred from $M(H)$ and MR fits are shown in Fig. 5.13. This relevant discrepancy shows that the Inoue-Maekawa formula (derived for a 3D granule distribution) does not fully describe layered systems. In such systems, the in-plane correlations prevail over the inter-plane ones, imposing an essential correction to this classical law written as:

$$MR(\theta) = \frac{P^2\,(1 - \langle\cos\theta\rangle_\perp)}{1 - P^2\langle\cos\theta\rangle_\perp}, \tag{5.35}$$

with the average $\langle\,\rangle_\perp$ limited to granules in the same layer [Kakazei *et al.*, 1999]. Unfortunately, a direct experimental access to this average is not available, but it is expected to be high at RT (due to the in-plane dipolar coupling) and to decrease near and below T_b (when a short-range disorder onsets). For this reason, a significant low temperature increase of maximum MR is observed (as shown in Fig. 5.15). Corrections to the Inoue-Maekawa model are often necessary to properly fit the experimental data. For instance, Z. Mao *et al.* [Mao *et al.*, 2008] has also presented a correction to the Inoue-Maekewa formula taking into account, phenomenologically, the field-dependent correlation length arising from the interparticle coupling in the SPM state. With such a correction they were able to properly fit the results of Hattink *et al.* [Hattink *et al.*, 2006].

It is interesting that both thicknesses lead to a similar maximum MR $\sim$ 6% with $H \approx 10$ kOe at RT, Fig. 5.12a. These values are slightly lower of those observed for the same batch films with $t = 1.0$ nm subjected to equal fields [Kakazei, 2001]. In fact, higher values can be deduced from extrapolation of the Inoue-Maekawa law through saturation field values ($H \approx 50$ kOe). Doing so the maximum MR values of $\sim$ 8% and $\sim$ 6.5% were found for the $t = 0.7$ and 0.9 nm samples, respectively. Anyway, our ratios are higher than the ones reported by Bručas *et al.* [Bručas *et al.*, 2007] studying DMIM's of [$Ni_{81}Fe_{19}$(t nm)/Al_2O_3(1.6 nm)] type and recently by García-García *et al.* [García-García *et al.*, 2009] considering [Fe(t nm)/MgO(3 nm)] multilayers.

Further on, an interesting critical behavior of maximum MR, maximum MR field sensitivity, and field H_i of maximum field sensitivity vs t (at RT) is found near the SPM/SFM transition $t_c \approx 1.3$ nm, Fig. 5.14. The phase transition occurs at the passage

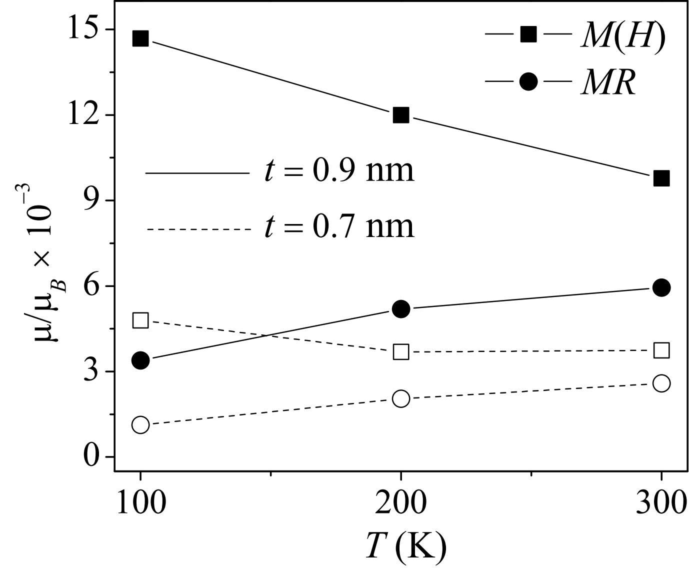

Figure 5.13: *Comparison between the mean magnetic moments of the granules (in unities of μ_B) calculated from the fits to the magnetoresistance, MR (•), and from the magnetization curves, $M(H)$ (■).*

from low to high t and displays a mean-field-like critical behavior when t approaches t_c from below with the field H_i playing the role of an *order parameter* from the SPM side, it follows the typical law: $H_i(t) \approx H_0\sqrt{t_c - t}$, with $H_0 \approx 1.14$ kOe. This transition is different from the formerly reported percolation-like behavior at approaching t_c from above [Kakazei *et al.*, 2003 and Sousa *et al.*, 2001].

Moreover, the temperature dependence of MR is shown in Fig. 5.15, both thicknesses have anomalous dependencies of $MR_{\max}$ on temperature. At $T \sim$ 40K, a significant enhancement of $MR_{\max}$ appears, in agreement with the low temperature increase of MR reported in literature, [Mitani *et al.*, 1998 and Zhu and Wang, 1999]. Then, both thicknesses display a tendency to slowly decrease with growing temperature up to $T \sim 160$ and 220 K, for $t = 0.7$ and 0.9 nm, respectively. Finally, above $T \sim 220$ K, the difference between $MR_{\max}$ values for the two thicknesses almost disappears, Fig. 5.13. Interestingly, MR_{max} vs T is not properly fitted by the $MR_{\max} \propto T^{-1}$ law proposed by Helman and Abeles [Helman and Abeles *et al.*, 1976] neither by the $MR_{\max} \propto \exp(-k_B T/E_m)$ law by the Mitani *et al.* model [Mitani *et al.*, 1998].

Anomalous MR temperature dependencies have been reported previously by Dey *et al.* in $La_{0.7}Ca_{0.3}$ MnO_3 and $La_{0.67}Sr_{0.33}MnO_3$ nanoparticles, [Dey and Nath, 2006].

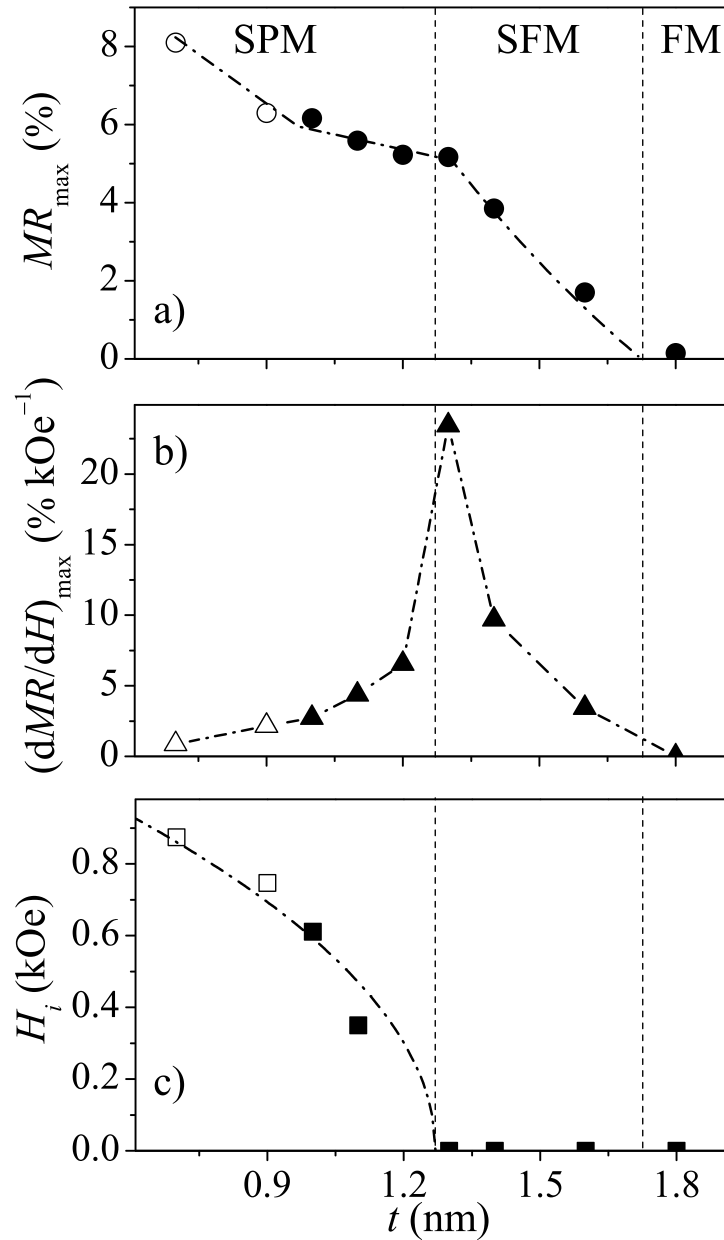

Figure 5.14: *Critical behavior at the SPM-SFM transition vs nominal thickness t of a granular layer:* ***(a)*** *maximum MR ratio ($MR_{\max}$);* ***(b)*** *MR field sensitivity (dMR/dH) at room temperature;* ***(c)*** *field H_i of maximum field sensitivity. Solid symbols stand for the previous data [Kakazei* et al.*, 2003 and Sousa* et al.*, 2001] and open symbols are for present measurements. Vertical lines delimit the ranges of SPM, SFM, and FM phases at this temperature.*

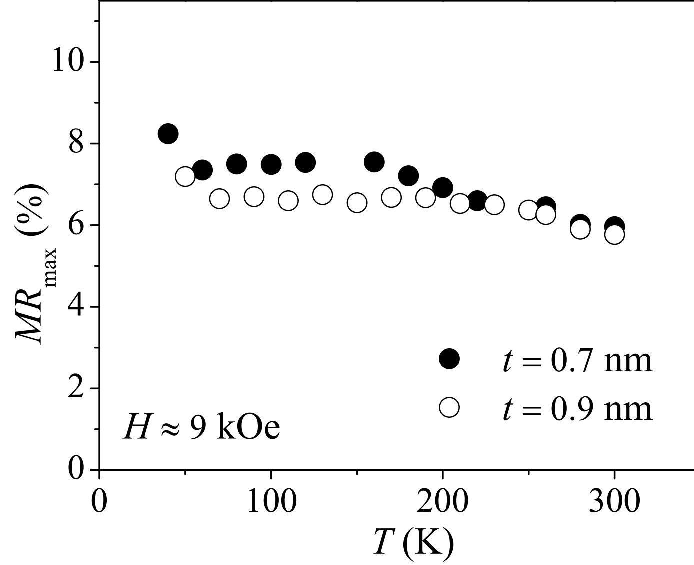

Figure 5.15: *Maximum MR ($H \approx$ 9 kOe) temperature dependence for both the thicknesses: $t = 0.7$ nm and $t = 0.9$ nm.*

These authors found that MR is constant up to $T \sim 220$ K and drops sharply after this temperature. Moreover, Bhattacharjee *et al.* [Bhattacharjee *et al.*, 2007] found in a calorimetric study an anomalous region around $T \sim 200$ K, claimed to be due to freezing of the orientational motion of the H_2O molecules present in the material.

Intriguingly, the temperature dependence of the MR loops for $t = 0.9$ nm reveals an anomaly consisting in a sudden change from a noisy behavior with $MR \propto |H|$ (for $H \to 0$) at $T \lesssim 220$ K to a low noise and $MR \propto H^2$ behavior as is shown in Fig. 5.16. This crossover temperature coincides with the temperature in which the I-V curves became noisy. This suggests that water contamination in our samples indeed causes a degradation of the I-V characteristics due to charge carriers trapping as well as a degradation of the MR. It is important to mention again that all the measurements were carried out in high vacuum. Even so and as mentioned before, it is known that water absorbed during sample processing and handling is very difficult to be removed.

Finally, the voltage dependence of MR shows no appreciable change in MR for bias voltage from ~ 0 to 30V (not shown). This contrasts with the high voltage dependence of MR in common magnetic tunnel junctions. Actually, a bias-independent MR has very important technological applications since MR ratios in granular films, although smaller than in MTJ, can be used in a wider range of bias voltage for a variety of electronic

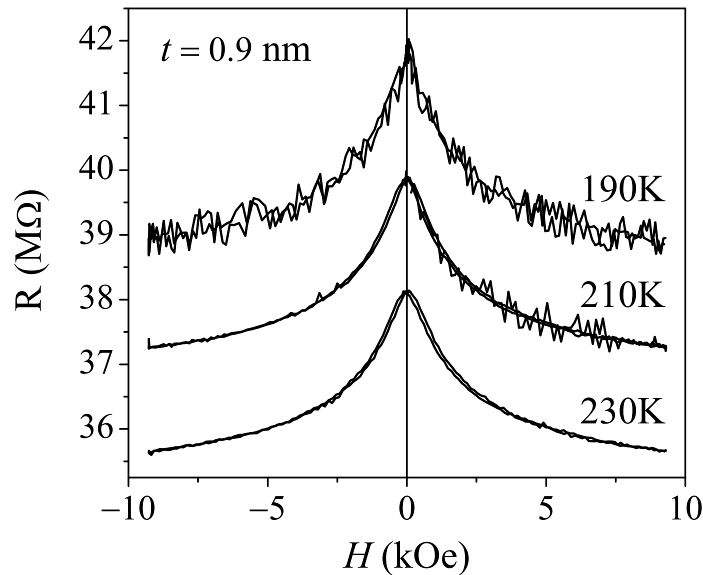

Figure 5.16: *Sudden change from a noisy MR behavior to a low noise behavior at $T \sim 220$ K for $t = 0.9$ nm.*

applications and keeping the same MR performance.

5.4 Resistive switching effects

In this Section, it is shown that the diluted magnetic granular samples studied in the previous Section also have interesting electrical switching properties, making them highly attractive for resistance random-access memory (ReRAM) applications, besides the common spintronic purposes. Further on, some interesting features were revealed, which may help to better understand the physics behind resistive switching. Is it important to mention that this Section is essentially focused in the $t = 0.9$ nm sample.

5.4.1 Resistive switching phenomena

Switching behaviors can be divided into two main classes: unipolar and bipolar. In unipolar RS, the switching direction depends on the amplitude of the applied voltage, but not on the electrical field direction (RS happens for both negative and positive voltages). Initially, the sample is in a high-resistance state (OFF) and is put into a low-resistance state (ON) by the application of high voltages. In the literature this is referred to the *forming process*. After the forming stage, the sample can switch from ON to OFF by

applying a *reset* voltage, and switch back to ON with a *set* voltage, typically larger than the *reset* voltage. Otherwise, in bipolar RS, a directional resistive switching appears, that depends on the polarity of the applied voltage. A very interesting review about bipolar switching can be found in Ref. [A. Sawa, 2008].

Furthermore, there are two main RS mechanisms discussed in the literature. A very popular one is the formation of *filamentary conducting paths* through the insulating matrix. In this context, switching is explained by reversible formation, in the *set process*, and rupture, in the *reset process*, of conduction filaments created in the insulator during the *forming process*. Details about this type of switching mechanism are presented in Ref. [Waser and Aono, 2007]. The other one is an *interface path* mechanism, in which the resistive switching takes place at the interface between the metal electrode and the oxide. It has various explanations, for example, electrochemical migration of oxygen vacancies [Nian *et al.*, 2007], trapping of charge carriers [Fujii *et al.*, 2005], and a Mott transition induced by carriers doped at the interface [Oka and Nagaosa, 2005]. Lets consider in more detail the basic processes for the mentioned mechanisms.

5.4.2 Forming process

Initially, the granular thin films behave as insulating[1] materials, in the OFF state. In this state, current-voltage (I-V) characteristics where measured by scanning the applied voltage from zero up to successively higher voltages. They exhibit a symmetrical behavior with a typical resistance of ~ 1 GΩ and little hysteresis. Such behavior is seen in Fig. 5.17a for the negative bias run.

When the scanning voltage range increases up to 30 V, the negative bias region maintains its normal behavior, however, in the return scan of the positive bias sweep, irregular behavior appears. The current becomes very noisy and its average value independent of voltage in the range from 30 to 10 V. Then, at 10 V, an abrupt switching event occurs increasing the current by more than two orders of magnitude, the ON state. After switching to ON, the noise in current also disappears.

After this event, the device I-V characteristics are from now on definitely modified and exhibit the behavior shown in Fig. 5.17b. As already mentioned this change in the behavior after a stressing voltage is known as *forming process* and is commonly reported

[1] In fact, it was just in this state that all the previous measurements were done.

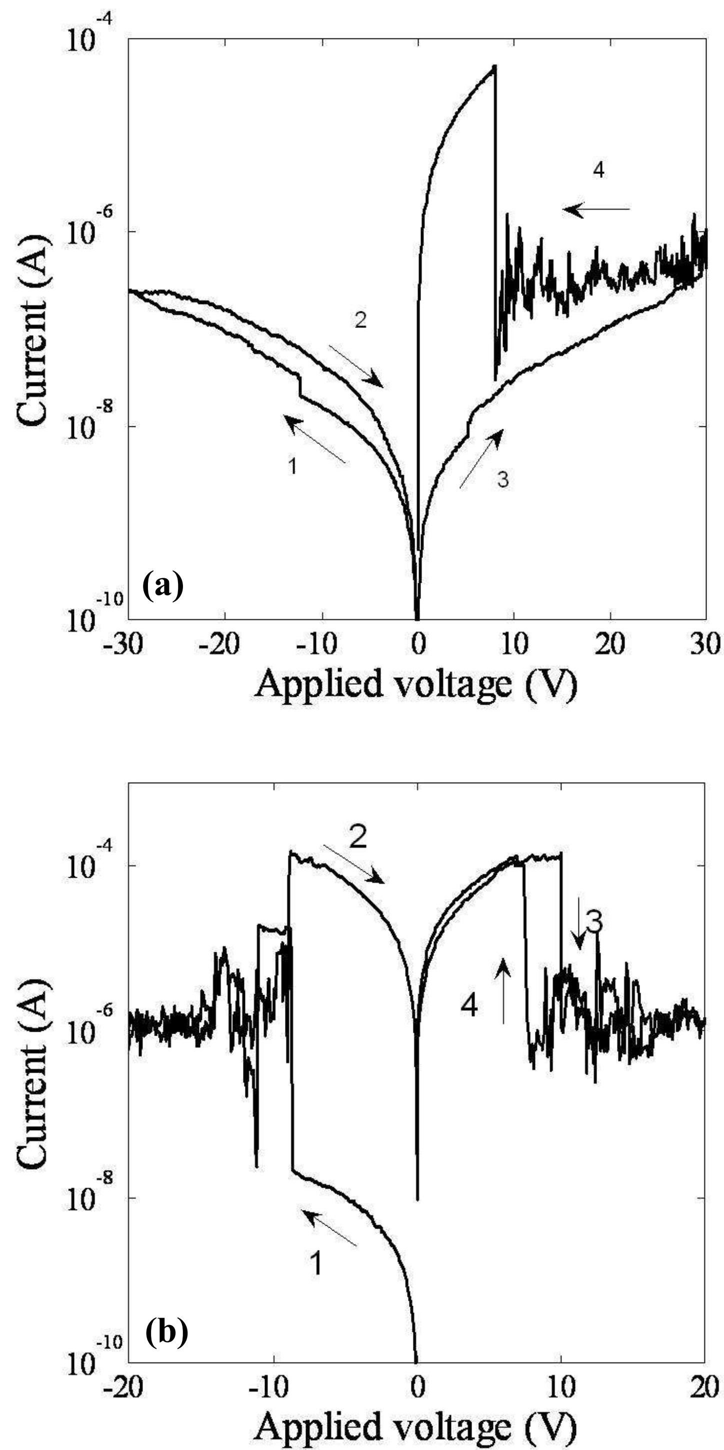

Figure 5.17: ***(a)*** *Current-voltage (I-V) plots showing a sudden and irreversible change (forming process). In the positive-bias return-voltage scan the current becomes noisy and switches between a low and a high conductive state at around* 10 *V.* ***(b)*** *I-V characteristics of a device obtained after forming.(Notice the logarithmic vertical scale of these plots).*

for other memory devices as previously noted [Blessing, 1978].

5.4.3 Memory resistive switching

Once the device is formed, the I-V characteristics can be programmed from a typical OFF state to an ON state. The up-scanning curve in the ON-state has a sudden drop at around 10 V, followed by a noisy behavior. This type of I-V characteristics resembles very much the negative differential resistance (NDR) characteristics reported in the literature for other memory devices [Tu *et al.*, 2006]. Reliable switching is now obtained by voltage pulses below and above the sharp drop in the current at the critical voltage of 10 V. For instance, switching from OFF to ON is achieved by applying a set voltage that is lower than 10 V. On the other hand, voltage pulse above the threshold voltage of 10 V must be applied to reset the device back to OFF. This type of switching behavior is typical for many insulating oxides. The ON and OFF states are stable for periods of several days. It is possible that these retention times are even longer but no detailed studies have been conducted yet.

5.4.4 Threshold resistive switching

Still, in one of the samples an additional effect was encountered, that might give an important insight on the way the effect occurs. After many cycles between the ON and OFF states, the low-voltage range begins to show a different behavior, as shown in Fig. 5.18. Most interestingly, there exists a switching of the PDR type (positive differential resistance): switching to ON occurs for higher biases, as can be seen in the figure. This switching is highly reproducible, occurring always at exactly the same threshold voltage, $V = 1.5$ V, and it corresponds to a weak programming field of the order of ~ 150 V/cm. Nonetheless, the retention time of the ON state is in a time scale of $1 - 3$ minutes and the device thus no longer behaves as a non-volatile memory. Non-volatile RS is called in literature the threshold resistive switching.

In addition, switching was also studied using small-signal impedance measurements. It was observed that resistive switching is accompanied by a single step change in capacitance from 2 pF to 15 pF at the same threshold voltage, as shown in Fig. 5.19a. When scanning the voltage slowly, it is possible to observe a series of capacitance jumps between the low and high capacitance states. These transitions are always located in a narrow

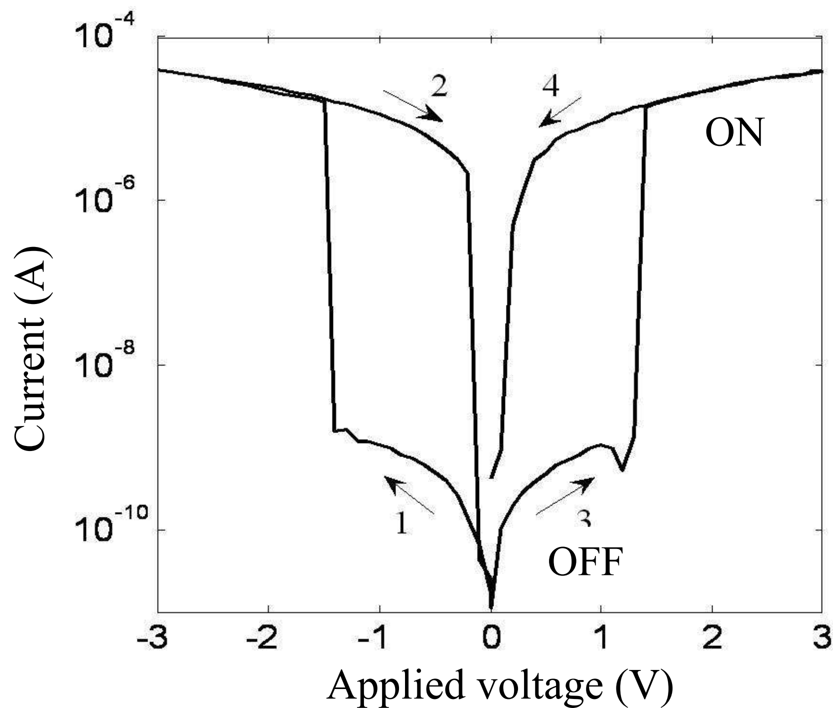

Figure 5.18: *Low-bias region of the final bistable current-voltage characteristics observed after many ON/OFF cycles.*

voltage range which overlaps with the voltage range where resistive switching occurs. This change between the two voltage independent capacitance states indicates that there are only two discrete states in the sample. As discussed above, RS is often attributed to the formation of filaments across the sample [Waser and Aono, 2007]. Even so, the observation here that the capacitance systematically switches between well-defined initial and final values, even after repeated switching as shown in Fig. 5.19b, seems counter-intuitive in a filamentary type of conduction. It is implausible that for every switching event, the same exact number of identical filaments are formed. Also one has to note that a single filament would be unable to carry the current observed ($\sim$ 0.1 mA). Therefore, this observation of discrete capacitance states cannot be simply explained by a discrete filamentary type of conduction.

5.4.5 New switching mechanism

The switching mechanism proposed here is mainly focused on the high electrical fields locally created when a single electron tunnels between neighbor grains. Just before the *jump* the local field can rise up to $\sim 10^6$ V/cm that is orders of magnitude higher

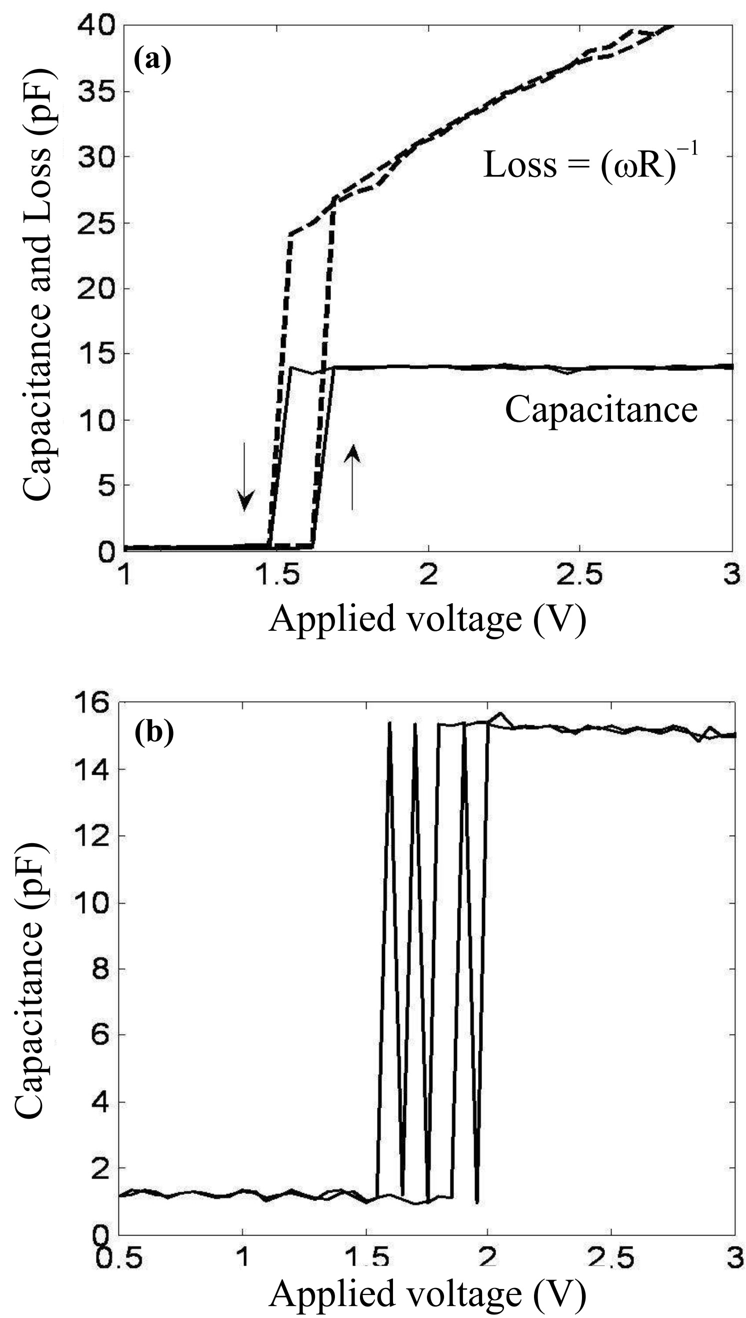

Figure 5.19: ***(a)*** *Step change in capacitance accompanying the resistive switching (f =1 kHz).* ***(b)*** *Capacitance jumps between two discrete states occurring at a constant voltage.*

than the external (uniform) applied field, typically of $\sim 10^2 - 10^3$ V/cm, and such a high local field can act on the defects in the insulating matrix, created during the forming process. This action can promote an atomic reconfiguration and thus facilitate tunneling processes between the grains, reducing the *waiting time* for a new tunneling event and increasing conductivity. If this reconfiguration process is extended through the whole sample, by an avalanche process of successive accumulation in the grains (not yet activated) and new reconfiguration events induced in their vicinity, conductive clusters can rapidly merge together reducing substantially the electrical distance between the electrodes. Such reduction also enhances the external applied field, reinforcing the process.

In this context, the increase in the capacitance is caused by the increase of free carrier density due to higher conductivity of layers containing the nanoparticles approximating the film capacitance to that of two parallel plate capacitor, formed by the gold electrodes and the conductive layer, which is a huge increase.

Obviously, both thermal energy and Joule effect are crucial in this mechanism and their role in switching phenomena have recently been clarified in Ref. [Chang *et al.*, 2009]. These effects also explain why two types of switching are found in these samples. First, the threshold RS, occurring at low bias, results from a metastable state of the reconfigured (highly conductive) matrix induced by low fields. In this case, when the field is removed, thermal energy can overcome the small energy barrier of such metastable state easily, recovering the initial low conductive state without any memory effect. Otherwise, if a high enough field is applied, a deep energy minima can be formed and the high conductive state is now more stable upon thermal activation, so a non-volatile (memory) effect can appear. In this configuration, a highly conductive state is maintained even without electrical field. If the voltage is further increased, well above the OFF/ON threshold voltage, a definitive (irreversible) highly conductive state is imposed and switching no longer occurs. A similar mechanism of electromigration of defects was suggested by J. Ventura, an IFIMUP member, in AlO_x based magnetic tunnel junctions [Ventura *et al.*, 2007]. Very interesting details about this effect can be found in his thesis [Ventura, 2006].

Additionally, the importance of grains in the overall switching mechanism was discussed in Ref. [Guan *et al.*, 2007]. In this work, a capacitor-like ZrO_2 structure with a middle Au granular layer was studied, and a clear demonstration that existence of a granular layer improves greatly the device yield compared with simple ZrO_2 structures

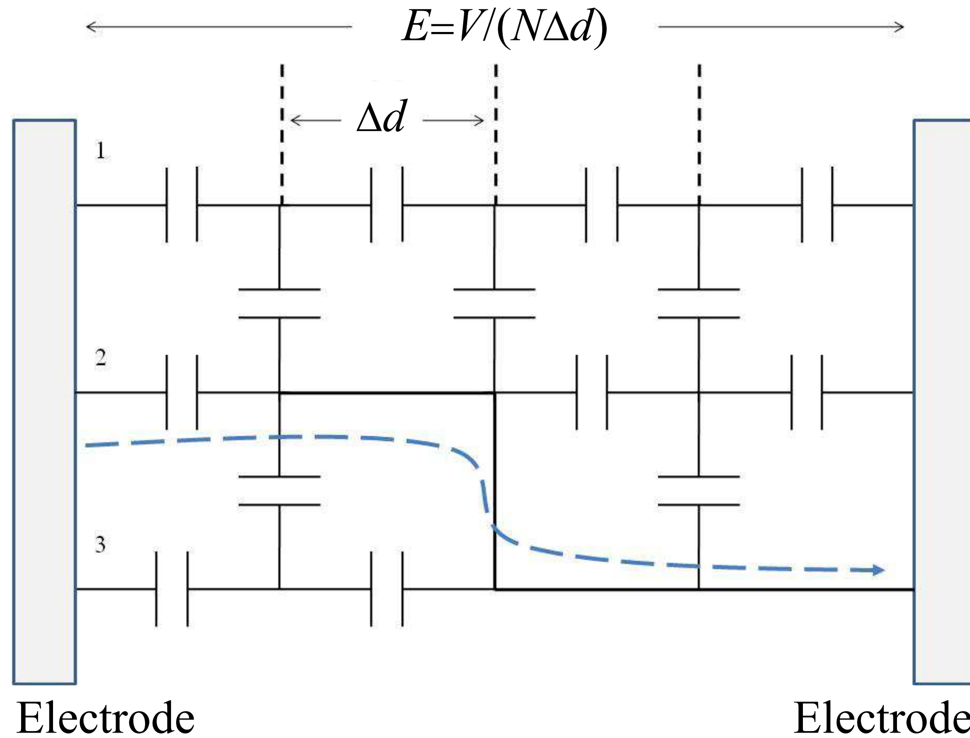

Figure 5.20: *Phenomenological model to explain the formation of a network of conducting paths across the sample.*

without this layer.

To, finally, exemplify this model the sample is represented by a network of N capacitors separated by a distance Δd, as shown in Fig. 5.20. The total applied field cross a straight path is then $E = V/(N\Delta d)$, where V is the applied voltage. If two neighbor regions merge together this is equivalent to a local electrical shortcut as shown in the path 2 in Fig. 5.20. The electric field across this particular path rises to $E = V/[(N - N_{\mathrm{sc}})\Delta d]$, where N_{sc} is the number of shortcuts. The higher electric field will favor the merging of more regions. Eventually, a cascade of connections will occur that rapidly creates an array of conducting paths across the entire sample in an avalanche process.

5.5 Conclusions

This chapter was constituted by two main parts: one devoted to the theoretical analysis of electronic transport in nanostructured granular films and the other to the experimental study of the magnetic and transport properties of granular multilayers,

$Al_2O_3/Co_{80}Fe_{20}$.

Theory revealed that the conduction in the free-area is basically ohmic and in the contact-area relevant non-linear effects appear. It is shown that for certain values of applied voltage the I-V curves follow a 3/2 power-law. This behavior agrees well with the experiments.

Additionally, the magnetic measurements revealed a narrow distribution of small sized granules in the *super-paramagnetic* state. The blocking temperature is found to increase with the films nominal thickness. Current-in-plane charge transport studies indicate *thermal assisted tunneling*, and a reasonable magnetoresistance ratio at room temperature is found. The study of magnetoresistance vs nominal thickness of granular layer permitted to detect critical behavior and to establish effective critical parameters of superparamagnetic/superferromagnetic transition. The importance of in-plane near neighbor granule correlations is evidenced by comparing magnetic and magneto-transport measurements. An unexpected temperature dependence of maximum magnetoresistance is found, with a significant decrease above a certain temperature (different from the blocking temperature) and unusual noisy behavior either in magnetoresistance and I-V characteristics was found near this temperature. This anomaly is attributed to water contamination (during processing/handling of samples). Water-related traps cause a reduction of the overall device current. This behavior appears suddenly at $\approx$ 200 K, suggesting its relation to a phase transition of supercooled water.

Furthermore, it was shown that the so-called negative differential resistance (NDR) region often observed in the current-voltage characteristics of memory devices is, in these structures, unusual and consists of a single abrupt switching event, and the impedance data reveal that there are only two capacitance states involved in the resistive switching, showing that switching is between two well-defined discrete states. The samples showed a large dynamic range of the resistance change. Most interesting, the threshold voltage for switching is highly reproducible and corresponds to a weak programming field, 150 V/cm, making these devices compatible with CMOS technology, an advantage for a realistic commercial device application. The discrete nature of capacitance switching presented here provides interesting information. While it is becoming accepted that switching is due to the establishment of discrete conducting filaments, the present results strongly suggests that, upon switching, there is also a charge trapping process in the device.

At least, this work thus also draws attention to the fact that the use of these granular materials in magnetic devices should also take their electrical resistive switching properties into account.

Chapter 6

Conclusions and Future Work

This thesis was mostly concerned with spin-dependent transport in magnetic nanostructures, such as magnetic multilayered junctions and magnetic granular thin films. The work was divided into two parts, one dedicated to the theoretical analysis of magnetic multilayered junctions and the second to the experimental study of magnetic granular thin films. Various conclusions were drawn and several ideas for future work were formulated, these will be summarized in the following:

6.1 Theory

6.1.1 Conclusions

The first five Sections of Chap. **3** were devoted to the investigation of single spacer junctions in the single-band tight-binding approximation revealing an enhancement of the magnetoresistance performance, higher than $\sim 3000\%$ (at zero temperature), when the atomic energy values of the spacer, ε_g, crossed from the ones typical for tunneling to those of metallic regimes, $\varepsilon_g \sim 1$ eV, in the so called *shallow band regime*. Another important feature found for this gate voltage regime is the calculated oscillatory behavior of MR with the number of atomic planes in the spacer.

In Sec. **3.6** of the same Chapter, the generalization of the model for a more realistic situation, including the effects of applied electrical voltage and finite temperature, revealed a monotonic decrease of ε_g^*, specific for shallow band regime effect, with temperature from $\varepsilon_g^* \sim 1$ eV at zero temperature to $\varepsilon_g^* \sim 0.5$ eV at room temperature, but still with a

measurable magnetoresistance performance of $\sim 700\%$ at this temperature.

Further, in the next Section, Sec. **3.7**, it was shown that already in absence of external electrical field, an essential perturbation of the equilibrium Fermi distribution appears for the antiparallel magnetic configuration of electrodes, leading to reduced occupation of one of the spin subbands (minority for negative or majority for positive band dispersion). This effect can locally influence the polarization of charge carriers and subsequently the magnetoresistance of the device.

At the end of Chap. **3**, in Sec. **3.8**, the fundamentals of charge and spin-torque transfer were also considered showing the possibility to calculate the dependence of both charge and spin currents in function of different parameters of the system (set invariable in usual treatments).

In Chap. **4**, the examination of complex multilayered magnetic structures using a simple matrix method (in the tight-binding approximation) revealed various resonant features causing even more significant magnetoresistance enhancement compared to that in simple trilayer case, reaching $\sim 15000\%$ values (for a junction of FIFNFIF type). In addition, this method allows the calculation of the magnetoresistance for an arbitrary multilayered system and can be readily used to investigate other types of junctions.

Finally, in Chap. **5** theoretical analysis of tunnel transport processes was done in a square lattice of metallic nanogranules embedded into insulating host. Based on a simple mean-field kinetic theory it was shown that the conduction in the free-area was basically ohmic and in the contact-area relevant non-linear effects appear. Also, it was found that for certain values of applied voltage the I-V curves follow a 3/2 power-law.

6.1.2 Future Work

There are many ideas that could be worth to be explored in future works.

1. It is important to generalize the single-band model to two bands with the aim of understanding how magnetoresistance performance will be affected upon passing to a more realistic band structure.

2. The effect of imperfections and lattices defects on the magnetoresistance should be considered.

3. It is also relevant to study junctions with semiconductor spacers and to investigate

the role of doping, for example, by magnetic materials. These studies could clarify which materials could be used to prepare real magnetic tunnel junctions with high magnetoresistance performance.

4. The model presented in this thesis for coherent spin-transfer torques could be applied in the context of the Landau-Lifshitz-Gilbert-Slonczewski equation to analyze possible new magnetization switching mechanisms arising from resonant effects near the *shallow band regime*.

5. It would be also interesting to study the spin-transfer torque across ferromagnetic/ superconductor/ ferromagnetic junctions. This effect was never considered in literature but could give an important insight for a new generation of spin-transfer torque based devices.

6.2 Experimental

6.2.1 Conclusions

Chapter **5** was dedicated to the study of diluted magnetic granular multilayered nanostructures. The Subsec. **5.2.1** revealed a slight deviation from the superparamagnetic state due to dipolar interactions among neighbor grains. The blocking temperatures are in the order of ~ 40 K, decreasing with the applied magnetic field. The anisotropy constant values found, $\sim 1.4 \times 10^6 \, \mathrm{erg\,cm^{-3}}$, are higher than the typical bulk ones, due to surface effects.

In the Subsec. **5.2.2**, charge transport measurements were performed in the current in plane geometry using two gold contacts evaporated on top of the samples. Current versus temperature measurements revealed activation energies typical of *thermally assisted tunneling*.

The next Subsection of the same Chapter, Subsec. **5.2.3**, analyzed the magnetotransport properties of the samples. The data revealed that at room temperature magnetoresistance has a sizeable value of 6% at fields of $H \sim 10$ kOe, and from an extrapolation of the Inoue-Maekawa law it is expected that magnetoresistance could reach $\sim 8\%$ near the saturation field, $H_s \sim 50$ kOe.

Further, in Sec. **5.3**, resistive switching properties also found in these samples (using

the same current geometry) were considered. It was shown that the resistive switching is followed by a capacitive switching of discrete nature, leading to the development of a new model for resistive switching phenomena, different from the common filamentary theory.

6.2.2 Future Work

Similarly to what happened in the theoretical part of the present thesis, plenty of new ideas appeared during its realization.

One promising perspective is the preparation of Fe/Cr/Fe and Co/Ru/Co in order to achieve the predicted MR enhancement near the *shallow band regime*. This work has already begun in the INESC-MN laboratories lead by Prof. Paulo Freitas with the collaboration of the post-doc researcher Jiangwei Cao, and now it should deserve a new attention. Other interesting possibility will be the preparation of organic spin-valves, like Fe/Pentacene/Fe, and compare the results with the model described above for semiconductor junctions. In fact, organic spintronics is an emergent field and relevant results are now been found.

Regarding the granular samples studied, it will be important to perform dielectric constant measurements in order to precisely determine the dielectric constant of this materials. Further, there are three experiments, not yet conducted, that are crucial to the understanding of the resistive switching properties:

1. Realization of ON/OFF cycles to test the reliability of the memory effect, and to estimate the *switching* and *dead* times;

2. Determination of the *retention* time;

3. The thermal dependence of resistive and capacitive switching that could clarify the importance of thermally activated process in the resistive switching.

Further on, it could be helpful to prepare new samples maintaining the Al_2O_3 matrix, but replacing CoFe by other metal, including non-magnetic ones, for example, gold (Au). This will elucidate the role of granules in the switching events.

Alternatively, there are new promising materials that could present a valuable magnetoresistive and resistive switching performance, for instance, granular CoFe embedded

into a MgO matrix. It is expected that coherent transport effects could enhance the MR of these devices, in a similar way as it does in common MgO tunnel junctions.

Appendix A

The orthogonalized eigen-states of the TB Hamiltonian, Eq. (3.50), can be built from its non-orthogonal eigen-states $|\alpha\rangle$, Eq. (3.55), for instance, with the known Gram-Schmidt procedure [Abramowitz and Stegun, 1964]. However, its algorithm of subsequent orthogonalization with respect to an arbitrarily chosen state can be optimized to a certain extent, taking account of the specific spin-incidence symmetry of the present problem. In this course, the first step is to build pairs of mutually orthogonal states from the states $|\alpha\rangle$ with the same incidence:

$$
\begin{aligned}
|1\rangle \quad \text{and} \quad |2\} &= \frac{|2\rangle - \langle 1|2\rangle|1\rangle}{W_{12}}, \\
|3\rangle \quad \text{and} \quad |4'\rangle &= \frac{|4\rangle - \langle 3|4\rangle|3\rangle}{W_{34}}.
\end{aligned}
\tag{A1}
$$

where $W_{12} = \sqrt{1 - |\langle 1|2\rangle|^2}$, $W_{34} = \sqrt{1 - |\langle 3|4\rangle|^2}$. Then the common Gram-Schmidt routine is followed for the $|3\rangle, |4'\rangle$ states with respect to the pair $|1\rangle$, $|2\}$ (already the elements of true basis), resulting in two next elements of this basis:

$$
\begin{aligned}
|3\} &= \frac{|3\rangle - \langle 1|3\rangle|1\rangle - \{2|3\rangle|2\}}{W_{123}}, \\
|4\} &= \frac{|4'\rangle - \langle 1|4'\rangle|1\rangle - \{2|4'\rangle|2\} - \{3|4'\rangle|3\}}{W_{1234}},
\end{aligned}
\tag{A2}
$$

where $W_{123} = \sqrt{1 - |\langle 1|3\rangle|^2 - |\{2|3\rangle|^2}$ and $W_{1234} = \sqrt{1 - |\langle 1|4'\rangle|^2 - |\{2|4'\rangle|^2 - |\{3|4'\rangle|^2}$. These formulas involve the following scalar products of modified states expressed through the scalar products of spin-incidence states:

$$
\begin{aligned}
\{2|3\rangle &= \frac{\langle 2|3\rangle - \langle 2|1\rangle\langle 1|3\rangle}{W_{12}}, \\
\langle 1|4'\rangle &= \frac{\langle 1|4\rangle - \langle 1|3\rangle\langle 3|4\rangle}{W_{34}}, \\
\{2|4'\rangle &= (\langle 2|4\rangle - \langle 2|3\rangle\langle 3|4\rangle - \langle 2|1\rangle\langle 1|4\rangle \\
&+ \langle 2|1\rangle\langle 1|3\rangle\langle 3|4\rangle) \,/\, (W_{12}W_{34}), \\
\{3|4'\rangle &= \left[\langle 3|4\rangle|123| - \langle 1234\rangle/\left(1 - |\langle 1|2\rangle|^2\right)\right] / \left(W_{12}W_{34}\right),
\end{aligned}
$$

with the following combinations of spin-incidence scalar products:

$$
\begin{aligned}
|123| &= |\langle 1|3\rangle|^2 + |\langle 2|3\rangle|^2 + |\langle 1|2\rangle\langle 2|3\rangle|^2 \\
&- 2\mathrm{Re}\left(\langle 1|2\rangle\langle 2|3\rangle\langle 3|1\rangle\right), \\
\langle 1234\rangle &= \langle 3|1\rangle\langle 1|4\rangle + \langle 3|2\rangle\langle 2|4\rangle \\
&- \langle 3|2\rangle\langle 2|1\rangle\langle 1|4\rangle - \langle 3|1\rangle\langle 1|2\rangle\langle 2|4\rangle.
\end{aligned}
$$

Finally the spin-incidence scalar products are expressed through the transport coefficients as:

$$
\begin{aligned}
\langle 1|2\rangle &= \frac{\Omega_1\Omega_2}{2}\left(\hat{r}_1^\dagger\hat{r}_2 + \hat{t}_1^\dagger\hat{t}_2\right), \\
\langle 1|3\rangle &= \frac{\Omega_1\Omega_3}{2}\left(\hat{r}_1^\dagger\hat{t}_3 + \hat{t}_1^\dagger\hat{r}_3\right), \\
\langle 1|4\rangle &= \frac{\Omega_1\Omega_4}{2}\left(\hat{r}_1^\dagger\hat{t}_4 + \hat{t}_1^\dagger\hat{r}_4\right), \\
\langle 2|3\rangle &= \frac{\Omega_2\Omega_3}{2}\left(\hat{r}_2^\dagger\hat{t}_3 + \hat{t}_2^\dagger\hat{r}_3\right), \\
\langle 2|4\rangle &= \frac{\Omega_2\Omega_4}{2}\left(\hat{r}_2^\dagger\hat{t}_4 + \hat{t}_2^\dagger\hat{r}_4\right), \\
\langle 3|4\rangle &= \frac{\Omega_3\Omega_4}{2}\left(\hat{r}_3^\dagger\hat{r}_4 + \hat{t}_3^\dagger\hat{t}_4\right).
\end{aligned} \tag{A3}
$$

Besides, the detailed calculation of different contributions to the orthogonalization coefficients $O_{\zeta,\alpha}$ can be facilitated by using specifical diagramatic technics where the products of matrix elements are represented by certain complexes of straight lines. Each line joins two points α and α' from a sequence 1,2,3,4 (seen as vertices of a square) and represents a matrix element $\langle\alpha|\alpha'\rangle$. The advantage of this approach is the easier way to find the common factors in numerators and denominators and to do their proper cancellations. An example of such diagrams is given in Fig. 6.1.

Using the above equations, Eq. (A3), the orthogonalization coefficients $O_{\alpha,\zeta}$ are

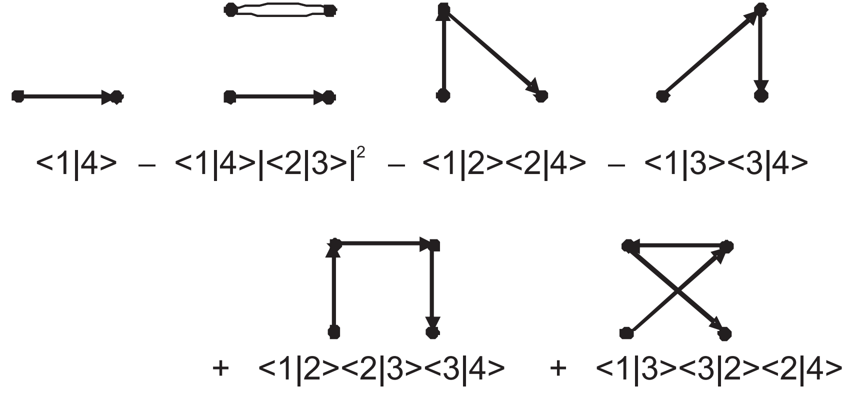

Figure 6.1: *An example of using the diagrammatic technics for calculation of orthogonal eigenstates. The set of diagrams defining the numerator of the orthogonalization coefficient O_{41} in Eq. (A4).*

defined as:

$$
\begin{aligned}
O_{11} &= 1, \\
O_{21} &= -\frac{\langle 1|2\rangle}{W_{12}}, \\
O_{22} &= \frac{1}{W_{12}}, \\
O_{31} &= \frac{-\langle 1|3\rangle + \langle 1|2\rangle\langle 2|3\rangle}{W_{123}W_{12}}, \\
O_{32} &= \frac{-\langle 2|3\rangle + \langle 2|1\rangle\langle 1|3\rangle}{W_{123}W_{12}}, \\
O_{33} &= \frac{W_{12}}{W_{123}}, \\
O_{41} &= \frac{W_{124}\left[\langle 1|4\rangle \left(W_{12}^2 - |\langle 2|3\rangle|^2 + |\langle 1|2\rangle\langle 2|3\rangle|^2\right) - W_{12}^2\,\langle 1|2\rangle\langle 2|4\rangle\right]}{W_{1234}W_{123}}, \\
O_{42} &= \frac{W_{123}\left[\langle 2|4\rangle \left(W_{12}^2 - |\langle 2|3\rangle|^2 + |\langle 1|2\rangle\langle 2|3\rangle|^2\right) - W_{12}^2\,\langle 2|1\rangle\langle 1|4\rangle\right]}{W_{1234}W_{124}}, \\
O_{43} &= -\frac{W_{12}^2\,\langle 3|4\rangle - \langle 3|1\rangle\langle 1|4\rangle - \langle 3|2\rangle\langle 2|4\rangle + \langle 3|1\rangle\langle 1|2\rangle\langle 2|4\rangle + \langle 3|2\rangle\langle 2|1\rangle\langle 1|4\rangle}{W_{1234}}, \\
O_{44} &= \frac{W_{12}W_{123}}{W_{1234}},
\end{aligned}
\tag{A4}
$$

with the explicit values for the W coefficients as:

$$\begin{aligned}
W_{12} &= \left[1 - |\langle 1|2\rangle|^2\right]^{\frac{1}{2}}, \\
W_{123} &= \left[W_{12}^2 - |\langle 1|3\rangle|^2 - |\langle 2|3\rangle|^2 + 2\mathrm{Re}\left(\langle 1|2\rangle\langle 2|3\rangle\langle 3|1\rangle\right)\right]^{\frac{1}{2}}, \\
W_{124} &= \left[W_{12}^2 - |\langle 1|4\rangle|^2 - |\langle 2|4\rangle|^2 + 2\mathrm{Re}\left(\langle 1|2\rangle\langle 2|4\rangle\langle 4|1\rangle\right)\right]^{\frac{1}{2}}, \\
W_{1234} &= \Big[W_{123}^2 W_{124}^2 - \big|W_{12}^2\,\langle 3|4\rangle - \langle 3|1\rangle\langle 1|4\rangle - \langle 3|2\rangle\langle 2|4\rangle \\
&\qquad + \langle 3|1\rangle\langle 1|2\rangle\langle 2|4\rangle + \langle 3|2\rangle\langle 2|1\rangle\langle 1|4\rangle\big|^2\Big]^{\frac{1}{2}},
\end{aligned} \tag{A5}$$

Appendix B

Lets consider the equation:

$$\frac{d}{d\xi}\left[g\left(\sigma\right)+\tau\right]\frac{d\sigma}{d\xi}-k^{2}\sigma=0 \tag{B1}$$

with certain boundary conditions $\sigma(0)=\sigma_0$, $\sigma'(0)=\sigma_0'$, resulting from Eqs. 5.25,5.26. For a rather general function $g\left(\sigma\right)$ it is possible to define the function:

$$f\left(\sigma\right)=\int_0^{\sigma} g\left(\sigma'\right)d\sigma', \tag{B2}$$

then Eq. B1 presents itself as:

$$\frac{d^{2}F\left(\xi\right)}{d\xi^{2}}=k^{2}\sigma\left(\xi\right), \tag{B3}$$

where $F\left(\xi\right)\equiv f[\sigma(\xi)]+\tau\sigma(\xi)$. Considered irrespectively of ξ:

$$f(\sigma)+\tau\sigma=F, \tag{B4}$$

this equation also defines σ as a certain function of F: $\sigma=\sigma(F)$. Hence it is possible to construct the following function:

$$\varphi\left(F\right)=2\int_0^{F}\sigma(F')dF'. \tag{B5}$$

Now, multiplying Eq. B3 by $2dF/d\xi$, the equation becomes:

$$\frac{d}{d\xi}\left(\frac{dF}{d\xi}\right)^{2}=k^{2}\frac{d\varphi}{d\xi}, \tag{B6}$$

with $\varphi(\xi)\equiv\varphi[F(\xi)]$. Integrating Eq. B6 in ξ, a 1st order separable equation for $F(\xi)$ is obtained:

$$\frac{dF}{d\xi}=\pm k\sqrt{\varphi(F)}. \tag{B7}$$

It is expected that the function F decreases at going from $\xi=0$ into depth of interface region, hence choose the negative sign on r.h.s. of Eq. B7 and obtain its explicit solution as:

$$\int_{F(\xi)}^{F_0} \frac{dF'}{\sqrt{\varphi(F')}} = k\xi \tag{B8}$$

with $F_0 = f(\sigma_0) + \tau\sigma_0$. Finally, the sought solution for $\sigma(\xi) = \sigma[F(\xi)]$ results from substitution of the function $F(\xi)$, given implicitly by Eq. B8, into $\sigma(F)$ defined by Eq. B4. Consider some particular realizations of the above scheme.

For simplified function $g(\sigma)$ given previously, the explicit integral, Eq. B2, is given in the form:

$$F(\sigma) = f(\sigma) + \tau\sigma = \left(\tau + \frac{\sqrt{\rho_0^2 + \sigma^2}}{2} - \rho_0^2 - \frac{\sigma^2}{3}\right)\sigma + \rho_0^2 \ln\sqrt{\frac{\sigma + \sqrt{\rho_0^2 + \sigma^2}}{\rho_0}}. \tag{B9}$$

In the case $\sigma \ll \rho_0 \ll 1$ (Regime I), Eq. B9 is approximated as:

$$F \approx (\rho_0 + \tau)\sigma + \frac{\sigma^3}{6\rho_0}, \tag{B10}$$

hence $\sigma(F)$ corresponds to a real root of the cubic equation, Eq. B10, and in the same approximation of regime I it is given by:

$$\sigma(F) \approx \frac{F}{\rho_0 + \tau}\left(1 - \frac{8F^2}{\sigma_1^2}\right), \tag{B11}$$

with $\sigma_1 = 4\sqrt{\rho_0(\rho_0 + \tau)^3}$. Using this form in Eq. B5, it results in:

$$\varphi(F) \approx \frac{F^2}{\rho_0 + \tau}\left(1 - \frac{4F^2}{\sigma_1^2}\right), \tag{B12}$$

and then substituting into Eq. B8:

$$\ln\frac{\left[1 + \sqrt{1 - (2F/\sigma_1)^2}\right]F_0}{\left[1 + \sqrt{1 - (2F_0/\sigma_1)^2}\right]F} = \lambda\xi. \tag{B13}$$

Inverting this relation, an explicit solution for $F(\xi)$ is defined:

$$F(\xi) \approx F_0 \mathrm{e}^{-\lambda\xi}\left[1 + \frac{F_0^2}{\sigma_1^2}\left(1 - \mathrm{e}^{-2\lambda\xi}\right)\right]. \tag{B14}$$

Finally, substituting Eq. B14 into Eq. B11, the result of Eq. 5.29 is presented in Fig. 6.2.

In a similar way, for the regime II it is found:

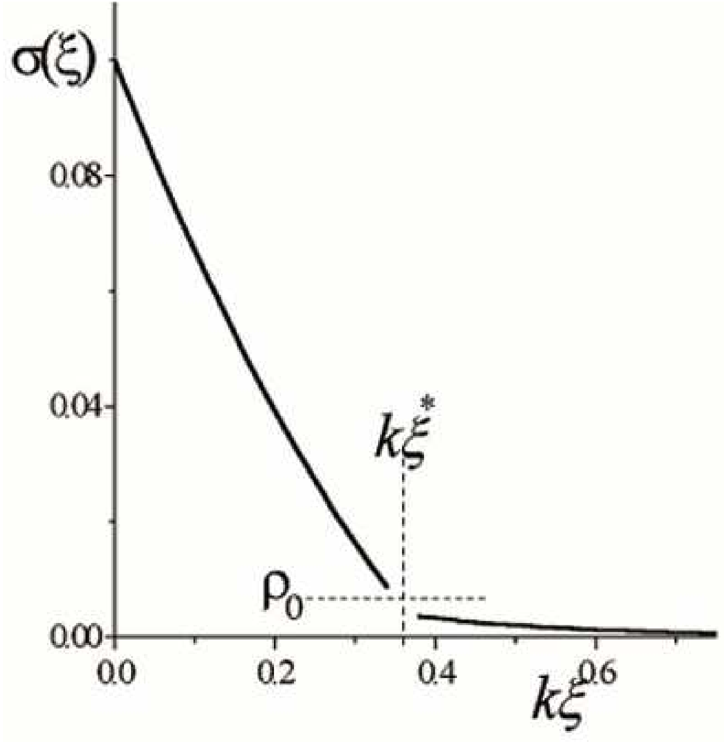

Figure 6.2: *Charge density and current distribution in CA region (regime I).*

$$
\begin{aligned}
F(\sigma) &\approx \sigma(\tau + \sigma/2), \\
\sigma(F) &\approx \sqrt{2F + \tau^2} - \tau, \\
\varphi(F) &\approx \frac{2}{3}\left[\left(2F + \tau^2\right)^{3/2} - \tau\left(3F + \tau^2\right)\right] \\
F(\xi) &\approx \left[F_0^{1/4} - \lambda_1 \xi + \frac{3\tau}{2^{5/4}\left(F_0^{1/4} - \lambda_1 \xi\right)}\right]^4,
\end{aligned}
\tag{B15}
$$

with $\lambda_1 = k/(2^{3/4}\sqrt{3})$, obtaining the charge density distribution (Fig. 6.3):

$$
\sigma(\xi) \approx \left(\sqrt{\sigma_0 + \tau} - \lambda_1 \xi\right)^2 - \tau. \tag{B16}
$$

This function seems to turn zero already at $\xi = (\sqrt{\sigma_0 + \tau} - \sqrt{\tau})/\lambda_1$, but in fact the fast parabolic decay by Eq. B16 only extends to $\xi \sim \xi^*$, such that $\sigma(\xi^*) \sim \rho_0$, and for $\xi > \xi^*$ the decay turns exponential, like Eq. 5.29. The I-V characteristics, Eq. 5.32, follows directly from Eq. B16.

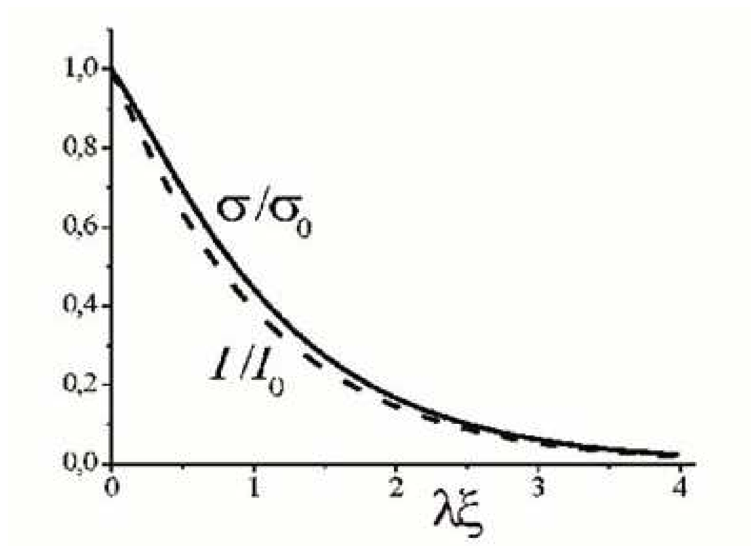

Figure 6.3: *Charge density in regime II. A fast decay is change to a slower exponential law, after density dropping below the characteristic value* ρ_0.

Appendix C

In order to fit the low-field magnetization dependence on temperature, we use the model by Respaud *et al.* [Respaud *et al.*, 1998], that presents the total magnetization $M(H)$ as a sum of contributions by SPM and blocked granules in the linear response approximation. The zero-field-cooled (ZFC) and field-cooled (FC) magnetizations are respectively given by the formulae:

$$\begin{aligned} M_{ZFC}(T,H) &= M_s^2 H \left(I_1 + I_2\right), \\ M_{FC}(T,H) &= M_s^2 H \left(I_1 + \alpha I_2\right), \end{aligned} \tag{C1}$$

where M_s is the granule saturated magnetization (taken temperature independent), V is the volume of ferromagnetic materials, α is related with the *measurement time* and is very often set as 30 s (but not necessarily), and the integrals

$$\begin{aligned} I_1(T) &= \frac{1}{3Vk_BT}\int_0^{v_m(T)} v^2 f(v)dv, \\ I_2(T) &= \frac{1}{3VK_{\text{eff}}}\int_{v_m(T)}^{\infty} vf(v)dv \end{aligned} \tag{C2}$$

include the log-normal distribution function for granule volumes:

$$f(v) = \frac{V}{\sqrt{2\pi}s\overline{v}v}\exp\left[-\frac{1}{2}\left(\frac{1}{s^2}\ln^2\frac{v}{\overline{v}} + s^2\right)\right], \tag{C3}$$

with mean value $\overline{v}$ and standard deviation s. The integrals (C2) account for the contributions by smaller (SPM, I_1) and bigger (blocked, I_2) granules, distinguished by the characteristic volume $v_m = \alpha k_{\text{B}}T/K_{\text{eff}}$, where K_{eff} is the effective uniaxial anisotropy constant and the Brown's theory [Brown, 1963] parameter (also present in Eq. (C1)) is taken as $\alpha = \ln\left(\tau_{meas}/\tau_s\right)$ for given measurement and spin precession times, τ_{meas} and τ_s.

Passing to the variable $x = \ln(v/\overline{v})$ and defining a usual Gaussian structure in the resulting integrands, it can be found that:

$$I_1(T) = \frac{\overline{v}}{6k_BT}\exp\left(\frac{3s^2}{2}\right)\left[1 + \text{Erf}\left(\frac{1}{\sqrt{2}s}\ln\frac{v_m}{\overline{v}} - \sqrt{2}s\right)\right] \tag{C4}$$

$$I_2(T) = \frac{1}{6K_{\text{eff}}}\left[1 - \text{Erf}\left(\frac{1}{\sqrt{2}s}\ln\frac{v_m}{\overline{v}} - \frac{s}{\sqrt{2}}\right)\right] \tag{C5}$$

These analytic formulas were used in Eq. C1 to fit the FC and ZFC magnetization data.

List of Communications

Journal Publications

1. *Magnetic and transport properties of diluted granular multilayers*, H.G. Silva, H. L. Gomes, Y. G. Pogorelov, L. M. C. Pereira, G. N. Kakazei, J. B. Sousa, J. P. Araújo, J. F. L. Mariano, S. Cardoso, and P.P. Freitas, (accepted in) Journal of Applied Physics.
2. *Temperature and voltage effects in high performance magnetic junctions*, H. G. Silva, Y. G. Pogorelov, Phys. Status Solidi (c) **6**, 2150 (2009).
3. *Matrix description of magnetotransport in perfect multilayered structures*, H. G. Silva and Yu. G. Pogorelov, J. Phys. D: Appl. Phys. **42**, 195003 (2009).
4. *Resistive switching in nanostructured thin films*, H. Silva, H. L. Gomes, Yu. G. Pogorelov, P. Stallinga, Dago M. de Leeuw, J. P. Araújo, J. B. Sousa, S. C. J. Meskers, G. N. Kakazei, S. Cardoso and P. P. Freitas, Appl. Phys. Lett. **94**, 202107 (2009).
5. *Simple tight-binding theory for magnetoresistance in perfect sandwiched structures*, H. G. Silva and Yu. G. Pogorelov, Phys. Rev. B **78**, 094428 (2008).
6. *Coherent effects for electronic equilibrium and transport in perfect magnetic junctions*, H. Silva and Yu. Pogorelov, IEEE Trans. Mag. **44**, 11 (2008).
7. *Coherent transport in high performance double-spacer magnetic junctions*, H. G. Silva, Y. G. Pogorelov, Journal of Non-Crystalline Solids **354**, 5318 (2008).
8. *Coherent transport in high performance double magnetic junctions*, H. G. Silva, Y. G. Pogorelov, (accepted in) Journal of Nanoscience and Nanotechnology.

Oral Communications

1. *Matrix description of magnetotransport in perfect multilayered structures*, 15th Workshop on Magnetism and Intermetalics, Lisbon, Portugal.

2. *Temperature and voltage dependencies for high performance magnetic junctions*, Trends in Nanotechnology 2008 (TNT2008) Oviedo, Spain.

Poster Communications

1. *Magnetic and transport properties of diluted granular multilayers*, International Conference in Magnetism (ICM 2009), Karlsruhe, Germany.
2. *Charge and spin-transfer by fully coherent magnetic junctions*, International Conference in Magnetism (ICM 2009), Karlsruhe, Germany.
3. *Magnetic and transport properties of diluted granular multilayers*, V International Materials Symposium MATERIAIS 2009, Lisboa, Portugal.
4. *Charge and spin-transfer by fully coherent magnetic junctions*, Magnetic Single Nano-Object Workshop (MSNOW2008), Nancy, France.
5. *Quantum coherent effects in double magnetic tunnel junctions*, Advanced Nano Materials 2008 (ANM 2008), Aveiro, Portugal.
6. *Coherent effects for electronic equilibrium and transport in perfect magnetic junctions*, International Magnetics Conference, Europe 2008 (INTERMAG EUROPE 2008), Madrid, Spain.
7. *Quantum spin-resonant tunneling in magnetic junctions with double-spacer structure*, 9th International Workshop on Non-Crystaline Solids (IWNCS 2008) Porto, Portugal.
8. *Non-linear electrical field effect in spin-dependent quantum transport*, 2nd Workshop on Low-Dimensional Structures: Properties and Applications (WLDS08) Aveiro, Portugal.
9. *Quantum coherence in spintronic devices with ultra-thin organic semiconductor spacer*, Workshop on Spintronic Effects in Organic Semiconductors (SpinOs 2007) Bologna, Italy.

10. *Quantum effects in multicomponent magnetoresistive systems*, 3th Seeheim Conference on Magnetism Frankfurt, Germany.

Bibliography

M. Abramowitz and I. Stegun, *Handbook of mathematical functions with formulas, graphs, and mathematical tables.* Dover, New York, 1964.

N. Agraït, A. Levy Yeyati and J. M. van Ruitenbeek, *Quantum properties of atomic-sized conductors*, Phys. Rep. **377**, 81-279 (2003).

A. Asamitsu, Y. Tomioka, H. Kuwahara, Y. Tokura, *An X-ray-induced insulator-metal transition in a magnetoresistive manganite*, Nature **388**, 50 (1997).

Y. Asano, A. Oguri, and S. Maekawa, *Parallel and perpendicular transport in multilayered structures*, Phys. Rev. B **48**, 6192 (1993).

N.W. Ashcroft and D. N. Mermin, *Solid state physics.* Saunders College Publishing, New York, first edition (1976).

D. Bagayoko, A. Ziegler, and J. Callaway, *Band structure of bcc cobalt*, Phys. Rev. B **27**, 7046 (1983).

M. N. Baibich, J. M. Broto, A. Fert, F. N. Van Dau, F. Petroff, P. Eitenne, G. Creuzet, A. Friederich and J. Chazelas, *Giant magnetoresistance of* (001) *Fe* / (001) *Cr magnetic superlattices*, Phys. Rev. Lett. **61**, 2472 (1988).

J. Baltrusaitis, J. Schuttlefield, J.H. Jensen and V.H. Grassian, *FTIR spectroscopy combined with quantum chemical calculations to investigate adsorbed nitrate on aluminum oxide surfaces in the presence and absence of Co-adsorbed water*, Phys. Chem. Chem. Phys., **9**, 4970 (2007).

J. Barnaś, A. Fert, M. Gmitra, I. Weymann and V. K. Dugaev, *From giant magnetoresistance to current-induced switching by spin transfer*, Phys. Rev. B **72**, 024426 (2005).

G. E. W. Bauer, *Perpendicular Transport through Magnetic Multilayers*, Phys. Rev. Lett. **69**, 2472 (1992).

S. Bedanta and W. Kleemann, *Supermagnetism*, J. Phys. D: Appl. Phys. **42**, 013001 (2009).

I. S. Beloborodov, A. V. Lopatin, V. M. Vinokur, and K. B. Efetov, *Granular electronic systems*, Rev. Mod. Phys.**79**, 469 (2007).

L. Berger, *Emission of spin waves by a magnetic multilayer traversed by a current*, Phys. Rev. B **54**, 9354 (1996).

A. Bhattacharjee, S. Saha, S. Koner and Y. Miyazaki, *Phase transitions in mixed-valence potassium manganese hexacyanoferrate Prussian blue analogue: Heat capacity calorimetric study*, J. Magn. Magn. Mat. **312** 435 (2007).

G. Binasch, P. Grünberg, F. Saurenbach and W. Zinn, *Enhanced magnetoresistance in layered magnetic structures with antiferromagnetic interlayer exchange*, Phys. Rev. B **39**, 4828 (1989).

R. Blessing and H. Pagnia, *Forming process, I-V characteristics and switching in gold island films*, Thin Solid Films **52**, 333 (1978).

W.F. Brown Jr, *Thermal fluctuations of a single-domain particle*, Phys. Rev. **130**, 1677 (1963).

R. Bručas, M. Hanson, R. Gunnarsson, E. Wahlström, M. van Kampen, B. Hjörvarsson, H. Lidbaum and K. Leifer, *Magnetic and transport properties of* $Ni_{81}Fe_{19}/Al_2O_3$ *granular multilayers approaching the superparamagnetic limit*, J. Appl. Phys. **101**, 073907 (2007).

M. Bütikker, *Symmetry of electrical conduction*, IBM J. Res. Dev. **32**, 317 (1988).

W. H. Butler, X.-G. Zhang, T. C. Schulthess, and J. M. MacLaren, *Spin-dependent tunneling conductance of Fe-MgO-Fe sandwiches*, Phys. Rev. B **63**, 054416 (2001).

J. Callaway and C. S. Wang, *Energy bands in ferromagnetic iron*, Phys. Rev. B **16**, 2095 (1977).

R. E. Camley and J. Barnaś, *Theory of giant magnetoresistance effects in magnetic layered Structures with antiferromagnetic coupling*, Phys. Rev. Lett. **63**, 664 (1989).

S. Cardoso, *Dual-stripe GMR and tunnel junction read heads and ion beam deposition and oxidation of tunnel junctions*, PhD thesis, Instituto Superior Técnico, 2003.

S. H. Chang, J. S. Lee, S. C. Chae, S. B. Lee, C. Liu, B. Kahng, D.-W. Kim, and T.W. Noh, *Occurrence of both unipolar memory and threshold resistance switching in a NiO film*, Phys. Rev. Lett. **102**, 026801 (2009).

W. Chandra, L. K. Ang, and K. L. Pey, and C. M. Ng, *Two-dimensional analytical Mott-Gurney law for a trap-filled solid*, Appl. Phys. Lett. **90**, 153505 (2007).

O. Chayka, L. Kraus, P. Lobotka, V. Sechovsky, T. Kocourek, and M. Jelinek, *High field magnetoresistance in Co-Al-O nanogranular films*, J. Magn. Magn. Mat. **300**, 293 (2006).

X. Chen, S. Bedanta, O. Petracic, W. Kleemann, S. Sahoo, S. Cardoso, and P. P. Freitas, *Superparamagnetism versus superspin glass behavior in dilute magnetic nanoparticle systems*, Phys. Rev. B **72**, 214436 (2005).

C. Cohen-Tannoudji, B. Diu, and F. Laloë, *Quantum mechanics.* Hermann, Paris, 1977.

S. Datta, *Electronic transport in mesoscopic systems*, Cambridge University Press, Cambridge, England (1995).

P. Dey and T. K. Nath, *Effect of grain size modulation on the magneto- and electronic-transport properties of $La_{0.7}Ca_{0.3}MnO_3$ nanoparticles: The role of spin-polarized tunneling at the enhanced grain surface*, Phys. Rev. B **73**, 214425 (2006).

A. Dorn, T. Ihn, K. Ensslin, W. Wegscheider, and M. Bichler, *Electronic transport through a quantum dot network*, Phy. Rev. B **70**, 205306 (2004).

D. M. Edwards, F. Federici, J. Mathon and A. Umerski, *Self-consistent theory of current-induced switching of magnetization*, Phys. Rev. B **71**, 054407 (2005).

G. Feng, S. van Dijken, and J. M. D. Coey, *Influence of annealing on the bias voltage dependence of tunneling magnetoresistance in MgO double-barrier magnetic tunnel junctions with CoFeB electrodes*, Appl. Phys. Lett. **89**, 162501 (2006).

P. P. Freitas and L. Berger, *Observation of s-d exchange force between domain walls and electric current in very thin Permalloy films*, J. Appl. Phys. **57**, 1266 (1985).

T. Fujii, M. Kawasaki, A. Sawa, H. Akoh, Y. Kawazoe, and Y. Tokura, *Hysteretic current-voltage characteristics and resistance switching at an epitaxial oxide Schottky junction* $SrRuO_3/SrTi_{0.99}Nb_{0.01}O_3$, Appl. Phys. Lett. **86**, 012107 (2005).

A. García-García, A. Vovk, J. A. Pardo, P. Štrichovanec, C. Magén, E. Snoeck, P. A. Algarabel, J. M. De Teresa, L. Morellón, M. R. Ibarra, *Magnetic properties of Fe/MgO granular multilayers prepared by pulsed laser deposition*, J. Appl. Phys. **105**, 063909 (2009).

J. F. Gibbons, and W. E. Beadle, *Switching properties of thin NiO films*, Solid-State Electron. **7**, 785 (1964).

J. L. Gittleman, Y. Golstein and S. Bozowski, *Magnetic properties of granular nickel films*, Phys. Rev. B **5**, 3609 (1972).

M. Gładysiewicz, R. Gonczarek and M. Mulak, *The form and properties of the tight-binding density of states in two dimensions. Possible application to superconductivity*, Acta Physica Polonica A **101**, 865 (2002).

H. L. Gomes, P. Stallinga, M. Cölle, D.M. de Leeuw and F. Biscarini, *Electrical instabilities in organic semiconductors caused by trapped supercooled water*, Appl. Phys. Lett. **88**, 082101 (2006).

F. Greullet, C. Tiusan, F. Montaigne, M. Hehn, D. Halley, O. Bengone, M. Bowen, and W. Weber, *Evidence of a symmetry-dependent metallic barrier in fully epitaxial MgO based magnetic tunnel junctions*, Phys. Rev. Lett. **99**, 187202 (2007).

W. Guan, S. Long, R. Jia, and M. Liu, *Nonvolatile resistive switching memory utilizing gold nanocrystals embedded in zirconium oxide*, Appl. Phys. Lett. **91**, 062111 (2007).

B. J. Hattink, M. G. Muro, Z. Konstantinovic, X. Batlle, A. Labarta and M. Varela, *Tunneling magnetoresistance in Co-*ZrO_2 *granular thin films*, Phys. Rev. B **73**, 045418 (2006).

M. Hayashi, L. Thomas, R. Moriya, C. Rettner, S. S. Parkin, *Current-controlled magnetic domain-wall nanowire shift register*, Science **320**, 209 (2008).

J. S. Helman and B. Abeles, *Tunneling of spin-polarized electrons and magnetoresistance in granular Ni films*, Phys. Rev. Lett. **37**, 1429 (1976).

T. W. Hickmott, *Low-frequency negative resistance in thin anodic oxide films*, J. Appl. Phys. **33**, 2669 (1962).

S. Ikeda, J. Hayakawa, Y. Ashizawa, Y. M. Lee, K. Miura, H. Hasegawa, M. Tsunoda, F. Matsukura, and H. Ohno, *Tunnel magnetoresistance of* 604% *at 300 K by suppression of Ta diffusion in CoFeB/MgO/CoFeB pseudo-spin-valves annealed at high temperature*, Appl. Phys. Lett. **93**, 082508 (2008).

J. Inoue and S. Maekawa, *Theory of tunneling magnetoresistance in granular magnetic films*, Phys. Rev. B **53**, 11927 (R) (1996).

H. Itoh, J. Inoue, A. Umerski and J. Mathon, *Quantum oscillation of magnetoresistance in tunneling junctions with a nonmagnetic spacer*, Phys. Rev. B **68**, 174421 (2003).

R. Jin, J. He, J. R. Thompson, M. F. Chisholm, B. C. Sales, and D. Mandrus, *Fluctuation effects on the physical properties of* $Cd_2Re_2O_7$ *near 200 K* J. Phys.:

Condens. Matter **14**, L117 (2002).

P.A.E. Jonkers, *Current perpendicular to plane giant magnetoresistance and tunneling magnetoresistance treated with unified model*, Phys. Rev. B **65**, 144444 (2002).

M. Julliere, *Tunneling between ferromagnetic films*, Phys. Lett. A **54**, 225 (1975).

G. N. Kakazei, P. P. Freitas, S. Cardoso, A. M. L. Lopes, Yu. G. Pogorelov, J. A. M. Santos, J. B. Sousa, *Transport properties of discontinuous $Co_{80}Fe_{20}/Al_2O_3$ multilayers, Prepared by ion beam sputtering*, IEEE Trans. Mag. **35**, 2895 (1999).

G.N. Kakazei, A.M.L. Lopes, Yu.G. Pogorelov, J.A.M. Santos, J.B. Santos, P.P. Freitas, S. Cardoso, E. Snoeck, *Time-dependent transport effects in CoFe/Al_2O_3 discontinuous multilayers*, J. Appl. Phys. **87**, 6328 (2000).

G. N. Kakazei, Yu. G. Pogorelov, A. M. L. Lopes, J. B. Sousa, P. P. Freitas, S. Cardoso, M. M. Pereira Azevedo and E. Snoeck, *Tunnel magnetoresistance and magnetic ordering in ion-beam sputtered CoFe/Al_2O_3 discontinuous multilayers*, J. Appl. Phys. **90**, 4044 (2001).

G. N. Kakazei, Yu. G. Pogorelov, J. A. M. Santos, J. B. Sousa, P. P. Freitas, S. Cardoso, N. A. Lesnik and P. E. Wigen, *Current-in-plane transport in granular single layers and multilayers of CoFe in Al_2O_3*, J. Magn. Magn. Mat. **266**, 57 (2003).

C. Kittel, *Quantum theory of solids.* John Wiley & Sons, Inc., New York, USA (1963).

W. Kleemann, Ch. Binek, O. Petracic, G.N. Kakazei, Yu.G. Pogorelov, M.M. Pereira de Azevedo, J.B. Sousa, P.P. Freitas, *Interacting ferromagnetic nanoparticles in discontinuous $Co_{80}Fe_{20}/Al_2O_3$ multilayers: from superspin glass to reentrant superferromagnetism*, Phys. Rev. B **63**, 134423 (2001).

I. N. Krivorotov, N. C. Emley, J. C. Sankey, S. I. Kiselev, D. C. Ralph, R. A. Buhrman, *Time-domain measurements of nanomagnet dynamics driven by spin-*

transfer torques, Science **307**, 228 (2005).

H. Kubota, A. Fukushima, K. Yakushiji, T. Nagahama, S. Yuasa, K. Ando, H. Maehara, Y. Nagamine, K. Tsunekawa, D. D. Djayaprawira, N. Watanabe, and Y. Suzuki, *Quantitative measurement of voltage dependence of spin-transfer torque in MgO-based magnetic tunnel junctions*, Nat. Phys. **4**, 37 (2008).

M. Lampert, *Simplified theory of space-charge-limited currents in an insulator with traps*, Phys. Rev. **103**, 1648 (1956).

L.D. Landau, E.M. Lifshitz. *Statistical Physics*, Pergamon Press (1985).

R. Landauer, *Spatial variation of currents and fields due to localized scatterers in metallic conduction*, IBM J. Res. Dev. **1**, 223 (1957).

P. LeClair, H. J. M. Swagten, J. T. Kohlhepp, R. J. M. van de Veerdonk, and W. J. M. de Jonge, *Apparent spin polarization decay in Cu-dusted Co/Al_2O_3 tunnel junctions*, Phys. Rev. Lett. **84**, 3029 (2000).

P. LeClair, J. T. Kohlhepp, H. J. M. Swagten and W. J. M. de Jonge, *Interfacial density of states in magnetic tunnel junctions*, Phys. Rev. Lett. **86**, 1066 (2001); P. LeClair, B. Hoex, H. Wieldraaijer, J. T. Kohlhepp, H. J. M. Swagten and W. J. M. de Jonge, *Sign reversal of spin polarization in Co/Ru/Al_2O_3/Co magnetic tunnel junctions*, Phys. Rev. B **64**, 100406(R) (2001).

N. A. Lesnik, P. Panissod, G. N. Kakazei, Yu. G. Pogorelov, J. B. Sousa, E. Snoeck, S. Cardoso, P. P. Freitas and P. E. Wigen, *Local structure in CoFe/Al_2O_3 multilayers determined by nuclear magnetic resonance*, J. Magn. Magn. Mat. **242**, 943 (2002).

A. Manchon, N. Strelkov, A. Deac, A. Vedyayev and B. Dieny, *Interpretation of relationship between current perpendicular to plane magnetoresistance and spin torque amplitude*, Phys. Rev. B **73**, 184418 (2006).

J. Mathon, M. Villeret, and H. Itoh, *Selection rules for oscillations of giant magnetoresistance with nonmagnetic spacer layer thickness*, Phys. Rev. B **52**, R6983

(1995).

J. Mathon, Phys. Rev. B **55**, 960 (1997).

J. Mathon and A. Umerski, *Theory of tunneling magnetoresistance in a junction with a nonmagnetic metallic interlayer*, Phys. Rev. B **60**, 1117 (1999).

J. Mathon and A. Umerski, *Theory of tunneling magnetoresistance of an epitaxial Fe/MgO/Fe(001) junction*, Phys. Rev. B **63**, 220403(R) (2001).

J. Mathon and A. Umerski, *Theory of resonant tunneling in an epitaxial Fe/Au/MgO /Au/Fe(001) junction*, Phys. Rev. B **71**, 2204021(R) (2005).

Z. Mao, D. Chen and Z. He, *Role of interparticle coupling on the tunneling magnetoresistance of granular films in interacting superparamagnetic system*, J. Magn. Magn. Mat. **320**, 642 (2008).

E. B. Myers, D. C. Ralph, J. A. Katine, R. N. Louie and R. A. Buhrman, *Current-induced switching of domains in magnetic multilayer devices*, Science **285**, 867 (1999).

S. Mitani, S. Takanashi, K. Yakushiji, S. Maekawa and H. Fujimori, *Enhanced magnetoresistance in insulating granular systems: evidence for higher-order tunneling*, Phys. Rev. Lett. **81**, 2799 (1998).

J. S. Moodera, L. R. Kinder, T. M. Wong, and R. Meservey, *Large magnetoresistance at room temperature in ferromagnetic thin film tunnel junctions*, Phys. Rev. Lett. **74**, 3273 (1995).

J. S. Moodera, J. Nowak, and R. J. M. van de Veerdonk, *Interface magnetism and spin wave scattering in ferromagnet-insulator-ferromagnet tunnel junctions*, Phys. Rev. Lett. **80**, 2941 (1998).

J. S. Moodera, J. Nowak, L. R. Kinder and P. M. Tedrow, *Quantum well states in spin-dependent tunnel structures*, Phys. Rev. Lett. **83**, 3029 (1999).

Ch. Morawe and H. Zabel, *Structure and thermal stability of sputtered metal/oxide multilayers: the case of* Co/Al_2O_3, J. Appl. Phys. **77**, 1969 (1995).

N. F. Mott and R. W. Gurney, *Electronic processes in ionic crystals*, Oxford University Press, New York, 1940.

Y. B. Nian, J. Strozier, N. J. Wu, X. Chen, and A. Ignatiev, *Evidence for an oxygen diffusion model for the electric pulse induced resistance change effect in transition-metal oxides*, Phys. Rev. Lett. **98**, 146403 (2007).

T. Nozaki, N. Tezuka, and K. Inomata, *Quantum oscillation of the tunneling conductance in fully epitaxial double barrier magnetic tunnel junctions*, Phys. Rev. Lett. **96**, 027208 (2006).

T. Oka and N. Nagaosa, *Interfaces of correlated electron systems: proposed mechanism for colossal electroresistance*, Phys. Rev. Lett. **95**, 266403 (2005).

O. Ozatay, P. G. Gowtham, K. W. Tan, J. C. Read, K. A. Mkhoyan, M. G. Thomas, G. D. Fuchs, P. M. Braganca, E. M. Ryan, K. V. Thadani, J. Silcox, D. C. Ralph and R. A. Buhrman, *Sidewall oxide effects on spin-torque- and magnetic-field-induced reversal characteristics of thin-film nanomagnets*, Nat. Mater. **7**, 567 (2008).

S. S. P. Parkin, C. Kaiser, A. Panchula, P. M. Rice, B. Hughes, M. Samant, and S.-H. Yang, *Giant tunneling magnetoresistance at room temperature with MgO (100) tunnel barriers*, Nat. Mater., **3**, 862 (2004).

S. Petit, C. Baraduc, C. Thirion, U. Ebels, Y. Liu, M. Li, P. Wang and B. Dieny, *Spin-torque influence on the high-frequency magnetization fluctuations in magnetic tunnel junctions*, Phys. Rev. Lett **98**, 077203 (2007).

M. Respaud, J. M. Broto, H. Rakoto, A. R. Fert, L. Thomas, B. Barbara, M. Verelst, E. Snoeck, P. Lecante, A. Mosset, J. Osuna, T. Ould Ely, C. Amiens and B. Chaudret, *Surface effects on the magnetic properties of ultrafine cobalt particles*, Phys. Rev. B **57**, 2925 (1998).

W. H. Rippard, M. R. Pufall, S. Kaka, S. E. Russek, and T. J. Silva, *Direct-current induced dynamics in $Co_{90}Fe_{10}/Ni_{80}Fe_{20}$ point contacts*, Phys. Rev. Lett. **92**, 027201 (2004).

B. Romeira, J. M. L. Figueiredo, T. J. Slight, L. Wang, E. Wasige, C. N. Ironside, J. M. Quintana, and M. J. Avedillo, *Synchronisation and chaos in a laser diode driven by a resonant tunnelling diode*, IET Optoelectron. **2**, 211 (2008).

A. Rose, *Space-charge-limited currents in solids*, Phys. Rev. **97**, 1538 (1955).

S. Sahoo, O. Petracic, W. Kleemann, S. Stappert, G. Dumpich, P. Nordblad, S. Cardoso, and P. P. Freitas, App. Phys. Lett. **82**, 4116 (2003).

S. Sahoo, O. Petracic, Ch. Binek, W. Kleemann, J. B. Sousa, S. Cardoso, and P. P. Freitas, Phys. Rev B **65**, 134406 (2002).

J. A. M. Santos, G.N. Kakazei, J.B. Sousa, S. Cardoso, P.P. Freitas, Yu.G. Pogorelov, E. Snoeck, *Peculiar CIP transport in $CoFe/Al_2O_3$ granular layered films across a micro-gap*, J. Magn. Magn. Mat. **242**, 485 (2002).

J. A. M. Santos, *Magnetismo e fenómenos de transporte com comportamento não-convencional: Filmes nano-granulares e sistemas de terras raras com interacções competitivas*, PhD thesis, Universidade do Porto, 2004.

A. Sawa, *Resistive switching in transition metal oxides*, Materials Today **11**, 28 (2008).

D. M. Schaadt, E.T. Yu, S. Sankar, A.E. Berkowitz, *Charge storage in Co nanoclusters embedded in SiO2 by scanning force microscopy*, Appl. Phys. Lett. **74**, 472 (1999).

K. M. Schep, P. J. Kelly, and G. E. W. Bauer, *Giant magnetoresistance without defect scattering*, Phys. Rev. Lett. **74**, 586 (1995).

P. Sheng and B. Abeles, *Voltage-Induced Tunneling Conduction in Granular Metals*

at Low Temperatures, Phys. Rev. Lett. **28**, 34 (1972).

P. Sheng, B. Abeles and Y. Aire, *Hopping conductivity in granular metals*, Phys. Rev. Lett. **31**, 44 (1973).

L. Sheng, Y. Chen, H. Y. Teng, and C. S. Ting, *Nonlinear transport in tunnel magnetoresistance systems*, Phys. Rev. B **59**, 480 (1999).

M. Silva, *Estudo experimental de estruturas magnéticas moduladas nos compostos intermetálicos $NdRu_2Si_2$ e $TbRu_2Si_2$*, PhD thesis, Universidade do Porto, 1999.

J. G. Simmons, and R. R. Verderber, *New conduction and reversible memory phenomena in thin insulating films*, Proc. R. Soc. London, Ser. A **301**, 77 (1967).

J. C. Slonczewski, *Conductance and exchange coupling of two ferromagnets separated by a tunneling barrier*, Phys. Rev. B **39**, 6995 (1989).

J.C. Slonczewski, *Current-driven excitation of magnetic multilayers*, J. Magn. Magn. Mat., **159** L1-L7 (1996).

J. B. Sousa, G. N. Kakazei, Yu. G. Pogorelov, J. A. M. Santos, O. Petracic, W. Kleemann, Ch. Binek, S. Cardoso, P. P. Freitas, M. M. Pereira Azevedo, N. A. Lesnik, M. Rokhlin and P. E. Wigen, *Magnetic states of granular layered CoFe-Al_2O_3 system*, IEEE Trans. Mag. **37**, 2200 (2001).

J. B. Sousa, J. A. M. Santos, R. F. A. Silva, J. M. Teixeira, J. Ventura, J. P. Arajo, P. P. Freitas, S. Cardoso, Yu. G. Pogorelov, G. N. Kakazei, and E. Snoeck, *Peculiar magnetic and electrical properties near structural percolation in metal-insulator granular layers*, J. Appl. Phys. **96**, 3861 (2004).

J. J. Sun, P. P. Freitas, *Dependence of tunneling magnetoresistance on ferromagnetic electrode thickness and on the thickness of a Cu layer inserted at the Al_2O_3/CoFe interface*, J. Appl. Phys. **85**, 5264 (1999).

S. M. Sze *Physics of Semiconductor Devices*, 2nd Edition. USA: John Wiley & Sons,

Inc., 1981.

C. Tanase, P. W. M. Blom and D. M. de Leeuw, *Origin of the enhanced space-charge-limited current in poly(p-phenylene vinylene)*, Phys. Rev. B **70**, 193202 (2004).

P.M. Tedrow and R. Meservey, *Spin-dependent tunneling into ferromagnetic nickel*, Phys. Rev. Lett. **26**, 192 (1971).

N. Tezuka and T. J. Miyazaki, *Barrier height dependence of MR ratio in Fe/Al-oxide/Fe junctions*, J. Magn. Magn. Mater. **177-181**, Part 2, 1283 (1998).

I. Theodonis, N. Kioussis, A. Kalitsov, M. Chshiev and W. H. Butler, *Anomalous bias dependence of spin torque in magnetic tunnel junctions*, Phys. Rev. Lett. **97**, 237205, (2006).

I. Theodonis, A. Kalitsov and N. Kioussis, *Enhancing spin-transfer torque through the proximity of quantum well states*, Phys. Rev. B **76**, 224406 (2007).

T. B. Tran, I. S. Beloborodov, Jingshi Hu, X. M. Lin, T. F. Rosenbaum, and H. M. Jaeger, *Sequential tunneling and inelastic cotunneling in nanoparticle arrays*, Phys. Rev. B **78**, 075437 (2008).

M. Tsoi, A. G. M. Jansen, J. Bass, W.-C. Chiang, M. Seck, V. Tsoi and P. Wyder, *Excitation of a magnetic multilayer by an electric current*, Phys. Rev. Lett. **80**, 4281 (1998).

C. Tu, D. Kwong, and Y. Lai, *Negative differential resistance and electrical bistability in nanocrystal organic memory devices*, Appl. Phys. Lett. **89**, 252107 (2006).

A. A. Tulapurkar, Y. Suzuki, A. Fukushima, H. Kubota, H. Maehara, K. Tsunekawa, D. D. Djayaprawira, N. Watanabe and S. Yuasa, *Spin-torque diode effect in magnetic tunnel junctions*, Nature **438**, 339 (2005).

T. Valet and A. Fert, *Theory of the perpendicular magnetoresistance in magnetic*

multilayers, Phys. Rev. B **48**, 7099-7113, (1993).

A. Vedyaev, N. Ryzhanova, C. Lacroix, L. Giacomoni, and B. Dieny, *Resonance in tunneling through magnetic valve tunnel junctions*, Europhys. Lett. **39**, 219 (1997).

A. Vedyaev, M. Chshiev, N. Ryzhanova and B. Dieny, *Magnetoresistance of magnetic tunnel junctions in the presence of a nonmagnetic layer*, Phys. Rev. B **61**, 1366 (2000).

J. Ventura, *Magnetic Nanostructures*, PhD thesis, Universidade do Porto, 2006.

J. Ventura, Z. Zhang, Y. Liu, J. B. Sousa and P. P. Freitas, *Electrical current induced pinhole formation and insulator-metal transition in tunnel junctions*, J. Phys.: Condens. Matter **19**, 176207 (2007).

J. Ventura, J. M. Teixeira, J. P. Araujo, J. B. Sousa, P. Wisniowski and P. P. Freitas, *Pinholes and temperature-dependent transport properties of MgO magnetic tunnel junctions*, Phys. Rev. B **78**, 024403 (2008).

J. Yang, J. Wang, Z. M. Zheng, D. Y. Xing and C. R. Chang, *Quantum oscillations of tunneling magnetoresistance in magnetic tunnel junctions*, Phys. Rev. B **71**, 214434 (2005).

S. Yuasa, T. Nagahama and Y. Suzuki, *Spin-Polarized resonant tunneling in magnetic tunnel junctions*, Science **297**, 234 (2002); S. Yuasa, T. Nagahama, T. Kawakami, K. Ando and Y. Suzuki, *A large quantum-well oscillation of the TMR effect*, J. Phys. D: Appl. Phys. **35**, 2427 (2002).

S. Yuasa, T. Nagahama, A. Fukushima, Y. Suzuki and K. Ando, *Giant room-temperature magnetoresistance in single-crystal Fe/MgO/Fe magnetic tunnel junctions*, Nat. Mater., **3**, 868 (2004).

S. Yuasa, A. Fukushima, H. Kubota, Y. Suzuki, and K. Ando, *Giant tunneling magnetoresistance up to* 410% *at room temperature in fully epitaxial Co/MgO/Co magnetic tunnel junctions with bcc Co(001) electrodes*, Appl. Phys. Lett. 89, 042505

(2006).

S. Yuasa and D. D. Djayaprawira, *Giant tunnel magnetoresistance in magnetic tunnel junctions with a crystalline MgO(001) barrier*, J. Phys. D: Appl. Phys. **40**, R337-354 (2007).

X. F. Wang, P. Vasilopoulos, and F. M. Peeters, Appl. Phys. Lett. **80**, 1400 (2002).

S. Wang, Y. Xu and K. Xia, *First-principles study of spin-transfer torques in layered systems with noncollinear magnetization*, Phys. Rev. B **77**, 184430 (2008).

R. Waser, and M. Aono, *Nanoionics-based resistive switching memories*, Nat. Mater. **6**, 833 (2007).

M. Wilczyński, J. Barnaś and and R. Świrkowicz, *Free-electron model of current-induced spin-transfer torque in magnetic tunnel junctions*, Phys. Rev. B **77**, 054434 (2008).

X. Zhang, B. Li, G. Sun and F. Pu, *Spin-polarized tunneling and magnetoresistance in ferromagnet/insulator(semiconductor) single and double tunnel junctions subjected to an electric field*, Phys. Rev. B **56**, 5484 (1997).

S. Zhang and P. M. Levy, *Magnetoresistance of magnetic tunnel junctions in the presence of a nonmagnetic layer*, Phys. Rev. Lett. **81**, 5660 (1998).

Z. Zheng, Y. Qi, D. Y. Xing and J. Dong, *Oscillating tunneling magnetoresistance in magnetic double-tunnel-junction structures*, Phys. Rev. B **59**, 14505 (1999).

T. Zhu and Y. J. Wang, *Enhanced tunneling magnetoresistance of Fe-Al_2O_3 granular films in the Coulomb blockade regime*, Phys. Rev. B **60**, 11918 (1999).